Mapping the dynamics, star-formation rates, and chemical properties of galaxies with integral field spectroscopy

Swinbank, Anthony Mark

Mapping the Dynamics, Star-Formation Rates, and Chemical Properties of Galaxies with Integral Field Spectroscopy

by Anthony Mark Swinbank
PhD Thesis, May 2005

Abstract

Major advances in the development of instruments for eight and ten meter class telescopes are revolutionising our understanding of galaxy formation. In particular, Integral Field Spectrographs (which produce a three dimensional $(x, y, velocity)$ map of a galaxy) now permit studies of distant galaxies in nearly as much detail as local galaxies in our cosmic neighbourhood.

These instruments can be employed to investigate specific problems in galaxy formation across 90% of the history of the Universe, and we demonstrate their capabilities by probing galaxy evolution from z=0.1 to z=3.

Locally, post-starburst (E+A) galaxies are thought to represent the transitional phase of galaxy evolution which links star-forming (late type) galaxies with their quiescent (early type) end products. We demonstrate that integral field spectroscopy can be employed to disentangle the stellar and dynamical structures of this post-starburst phase and therefore constrain the trigger (or triggers) of this phase of galaxy evolution.

At higher redshift, (i.e., above z=1), "normal" galaxies are frequently too small and faint to observe via conventional observations. However, gravitational lensing by galaxy clusters provides us with a unique tool to study distant galaxies. By coupling the lensing phenomenon with Integral Field Spectroscopy, we investigate the evolution of the relation between the baryonic and non-baryonic components of galaxies from z=1 to the present day through the Tully-Fisher Relation. By reconstructing the source morphologies and velocity fields of lensed galaxies, we find evidence for 0.5mag of brightening in the rest-frame B-band, but <0.1mag of evolution in the rest frame I-band, suggesting a clear preference for hierarchical growth of structure and increased star-formation activity at z=1. At these high redshifts, some galaxies (such as radio galaxies and SCUBA galaxies) are frequently bright enough and extended enough to study without the boost of a gravitational lens, and therefore can provide important comparison samples with which we can understand how high redshift proto-galaxies evolve into their present day descendants.

By targeting the rest frame optical properties of SCUBA galaxies with traditional near-infrared longslit spectroscopy we find that the high redshift sub-mm population share many characteristics with the somewhat less luminous far-infrared galaxies identified in the local Universe. This includes the Hα equivalent widths, the proportion of obvious AGN and the typical spectral classification. Yet there remain important differences, with proportionally more highly-obscured activity in the high-redshift population, apparently larger dynamical mass, lower metallicities and much higher gas fractions on 10-kpc scales.

With this sample of far-infrared luminous galaxies in hand, we use integral field spectroscopy to study the structural and dynamical properties of powerful high redshift SCUBA galaxies. We show the power of combining optical and near-infrared integral field spectroscopy to probe the power sources, masses and metallicities of powerful, distant galaxies, as well as understanding the role of AGN- and star-burst driven feedback processes in these high redshift systems.

PREFACE

The work presented in this thesis was carried out between October 2002 and May 2005 while the author was a research student under the joint supervision of Prof. Richard Bower and Prof. Ian Smail, in the Department of Physics at the University of Durham.

The major part of the work presented in this thesis is the author's own work except where specifically noted in the text, as summarised below.

- Dr. George Hau (Durham) performed the cross correlation analysis and age dating of the A-star population in the E+A galaxy in Chapter 2
- Dr. Graham Smith (Caltech) constructed the lens models and provided the lens inversion matrices for the arcs in Chapters 3 & 4 using the same techniques developed by Kneib et al. (1993).
- Prof. Richard Bower (Durham) and Dr. Andrew Bunker (Cambridge) conducted the GMOS IFU observations of A 2218 arc#289 and SCUBA galaxy N2-850.4
- Prof. Andrew Blain (Caltech) computed the far-infrared luminosities of the SCUBA galaxies in Chapter 5 using the techniques described in Blain et al. (2003)

Mapping the Dynamics, Star-Formation Rates, and Chemical Properties of Galaxies with Integral Field Spectroscopy

by Anthony Mark Swinbank

A thesis submitted to the University of Durham
in accordance with the regulations for
admittance to the Degree of Doctor of Philosophy.

Department of Physics
University of Durham
May 2005

Contents

List of Figures

List of Tables

Declaration

This work has not been submitted for any other degree at the University of Durham or any other University.

Portions of this work have appeared in the following papers:

- Swinbank, A. M., Smith, J., Bower, R. G., Bunker, A., Smail, I., Ellis, R. S., Smith, G. P., Kneib, J.-P., Sullivan, M., Allington-Smith, J. R., 2003, ApJ, 598, 162: **Galaxies Under the Cosmic Microscope: A GMOS Study of the Lensed Galaxy #289 in A2218**
- Swinbank, A. M., Smail, I., Chapman, S. C., Blain, A. W., Ivison, R. J., Keel, W. C., 2004 ApJ, 617 64: **The Rest Frame Optical Spectra of SCUBA galaxies**
- Swinbank, A. M., Balogh, M. L., Bower, R. G., Hau, G., Allington-Smith, J. R. 2004 ApJ 622 260: **GMOS Integral Field Spectroscopy of a Merging System with Enhanced Balmer Absorption**
- Swinbank, A. M., Smail, I., Bower, R. G., Borys, C., Chapman, S. C., Blain, A. W., Ivison, R. J., Keel, W. C., Ramsey Howat, S. K., Bunker, A. J., 2005 MNRAS 359 401: **Optical and Near Infrared Integral Field Spectroscopy of the SCUBA Galaxy N2 850.4**
- Swinbank, A. M., Bower, R. G., Smail, I., Smith, G. P., Ellis, R. S., Kneib, J.-P., Stark, D., Bunker, A. J., 2005 MNRAS submitted: **Galaxies Under the Cosmic Microscopy: Resolved Spectroscopy and New Constraints on the z~1 Tully Fisher Relation**
- Swinbank, A. M., Smail, I., Borys, C., Chapman, S. C., Blain, A. W., Ivison, R. J., 2005 MNRAS submitted: **Near Infrared Near-Infrared Integral Field Spectroscopy of SCUBA Galaxies**

The author has also either worked on, or been involved in the following work:

- Smith, J., Bunker, A., Vogt, N., Abraham, R., Bower, R., Parry, I., Aragon-Salamanca, A., Sharp, R., Swinbank, A. M., 2004, MNRAS 354 19: *Near-infrared integral field spectroscopy of CFRS 22.1313 with CIRPASS*
- Ivison, R. J., Greve, T., Dunlop, J., Swinbank, A. M., Stevens, J., Mortier, A., Serjent, S., Bertoldi, F., Smail, I., Blain, A. J., Chapman, S. C., 2005, MNRAS submitted *A Robust Sample of Submillimeter Galaxies: Constraints on the Prevalence of High-Redshift Starbursts*

Conference Proceedings:

- Bunker, A. J., Smith, J. K., Parry, I., Sharp, R., Dean, A., Gilmore, G., Bower, R. G, Swinbank, A. M., Davies, R., Metcalf, R., Grijs, R., 2004 AN 325 139 *Extra-Galactic Integral Field Spectroscopy on the Gemini Telescopes* Proceedings from the Euro3D anual network meeting (ed. J. Walsh).
- Morris, S. L., Gerssen, J., Swinbank, A. M., Wilman, R., 2005 (Elsevier Science submitted) *Potential Science for the OASIS Integral Field Unit with Laser Guide Star Adaptive Optics* Proceedings from the William Hershel Adaptive Optics Integral Field Spectroscopy Confrence

Acknowledgements

It is a real privilege to thank my supervisors Richard Bower and Ian Smail for all of their excellent guidance over the last three years. Richards enthusiasm and knowledge of the subjects, coupled to Ian's efficiency for getting things done. To them both I would like to say a heartfelt *thankyou*.

There are many other people in Durham to whom I am also indebted. In particular I would like to thank David Gilbank for always knowing everything. I am very grateful to Alastair Edge, whose ability to look at the big picture significantly contributed to keeping me on the straight and narrow. I am also grateful to Chris Simpson and Richard Wilman for countless conversations and advice over the last three years. I would also like to thank Carlton Baugh, who always managed to give a fair theoreticians view of observational astronomy, (although his views on the football are somewhat misguided!).

There are many other astronomers which I would like to thank, in particular: Mike Balogh, Andrew Blain, Scott Chapman, Shaun Cole, Vince Eke, Graham Smith, John Lucey, Simon Morris, George Hau, Phil Outram, and Tom Shanks to name a few.

Thanks to Alan Lotts and Lydia Heck for keeping the Durham computer network going, and Peter Draper for the many useful chats about the Starlink software, without which I would still be trying to reduce the data in this thesis to this day.

I would also like to thank all of the other postgraduates in Durham, my office mates: Nathan Courtney, John Helly, Craig Booth, and Greg Davies; Next door: Dave Wilman, Richard Whitaker, Rowena Malbon, Claudio Dalla-Vecchia, Noam Libeskind, and across the corridor Rob Crain, Jim Geach, Bill Frith, and Nick Ross all of whom deserve much praise.

I am also deeply grateful to John McCue who first got me interested in Astronomy. Without John's astronomy classes in the early 90's I would never have come this far.

I am, of course, deeply indebted to my parents for all of their support over the last twenty-something years. There are only two things I've ever really wanted to do, astronomy and farming, and over the last few years I've been luckily enough to be able to do both (sometimes simultaneously!).

Finally, to the person who I first met in Tom Shanks' tutor group all of those years ago. Words can not express how lucky I am to have Julie as my wife. She is an inspiration to me and I just want to say "thank you".

Chapter 1 | *Introduction*

1.1 Introduction

Understanding the processes which take the initial perturbations in the primordial density field and produce the dense, gravitationally bound galaxies is a key observational goal in modern cosmology. By combining general relativity, radiative transfer, gas dynamics and cooling with models of non-linear growth the wide range of these (well understood) physical processes can be investigated both analytically and numerically. However, the wide range of possible outcomes from these intimately connected processes ensures a wealth of variety in galaxy types and evolution across the whole history of the Universe, and therefore one of the most active areas of observational cosmology is to constrain models for galaxy formation. This is achieved by observing both the fossil records in nearby galaxies and by observing the morphologies, kinematics, sizes and chemical abundances of distant (and therefore younger) galaxies in a level of detail comparable to their local counterparts.

Such contemporary scientific programs, by their very nature, push the limits of astronomical instrumentation. In turn, advances in instrumentation (particularly in the near-infrared) have provided efficient spectrographs which can take advantage of the increased light grasp of eight and ten meter class telescopes. Only recently reaching maturity on large telescopes, integral field spectrographs now allow us to study distant galaxies in an unprecedented level of detail and therefore to resolve some of the most pressing questions regarding galaxy formation. In particular, in the last decade a wealth of observational data, gathered with both eight meter class telescopes and the Hubble Space Telescope have probed important epochs in the evolution of the Universe and its constituents. One of the most remarkable results is the ubiquitous presence of galaxies at $z>3$. At such high redshifts the Universe was only around one eighth of its present age (between one and two billion years after the Big Bang). Although numerous, little is known about galaxies at these redshifts and therefore one of the major areas of extragalactic astronomy is to gain insight into some of their intrinsic properties. Indeed, the remarkable fact that some of these galaxies are already massive, with super-massive black holes is a powerful constraint for galaxy formation models.

In this thesis we exploit traditional longslit and Integral Field Spectroscopy of nearby and distant galaxies to study the processes of galaxy evolution by observing the fossil records of local galaxies and the star-formation rates, chemical properties and dynamics of high-redshift galaxies.

1.2 Island Universes

The first detailed studies of galaxies external to our own (excluding the Magellanic Clouds which are visible with the naked eye and have therefore undoubtedly been viewed by human eyes for a millenia) were made by the Irish Astronomer, the Earl of Rosse in the 1840's. Lord Rosse build a 72-inch (1.8m) reflecting telescope in the grounds of Birr

Castle, Parsontown. The telescope (by far the largest in the world at the time) was 17 meters long and required the supporting force of two masonry walls. The so-called Leviathan of Parsontown was used mainly for the study of "spiral nebulae", with the most noticeable discovery being the spiral nature of M51 (the Whirlpool Galaxy). Debate about the true nature of these "spiral nebulae" (as they were then known) raged, indeed around a hundred years earlier, both the Durham-based Thomas Wright and Immanuel Kant had already suggested these spiral nebula were "island universes" (i.e. stellar systems comparable to our own Milky-Way rather than gaseous nebula internal to our Milky-Way). The debate was finally resolved when, in 1929 Hubble postulated that a Cepheid Variable in the Andromeda nebulae was external to the Milky-Way. Using a Period-Luminosity relation his distance measurement provided the first evidence that an object lay beyond our own galaxy (Hubble, 1929). The distance to M31, which is known to be around 1 Mpc provided the first conclusive evidence that a galaxy lay outside our own (the size of the Milky-Way (although uncertain) was already known to be much smaller than 1 Mpc; Shapley 1919).

As early as the eighteenth century, the French astronomer, Messier recorded the positions of about 100 of these nebulae, and noted the exceptional concentration in (which we now know to be) the Virgo constellation of galaxies (Messier, 1784). William Hershel also noted that the positions of these objects weren't simply random, they were correlated with some patches of sky having noticeably higher than average numbers of these nebulae. In particular he noticed the Coma Cluster was particularly over-dense (Herschel, 1785). Hubble's discovery in the early twentieth century that these nebulae were in fact extra-galactic galaxies quickly lead to the conclusion that the Universe contained thousands of galaxies, groups and clusters.

Today, millions of galaxies and thousands of groups and clusters are known. In fact the first major cluster catalogues was constructed by Abell (1958) containing 2,712 clusters north of $\delta = -20°$.

1.3 The Standard Model

1.3.1 The Big Bang

In 1917 Einstein postulated the existence of a cosmological constant (Λ) which he required in order to force a static Universe from collapsing under the force of gravity. The Universe, as Einstein knew it, was infinite, static and unchanging. However, in 1931 Hubble not only proved galaxies external to our own, but also discovered a correlation between distance and recessional velocity of nearby galaxies (Hubble and Humason, 1931). Arguably, Hubble made one of the greatest discovery in scientific history – the Universe was expanding.

The detection of the 3°K cosmic microwave background (CMB) by Penzias and Wilson in 1966 furthered the evidence that the Universe was once much hotter and smaller (Penzias and Wilson, 1965). More recently WMAP mapped the CMB in unprecedented detail, tying down the temperature as 2.726°K. The resulting CMB power spectrum (P_k) is sensitive to the parameter $\Omega_{dm}h^{-2}$. In contrast, the matter power spectrum (which has been well constrained from the galaxy correlation function from galaxy redshift surveys, such as 2dF) is sensitive to $\Omega_{dm}h$. The incorporation of P_k from the galaxy redshift surveys into the CMB analysis therefore breaks the degeneracy between Ω_{dm} and h and has therefore be used to infer a Hubble Constant of H_o=72±5 km s^{-1} Mpc^{-1} (Spergel et al., 2003) (which results in an age of 13.7±0.2 Gyr). Moreover, WMAP mapped the small (10^{-5}) irregularities in the last scattering surface (the "surface of last scattering" is essentially a snapshot from when the photons first freed themselves from the baryonic-photon plasma of the early Universe and shows an imprint of the quantum fluctuations in the

primordial density field). Driven by the initial scalar field, these tiny irregularities were expanded to cosmological scales shortly after the Big-Bang when the Universe underwent a rapid period of inflation (Guth, 1981). These irregularities eventually grew into the galaxies, groups and clusters we see today; (Inflation also offers natural explanations of the flatness and horizon problems and drives the mean density of the Universe close to unity).

1.3.2 Dark Matter

In 1933 Fritz Zwicky used spectroscopic observations of the Shapley 8 super-cluster to prove that the galaxies were moving far too fast to be gravitationally bound, requiring ~10–100 times more matter if the galaxies were in bound orbits (Zwicky, 1933). Zwicky postulated the existence of invisible mass, or "Dark Matter" which was keeping the galaxies bound within the cluster. On smaller scales, evidence for Dark Matter came from observations of spiral galaxy rotation curves, which indicate that the rotation speed of such galaxies is almost constant with radius over a range of scales whereas the enclosed mass of the luminous galaxy is increasing only very slowly (see, for example, Faber and Gallagher, 1979). Such a result suggests the existence of a significant quantity of non-luminous matter within these galaxies.

Both theoretical and observational results lead to the conclusion that the Universe is dominated by dark matter. Whilst the particle responsible has yet to be directly detected, it is clear that it does not reflect light and only interacts through gravity. Theories of the nature of this dark matter include both baryonic and non-baryonic material. For example, the dark matter could consist of brown dwarfs, planets or even black holes. Barring the possibility for a low value of H_0, the dark matter is most likely non-baryonic (the Hubble constant would need to be $\sim 25\,\mathrm{km\,s^{-1}Mpc^{-1}}$ rather than the preferred value of $\sim 75\,\mathrm{km\,s^{-1}Mpc^{-1}}$ for the dark mass to be baryonic). However, from current estimates of the Hubble constant from WMAP, estimates of the abundances of the light elements from primordial nucleosynthesis indicated that only a very small fraction of the required dark mass could be baryonic (Walker et al., 1991). The most likely candidate for non-baryonic dark matter is cold dark matter (i.e. particles that become sub-relativistic shortly after the big bang). Hot dark matter, on the other hand has been ruled out by particle physicists. Hot dark matter consists of light particles (around 30eV) which move relativistically. Numerical simulations show that such particles free stream out of growing density perturbations in the early Universe, producing clustering scales at the present day which are incompatible with observations (White et al., 1983). Cold dark matter, however allows structure to build hierarchically (larger objects are build up by the merging of smaller ones), with a wide range of allowed halo masses at any epoch. Simulations which include cold dark matter also have similar amplitude clustering as the observed galaxy distribution.

1.3.3 The Cosmological Model

Until recently, most of the focus in cosmology has been to tie down the key cosmological parameters; the Hubble constant, (H_0); the matter density, (Ω_m) and the cosmological constant, (Ω_Λ). Large galaxy redshift surveys (such as Sloan and 2dF) have concentrated on measuring the number of galaxies brighter than a given magnitude, which in turn, can be used to constrain the matter density. Coupled to spectroscopic surveys of distant galaxies these can also be used to infer the Hubble constant (e.g., Percival et al., 2002; Hawkins et al., 2003; Cole et al., 2001; Tegmark et al., 2004). However, one of the most remarkable recent results is that the Universe is not only expanding, but also accelerating.

Using distant (z∼1) type 1a supernovae (which are thought to be exploding carbon-oxygen white dwarf stars) as standard candles out to $z \sim 1$, the data show an upturn in the velocity-distance relation at large look-back times (Wang et al., 2003; Tonry et al., 2003). The resulting best fit models suggest a Universe with a "self-repelling" property of space which has become known as the cosmological constant. These results have been combined with the WMAP observations of the CMB. These anisotropies in the CMB show up as temperature variations which, in turn, reflect the maximum over-density or under-densities at the time. Since the maximum size of these snapshot regions is fixed, the observed angle they subtend on the sky is largely a function of the geometry of the universe. By coupling the most recent results on the analysis of these anisotropies (Spergel et al., 2003), the SN1a results and those from large galaxy redshift surveys (such as 2dF and Sloan) a coherent picture is emerging, and it is now generally accepted the baryonic component makes up only 4% of the universe, whilst cold dark matter makes up for 23% and dark energy (the "cosmological constant") accounts for the remaining 73%.

1.3.4 Gravitational Lensing by Galaxy Clusters

Newton (1704) was the first to postulate that light should be deflected by a gravitational field. In particular, Soldner (1804) (assuming Newtonian gravity) calculated the projected angle by which light should be deflected as it passed by the Sun as $\sim 1''$. Over a century later, Einstein's General Theory of Relativity (Einstein, 1915) was employed to predict the deflection angle of a photon as it grazed the surface of the Sun and shortly after Dyson and Eddington (1920) used a total eclipse of the Sun to measure this deflection, and found quantitative agreement between the theoretical value predicted by Einstein (∼1.75″) and their observational value. This provided the first observational evidence in support of Einsteins General Theory of Relativity.

After Hubble's pioneering work which proved that there were galaxies/groups and clusters of galaxies external to our own, Einstein postulated that galaxy clusters could act as gravitational telescopes, although (before Dark Matter was known) the mass of these clusters was thought to be insufficient to cause strong lensing (Einstein, 1936). However, Zwicky applied the virial theorem to clusters of galaxies and derived a mass estimate greater than 100× that of previous estimates (Zwicky, 1933). Zwicky (1937a) then calculated that galaxy clusters should be able to strongly lens and magnify distant galaxies which otherwise would be too faint to observe. Zwicky also noted that precise measurements of the mass of galaxy clusters could also be made by observing these strongly lensed galaxies (Zwicky, 1937b).

Observational evidence of strong lensing by galaxy clusters was finally made when a feature in the core of a rich lensing cluster was spectroscopically identified as a background galaxy. The strongly lensed (z=0.7) galaxy in the core of Abell 370 was the first confirmation of strong lensing by a galaxy cluster (Soucail et al., 1987). Shortly after this discovery, Fort et al. (1988) detected a number of distorted galaxy images in the same cluster which are magnified, but on a weaker level that the giant arc. This result sparked much of the research into gravitational lensing in the late 1980's and early 1990's.

Studies of these strongly lensed galaxies continue to the present day. The launch of the *Hubble Space Telescope* in the early 1990's revolutionised our understanding of the Universe. In particular, observations of the cores of rich lensing clusters turned up numerous strongly lensed arcs and arclets in several clusters. The best studied cluster, Abell2218 (Fig. 1.1) shows several multiply imaged galaxies.

The magnifying power of gravitational lensing thus provides us with the opportunity to study galaxies and galaxy clusters in an level of detail that would otherwise be impossible.

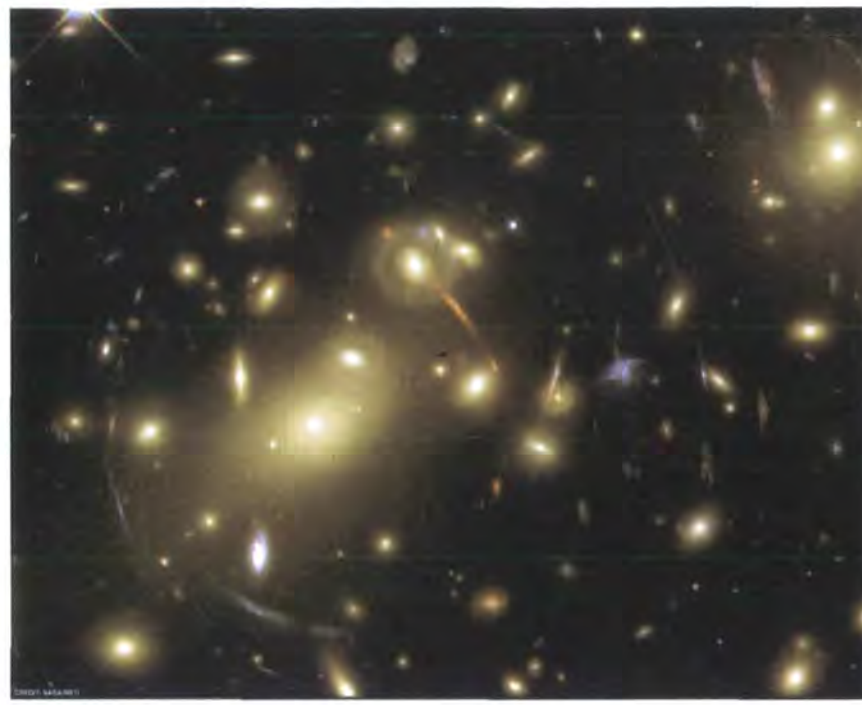

Figure 1.1: True colour *bvi* image of the lensing cluster Abell 2218 at z=0.17. A 2218 is arguably the best studied galaxy cluster lens. The cluster contains a central clump of galaxies with a sub-clump to the East. The cluster also shows several (spectroscopically confirmed) multiply imaged arcs and arclets in the cluster core.(The figure is orientated suc that North is down and East is right)

1.4 Gravitational Lens Modelling

Strong lensing by galaxy clusters can only be used as a useful tool for measuring astrophysical parameters if a suitable model for the lens can be constructed so as to correct for the magnification and distortion produced by the lens. One of the first models was developed by Kneib et al. (1993), and using lens modelling to study galaxies and galaxy clusters is now commonplace and can be used to study several physical properties of clusters. In particular, strong lensing can be employed to measure the total projected mass in the core of a galaxy cluster (e.g., Kneib et al., 1993), as well as the structure and substructure in the cluster core (e.g., Smith, 2003; Smith et al., 2002). If a detailed mass model can be constructed, the background galaxies which have been magnified can also be reconstructed and their properties studied in great detail (e.g., Smail et al., 1996; Soucail et al., 1998). Lens models can also be used to predict the redshifts of arcs and arclets (e.g., Ellis et al., 2001; Ebbels et al., 1998), and can also be used to search for very high redshift galaxies which have been highly magnified by the cluster (e.g., Kneib et al., 2004b,a; Ellis et al., 2001).

In this thesis, we make extensive use of gravitational lens models to study distant (background) galaxies which have been magnified by the foreground cluster. These models were constructed by Dr. Graham Smith (Caltech) and Dr. Jean-Paul Kneib (LAM, Marseille), and whilst the author was not involved in the detailed mass modelling, it is important to review the basics of gravitational lensing and lens modelling here.

1.4.1 The Parametric Technique

Strong lensing is best described by the parametric technique with which one can reconstruct a detailed map of the total cluster mass from the multiple images observed in the central regions of the galaxy cluster. This technique uses the position, shape, relative flux and redshift of multiple images of background galaxies to constrain an analytical description of the mass distribution in a galaxy cluster. The analytical description comprises a super-position of mass components that make up the cluster. Conceptually, therefore, this technique requires solving an equation of the form:

$$\theta_s = \theta_I^j - \alpha(\theta_I^j) f(z_L, z_s, \Omega_o, \Lambda_o, H_o) \tag{1.1}$$

where θ_s is the position on the sky that the lensed galaxy would have in the absence of the foreground cluster lens, θ_I^j is the position on the sky of the j^{th} image of the lensed galaxy, α is the angle through which the light ray is deflected due to the cluster lens and f is a function of redshift of the lens z_L and the source z_s (with geometry (Ω_o, Λ_o) and Hubble constant H_o). Einstein showed that the deflection angle caused by a point mass is given by:

$$\alpha = \frac{4GM}{c^2\eta} \tag{1.2}$$

where M is the mass of the deflecting body, G is Newtons gravitational constant, c is the speed of light in a vacuo and η is the distance that the light passes from the deflector.

Combining equations 1.1 and 1.2 shows that the deflection angle is related to the mass of the lens, and therefore this method produces an analytical mass distribution that best fits the observed positions of the lensed galaxies on the sky. This is best achieved by identifying several images of the same source which have been multiply imaged.

Early progress in developing mass models for galaxy clusters using this technique was encouraging (e.g., Kneib et al., 1993, 1994; Mellier et al., 1991; Kneib et al., 1995). However, the modest spatial resolution of ground-based imaging (FWHM~1") limited the accuracy of the mass models. However, a major improvement was provided by *HST*. With a resolution $FWHM$ ~0.15", *HST* revolutionised observations of clusters and allowed multiple arcs and arclets in crowded cluster cores to be identified. *HST* observations thus allow a dramatic improvement in the precision of cluster lens modelling.

Having identified arcs and arclets in the cluster core of a galaxy cluster, the next step is to spectroscopically identify the redshift of the cluster and the lensed galaxies. Fig. 1.2 shows the geometry of a typical cluster lens. A light ray from a source, S is deflected by an angle, α, and reaches the observer O. The angle between the (arbitrarily chosen) optic axis and the true source position is $\vec{\theta}_s$ and the angle between the optic axis and the image, I, is $\vec{\theta}_I$. Using simple geometry, we can write down that the relationship between the source and image positions and the deflection angle:

$$\vec{\theta}_s = \vec{\theta}_I - \frac{D_{LS}}{D_{os}} \vec{\alpha}(\vec{\theta}_I) \tag{1.3}$$

In general, the lens equation is non-linear and therefore it is possible to have multiple values of $\vec{\theta}_I$ for a single $\vec{\theta}_s$ (which gives rise to the multiple images of a single source often seen in strong lensing, and illustrated in Fig. 1.1).

1.4.2 Working Assumptions

In order to obtain information about the mass distribution in the gravitational lens a set of working assumptions are required since the propagation of light in an arbitrarily curved space-time is complex.

A Peturbative Approach - we assume that the Universe is homogeneous and isotropic on large scales (and therefore matter inhomogeneities which deflect light are local perturbations). Conceptually therefore, we think of a light path from a source to an observer as consisting of three discrete journeys: first, the light travels (unperturbed) from the source to a point near the lens, second, the light path is deflected (perturbed) as it passes through the lens, before third part of its journey in which it then travels unperturbed again to the observer. This can be quantified by considering a gravitational lens at z=0.2 which is lensing a background galaxy at z=1. Both the distance from an observer to a lens and from the lens to the source is ~1 Gpc, which is two to three orders of magnitude greater than the typical size of a galaxy cluster (~5 Mpc). Thus the fraction which the light is deflected by the gravitational lens is far smaller than the total distance travelled by the light. In turn, this leads to our second assumption.

Thin Lens Approximation - we replace the three-dimensional mass distribution in the lens with a two-dimensional mass sheet, orthogonal to the line of sight. This two-dimensional surface is often called the "lens plane" and its surface mass density is characterised by:

$$\Sigma(\vec{\eta}) = \int \rho(\vec{\eta}, l) dl \tag{1.4}$$

where $\vec{\eta}$ is a two dimensional vector in the lens plane and l is the line of sight co-ordinate.

Small Deflection Angles - the angular separation between multiple images in the lens plane is typically small ($\lesssim 30''$). The typical deflection angle is therefore of the same order of magnitude as this angular separation, and the small angle approximation applies ($\sin\theta \simeq \tan\theta \simeq \theta$).

Weak, Stationary Gravitational Fields - we assume that the space-time local to the lens is flat, and that it is weakly perturbed by the Newtonian gravity potential of the lens (which is justified if the gravitational potential of the lens Φ is small, $|\Phi| < c^2$, and if the peculiar velocity of the lens is also small, $v \ll c$). This is justified by again considering a galaxy cluster at z=0.2. If the light from a distant (z=1) galaxy is observed ~5″ from the centre of the cluster, it will have experienced a Newtonian potential of $|\Phi| \sim 10^{-5}c^2 \ll c^2$ at its closest approach to the centre of the galaxy cluster (assuming the mass of the cluster is of the order of 10^{13} $M_\odot$ interior to a 5″ radius around the centre of mass). Typical peculiar velocities for galaxy clusters are $\sim 10^3$ km s^{-1}, far less than the speed of light.

1.4.3 The Lens Equation

The detailed mathematics required to constrain the distribution of mass in a galaxy cluster lie beyond the scope of this work. Instead, we aim to give an account of the products of gravitational lensing which can be employed to probe the evolution of high redshift galaxies. Using the lens equation (1.3) we derive the general form of the lens equation in term of the mass distribution of a galaxy cluster and then state some of the consequences which arise in gravitational lensing (such as critical density, lens magnification, parity and multiple image configuration). We refer the reader to the work of Smith (2003) and references therein for a detailed description of the mathematical problem and modelling methodology required to parameterise, constrain and optimise gravitational lens models.

In order to gain information about the mass distribution in a gravitational lens, we need to solve the lens equation. As can be seen from Fig. 1.1, *HST* observations provide the positions, $\vec{\theta_I}$ of several multiply imaged arcs and arclets in the cluster core. Identifications of several images of the same galaxy are usually made through their colour (gravitational lensing is a pure geometrical effect and is therefore achromatic), location (lensed images usually conform to simple configurations), surface brightness (gravitational

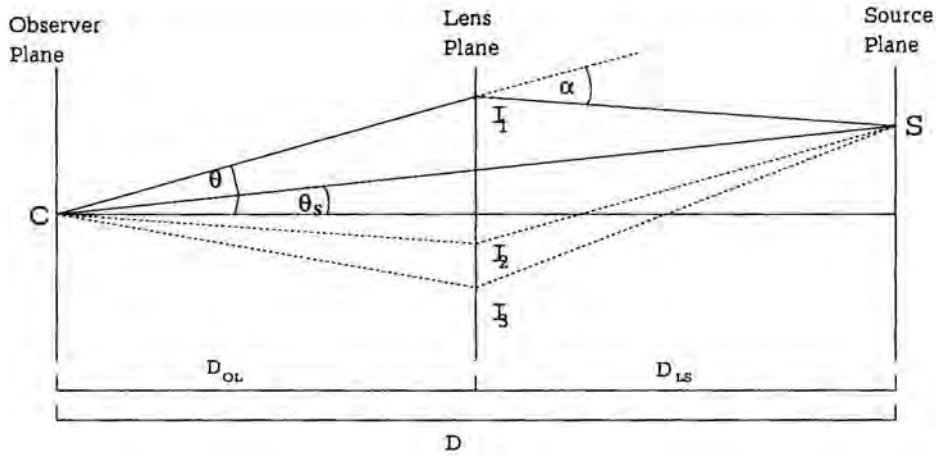

Figure 1.2: Optical diagram of a typical lens cluster; three images, I_1,I_2 and I_3 are formed from a single source, S.

lensing conserved surface brightness, and so in the absence of colour information, one can examine the monochromatic surface brightness of candidate multiple images), redshift (spectroscopic identification of candidate multiple image systems is a robust test of the redshifts of the sources) and morphology (multiple images are often tangentially or radially distorted, making it possible to resolve and compare component parts of multiply imaged galaxies).

Identifying several images of the same background galaxy, ($\vec{\theta_I}$) allows us to constrain the positions of (the yet unknown) $\vec{\theta_s}$. The other quantity in the lens equation is $\vec{\alpha}$, the deflection angle, which links $\vec{\theta_I}$ and $\vec{\theta_s}$. Applying Fermat's Principle we can derive an expression for the deflection angle in terms of the two dimensional Newtonian Potential of the lens, $\vec{\theta_I}$, (equation 1.3).

For a weak gravitational field, a photon emitted by a source, S at time $t = 0$, deflected by a thin lens, L, arrives at the observer, O at time t_a, where t_a is given by:

$$t_a = c^{-1} \int (1 - \frac{2\Phi}{c^2}) dl = \frac{l}{c} - \frac{2}{c^3} \int \Phi dl \tag{1.5}$$

where Φ is the three dimensional Newtonian potential of the galaxy cluster and l is the distance travelled by the photon (Schneider et al., 1992). Concentrating on the right hand side of equation 1.5 and neglecting high order terms in $\vec{\theta_I}$ and $\vec{\theta_s}$ we can write l as:

$$l = l_{OI} + l_{IS} = D_{OL} + \frac{D_{OL}\vec{\theta_I}^2}{2} + D_{LS} + \frac{(D_{OL}\vec{\theta_I} - D_{OS}\vec{\theta_S})^2}{2D_{LS}} \tag{1.6}$$

We also write the integral of the Newtonian potential along the line of sight as a projected two-dimensional potential:

$$\int \Phi dl = \phi(\vec{\eta}) = D_{OL}^2 \phi \vec{\theta_I} \tag{1.7}$$

substituting equation 1.7 into equation 1.5 we obtain (upto an additive constant):

$$ct_a(\vec{\theta_I}\vec{\theta_s}) = \frac{(D_{OL}\vec{\theta_I} - D_{OS}\vec{\theta_S})^2}{2D_{LS}} + \frac{D_{OL}\vec{\theta_I^2}}{2} - \frac{2D_{OL}\phi(\vec{\theta_I})}{c^2} \tag{1.8}$$

Applying Fermat's Principle, the light paths that connect observer and source are stationary points on the time arrival surface density by $t_a(\vec{\theta_I})$, i.e. they satisfy $\nabla_{\vec{\theta_I}} t_a(\vec{\theta_I}) = \vec{0}$. Differentiating equation 1.8 therefore yields the requirement that:

$$\frac{(D_{OL}\vec{\theta_I} - D_{OS}\vec{\theta_s})}{D_{LS}} + \vec{\theta_I} - \frac{2D_{OL}}{c^2}\vec{\nabla}_{\vec{\theta_I}}\phi(\vec{\theta_I}) = 0 \tag{1.9}$$

which reduces to the following expression for the deflection angle $\vec{\alpha}$ in terms of the projected Newtonian potential of the lens:

$$\vec{\alpha}(\vec{\theta_I}) = \frac{2D_{OL}}{c^2}\vec{\nabla}_{\vec{\theta_I}}\phi(\vec{\theta_I}) = \frac{D_{OS}}{D_{LS}}\vec{\nabla}_{\vec{\theta_I}}\varphi(\theta_{\vec{\theta_I}}) \tag{1.10}$$

where φ is called the lensing potential and is defined as $\varphi = (2D/c^2)\phi$, with $D = (D_{OL}D_{LS}/D_{OS})$. Combining equations 1.3 and 1.10, we can rewrite the lens equation as a gradient mapping from the source to the image plane:

$$\vec{\theta_S} = \vec{\theta_I} - \vec{\nabla}_{\theta_I}\varphi(\vec{\theta}) \tag{1.11}$$

We can see from equation 1.11 that knowledge of θ_I and multiple image identifications enable us to place constraints on φ, and thus on the total projected mass density of the lens.

1.4.4 Consequences of the Lens Equation and Terminology

The lens equations (equation. 1.11) can now be employed to calculate the properties of gravitational lensing. The main consequences of the lens equation (and of particular interest) are the critical density, lens magnification, critical lines and parity.

Critical Density – The projected mass density of a gravitational lens is often referred to in terms of the "critical density", Σ_{crit}, of the lens. Multiple image configurations will occur when the projected mass density exceeds the critical density and the source is sufficiently well aligned behind the supercritical region (see Smith 2003; Subramanian and Cowling 1986; Schneider et al. 1992 for a review).

Magnification – The magnification of a background galaxy will depend on its location (with respect to the lens) in the source plane. Specifically, the solid angle of a light bundle is distorted by the deflection and, since the total photon number is conserved, this alters the flux of the image relative to the unlensed flux of the source, thus causing a magnification.

Critical and Caustic Lines – Under idealised conditions, background galaxies will suffer infinite magnification. This occurs if the position of the source galaxy falls on continuous curves that are called *critical lines*. Under the lens mapping, these *critical lines* transform to another set of curves in the source plane called *caustics*. Furthermore, the critical lines divide into two categories, radial and tangential caustics (both of which give rise to multiple image configurations). Radial images (or arcs) can be used to constrain the slope of the lens mass distribution whilst tangential images (or arcs) constrain the mass enclosed within the radial position of the observed image. All of the arcs studied in this thesis are tangential in nature.

Parity – The observed parity of multiply imaged galaxies is conserved by the lensing transformation Schneider et al. (1992). In general, multiple images of a background galaxy are formed if the galaxy lies within one or more of the caustics of the foreground cluster lens in the source plane. Conceptually, for a galaxy in the source plane with

parity denoted by "+", the set of observed multiple images which are produced by the galaxy crossing the caustic must have the same overall parity and therefore two more galaxies (with opposite parities) must be produced, leaving an overall parity of "+". This is repeated for every caustic crossing, with the result that an odd number of images is always produced. Regions of opposite parity in the image plane are bounded by the critical curves. When a galaxy crosses the caustic in the source plane, a single image becomes three images, two of which lie outside the critical curve, and one of which lies inside the critical curve (an example of this can be found in Appendix 1 - A1201).

1.5 Galaxy Evolution

This thesis demonstrates the power of Integral Field Spectroscopy (IFS) for studying galaxy evolution across a range of redshifts. In chapters 3 & 4 we exploit galaxy clusters as natural telescopes to study intrinsically faint galaxies at $z \sim 1$. IFS is a unique tool which can be employed to investigate various aspects of galaxy evolution at various epochs. In this thesis this technique is used to investigate the triggers of the E+A phase of local galaxies at $z \sim 0.1$, the evolution of galaxy mass using gravitationally lensed galaxies at $z \sim 1$ and the power sources, masses and metallicities of SCUBA galaxies at $z \sim 2$. Since these are very different galaxy populations at a range of look-back times, we briefly desribe the physical motivation for these studies in this next section.

1.5.1 Galaxies

Although dark matter seems to be the gravitationally dominant component of our Universe, it is not visible since, by definition, it emits no light. The luminous galaxies that we see are made from the small component of baryonic material present in the Universe. It is believed that there are more than $\sim 10^{10}$ galaxies in the observable Universe, yet despite the enormity of this number, Hubble found that the morphologies of galaxies could be classified into four main groups: spiral galaxies, ellipticals, barred spirals and irregulars (Fig. 1.3). Given the small number of basic types, it seems likely that there must only be a handful of processes which drive galaxy evolution and cause galaxies to look the way they do. For example, early work postulated that as gas cooled and condensed in dark matter halos, it would become centrally concentrated. As the gas collapses, conservation of angular momentum (introduced from tidal torques) may cause the gas to form into a centrifugally supported disk, perhaps similar to a spiral galaxy (e.g., White and Rees, 1978). However, it seems inexplicable that such galaxies should exist in a Universe in which galaxies grow through hierachical merging, yet merging systems might explain the irregular morphologies of some galaxies. Furthermore, since there only appear to be a handful of morphological classifications in the local Universe, it seems likely that at early times the morphologies may be grouped in the same way (although in different proportions). For this reason, galaxy evolution studies are constantly attempting to identify trends in order to address questions such as how the progenitors of familiar local spiral and elliptical galaxies evolved to the present day.

At large lookback times, hierachical growth implies that galaxies should be intrinsically smaller (and fainter?) and therefore gaining high signal-to-noise observations becomes more difficult with increasing redshift. It is therefore important to identify the physical processes driving star formation, galaxy transformations, feedback and their effects on environment in local galaxies in order to interpret observations of their high redshift counterparts.

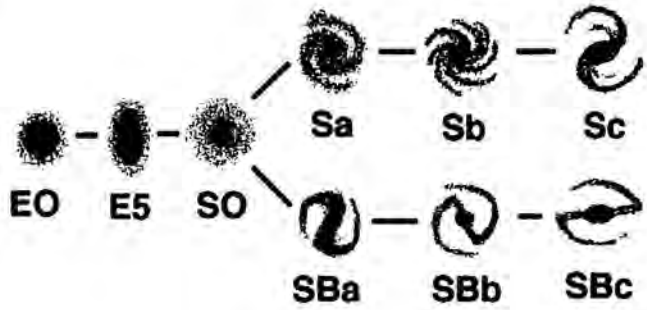

Figure 1.3: The classical "tuning fork" diagram which Hubble used to morphologically classify galaxies.

1.5.2 Galaxies Interactions

The most obvious method for understanding how galaxies transform from one type to another is to "catch galaxy evolution in the act". However, this is a difficult thing to do, particularly at low redshift (where the most detailed observations can be made) since the local Universe is a relatively inert place, with most activity long over, yet it may provide important clues as to how galaxy interactions and transformation occur at early times. Rare exceptions to this appear to be galaxies whose unusual spectra (strong Balmer absorption lines indicative of massive, short lived A-type stars but no emission lines indicative of ongoing star formation) suggest that a massive burst of star formation recently took place but was subsequently truncated. The mechanism of this unusual star-formation history is unknown, but the most likely mechanism responsible is that these galaxies represent a short lived period of galaxy formation which link the otherwise distinct (bimodal) populations of actively star forming (late type) galaxies and their quiescent (early-type) end products. For example, galaxy mergers are an effective method of transforming gas-rich, star-forming galaxies into gas-poor, passively star-forming ellipticals (Springel, 2000).

Such post-starburst galaxies have been found both in the field and in clusters (Dressler and Gunn, 1992; Zabludoff et al., 1996; Goto et al., 2003; Quintero et al., 2004). Stellar population synthesis shows that these galaxies are best fit by post-starburst galaxies, with the star-formation ceasing following the burst (Couch and Sharples, 1987; Dressler and Gunn, 1992; Poggianti et al., 1999; Balogh et al., 1999). Less extreme examples (i.e. with weak Balmer absorption lines) do not necessarily require a burst, but can be modelled as a normal star-forming galaxy in which the star formation is suddenly truncated. Since the lifetime of the enhanced Balmer absorption is short ($\lesssim$0.5 Gyr), even a small observed population may indicate that a significant fraction of galaxies undergo this transformation: it is even possible that they represent the route by which all early-type galaxies form.

These galaxies may therefore represent an important, short-lived phase in galaxy evolution. The stellar and gas kinematics of some of these galaxies suggest a transition from rotationally-supported, gas-rich galaxies to pressure-supported, gas-poor galaxies – furthering the picture that they represent one path of evolution from late to early types (Norton et al., 2001). Even though understanding the physical processes which drive the unusual activity in these galaxies is therefore critical to theories of galaxy evolution, important questions remain unanswered. In particular, we do not yet understand the trigger (or triggers) which cause the transformation of post-starburst galaxies. For example, some authors have proposed mechanisms that rely on rich cluster environments to truncate star formation via the ram pressure stripping of the progenitor's gas (Bothun

and Dressler, 1986), while others have suggested that galaxy-galaxy mergers, occurring principally in poor groups and sub-clusters, cause gas to be consumed by a starburst (Lavery and Henry, 1988; Liu and Kennicutt, 1995).

To resolve this issue requires careful analysis of the 2-D kinematics and morphologies in order to map the distribution of A, OB, and K-stars and the gas. This can be used to investigate the differing spatial distributions and kinematics allowing us to investigate the triggers of their formation. In Chapter 2 we study the two dimensional spatial and velocity distributions stars and gas in a local post-starburst (E+A) galaxy. By studying the physical processes in this galaxy, we aim to further understand how galaxy transformations take place. This is important for understanding these processes at high redshift, where such transformations are likely to be much more common.

1.5.3 Galaxy Evolution During Half the Age of the Universe

At large lookback times ($z \gtrsim 1$), observing individual galaxies in great detail becomes increasingly difficult since the angular size of galaxies makes it difficult to identify their intrinsic small scale properties and this couples with their increasing faintness due to their great distances. At $z \sim 1$, the Universe was only half its present age and therefore by constraining the masses and star formation properties of galaxies at this epoch we can constrain the relationships between the dark and baryonic masses. By neccesity, most detailed studies of individual galaxies at these times have had to concentrate on the most luminous or massive systems.

Galaxy clusters act as a *natural telescope*, amplifying intrinsically faint galaxies, allowing studies which would otherwise require the light grasp of thirty or one-hundred meter telescopes, advancing research perhaps fifteen years ahead of its time. By coupling this lensing phenomenon with integral field spectroscopy we can target "normal" galaxies in order to answer the following fundamental question:

- **What are the masses of these high redshift galaxies?** It is important to firmly establish whether high redshift galaxies have regular disk kinematics. Constraining the structure of any disk and the nature of the dark matter halo will allow us to measure their masses and determine whether these are massive galaxies (the "classical" formation scenario), or whether their luminosity comes from a burst of star formation in an intrinsically low mass sub-galactic system (the "hierarchical" formation model).

Using detailed and precise mass models, we can reconstruct the source frame morphologies and velocity fields of lensed galaxies. Moreover, by comparing the luminosity – circular velocity relation of a sample of these galaxies with local galaxy populations we can trace the evolution of the dark halo to test these competing models.

Whilst gravitational lensing allows us to study "normal" galaxies, important parallels can be drawn between these and other classes of galaxies at these early epochs. As we have argued, most galaxies at $z \gtrsim 1$ are small and faint, however some galaxies (such as radio, SCUBA and Spitzer selected) galaxies are frequently bright enough to study individually. By comparing and contrasting the differences in metals, masses and dynamics we can provide a link between various populations and investigate how galaxies evolve from high redshift proto-galaxies to their present day descendants.

1.5.4 SCUBA Galaxies

Identifying how galaxies build up and evolve can also be measured in another way, through determinations of the universal star formation rate as a function of redshift. Original esti-

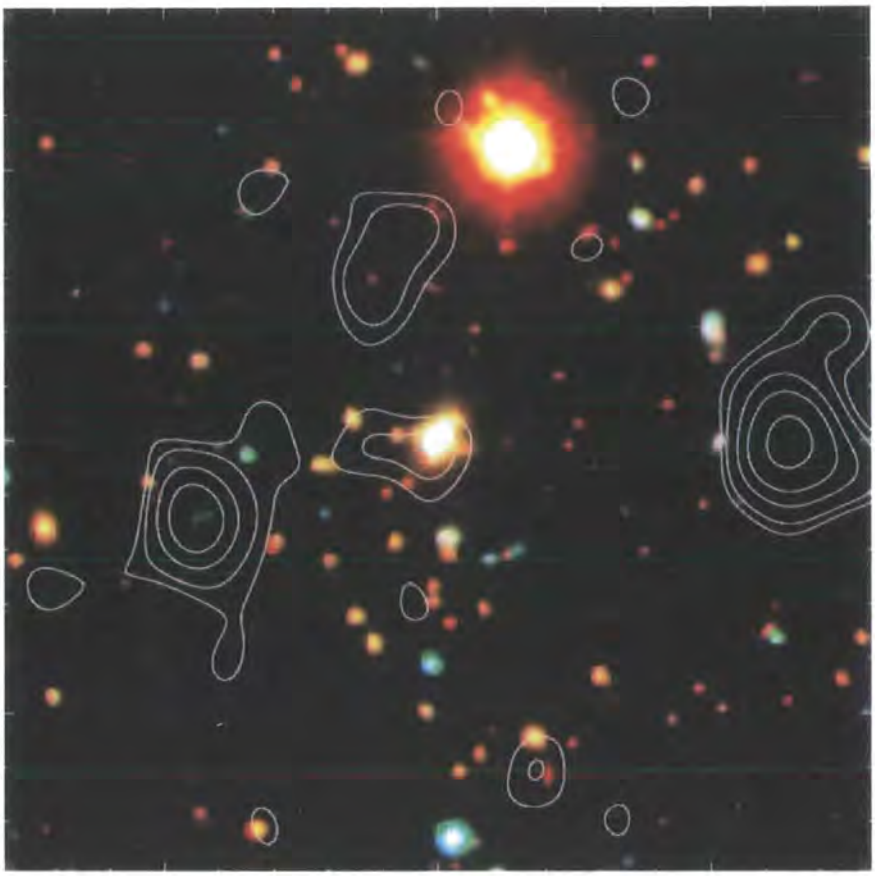

Figure 1.4: A comparison of deep optical and sub-mm views of the sky. The background image is a three colour optical image of the rich cluster of galaxies Abell 1835 at the low redshift z=0.25 (Smail et al. 1998) taken using the 5-m Hale Telescope, overlaid with the 15″ resolution contours of a SCUBA 850μm sub-mm image of the same field (Ivison et al. 2000). North is left and East is to the right. The brightest SCUBA galaxies at (-45,-15), (65,0) and (20,-60) and the central cD galaxy (Edge et al. 1999), all have clear radio detections at a frequency of 1.4GHz in images with higher spatial resolution than the SCUBA contours, obtained at the Very Large Array (VLA), supporting their reality. The bright SCUBA galaxy at (-45,-15) is associated with SMMJ14011+0253, and interacting pair of galaxies at z=2.56 in the background of the cluster (Frayer et al. 1999; Tecza et al. 2004; Swinbank et al. 2004).

mates of this quantity at low redshift (Gallego et al., 1995) have now been supplemented by determinations of the star formation rates at higher redshifts Madau et al. (1996). Although uncertain (due to the uncertainties in extinction corrections from dust), these measurements suggest over an order of magnitude increase in the star-formation activity between $z = 0$ and $z = 1$, indicating galaxy (and star) formation began very early in the history of the Universe.

The SCUBA camera on the James Clerk Maxwell Telescope (JCMT) (which observes a 2.5-arcmin field of view in atmospheric windows at 450μm and 850μm) recently turned up a population of high redshift, far-infrared luminous galaxies which appear to be responsible for much of the energy generated over the history of the Universe (Blain et al., 1999). Indeed, first identified through the boost of gravitational lenses (Smail et al., 1997), this galaxy population dominate the star-formation activity at $z > 2$.

However, the large JCMT beam size (FWHM$\sim$15″ at 850μm) has conspired with

the optical faintness of the submm galaxy population (and concomitantly large numbers of possible source identifications) to render identification and redshift measurements for these systems difficult. Until recently, robust spectroscopic redshifts have been published for only a handful of sub-mm galaxies (e.g., Ivison et al., 1998, 2000; Barger et al., 1999; Ledlow et al., 2002; Smail et al., 2003a,b). To overcome this problem, we can take advantage of high-resolution 1.4-GHz VLA maps sensitive to the synchrotron emission from star formation (and AGN) in the submm galaxies (Ivison et al., 2002; Chapman et al., 2004b). Using these precise positions and both LRIS and NIRSPEC on Keck, redshifts of a large sample of these sub-mm detected galaxies have been measured (Chapman et al., 2003a, 2005; Swinbank et al., 2004).

The results of these surveys provide complementary information to other populations of galaxies made in deep surveys in the radio (radio galaxies); Richards (2000), far-IR (ultra-luminous infrared galaxies); Puget et al. (1999), optical (Lyman-break galaxies); Steidel et al. (2000) and X-rays Alexander et al. (2003a).

About 99% of the energy released by galaxies in the sub-mm and far-infrared wavebands is produced by thermal emission from dust grains; the remainder comes from fine structure atomic and molecular rotational line emission. However, the source of energy to power the emission by heating dust is contentious. Any intense source of optical/ultraviolet (UV) radiation, either young, high-mass stars or an accretion disk surrounding an AGN would heat dust grains, and, since dust emits a featureless modified black-body spectrum, sub-mm continuum observations reveal little information about the physical conditions within the source. Alternative routes to probing the energy sources in these galaxies are provided by optical and near-infrared spectroscopy and radio imaging. At z=2–3, emission lines such as Ly$\alpha\lambda$1215, CIVλ1549, [SiII]λ1527, H$\alpha\lambda$6563,and [NII]$\lambda\lambda$6548,6583 are redshifted into the optical and near-infrared respectively. By targeting these emission lines it is possible not only to derive redshifts, but also to gauge the power sources (through line ratios), dynamics, metallicities, dust obscuration and star-formation rates. Furthermore, ultra-high resolution radio observations provide a route to probing the structure of the power-source since resolved radio emission can only come from extended starburst regions.

To date, one of the most important observations has been from emission lines produced by molecular CO rotation which have been able to tie down absolutely an optical and sub-mm redshift and the position of the galaxy, although only a handful of galaxies have so-far been detected.

Since this class of galaxy is relatively new, the relation between sub-mm galaxies and other galaxy populations is important for understanding how galaxies build up over cosmic time. At these redshifts, the best studied galaxy populations are Lyman-Break Galaxies (LBGs), Extremely Red Objects (EROs) and faint radio galaxies.

1.5.5 Other High Redshift Galaxy Populations

Since this thesis covers a diversity of galaxy populations it is also important to briefly review some of the other galaxy populations and their relevance to galaxy formation models.

LBGs are sufficiently numerous to have reasonably well defined luminosity functions (Adelberger and Steidel, 2000). Optical and near-infrared spectroscopy of these galaxies have investigated the dust content and star-formation rates, as well as providing mass and metallicity estimates for these galaxies (Shapley et al., 2003, 2004; Erb et al., 2003; Pettini et al., 2001). These observations indicate typical masses of $\sim 10^{10}$ $M_{\odot}$ and star-formation rates of $\sim$20$M_{\odot}$ yr^{-1}. Observations of LBGs with the SCUBA camera have determined 850μm flux densities of order 1mJy, well below the confusion limit at the resolution of

existing sub-mm images.

EROs (galaxies with colours in the range R-K$\gtrsim$5.5) have been detected in sufficient numbers in near-infrared imaging surveys that their relevance to other galaxy populations can be investigated (Thompson et al., 1999; Yan et al., 2000; Daddi et al., 2000; Totani et al., 2001; Smail et al., 1999; Pierre et al., 2001; Smith et al., 2001b). Extragalactic EROs fall into two main classes: very old, evolved galaxies, containing only old, low-mass cool stars; and strongly reddened galaxies with large amounts of dust absorption but which potentially are strongly star forming. However, most radio and sub-mm follow-up surveys of EROs have concluded that they are roughly equally made up of passive, non-star-forming galaxies with about half showing signatures of dust-enshrouded star-bursts or AGN activity (Smail et al., 2002). A small number of sub-mm galaxies appear to be associated with EROs. It may be no coincidence that the extreme optical faintness of sub-mm galaxies would be well matched by the colours of EROs at similar redshifts. Furthermore, the clustering of EROs (Daddi et al., 2000) is observed to be strong, fuelling the speculation that EROs reside in the deepest potential wells that have the greatest density contrasts at any epoch. This argues in favour of their association with the progenitors of local elliptical galaxies in formation (Lilly et al., 1999; Dunlop, 2001).

1.6 The Benefits of Integral Field Spectroscopy

Traditionally, astronomical observations are made with a two-dimensional detector, sufficient for imaging programs. For spectroscopic measurements, however, one spatial dimension of the sky is usually lost, to allow dispersion of the image across one axis of the detector. Spectrographs placing a long slit over the object lose spatial information orthogonal to the slit width.

Many astronomical programs require spectroscopic information over the whole of a two-dimensional field. That is, they require wavelength information for each point in the image or three-dimensional data (usually referred to as a (x, y, λ) data-cube). Ideally, an instrument simultaneously producing both two-dimensional imaging data and a spectrum for each point in the image, would make best use of telescope time. An instrument fulfilling this criterion provides integral field spectroscopy. In integral field spectroscopy the two dimensional sky data is reformatted into a one dimensional slit using an integral field unit allowing the data to be dispersed onto the detector without loss of spatial information.

Integral field spectroscopy thus allows spectra to be simultaneously obtained for a number of contiguous areas across a two-dimensional field. Spectroscopic observations of objects with a complex spatial structure are best studied with an IFU. The spatially resolved spectroscopy allows the variation with positions of object spectra to be measured, and this information can be used, for example, to determine the object's internal kinematics, or the star formation rate across and object, providing insight into its process of evolution. Studies of high redshift merging galaxies are amongst the most numerous objects suited to observations with an IFU, as summarised by Eisenhauer et al. (2000).

Galaxies typically have angular sizes of a few arcseconds for the redshift range $1 < z < 3$, which is well matched by most current optical and near-infrared IFUs (e.g. GMOS, GNIRS, UIST, CIRPASS). An IFU is essential for the observations of gravitationally lensed galaxies and merging galaxies. Gravitationally lensed galaxies usually appear highly sheared, and velocity and intensity gradients can be mixed in traditional longslit spectroscopy (even if the slit can be especially shaped; Gladders et al., 2002). Similarly, the complex spatial and velocity structure of merging galaxies can only be truly decoupled using an IFU.

Whilst in this thesis we concentrate on observations of galaxies which are spatially

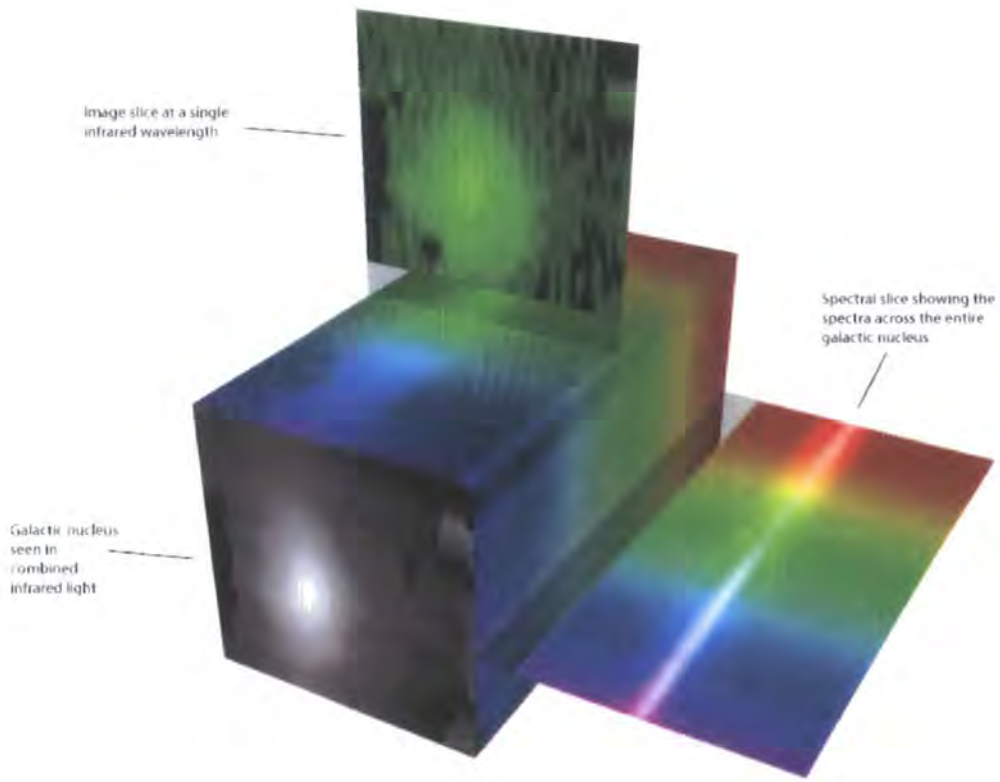

Figure 1.5: Schematic of an IFU datacube. At every wavelength an image is produced, whilst at every spatial pixel, a spectrum is produced.

extended in order to study the star-formation properties, kinematics and metallicities of high redshift galaxies, an IFU can also be used to study objects which are typically targeted with longslit spectroscopy. For example, an IFU may reduce system throughput, but it avoids slit losses (which may be useful in poor seeing conditions).

An IFU basically consists of five elements. First the image is sampled at the focal plane, either by lenslets, or by slicing mirrors (see below). The light is then passed through a slit and then through a collimating lens. The collimated light then passes through a diffraction grating (either a series of rulings or indentations on a glass plate). The dispersed light is then focused onto the CCD by a camera.

A number of different techniques have been adopted to perform the reformatting of the sky image for the spectrograph, three of which are summarised in Fig. 1.6. Lenses alone can be used to sample the telescope focal plane. The lenses form images of the telescope pupil, which are then dispersed by the spectrograph. The dispersion direction is chosen to maximise the wavelength coverage and to minimise the spectral overlap on the detector. Although this technique has relatively high throughput, it is difficult to achieve large wavelength coverage without the spectra overlapping.

The third row of the figure illustrates the slicing technique. An array of mirrors is used to segment the telescope focal plane, the light from each mirror being sent in slightly different directions to a second array of mirrors. The second array reformats the image segments to form the slit. When image slicing, the spatial information in each slice is maintained in the direction perpendicular to the dispersion direction. Examples of infrared instruments with image slicers include GNIRS (Allington-Smith et al., 2004) and UIST (Ramsay Howat et al., 1998).

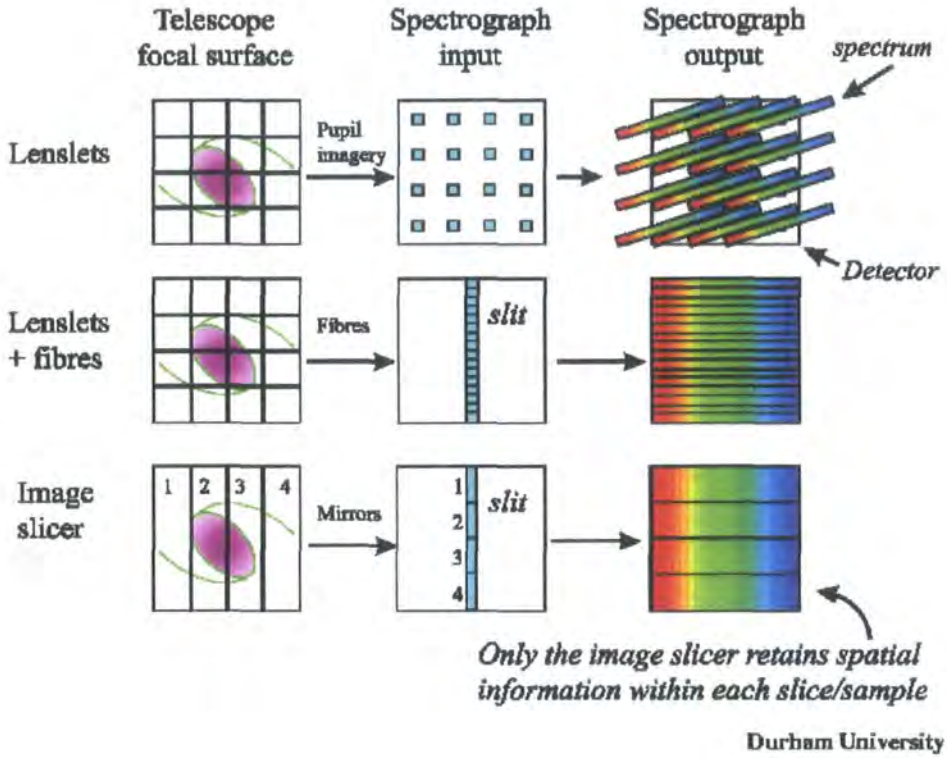

Figure 1.6: Summary of the techniques available to perform integral field spectroscopy. The left panels show the sampling of the telescope focal plane. The image at the telescope is then reformatted for the spectrographs as shown in the middle panels. The right panels show the output from the spectrograph at the detector.

In general slicers are preferable to lenslets since there are no fiber-to-fiber variations, and increased diffraction is limits to one direction. However, lenses are more preferable at short wavelengths since it is difficult to produce lenses without scatter.

1.6.1 Emission Line Spectra

Before we discuss what we can learn from spectroscopic observations of a galaxy, we first breifly outline the atmomic physics responsible for producing emission line spectra.

The radiation from normal galaxies is usually dominated by thermal processes (such as starlight, thermal radio emission and infrared radiation from heated interstellar dust grains). In contrast, active galaxies also feature either non-thermal processes (such as molecular massers and synchroton radiation or thermal processes with unusually high energies). An important indication of activity is the presence of a strong emission line component in the galaxy spectrum.

Emission lines come from bound-bound atomic transitions, in which an electron drops from an excited state. The energy lost is carried away by a single photon. For example, the hydrogen Balmer emission lines are produced by electrons "falling" from higher orbits down to the $n = 2$ orbit. Often the emission lines arise from an initially ionised atom in which the electron recombined and subsequently cascades down through a series of levels. Since most interstellar gas remains in, or close to, the ground state, it is important to

review the mechanism responsible for ionising or exciting the gas.

There are two mechanisms which are particularly relevant in this work; collisional excitation and radiative processes. Collisional excitation occurs when a free particle (either an electron or another atom) collides with another atom, transfering part of its kinetic energy. This inelastic collision does not involve any photons.

On the other hand, radiative processes (or a source of photons whose energies exceed that of the excitation or ionisation energy of the transition) are an efficient way of producing emission line spectra. The photon either excites or ionises the atom, which is followed by a subsequent recombination and cascade of the electron back to the ground state. Some of the most important emission lines are HI (Lyα), NV, CIV, [OII], Hβ, [OIII], MgII and Hα. The emission lines that are enclosed by a square bracket are forbidden (from electric quadrupole, magnetic dipole, or magnetic quadrupole transitions). An absence of brackets indicates permitted line.

Forbidden transitions are those in which electrons decay from metastable states (in quantum mechanics, ordinary transitions take place in about 10^{-8} seconds, whereas in a metastable state the downwards transition can take seconds or even days). In high density environments, metastable levels very rapidly decay through collisional deexcitation (there simply isn't enough time for the states to decay through forbidden transitions).

The intensitites of these emission lines therefore depends on several factors: the density and temperature of the gas, and the source of the ionising radiation. The spectra of galaxies can therefore be used to differentiate between hot, dense gas; hot, diffuse gas; and cold, diffuse gas.

A hot, dense gas produces a continuum spectrum with no spectral lines (this continuous spectrum is best described by blackbody radiation, described by the Planck function).

A hot, diffuse gas produces bright emission lines (including forbidden lines). If the gas density is high, collisional deexcitation prevents forbidden emission lines from being seen. The intensities and emission line ratios allow us to place constraints on the properties of the galaxy. For example, in a star forming galaxy, HII regions may contribute a strong emission line component (Hα and [OII]) to the galaxy spectrum. Diagnostic diagrams which use the emission line flux ratios to differentiate between HII regions and AGN are shown in Chapter 5.

A cool, diffuse gas in front of a source of continuous spectrum produces dark absorption lines in the continuous spectrum. Absorption lines are produced when an electron makes a transition from a lower to a higher orbit.

1.7 Motivation For This Work

We have set out a number of questions concerning the formation and evolution of galaxies which can be investigated by observing distant galaxies with Integral Field Spectroscopy. In this thesis we will study in detail the spatial, velocity and chemical properties of both local and distant galaxies.

Here we aim to map the following specific problems:

- What are the processes which take local galaxies from star-forming to quiescent end products? (Chapter 2)
- How are the baryonic and dark matter components of "ordinary" galaxies related as a function of look-back time? (Chapter 3 and 4)
- What are the power sources and masses of SCUBA galaxies, how do they relate to galaxy formation theories and what are their present day descendants? (Chapter 5, 6 and 7)

- How are AGN and superwind feedback mechanisms in high redshift galaxies related and how do they regulate galaxy formation? (Chapter 6, 7 and 8)

Chapter 2

GMOS Integral Field Spectroscopy of E+A Galaxies

Motivation

Catching galaxy evolution in the act is a difficult thing to do, particularly at low redshift (where the most detailed studies can be made) since the local Universe is a mostly inert place, with almost all activity long over. Galaxy-Galaxy interactions are thought to be the dominant mechanism which cause galaxies to transform from one galaxy type to another. Locally, galaxies undergoing this transformation are rare, however, these galaxies (termed E+A galaxies) can be readily picked out from spectroscopic surveys. These galaxies have unusual spectra (strong Balmer absorption times indicative of massive, short lived A-stars; but no emission lines indicative of ongoing star formation activity) which suggest that a massive burst of star formation recently took place ($\lesssim$500Myr), but was subseqently truncated. The mechanism responsible is unknown, but the most likely interpretation is that these galaxies represent a short lived phase of galaxy evolution which links the otherwise distinct (bimodal) galaxy populations of actively star forming (late type) galaxies with quiescent (early type) galaxies. Recent results (e.g. Tran et al. 2004; 2SLAQ survey) show that the number of E+A galaxies increases strongly with redshift, which makes it very likely that they play a key role in the evolution of the global star formation rate Madau et al. (1996). Although they are rare, evidence for recent, intense bursts of star formation means that they contribute significantly to the local star formation rate density (SFRD) of the Universe. Detailed studies of these galaxies are therefore crucial in order to understand both the local SFRD and (perhaps more importantly) to understand how galaxy-galaxy interactions and mergers drive galaxy formation in the distant Universe. This chapter is based on observations taken with the new Integral Field Unit on Gemini South which can be used in Nod & Shuffle mode. In February 2004 we were awarded four hours of Science Verification time to observe an E+A galaxy (published in Swinbank et al. 2005a). Following this succesful pilot study, we embarked on a programme to use the GMOS IFU to study the properties of these galaxies as a function of environment.

Abstract

In this chapter we present the three dimensional dynamics of the galaxy SDSS J101345.39+011613.66, selected for its unusually strong Balmer absorption lines [$W_o(H\delta)$=7.5Å]. Using the GMOS-South Integral Field Unit (IFU) in nod & shuffle mode we have mapped the continuum and optical absorption lines of this z=0.1055 field galaxy. This galaxy has a disturbed morphology, with a halo of diffuse material distributed asymmetrically toward the north. Using the [OII] emission line (W_o[OII]=4.1Å) we find that

the gas and hot OB stars are offset from the older stars in the system. The gas also has a spatially extended and elongated morphology with a velocity gradient of $100 \pm 20\,\mathrm{km\,s^{-1}}$ across 6 kpc in projection. Using the strong $H\gamma$ and $H\delta$ absorption lines, we find that the A-stars are widely distributed across the system and are not centrally concentrated arguing that the A-star population has formed in molecular clouds outside the nucleus. By cross correlating the spectra from the datacube with an A-star template, we find evidence that the A-star population has a $40\,\mathrm{km\,s^{-1}}$ shear in the same direction as the gas. The disturbed morphology, strong colour gradients and strong Hδ and Hγ absorption lines in SDSS J101345.39 argue that this is a recent tidal interaction/merger between a passive elliptical and a star-forming galaxy. Although based on a single object, these results show that we can spatially resolve and constrain the dynamics of this short lived (yet important) phase of galaxy formation in which the evolutionary process take galaxies from star-forming to their quiescent end products.

2.1 Introduction

Galaxies with strong Balmer absorption lines in their spectra (Hδ-strong, [HδS] galaxies) represent a short-lived but potentially important phase in galaxy evolution. Such lines indicate a stellar population dominated by A-stars which are normally either absent or overwhelmed by the much brighter OB stars. There is likely a variety of physical mechanisms that can lead to such a stellar population (e.g. Dressler and Gunn, 1982; Couch and Sharples, 1987; Poggianti et al., 1999; Balogh et al., 1999), but most invoke a major transformation from one galaxy type to another. Although such galaxies are very rare in the local Universe, their short lifetimes mean they could potentially represent an important phase in the evolution of most normal galaxies.

While high-resolution imaging has demonstrated that most bright, nearby HδS galaxies are spheroidal, often with signs of interaction (Yang et al., 2004), the dynamics have been extremely difficult to observe and understand. Norton et al. (2001) have obtained longslit spectra of galaxies in the Zabludoff et al. (1996) sample and find evidence that most of the galaxies are in the process of transforming from rotationally-supported, gas-rich galaxies to pressure-supported, gas-poor galaxies.

However, longslit spectroscopy mixes spatial and spectral resolution, and a better understanding of the dynamics can be obtained from integral field spectroscopy. This allows us to identify the physical locations of the gas, old (K) stars, young OB-stars and (the short-lived) massive A-stars, and to decouple their dynamics from their spatial distribution. In this paper we demonstrate the feasibility of using an integral field unit (IFU) to study the dynamics of HδS galaxies. We have selected one field galaxy from the Sloan Digital Sky Survey (SDSS) and used the GMOS-South IFU in nod & shuffle mode to study the rest-frame optical spectra. Using this technique, we can investigate the spatial distribution of star formation through the [OII] emission and the distribution of the young A-stars through the (much stronger) Hδ and Hγ absorption lines.

In § 2.2 we present the data reduction and analysis. The results are presented in § 2.3. Finally we summarise our results and present the implications in § 2.4. We use a cosmology with Ω_m=0.3, Λ =0.7 and a Hubble constant of $70\,\mathrm{km\,s^{-1}Mpc^{-1}}$. In this cosmology, 2 kpc subtends 1″ on the sky at $z = 0.10$.

2.2 Observations and Data Reduction

The target was selected from the SDSS First Data Release (Abazajian et al. 2003), and was identified as a HδS galaxy by Goto et al. (2003). This field galaxy has a redshift

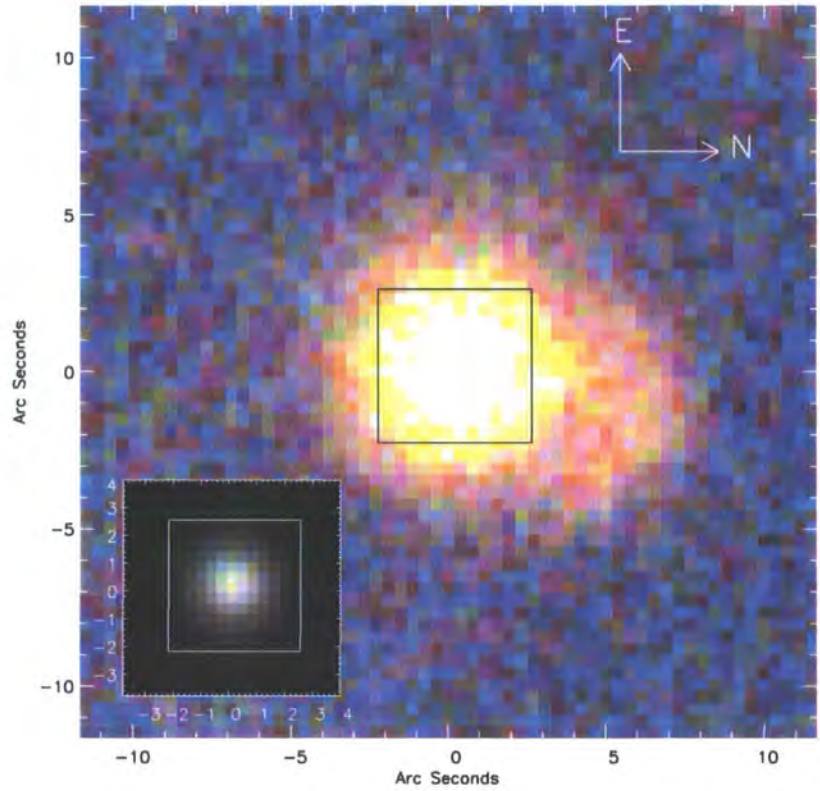

Figure 2.1: True colour *gri* image of SDSS J101345.39 from the SDSS imaging. Both panels show the GMOS-IFU field of view. The main panel has been thresholded to emphasise the low surface brightness material outside the nucleus as well as the extension of material to the north, suggesting that SDSS J101345.39 may have recently undergone an interaction. The inset is the same image but scaled to emphasise the full range of surface brightness and shows that most of the stars are located inside the GMOS-IFU field of view. We have rotated this image to agree with the IFU observation, and so North is right and East is up.

of $z = 0.1055$, with J2000 coordinates RA: 10:13:45.39, Dec: +01:16:13.66. Absorption lines in the SDSS spectra were fitted with a double-Gaussian profile model to account for a narrower emission filling within the absorption line, and all galaxies with rest-frame equivalent widths (EWs) > 4Å were identified as HδS. For this pilot study, we chose a relatively bright example, with $r = 16.3$ mag (which corresponds to $\sim 1/3L_*$). SDSSJ101345.39 has strong absorption lines and weak (but non-negligible) emission lines (Fig. 2.2). Post-starburst galaxies with strong Hδ absorption, but with non-negligible [OII] or Hα emission lines are usually referred to as e(a) galaxies. However as Balogh et al. (2005) show, e(a) galaxies with W_o([OII])<10Å and W_o(Hα)<10Å appear to have the same properties as strict k+a galaxies (which are HδS but have no detectable [OII] or Hα emission). The k+a galaxies are predominantly bulge dominated with little sign of spiral structure and signatures of recent (substantial) bursts of star-formation (Balogh et al., 2005). In this study, we have selected one galaxy which falls within this *"k+a plus weak emission"* category, in order to compare and contrast the dynamics and spatial distribution of the gas with that of the young stellar component.

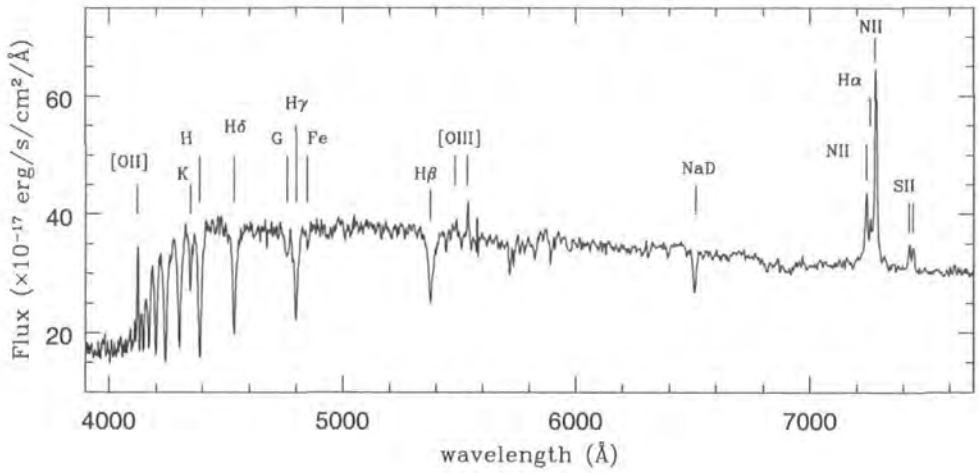

Figure 2.2: SDSS spectra of SDSS J101345.39. This spectrum has a lower resolution than the GMOS spectrum but shows the [OII] emission line, as well as the much stronger Hγ and Hδ absorption lines. The SDSS spectrum also covers the Hα emission line.

2.2.1 Imaging

Using the SDSS *gri*-band imaging we construct a true colour image of SDSS J101345.39. Each image has an exposure time of 60s and was obtained in $\sim$1.2″ seeing. The final images have a plate scale of 0.4″/pixel. The high surface brightness material in SDSS J101345.39 looks like a bulge dominated galaxy, however the lower surface brightness structure has a disturbed morphology (Fig. 2.1) of diffuse material, distributed asymmetrically toward the north, which may be indicative of a tidal interaction or merger. The GMOS-IFU field of view covers the central nucleus (where most of the stars are located), but the much lower surface brightness material is located outside the IFU field and extends over a $\sim$ 10" radius.

2.2.2 SDSS Spectroscopy

The SDSS spectroscopy of SDSS J101345.39 shows strong Hγ λ4340.5Å and Hδ λ4101.7Å absorption lines, as well as emission lines. From the original SDSS spectra, we measure W_0(Hδ)=7.5Å in absorption, and W_0(O[II])=4.1Å in emission. The galaxy also shows Hα λ6562.8Å and [NII] λ6583.0Å emission; although the measured equivalent width of Hα is 7.9Å, this is compromised by the strong underlying Balmer absorption. Taking into account the underlying absorption, the emission line ratios may be indicative of weak active galactic nucleus (AGN) activity in the galaxy (although as we show in §3, most of the emission is from a resolved component, and we therefore attach a cautionary note that, from our current data, the evidence for an AGN is tentative).

2.2.3 GMOS Spectroscopic Imaging

New observations of SDSS J101345.39 were taken with the GMOS-South IFU in nod & shuffle mode on 2004 February 28th U.T. during science verification time for a total of 3 hours in 0.8″ seeing and photometric conditions[1]. Using the nod & shuffle mode, we chopped away from the target by 30″ every 30 seconds. In this configuration, the IFU uses a fiber fed system to reformat the 5″ $\times$ 5″ field onto two long slits. Using the *B*-band filter in conjunction with the B600 grating results in two tiers of spectra being recorded.

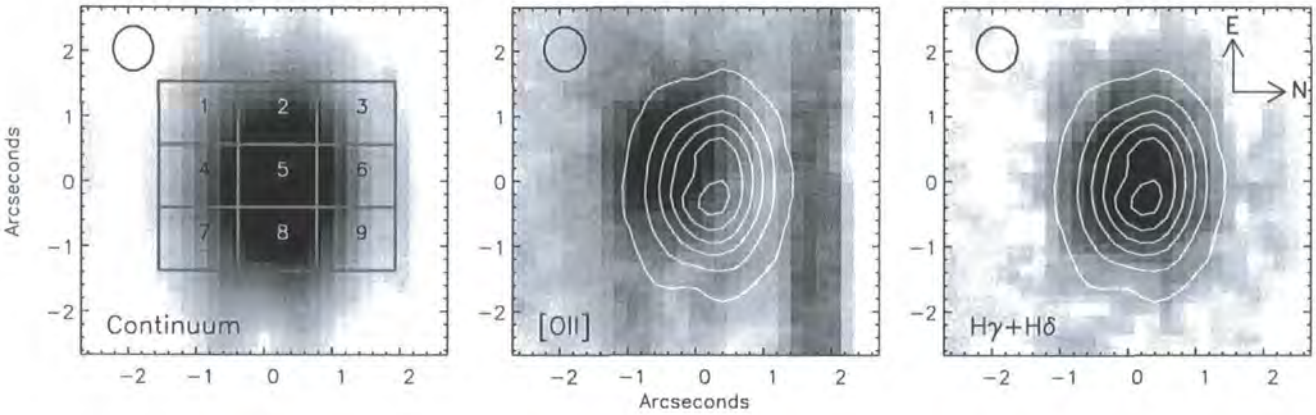

Figure 2.3: *Left*: Continuum image generated from the datacube between 4900 and 5400Å; *Middle*: continuum subtracted two dimensional [OII] emission line map with the continuum from the left panel overlaid as contours. *Right*: continuum subtracted two dimensional (inverted) Hγ+Hδ absorption line map with the continuum contours from the left panel overlaid. The circles in the upper left corners of each panel represent the size of the seeing disk.

The spectral resolution in this configuration is $\lambda/\Delta\lambda \sim 1700$. The [OII]($\lambda\lambda$3726.1,3728.8Å) emission line and Hγ and Hδ absorption features all fall in regions of low sky emission and absorption.

In the nod & shuffle mode, the object and background regions are observed alternately through the same fibres by nodding the telescope. In between each observation the charge is shuffled on the CCD by a number of rows corresponding to the center-to-center spacing of the blocks of 50 fibres into which each slit is divided. For the nod & shuffle mode, each alternate block is masked off so that it receives no light from the sky but acts simply as an image store. The slit to field mapping was arranged so that the resulting half of the total object and background field (7"×5" + 3.5"×5") formed a contiguous sub-field of 5"×5". Since each alternate block is masked, each exposure can be stored in different regions of the CCD without contamination from any other region of the sky. The sequence of object and background exposures can be repeated as often as desired with the photoelectrons from each exposure being stored in their own unique regions of the detector. At the end of the sequence, the CCD is read, incurring a read-noise penalty only once (see Glazebrook and Bland-Hawthorn (2001) for further details of this general approach). For each fiber (and corresponding spectrum), we identify the corresponding sky spectrum in the shuffled position and subtract them to achieve Poisson-limited sky subtraction.

The GMOS data reduction pipeline was used to extract and wavelength calibrate the spectra of each IFU element. The variations in fiber-to-fiber response were removed using twilight flat-fields and the wavelength calibration was achieved using a CuAr arc lamp. The wavelength coverage of the final data is 4080–5400Å. No flux standards were observed, as the spectral features of interest are narrow enough that the standard sensitivity is sufficient.

Since the datacube has a large wavelength coverage, we correct for the parallactic angle

[1]Based on observations obtained at the Gemini Observatory, which is operated by the Association of Universities for Research in Astronomy, Inc., under a cooperative agreement with the NSF on behalf of the Gemini partnership: the National Science Foundation (United States), the Particle Physics and Astronomy Research Council (United Kingdom), the National Research Council (Canada), CONICYT (Chile), the Australian Research Council (Australia), CNPq (Brazil) and CONICET (Argentina).

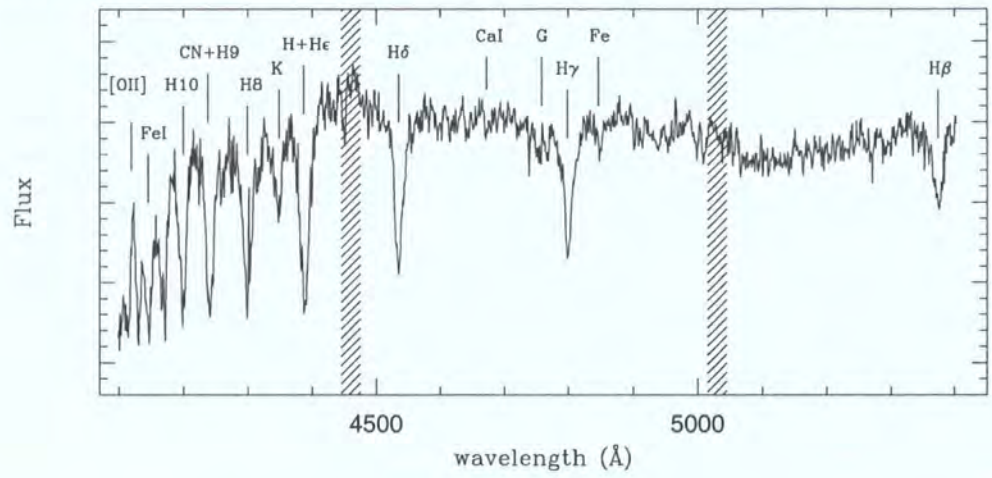

Figure 2.4: Reduced, sky-subtracted spectrum of SDSS J101345.39, generated by collapsing the central $2''\times2''$ of the galaxy. We have marked the strongest emission and absorption features. The hashed regions show the positions of the GMOS chip gaps.

by modelling a 2-hour observation running from a -1 to +1 hour angle and corresponding minimum and maximum airmasses of 1.17 and 1.21. The average atmospheric dispersion between 400nm and 540nm is 0.67" at an angle roughly North–South. After building the datacube, we use IDL to model and correct this aberration using a linear interpolation at each slice of the datacube along the wavelength axis.

We show the reduced, sky-subtracted spectrum, collapsed over the central $2''\times2''$ arcseconds of the galaxy in Fig. 2.4 and identify the strongest features.

2.3 Results

2.3.1 Spatial Light Distribution

To investigate the spatial distribution of the gas and stars in the galaxy we begin by extracting narrow-band slices from the datacube around the emission and absorption lines. We fit and subtract the continuum around the line of interest using a 3–σ clip to be sure that neighboring emission and absorption lines are omitted. We then extract the narrow-band images from the datacube by collapsing each spectrum over the feature of interest. We also extract the continuum regions by median filtering each spectral pixel in the datacube between 4900 and 5300Å.

In Fig. 2.3 we show the spatial distribution of the relatively older stars (as traced by the continuum light between 4900Å and 5300Å), the gas (as traced through the [OII] emission line) and the young, massive stars (traced by the Hγ and Hδ absorption lines). Fig. 2.3 shows that, while both the [OII] emission and Balmer absorption lines are extended, they do not have the same spatial distribution. In particular, the centroid of the [OII] emission is offset $\sim$ 2 kpc to the southeast from the older stars and the Hδ and Hγ absorption lines.

This difference is shown in Fig. 2.5, where we split the datacube into nine spatial bins. It is clear that the shape of the continuum is not constant across the galaxy. This is confirmed by comparing with the colour gradients in the SDSS imaging. By binning the imaging data into 3 × 3 pixels (1.2" × 1.2" bins, matching the same spatial bins as in Fig. 2.3) we investigate the colour gradients across the galaxy (which can be seen in

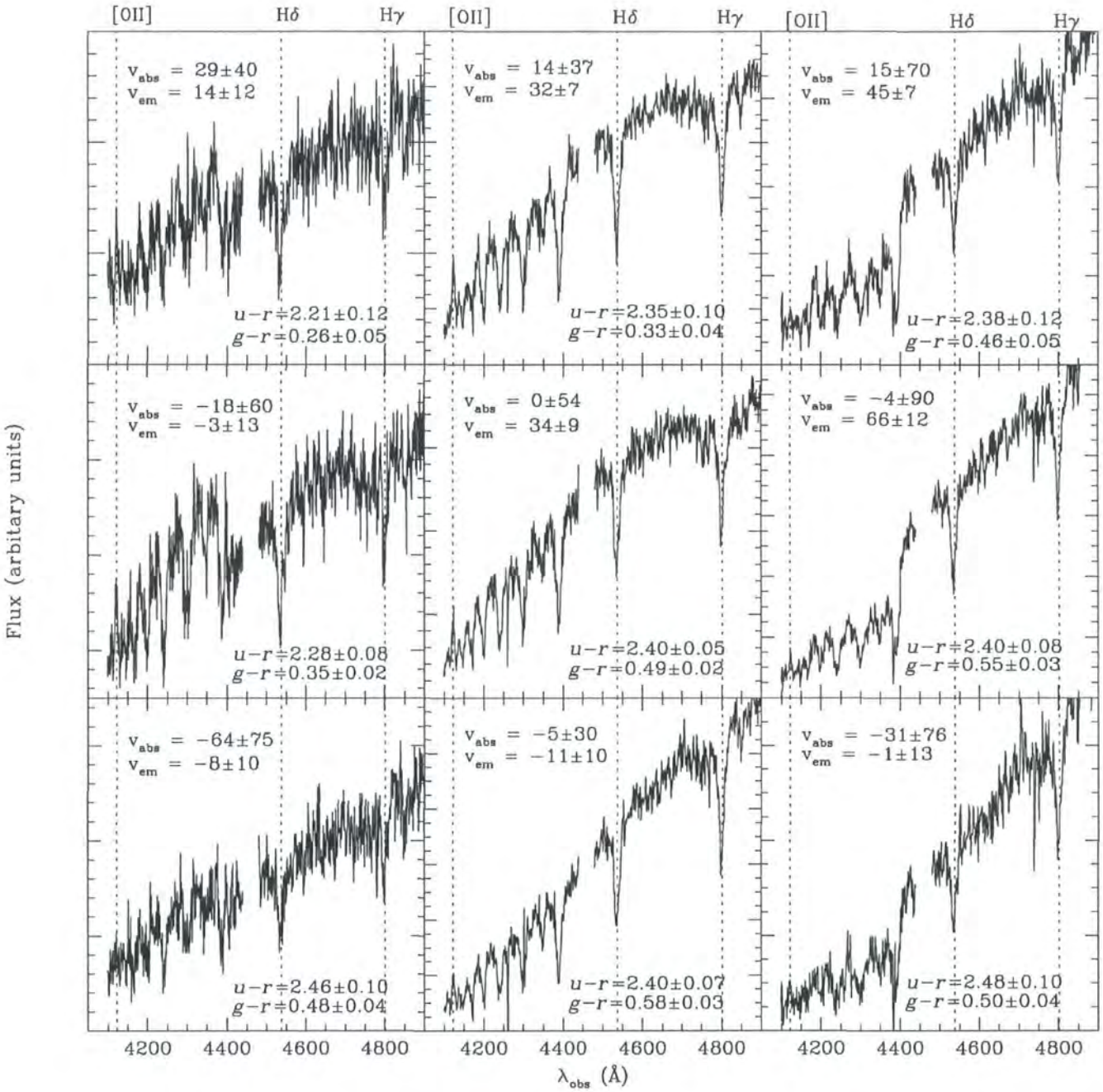

Figure 2.5: Spectra from nine spatial bins from the datacube split up according to the labels in Fig. 2.3. The dashed lines show the positions of the [OII], Hγ and Hδ emission/absorption lines for a fixed redshift of $z = 0.1055$. The spectra which fall in the GMOS chip gaps have been masked out. We also state the average [OII] emission line velocity, (v_{em}) found by fitting the [OII] emission line doublet, as well as the absorption line velocity from the A- stars (v_{abs}) found by cross correlating each spectrum with an A2 stellar template (all velocities are in $\mathrm{km\,s^{-1}}$). The zero-point in the velocity is defined to be the rest-frame of the A-stars in the middle panel. The change in the shape of the continuum which gives rise to the colour gradients in Fig. 2.1 is reflected in the spectra.

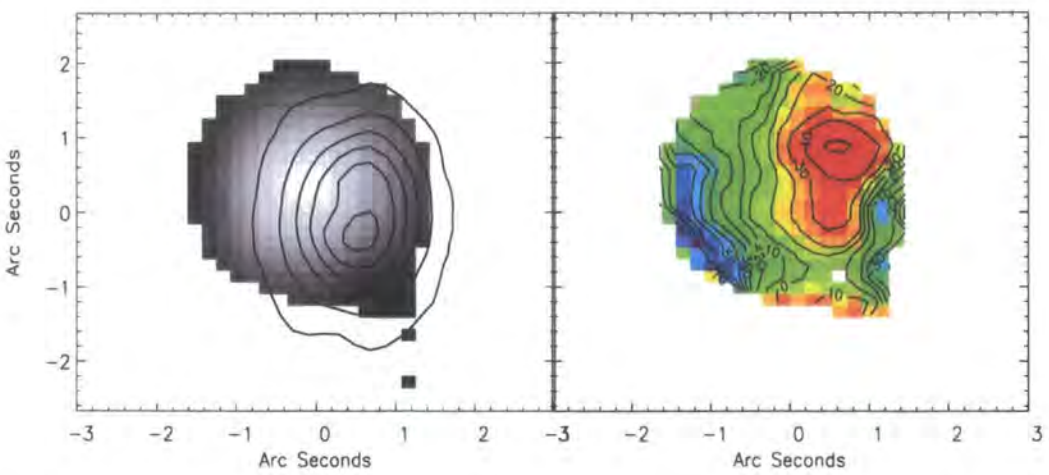

Figure 2.6: *Left*: The UV continuum intensity (colour scale) with the continuum from the older stellar population overlaid as contours. *Right*: Two dimensional velocity field of the galaxy derived from the [OII] emission line. The galaxy shows a shear across the galaxy with peak-to-peak velocity difference of $100 \pm 20\,\mathrm{km\,s^{-1}}$.

the inset panel of Fig. 2.1). In each panel of Fig. 2.5 we show the corresponding g-r and u-r colours determined from the SDSS imaging data. Both the spectroscopic and imaging data show the colour gradient across the galaxy with panels [1,2&4],[3,5&7] and [6,8&9] having average g-r colours of 0.31 ± 0.06,0.48 ± 0.06 and 0.54 ± 0.07 and u-r colours of 2.28 ± 0.10, 2.41 ± 0.10 and 2.42 ± 0.09 respectively confirming that the changing shape of the continuum seen in the IFU data is real and not simply an artifact of the observations.

The spatial distribution of the young OB stars, as traced by the rest-frame UV continuum, is consistent with that of the [OII] emission, and offset by $\gtrsim$2 kpc in projection from the older stellar population (indicated also by the colour gradient in the imaging). The colour gradient is in approximately the same direction as the surface brightness asymmetry, and suggests that the galaxy consists of at least two components, possibly as the result of a recent merger.

2.3.2 Emission Line Dynamics

To investigate the dynamics in more detail we return to the datacube and fit the emission and absorption lines on a pixel-by-pixel basis. The [OII] emission line doublet and underlying (rest frame UV) continuum was fitted using a χ^2 minimisation procedure. The spectra were averaged over a 3×3 spatial pixel region, except where the signal was too low to give a significant detection of the line, in which case the smoothing area was increased to 4×4 pixels. In regions where this averaging process still failed to give an adequate χ^2 (i.e. the inclusion of an emission line component does not improve the fit), no fit was made. We required a minimum χ^2 of 25 (S/N of 5) to detect the line, and we allow the signal to drop by a χ^2 of 9 to calculate the error in the velocity. This corresponds to a formal 3σ error. In Fig. 2.6 we show the [OII] velocity structure. This shows a velocity shear of $100 \pm 20\,\mathrm{km\,s^{-1}}$ across $\sim$6 kpc in projection . The velocity field of the gas does not resemble that of a disk. However, if one of the progenitors was a gas rich disk, then the observed shear may arise through the residual motion of a gas disk following a merger. Assuming this is the case, we estimate that the mass of the gas-rich progenitor was ($M = v^2 r/G$) $\sim 1.2 \times 10^{10} \mathrm{M}_{\odot}$.

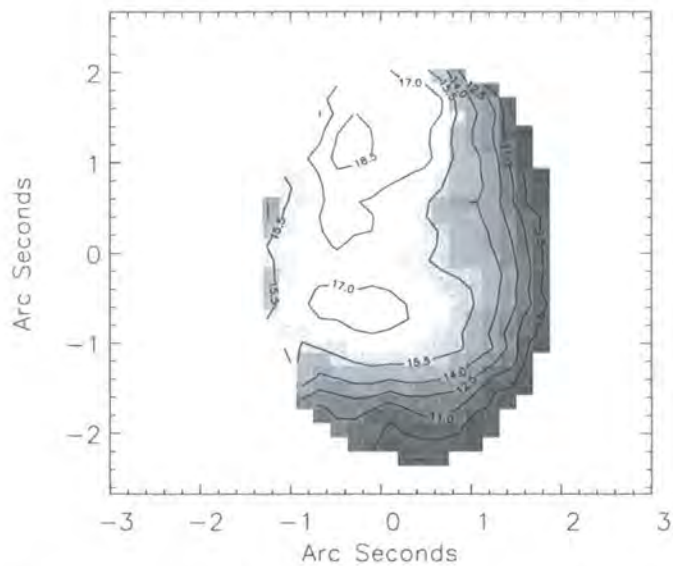

Figure 2.7: Two dimensional map of the equivalent widths of the Hδ+Hγ absorption lines. This shows two peaks in the EWs, one at the peak location of the old stellar population, and one at the peak location of the younger OB stellar population. The contours are spaced by 1–σ found by varying the fit such that $\Delta\chi^2 = 1$.

2.3.3 A-type Stars

To investigate the EWs of the short-lived A- stars we turn to the Hγ and Hδ absorption lines. Using a similar procedure as that used to fit the [OII] emission features we simultaneously fit the Hγ and Hδ absorption features (with a fixed separation but variable intensity and width) and show the resulting two dimensional distribution of EWs in Fig. 2.7. We estimate the 1–σ uncertainties by perturbing all of the parameters of the best fit such that $\Delta\chi^2 = 1$. From the distribution of EWs it is clear that the A- star population is most prominent at the same location as the old stellar population, but also has a large contribution near the peak in the [OII] distribution. Whilst the two peaks in the distribution of EWs in the galaxy are statistically significant, we note that systematic uncertainties such as emission line filling of the Hγ and Hδ absorption lines may cause the EW to appear artificially low. We therefore attach little significance to the 'double peaked' distribution of EWs, but rather note that the distribution of A-stars in the galaxy is widespread. This is particularly important for understanding the formation of the A-star population since it suggests that the A-stars are not formed from gas funneled into the nucleus but rather from material which is much more widespread.

To obtain the velocity structure of the A-type stars, the spectra from the nine spatial bins in Fig. 2.3 are cross-correlated with a template star of type A2V. The absorption line velocities in individual panels are shown in Fig. 2.5, with the zero-point defined such that the A-stars in the center panel have zero velocity. The A-stars velocity field appears to have a $\sim 40\,\mathrm{km\,s^{-1}}$ shear in the same direction as that of the gas, although the lines have a greater intrinsic width and therefore the large error bars preclude any stronger conclusion.

We can obtain an estimate of the age of the A-star population by comparing the average galaxy spectrum with the spectral library of Jacoby et al. (1984). The strength of the K-line at $\sim$ 3932Å is especially sensitive to the spectral type of the early A-type stars (Rose, 1985). Based on the relative strength of the K-line and the neighboring

H+Hϵ line at $\sim$ 3970Å the galaxy spectrum best resembles that of an A2$\pm$1 star (hence the choice of the A2 stellar template for cross correlation above). Taking the effective temperature of an A2 dwarf to be 9100 K (di Benedetto, 1998), and interpolating the theoretical isochrones of Bertelli et al. (1994) we arrive at an estimate of 0.44 Gyr for a MS turnoff at A2. Likewise, the ages for A1 and A3 dwarfs are estimated to be 0.39 and 0.47 Gyr respectively although stellar mixes and metallicity make this estimate uncertain.

2.4 Discussion and Conclusions

We have selected one field galaxy from the SDSS which shows strong Balmer absorption lines (which are indicative of a strong A- star population), but has only a small ongoing star-formation rate. In this pilot study, we have demonstrated the ability of IFU observations to disentangle the spatial and velocity distributions of the stellar and gaseous components through the measurement of both emission and absorption features.

The main results are summarised as follows:

1. The SDSS images show a bright nucleus and more diffuse material distributed asymmetrically toward the north (Fig. 2.1). The disturbed morphology of the field galaxy SDSS J101345.39 is suggestive of an interaction (or merger) between two galaxies.

2. The continuum from the older stellar population is spatially offset by $\sim$2 kpc from the young, hot OB stars (traced from the rest-frame UV continuum) and is easily seen from the changing shape of the continuum across the spatial domain of the datacube in the IFU observation (Fig. 2.5). This colour gradient is also confirmed by the strong colour gradient seen in the SDSS imaging.

3. By extracting narrow-band slices of the emission and absorption lines in the the GMOS IFU datacube, we find that the gas (traced through the [OII] emission line) is spatially extended with an elongated morphology, approximately coincident with the young, hot, OB star population (Fig. 2.3).

4. The $H\gamma$ and $H\delta$ absorption lines are widely distributed (Fig. 2.7). The peaks of these absorption lines are spatially co-incident with the older stellar population and the centre of the gas. The A-star population are not confined to the nuclear regions. Their spatial distribution is different from that of the [OII] emission, but the two appear related.

5. The gas has a velocity shear of $100 \pm 20\,\mathrm{km\,s^{-1}}$ across 6 kpc in projection (Fig. 2.6), but the velocity field does not resemble that of a disk. However, assuming that the velocity shear arises due to residual motion of a gas disk which has been disturbed as the result of an interaction, we estimate that the gas rich progenitor had a dynamical mass of $\sim 1.2 \times 10^{10}\,\mathrm{M_\odot}$).

6. The A-stars do not show the same amplitude of velocity motion as the gas, however, there is evidence of a $40\,\mathrm{km\,s^{-1}}$ shear in approximately the same direction as the velocity motion of the gas (although the large error bars preclude any strong conclusions).

Our observations suggest that the activity in SDSS J102145.39 may be the result of a strong tidal interaction between a passive (possibly elliptical) galaxy (giving rise to the old stellar population), and a gas-rich, star-forming (spiral or irregular?) galaxy (giving rise to the spatial offset of hot stars and nebular emission). The interaction between

the two components is likely to have been responsible for the production of the A-star population in a burst of star formation.

By comparing the galaxy spectrum with spectral libraries and stellar population models (Jacoby et al., 1984; Vazdekis and Arimoto, 1999), we estimate a burst age of ~0.5Gyr although we caution that systematic uncertainties such as hidden emission, differing metallicities and pollution of K- type stars make this estimate uncertain. Unfortunately the wavelength coverage of our GMOS data does not extend to MgII or Hα, making it difficult to constrain the underlying old population or dust absorption. Future observations at these wavelengths would allow us to trace the dynamics and metallicities of the old stars and further constrain the burst age, as well as locate the position of any possible AGN (which may be important for understanding black hole growth in these galaxies).

We can estimate the mass of the underlying old population from the K-band magnitude (K=13.2+/-0.001, Balogh et al. 2004) and by assuming a canonical value of 1.0 for the stellar mass-to-light ratio (Bruzual and Charlot, 2003). We estimate that the total stellar mass is $\sim 2 \times 10^{11}$ $M_{\odot}$. It is interesting to contrast this with the mass of the young A-star population, and the current star formation rate. If we assume a Salpeter initial mass function (IMF) (Salpeter, 1955), we can estimate the mass of the burst population by comparing the equivalent width of Hδ (7.5Å) with the models of Shioya et al. (2004). In order to produce absorption of this strength, their models require a burst population of at least $\sim$ 10% by mass (ie., $\sim 2 \times 10^{10}$ $M_{\odot}$). We note that this agrees well with the dynamical mass estimated from the velocity shear in the [OII] emission. If the burst mass fraction was skewed towards higher mass stars, the burst mass could be a factor of $\sim$ 3 lower. The current residual star formation rate inferred from the [OII] flux is $\sim 0.5 \pm 0.1 M_{\odot} yr^{-1}$ (Kennicutt, 1998), so that in 0.5Gyr, a mass of only $\sim 2 \times 10^{8}$ $M_{\odot}$ would be converted into stars. Thus, it seems that the residual star formation rate is at least $1/100^{th}$ of the rate during the burst, while the mass involved in the burst is about $1/10^{th}$ of the mass of the old stellar population. These mass ratios appear consistent with the scenario in which a burst is triggered in a gas rich secondary.

The spectra, morphological information and kinematics of SDSS J121345.39 appear very similar to local field E+A galaxy NGC 2865 (Hau et al., 1999) in which a 0.4–1.2Gyr old burst has occurred due to the merger of a gas-rich (Sb or Sc) spiral and an elliptical galaxy. A quantitative discussion of the star-formation truncation mechanism will have to wait until we have a statistically significant sample, but we can outline the possibilities which cause this process. Competing models for E+A galaxy formation predict very different distributions of stellar populations following the interaction. In smoothed particle hydrodynamics (SPH) simulations for mergers between spiral and elliptical galaxies the gas tends to sink to the galaxy centre on timescales much shorter than the starburst duration, and therefore suggest that the gas and A-stars should be centrally concentrated and segregated away from the older stellar population (e.g. Hernquist and Weil, 1992) (although these models do not take into account the hot interstellar medium (ISM) in the elliptical). However, other models suggest that the gas in the progenitor should be clumpy (in molecular clouds) rather than distributed as a smooth medium, and the result of the merger is to scatter these star forming regions across the galaxy (compressing/squeezing the gas and causing the A-star starburst as the interaction occurs). As the gas clouds scatter either in the spiral arms of the progenitor or in the new intercluster medium (ICM), they evaporate and the star formation is truncated as the density of the clouds falls (e.g. Mihos and Hernquist, 1996; Kojima and Noguchi, 1997). In our pilot study we have shown that the A-stars are widely distributed across the galaxy, which when coupled with the spatially extended morphology of the gas suggests a clear preference for the latter model.

Although these observations show a clear preference for the *squeezed cloud* model, it is not yet clear that this is true for the HδS galaxy population as a whole. The next step is to generate a statistically useful sample of such galaxies, in a variety of environments, to be able to generalise our conclusions. Furthermore, since the local Universe is a mainly inert place, and these galaxies show signs of recent, intense star formation activity, they may significantly contribute to the local star formation rate density. Constraining their properties may therefore be particularly important for current models for galaxy formation in which these HδS galaxies may represent an important phase in the evolution of today's local luminous spheroidal galaxies.

Chapter 3

Galaxies Under the Cosmic Microscope: A GMOS Study of Lensed Disk-Galaxy #289 in A 2218

Motivation

Understanding the processes by which galaxies evolve requires searching for trends in the properties of both local galaxies as well as the distant galaxy population. Many studies concentrate on the statistical properties of galaxies derived from large redshift surveys, however, it is also crucial to study the detailed properties of distant galaxies in great detail in order to build up a complete picture of galaxy evolution. Of course, at high redshift this becomes increasing difficult since galaxies are fainter and smaller and therefore obtaining high signal-to-noise imaging or spectroscopy requires significant investments of time, even on eight or ten meter class telescopes. Indeed, even with long integrations on such telescopes, the limit of the sky background can limit faint object spectroscopy.

As we argued in Chapter 1, one way to overcome this problem is to use galaxy clusters as natural telescopes. Galaxy cluster lensing has two effects, (i) the total signal is amplified so that we can study objects which would otherwise be too faint to observe in detail and (ii) the galaxy image is not only amplified, it is also stretched. As a result, the component parts of the galaxy can be spatially resolved, making it possible to study the galaxy even though the unlensed image of galaxy at z$\sim$1 is smaller than 0.4″ (FWHM). Thus gravitational lensing provides us with galaxies which are bright enough and extended enough that we can compare them with starburst galaxies in the local Universe.

In June 2003 we were awarded directors discresionary time with the GMOS IFU on Gemini North. We used the time to observe a gravitationally lensed galaxy ($z = 1.034$) behind the rich cluster Abell 2218. We use a detailed mass model to correct for the distortion introduced by the lensing potential and reconstruct the source frame morphology and velocity field of the galaxy. We use the results to investigate the relationship between the stellar and dark matter components of the galaxy and how they compare to disk galaxies in the local Universe (published in Swinbank et al. 2003). This chapter describes this pilot study, and in the next chapter (Chapter 4 we expand this sample to a further six galaxies behind other, rich lensing clusters and apply the same techniques (Swinbank et al. 2005, MNRAS submitted).

Abstract

In this chapter, we exploit the gravitational potential of the rich cluster A 2218 as a magnifying glass. We demonstrate that the amplification due to the cluster allows us to observe distant background galaxies at a comparable level of detail to galaxies at $z \sim 0.1$. Using the GMOS Integral Field Unit on Gemini North we observed the spatially-resolved [OII] λ3727 emission line spectrum for a lensed disk-galaxy at z=1.034. Using a detailed model for the cluster mass distribution, we are able to correct for the lensing by the cluster and reconstruct the source morphology. We find that the overall magnification is a factor of 4.92 ± 0.15, and the rest-frame absolute I-band magnitude is $M_I^{rest} = -22.4 \pm 0.2$, where the error bars include conservative estimates of the uncertainty in the source-plane reconstruction. The inclination-corrected circular velocity is $206 \pm 18\,\mathrm{km\,s^{-1}}$. The galaxy lies very close to the mean Tully-Fisher relation of present-day spirals. Although our results are based on a single object, they demonstrate that gravitational lensing can be viably used to make detailed studies of the evolution of the structure of distant field galaxies.

3.1 Introduction

The deflection of light-rays by the deep gravitational potential of galaxy clusters can be harnessed to greatly increase the effective collecting area of astronomical telescopes. Such "gravitational telescopes" magnify the images of background objects allowing us to study faint distant galaxies in a level of detail that would simply not be possible by conventional means (Smail et al., 1996; Franx et al., 1997; Teplitz et al., 2000; Ellis et al., 2001; Campusano et al., 2001). In particular, many of the selection biases that require us to only observe bright, extended galaxies are removed, allowing us to test models for galaxy formation in a much fairer way than otherwise possible.

In this chapter, we will concentrate on the dynamics of galaxies seen at $z \sim 1$ by measuring the rotation speeds of gas in these systems through the [OII] λ3727 emission line. By observing the distant ($z > 1$) universe, we sample cosmic history at a time before many present-day stars had formed. In the "classical" galaxy formation model, most of the dark matter in a galaxy halo is thought to be in place at high redshift, with the formation of the galaxy's disk subsequently growing over an extended period of time through the gradual accretion of gas from the halo (e.g. Eggen et al., 1962; Larson et al., 1980; Sandage, 1990). In this scenario, the circular velocity of galaxies at high redshift would be similar to those at the present day, but the stellar masses at a given circular velocity will be much lower at $z = 1$ (by about a factor of 2). In contrast, CDM hierarchical models predict that the stellar mass versus circular velocity correlation should be similar at all redshifts since an in increase in mass of dark matter halo (due to the merging of smaller halos) should be accompanied by an increase of stellar mass, i.e. galaxies are expected to evolve along the circular velocity-luminosity relation. Previous work in this area has, by necessity, concentrated on galaxies which are intrinsically bright. and mostly at $z < 0.5$ (Vogt et al., 1997; Verheijen, 2001; Böhm et al., 2003; Ziegler et al., 2002), with only a few galaxies being studied at higher redshift (Vogt et al., 1996; Milvang-Jensen et al., 2003; Barden et al., 2003). The results suggest an increase in B-band luminosity for a given circular velocity (Vogt et al., 2002; Kannappan et al., 2002) – suggesting a preference for hierarchical formation models.

Here we demonstrate the feasibility of using lensing to study the evolution of the Tully-Fisher relation at much higher redshift. We use the GMOS IFU on Gemini-North to target the gravitationally lensed $z = 1.034$ arc (object # 289 – we use the same

numbering system as Pello et al. (1992) in the cluster A 2218. We use a cosmology with $H_o = 75\,km\,s^{-1}Mpc^{-1}$ and $q_o = 0.05$ to be consistent with Vogt et al. (1997). We note that for a cosmology with $\Omega_M = 0.3, \Omega_\Lambda = 0.7$, the results are very similar (the physical distances are only 6% larger and the luminosities 12% brighter).

3.2 Observations, Analysis & Results

The galaxies lensed by the A 2218 cluster were first studied by Pello-Descayre et al. (1988), and later a number of arcs and arclets were discovered in the cluster core (Kneib et al., 1996; Ebbels et al., 1998; Ellis et al., 2001). Spectroscopy of the arcs in the cluster have confirmed a redshift for arc # 289 of 1.034 (Pello et al., 1992; Ebbels et al., 1998).

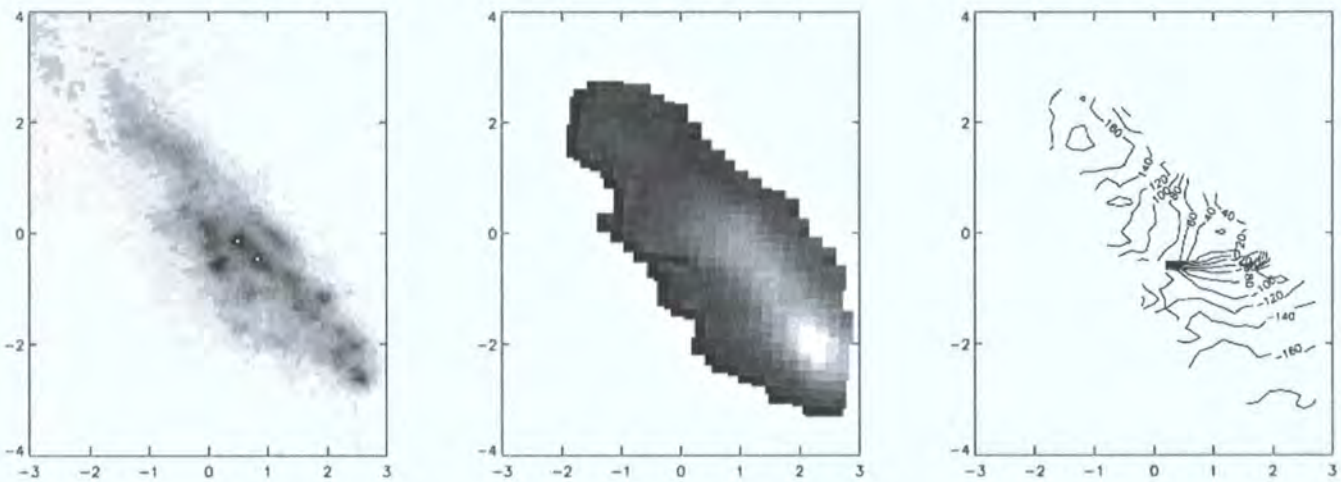

Figure 3.1: Left: Arc #289 in A 2218 generated by combining the *HST* WFPC2 B_{450},V_{606} and I_{814} drizzled images. (Middle) The [OII] λ3727 emission map of the arc measured from our IFU observations. The distribution of [OII] emission agrees well with the UV flux seen in the left panel (the seeing for the observations was 0.7″). (Right) The contour map of the derived velocity field of the galaxy. The scale is marked in arcsec, North is up and East is left.

3.2.1 HST Observations and Lens Model

The cluster was first observed by the Hubble Space Telescope *(HST)* WFPC2 in September 1994 in the R_{702} filter for a total of 6.4 ks (see Smail et al., 1996). It was subsequently observed again in January 2000 using the B_{450},V_{606} and I_{814} filters for totals of 12.0, 10.0 and 12.0 ks respectively (discussed in Smail et al., 2001).

Arc#289 is a fairly blue disk-galaxy at $\alpha = 16^h35^m55^s.1$, $\delta = +66^o11'51''.0$ lying in a saddle between the central dominant galaxy of the cluster (# 301) and a sub-clump of elliptical galaxies (# 307 & # 292, Figure 1 in Smail et al. (2001)). The *HST* images of the galaxy show a large amount of internal structure with the knotted, disk-like morphology resembling a late-type galaxy (especially the B-band flux which samples the rest-frame UV and is therefore dominated by the star-forming HII regions – Figure 3.1 - left). We calculate the magnitude of the arc in various passbands in Table 3.1 by using the IRAF IMSURFIT package with the sky estimated from a 2^{nd} order polynomial surface fit to regions around the galaxy. We then use SEXTRACTOR (Bertin and Arnouts, 1996) to estimate the residual background within the frame.

PHOTOMETRIC PROPERTIES OF #289

Filter	Magnitude	b/a	inclination
B_{450}	21.66 ± 0.04	0.37	68
V_{606}	20.86 ± 0.10	0.41	66
R_{702}	20.53 ± 0.04	0.40	66
I_{814}	19.79 ± 0.05	0.53	58
J	18.63 ± 0.06	–	–
K	17.32 ± 0.06	–	–
IFU	–	0.5184	58.8

Table 3.1: Aperture magnitudes of the arc are in the Vega-based system. Inclination is computed in the source (reconstructed) frame

To correct for the distortion and magnification of the galaxy image by the cluster lens we need to employ a lens model. A detailed mass model for A 2218 was originally developed by (Kneib et al., 1996) from *HST* imaging and this has been updated by Ellis et al. (2001) and Smith (2003). In particular, Smith (2002) (see also Smith et al. 2003) incorporated all of the strong lensing constraints to produce one of the best constrained strong lensing clusters, with three spectroscopically confirmed multiple-image systems. The precision of this lens model makes this cluster an ideal gravitational telescope with which to study (and reconstruct) the detailed properties of high redshift galaxies.

While the giant blue arc # 289 is highly distorted at the northern end (Fig. 3.1), extending across the halo of the cluster galaxy # 244, the majority of the source lies outside the caustic producing a highly magnified, weakly sheared image. The southern end of the arc does not suffer the same strong shear, and is not so distorted although it has a higher surface brightness than the northern end. Exploiting the fact that gravitational lensing conserves surface brightness, we compute the magnification in each band by using the transformation between the sky-plane and source-plane coordinates and compare the flux in the (reconstructed) source and (observed) sky frames (Fig. 3.2 - left). We use Smith's (2002) model of A 2218 to compute the magnification (μ) of # 289, obtaining a mean luminosity weighted magnification of $\mu = 4.92$ across the whole galaxy image. Since different bands sample slightly different morphologies, the luminosity weighted amplification varies by ± 0.15 depending on the band. The statistical error bar on μ is derived from the family of models which adequately reproduce the multiply images arcs in the cluster. We estimate the $1\text{-}\sigma$ uncertainty by perturbing the parameters of the best fit lens model such that $\Delta\chi^2 = 1$. For each model we recompute the magnification of #289. The error corresponds to the largest variation in magnification that we found and is converted into a conservative estimate of ± 0.05 magnitudes in the source plane photometry of # 289.

3.2.2 Ground-based Imaging

Additional constraints on the spectral energy distribution (SED) of the galaxy comes from the near-infrared imaging of this field using the INGRID camera (Packham et al., 2003) on the William Herschel Telescope. The reduction and analysis of these data are described by Smail et al. (2001). With our multi-wavelength photometry (Table 3.1) we construct an SED of this very blue galaxy whose colors indicate a current to past star formation rate consistent with that seen for late-type spirals at the present day. The rest frame I-band luminosity is approximately equivalent to the observed H-band and so is calculated from the J and K photometry (Table 3.1). We co-add the J, K images to obtain an aperture which is used to extract the J, K magnitudes and interpolate for the relevant SED type. We derive a rest-frame I-band magnitude of $M_I = -24.1 \pm 0.1$.

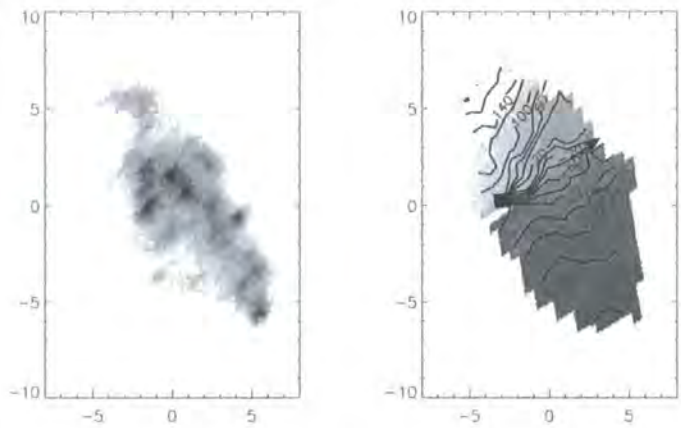

Figure 3.2: The reconstructed image of the arc corrected for lens amplification using the mass model of Smith et al. (2003). Left: the reconstructed image of the galaxy based on *HST* imaging. Right: The velocity map of the galaxy in the source frame. The dark and light regions represent redshift and blueshift respectively and the contours map the velocity in the source plane. The luminosity weighted amplification of the source is 4.92 ± 0.15, but varies from ~ 5.6 to ~ 4.9 from the northern to southern end of the arc. The scale shows the size of the galaxy in the source frame in units of h_{75}^{-1}kpc. Without a lens, at $z = 1$, $1''$ corresponds to 7.7kpc.

Correcting for the magnification due to the lens, the absolute rest-frame I-band magnitude is $M_I^{rest} = -22.4 \pm 0.2$. We apply the same technique for the rest-frame B-band magnitude, (at $z \sim 1$, I and R-bands are the closest match to rest-frame B-band) and estimate its uncertainty by computing the magnitude for a variety of SED types which are consistent with the observed optical colours. We compute a corrected rest frame B-band magnitude of $M_B^{rest} = -21.1 \pm 0.2$. Accounting for the $(1+z)^4$ dimming, the central surface brightness of the galaxy ($\mu_{b,0} \sim 20.6$) confirms #289 as a high-surface brightness (HSB) galaxy.

The inclination is determined by transforming the *HST* images of the galaxy to the source plane. We fit ellipses to an isophote of the galaxy image in the source plane using the IDL GAUSS2DFIT routine. The ellipticity is then $e = 1 - b/a$ (where a and b are the major and minor axis of the ellipse) and the inclination, i, is $\cos i = b/a$. The average axis ratio of the ellipses in the four passbands (Table 3.1) is 0.43 ± 0.07 which translates to an inclination of 64 ± 6 degrees assuming an intrinsically circular disk.

3.2.3 GMOS Spectroscopic Imaging

A 2218-arc # 289 was observed with the GMOS-IFU on Gemini North on 2002 June 12$^{\text{th}}$ U.T. during Science Demonstration time for a total of 5.4 ks in $0.7''$ seeing and photometric conditions. The IFU uses a lensed fiber system to reformat the $7'' \times 5''$ field into two long slits (Allington-Smith et al., 2002). Using an I-band filter in conjunction with the R400 grating results in two tiers of spectra recording a maximum field of view. The spectral resolution of this configuration is $\lambda/\Delta\lambda = 2000$. For the galaxy at $z = 1.034$, the emission for the [OII] doublet falls at a wavelength of $7581\mathring{A}$, in a region of low sky emission.

The GMOS data reduction pipeline was used to extract and wavelength calibrate the spectra of each IFU element. The variations in fiber-to-fiber response were removed in IDL by using continuum regions either side of the expected range of [OII] emission. The [OII] doublet is clearly resolved in the GMOS spectra (Fig. 3.3). This is useful, since one of the [OII] lines can clearly be identified even when the other lies immediately under the narrow sky line at $\sim 7580\mathring{A}$. The emission line doublet was fitted using a χ^2 minimisation

procedure, taking into account the greater noise at the position of the sky line. The spectra were averaged over a 3 × 3 spatial pixel region, increasing this region to 4 × 4 pixels if the signal was too low to give a sufficiently high χ^2 improvement over a fit without the line. In regions where this averaging process still failed to give an adequate χ^2, no fit was made. We required a minimum χ^2 of 25 (S/N of 5) to detect the line, and allow the signal to drop by a χ^2 of 9 to calculate the error in the velocity. This corresponds to a formal 3σ error.

We use the velocity field to infer the rotational velocity of the galaxy's gas disk. As can be seen from the major axis cross section, (Fig. 3.4 inset) the asymptotic rotation speed is $v_{rot} = 186 \pm 16\,\mathrm{km\,s^{-1}}$, (i.e. the total velocity shift across the galaxy is $2v_{rot}$). The inclination corrected velocity of the galaxy is 206 ± 17 $\mathrm{km\,s^{-1}}$. This corresponds to a dynamic mass of $1.4 \times 10^{11} M_{\odot} h_{75}^{-1}$ within a radius $\sim 14 h_{75}^{-1} kpc$ in this cosmology.

3.2.4 Modelling the Rotation Curve

In addition the shape of the rotation curve can be compared to the low redshift ($z \sim 0.03$) sample of spiral galaxies by Courteau and Rix (1997). Modelling the shapes of galaxy rotation curves has the obvious disadvantage that we must make assumptions about the shape of the rotation curve. However, the major advantage is that all of the points (and their errors) are used to simultaneously derive a robust line shape. Physical modelling of rotation curves is not simple since it requires a complete description of the bulge, disk and dark matter components of the galaxy dynamics. Such rotation curves have been proposed, culminating in the "Universal Rotation Curve" (URC) of galaxies by Persic et al. (1996) which accounts for luminous and dark matter. The simplest parameterisation is one which naturally defines the shape of the rotation curve, with no pretence of a physical basis, but has the smallest number of free parameters. Use of such a smooth rotation curve will allow us to measure asymptotic rotation speeds. The simplest of these smooth rotation curves is the ARCTAN function given by:

$$v_r = v_0 + \frac{2}{\pi} v_c arctan(R) \tag{3.1}$$

where $R = (r - r_0)/r_t$, and v_0 is the center of rotation, r_0 is the spatial center of the galaxy, v_c is an asymptotic velocity and r_t is a transition radius between the rising and flattening part of the rotation curve. The shape of this function reproduces the shape of local galaxy rotation curves well (e.g. Gilmore et al., 1989; Courteau and Rix, 1997).

A more elaborate (purely phenomenological) model is given by:

$$v_r = v_0 + v_c \frac{(1+x)^{\beta}}{(1+x^{\gamma})^{1/\gamma}} \tag{3.2}$$

where $x = 1/R = r_t/(r - r_0)$ and v_0, r_0, v_c and r_t have the same definitions as in model 1, but v_c and r_t do not have the same values. The term γ governs the degree of sharpness of the turn over, and β can be used to model the drop off, or steady rise of the outer part of the rotation curve. We note in this model, solid body rotation, or $v(r) \propto r$ is recovered for $|r - r_0| << r_t$, and flat rotation, or $v(r) \propto v_c$ is acheived for $|r - r_0| >> r_t$ (see also Schlegel, 1995; Rix et al., 1997; Kravtsov et al., 1998)

Using these models, we compare the shape of the rotation curve to the low redshift ($z \sim 0.03$) sample of spiral galaxies by Courteau and Rix (1997). We fit the observed source plane 1-D rotation curve by convolving the ARCTAN and multi-parameter models (Courteau and Rix, 1997) with $0.7''$ seeing (transformed to the source plane). Using a χ^2 fit the observed rotation curve is best described with an ARCTAN function with transition radius, $r_t = 1.7$kpc or a multi-parameter fit with $r_t = 2.1$kpc and $\gamma = 1.5$. If we do

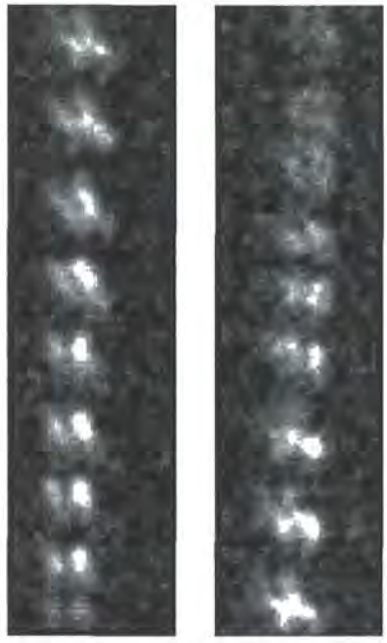

Figure 3.3: e
mission doublet as seen in the reduced IFU data of Abell2218]The [OII] emission doublet as seen in the reduced IFU data. Each line of the image is the spectrum from a single IFU lenslet. These are arranged in blocks, each block correspond to an East-West slice through the short dimension of the galaxy. The rotation of the galaxy can be seen in each block as well as between blocks, clearly showing that the lensed galaxy's dynamics are resolved in both dimensions.

not convolve the models with the seeing, the inner rotation curve steepens causing the transition radius to increase by $\Delta r_t = 0.5$ and $\Delta r_t = 0.7$, $\Delta\gamma = 0.2$ in the ARCTAN and multi-paramater fits respectively. To compare the shape of the rotation curve with Courteau's sample we compute r_t/r_{opt} (where r_{opt} is the radius enclosing 83% of the light in the source plane photometry) to be ~ 0.25. This ratio is higher than most galaxies in the local sample, but not anomalous. Around 10% of local bright galaxies have similarly shaped rotation curves.

3.3 Discussion

The tight correlation between luminosity and rotation velocity for spiral galaxies in the local universe is known as the Tully-Fisher (TF) relation (Tully and Fisher, 1977). With a single high redshift galaxy, we can measure the evolution of the offset in the TF relation under the assumption that the slope remains fixed. In Fig. 3.4, we compare the rotation velocity and source brightness of arc # 289 with that of local and other high redshift galaxies in rest frame B and I. Whilst the current high redshift data are concentrated in rest frame B-band, rest frame I-band observations will prove a more rigorous test of evolution of the TF relation since the corrections for dust and on-going star formation are much smaller at longer wavelengths. The rest frame I-band TF therefore gives a clearer indication of the true stellar luminosity and hence the ratio of stellar mass to total halo mass.

The position of the galaxy on the TF relation in both the B and I bands shows good agreement with local data (Pierce and Tully, 1992; Mathewson et al., 1992; Haynes et al.,

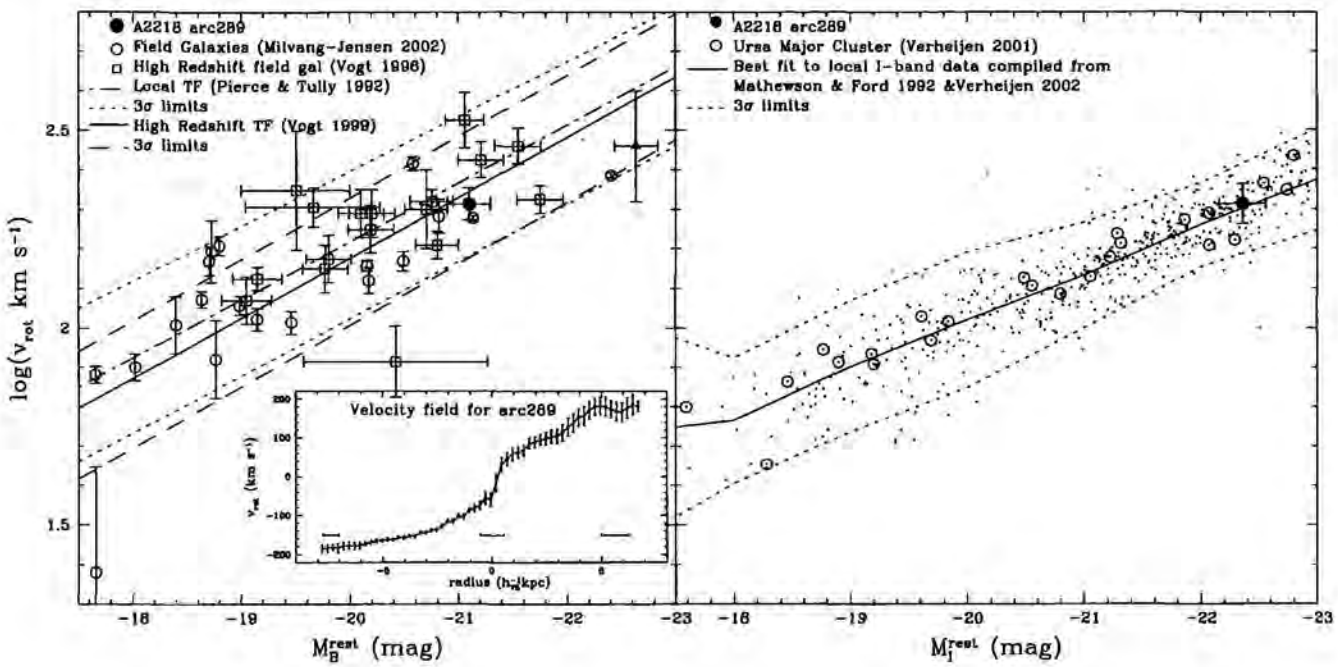

Figure 3.4: Left: *Arc*#289 on the Tully-Fisher relation in rest frame B-band compared to high redshift ($z \sim 0.83$) field galaxies (Milvang-Jensen et al., 2003) and the high redshift sample from Vogt et al. (1999). For comparison we show the low redshift local fit from Pierce & Tully (1992). The solid triangle shows a massive disk galaxy (L451) at $z = 1.34$ (van Dokkum & Stanford 2001). The galaxy rotation curve (inset) shows the peak-to-peak rotation velocity of the arc in [OII] emission built from the IFU image in the source plane. The error bars shown are formally 3-σ and alternate points are independent. The horizontal error bars show 0.7″ seeing transformed to the source plane. Right: The rest frame I-band Tully-Fisher relation compiled from Mathewson & Ford (1992) and from the Ursa-Major Cluster (Verheijen 2001). Arc#289 is shown by the solid point and lies very close to the mean TF relation for present day spirals. The small change in the I-band magnitude shown by arc#289 suggests a preference for hierarchical rather than the "classical" formation model

1999; Tully and Pierce, 2000; Verheijen, 2001). The galaxy is slightly offset to brighter magnitudes in the B-band relation, as we would expect from its blue colors. This data is in agreement with existing intermediate ($z \sim 0.5$) (Vogt et al., 1997; Milvang-Jensen et al., 2003; Böhm et al., 2003; Ziegler et al., 2002) and high redshift studies ($z \sim 1$), (Vogt et al., 2002; Barden et al., 2003). It should be noted, however, that these studies generally have to infer the turn over in the rotation curve from deconvolution of the rising rotation speed and the seeing. This might lead to a systematic underestimate of the asymptotic rotation speed. In contrast, our data clearly resolve the shape of the rotation curve (Fig. 3.4 inset) leading to much smaller uncertainty in the rotation speed of an individual galaxy.

Clearly, it would be dangerous to draw far reaching conclusions from a single galaxy, but the following comparison illustrates the sensitivity that can be expected if this level of evolution is confirmed by further observations. The theoretical evolution of the I-band TF relation from hierarchical models of galaxy formation from Cole et al. (2000) predict that for any given disk circular velocity, the I band luminosity should decrease by ~ 0.1 magnitudes from $z = 0$ to $z = 1$, whilst in the B-band such models predict an increase in luminosity of ~ 0.5 magnitude for the same redshift change. In contrast, we would expect a decrease in luminosity of ~ 0.7 magnitudes from $z = 0$ to $z = 1$ if all of the galaxy's mass were already in place at $z = 1$, but only half of the stars had yet formed. The small

change in the I-band magnitude shown by arc#289 suggests a preference for hierarchical rather than the "classical" formation model.

The methods we have developed in this chapter show the potential of gravitational lensing as a means of studying distant galaxies in a remarkable level of detail. While we have concentrated here on the dynamics of the galaxy #289, our data can also be used to investigate the spatial distribution of star formation. By combining these optical data with future observations with near-infrared integral field units, it will be possible to study the emission line ratios of [OII]:[OIII] and Hα:Hβ. We could then determine the distribution of reddening across the galaxy and its spatially resolved chemical abundance. This would provide powerful insight into the nature of star forming galaxies at this early epoch.

Chapter 4

Galaxies Under the Cosmic Microscope: Resolved Spectroscopy and New Constraints on the z=1 Tully-Fisher relation

Having pioneered the use of integral field spectroscopy of gravitationally lensed galaxies in the previous chapter, we now expand this sample to include six more ($z \sim 1$) lensed galaxies behind four rich clusters. Our main conclusions are summarised in § 4.5.

4.1 Abstract

In this chapter, we exploit the gravitational potential of four rich, lensing clusters to probe the kinematics of six $z \sim 1$ giant luminous arcs. Using detailed cluster-mass models we are able to reconstruct the two-dimensional velocity fields (observed using the GMOS integral field unit). Four of the galaxies have stable disk kinematics, whilst the other two resemble interacting or starburst galaxies. The galaxies which show stable disk kinematics have much slower rising rotation curves than expected from galaxies with similar surface brightness in the local universe. These galaxies lie very close to the mean rest-frame I-band Tully-Fisher relation for nearby spirals, but we also find evidence for ~ 0.5mag brightening in the rest-frame B-band, suggesting a clear preference for hierarchical growth of structure and increased star-formation activity at $z = 1$.

4.2 Introduction

Galaxy clusters magnify the images of distant galaxies that serendipitously lie behind them. This natural magnification provides the opportunity of studying young and intrinsically faint galaxies with a spatial resolution that cannot be attained via conventional observations (Smail et al., 1996; Franx et al., 1997; Teplitz et al., 2000; Ellis et al., 2001; Campusano et al., 2001; Swinbank et al., 2003; Kneib et al., 2004a). At these high redshifts some of the fundamental questions regarding the relationships between the total mass of a galaxy and the baryonic mass locked up in stars remain unanswered. Locally, this relation is best described by the Tully-Fisher relation; (Tully and Fisher, 1977) which is an empirical correlation between the "peak" rotational velocity (or line width) and the absolute magnitude of a spiral galaxy. Together these two parameters define a plane of structural parameters for spiral galaxies which may reflect the way in which they were initially formed, perhaps suggesting the presence of self regulating processes of star for-

mation in galactic disks. Observing how this correlation evolves over a substantial history of the Universe thus provides a powerful test of the evolution of galaxy mass (Vogt et al., 1997; Böhm et al., 2003; Milvang-Jensen et al., 2003). However, at these large look back times, (i.e. $z \gtrsim 1$) galaxies appear small (at $z \sim 1$, 1″corresponds to ~7.5 kpc) and therefore obtaining spatially resolved rotation curves is a challenge. Fortunately, the amplification caused by the deep potential well of galaxy clusters causes the image of the background galaxy to be magnified and stretched. This allows us to both target galaxies which would otherwise be too faint, and also spatially resolve the kinematics in a level of detail far greater than normally possible. Furthermore, by targeting these galaxies with Integral field spectroscopy (which produces a contiguous *x,y,velocity* map at each point in the galaxy), we are able to cleanly decouple the spatial and spectral resolution which are often mixed in traditional longslit observations.

Various calibrations of both the local and distant TF relation have been obtained, however, these results usually depend on the choice of bandpass, and the preferred measurement of the rotation speed. Furthermore, corrections for various intrinsic, environmental and instrumental effects all contribute to the shape, zero-point and scatter in the TF relation. It is now generally accepted that the shape, zero-point and scatter of the TF relation depend on bandpass and that a smaller dispersion is obtained for near-infrared band-passes (i.e. rest-frame R rather than rest-frame B-band). The dust-correction is much smaller in near-infrared photometry, and, moreover, is more sensitive to the underlying, evolved stellar population which best traces the optical mass and thus correlates more tightly with the maximum rotational speed (or total galaxy mass).

In this paper we present a study of $z \sim 1$ gravitationally lensed galaxies in the cores of the lensing clusters Abell 2390, Cl2236 and RGB1745 observed with the GMOS IFU on Gemini-North. We concentrate of the dynamics of galaxies observed through the [OII]$\lambda\lambda$3726.1,3728.8Å emission line doublet. We use the velocity fields and rotation curves to investigate the rest-frame B and I-band Tully Fisher relations. We use a cosmology with $H_0 = 72\,\mathrm{km\,s^{-1}}$, $\Omega_0 = 0.3$ and $\Lambda_0 = 0.7$.

4.3 Observations and Data Reduction

4.3.1 HST and Ground Based Imaging

Optical and near-infrared imaging of the target fields comes from a variety of sources, and we briefly describe the observations and reduction here.

Hubble Space Telescope (HST) WFPC2 $I_{814}-$ and $V_{555}-$band observations of Abell 2390 were obtained from the *HST* public archive[1]. Both the I_{814} and V_{555}-band observations were 2.1 ks and the data were reduced using the standard *stsdas* package in *iraf*. Further *HST* ACS z_{850}-band observations were taken in Cycle 11 (PID #9292). The data consist of dithered exposures with the F850LP filter and the total integration time was 1.2 ks. We reduced the data using the latest version of the MULTIDRIZZLE software (Koekemoer et al., 2002), using the default parameters and the resulting image has 0.05″ pixels and is free from artifacts. The resulting image has a field of view of 2.5′ × 1.7′ and covers the brightest central cluster galaxies and the two $z = 1$ arcs (see §4).

Near-infrared imaging of Abell 2390 was taken with the Palomar 200″ telescope on 2004 August 27 in ~0.7″ seeing and photometric conditions. We used the J and K-band filters and employed a nine-point dither pattern, and a total integration time in each band

[1]Obtained from the Multimission Archive at the Space Telescope Science Institute (MAST). STScI is operated by the Association of Universities for Research in Astronomy, Inc., under NASA contract NAS5-26555. Support for MAST for non-HST data is provided by the NASA Office of Space Science via grant NAG5-7584 and by other grants and contracts.

	Photometry						Amplification	inclination
	B	V	R	I	J	K	(μ)	(i)
Cl2236	20.50 ± 0.11	...	20.05 ± 0.11	...	19.47 ± 0.14	18.09 ± 0.12	11.2 ± 2.5	45 ± 10
RBB1745	21.90 ± 0.12	21.26 ± 0.10	20.90 ± 0.07	19.6 ± 0.3	18.29 ± 0.09	16.72 ± 0.07	10.4 ± 1.0	68 ± 9
A2390arcA	...	21.64 ± 0.06	...	19.91 ± 0.04	18.64 ± 0.10	17.42 ± 0.08	12.6 ± 0.8	69 ± 4
A2390arcB	...	23.34 ± 0.07	...	21.65 ± 0.05	20.10 ± 0.10	19.41 ± 0.06	18 ± 1	...
A2390arcD	24.55 ± 0.17	21.62 ± 0.04	...	19.53 ± 0.03	17.31 ± 0.03	15.64 ± 0.02	3.0 ± 0.4	...
A2218#289	21.66 ± 0.04	20.86 ± 0.10	20.53 ± 0.04	19.79 ± 0.05	18.63 ± 0.06	17.32 ± 0.06	4.9 ± 0.2	64 ± 6

Table 4.1: Notes: μ denotes luminosity weighted magnification. The inclinations are measured in the source-frame.

of 2.1ks (each individual exposure was 120s). The data were reduced using the standard iraf techniques and calibrated using 2MASS magnitudes from stars in the nine arcminute field of view.

The optical imaging of Cl2236 and RGB1745 is taken from Kneib et al. (1994) and Nilsson et al. (1999) respectively. These consist of B, R and B, V, R, I-band imaging of these clusters. We supplement this data with near-infrared $J-$ and $K-$band imaging of Cl2236 and RGB1745 which was carried out on UKIRT between 2004 August 15 and 2004 August 20[2]. The observations were made in photometric conditions and $\sim 0.7''$ seeing. We used the UIST imaging camera (Ramsay Howat et al., 1998) which employs a 1024×1024 InSb detector at $0.12''$ pixel^{-1} to give a $2'$ field of view. The observations were taken in a standard nine-point dither pattern and reduced using the relevant ORAC-DR pipeline. The total integration times for each band was 2.4 ks. To calibrate our data, we observed UKIRT faint photometric standards (Hawarden et al., 2001). These standards were observed at similar air masses and using the same instrumental configuration as the target galaxies.

From our multi-wavelength imaging, we constrain the spectral energy distribution (SED) of each galaxy. We calculate the magnitude of the arcs in various passbands (Table 4.3.1) by using the IRAF IMSURFIT package with the sky estimated from a 2nd order polynomial surface fit to regions around the galaxy. We then use SEXTRACTOR (Bertin and Arnouts, 1996) to estimate the residual background within the frame. We use the observed colours (at the known redshift) to calculate the current to past star formation rate and use this to find the best fit SED. At $z \sim 1$ the rest frame I-band luminosity is approximately equivalent to the observed H-band and so is calculated from the J and K photometry. We co-add the J, K images to obtain an aperture which is used to extract the J, K magnitudes and interpolate for the relevant SED type. We apply the same technique for the rest-frame B-band magnitude, (at $z \sim 1$, I and R-bands are the closest match to rest-frame B-band) and estimate its uncertainty by computing the magnitude for a variety of SED types which are consistent with the observed optical colours.

4.3.2 GMOS Spectroscopic Imaging

Three-dimensional spectroscopic observations of the galaxies were made in queue mode with the Gemini Multi-Object Spectrograph (GMOS) on Gemini-North[3] between 8 June and 14 August 2003 in photometric conditions and $\lesssim 0.7''$ seeing. Details of the observations and source redshifts are listed in Table 4.3.2. The IFU uses a lensed fiber system to reformat the $7.9'' \times 5.3''$ field into two long slits (Allington-Smith et al., 2002). All observations were made using an I-band filter in conjunction with the R400 grating which results in two tiers of spectra recording a maximum field of view. The spectral resolution

[2]The United Kingdom Infrared Telescope is operated by the Joint Astronomy Centre on behalf of the U.K. Particle Physics and Astronomy Research Council.

Source	α_{J2000} (h m s)	δ_{J2000} (° ′ ″)	redshift (z)	t_{exp} (ks)
A2390arcA	21 53 34.52	+17 42 02.32	0.912	14.4
A2390arcB	21 53 34.30	+17 41 56.01	1.032	12.0
A2390arcD	21 53 34.39	+17 42 21.19	0.912	10.8
Cl2236	22 39 33.00	-04 29 19.83	1.116	10.8
RGB1745	17 45 38.11	+39 51 23.80	1.056	10.8

Table 4.2: Positions and redshifts for the arcs in our sample

of this configuration is $\lambda/\Delta\lambda = 2000$. Each observation was split into 2.4 ks exposures and dithered by one IFU lenslet to account for bad pixels. The data was reduced in IRAF using the GMOS-IFU data reduction pipeline which extracts, flat-fields and wavelength calibrates the data. To subtract the sky emission lines the GMOS IFU employs a second ($5'' \times 3''$) IFU separated by one arcminute on the sky. We used IDL to identify and extract sky-fibres adjacent to object fibres on the spectrograph and used these to achieve the sky-subtraction. We also improved the flattening of the data by using continuum regions either side of the emission lines. The output pixel scale is 1.3Å/pixel and the instrumental profile has a FWHM of 3.4Å (measured from the widths of the skylines). In all following sections we have deconvolved the instrumental resolution from the FWHM of the galaxy.

For one of the targets, (Abell 2390 *arc A*), we required two pointings to cover the large spatial extent ($\sim 12'' \times 4''$) of the galaxy. During the second pointing the much smaller arc ($\sim 2'' \times 3''$ at z =1.033; Abell 2390 *arc B*) was also covered. To accurately align and mosaic the datacubes (which is particularly important in order to accurately reconstruct the galaxy in the source frame) we constructed (wavelength collapsed) [OII] emission line maps of the two arcs (between -300 and +300 $\mathrm{km\,s^{-1}}$) and overlaid and aligned these intensity maps with *HST I*-band imaging (which includes the [OII] emission line at $z \sim 1$). We note that the amplitude of the parallactic angle from the [OII] emission between the z=0.912 and z=1.033 arc is less than 0.02″.

We also note that the redshift of the arc in RGB1745+39 places the [OII] emission at 7660Å(in a region near the atmospheric absorption). To correct for this absorption, we extracted the spectrum of the foreground cluster galaxy (which is a strong continuum source; see §4.4.4) and use this to model and correct for the telluric absorption.

After constructing the datacubes, we proceed to fit the [OII] emission line doublet from each galaxy using a χ^2 minimisation procedure, taking into account the greater noise at the position of the sky lines. The spectra were averaged over a $0.6'' \times 0.6''$ spatial pixel region, increasing this region to $0.8'' \times 0.8''$ pixels if the signal was too low to give a sufficiently high χ^2 improvement over a fit without the line. In regions where this averaging process still failed to give an adequate χ^2, no fit was made. Using a continuum fit, we required a minimum χ^2 of 25 (S/N of 5) to detect the line, and allow the signal to drop by a χ^2 of 9 to calculate the error in the velocity. This corresponds to a formal 3σ error.

4.4 Analysis

4.4.1 Gravitational Telescopes

Before we discuss what can be learnt from our IFU observations, we must first correct for the distortion and magnification of the galaxy image by the cluster lens. In this section

[3]Programme ID: GN-2003A-Q-3

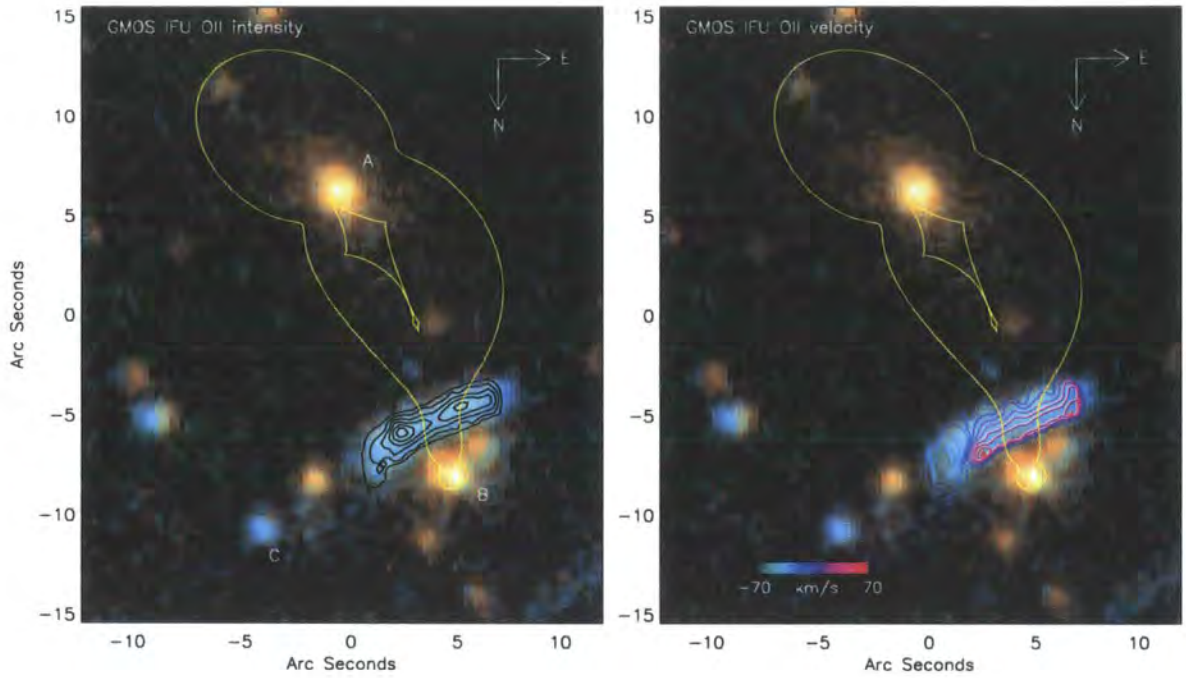

Figure 4.1: *Left:* True colour BVR image of the lensing cluster Cl2236 at z=0.58 with the [OII] emission line intensity overlaid as contours. Right: The velocity field of the $z = 1.116$ arc derived from the [OII] emission line. In both diagrams we show the brightest two cluster galaxies (A and B), as well as the $z = 1.116$ radial critical line and caustic lines.

we briefly describe the mass models for the clusters in our sample and then use these to reconstruct the source morphology and dynamics of each galaxy.

4.4.2 Abell 2390

A detailed mass model for A2390 (z_{cl}=0.233) was originally developed by Pelló et al. (1999).This cluster is extremely luminous, hot in X-rays, and has a significant early type galaxy population that is concentrated in the inner regions (Fritz et al., 2003). The cluster consists of a bright central cluster galaxy, but also has a subclump of galaxies to the west, one of which causes the straight arc to be highly magnified. We have updated the cluster mass model developed by Pelló et al. (1999) using new *HST* ACS observations. Pelló et al. (1999) (see also Bunker et al., 2000) spectroscopically identify two pairs of z=4.04 and z=4.05 multiply imaged galaxies (the small field of view of WFPC2 did not allow the third counter-image of the z=4.05 arc to be identified). This brings the number of multiply images $z \sim 4$ arcs in this cluster to two, and the number of spectroscopically confirmed $z \sim 1$ arcs to four. *HST* ACS I_{850LP}-band observations of this cluster have sufficient field of view that we can search for the counter images of the $z \sim 4$ galaxies in Pelló et al. (1999) and we identify these at α =328.4056, δ =17.706155. These (spectroscopically confirmed) strongly lensed galaxies can be used as constraints to produce one of the best constrained mass models for a strong lensing cluster. The precision of this lens model

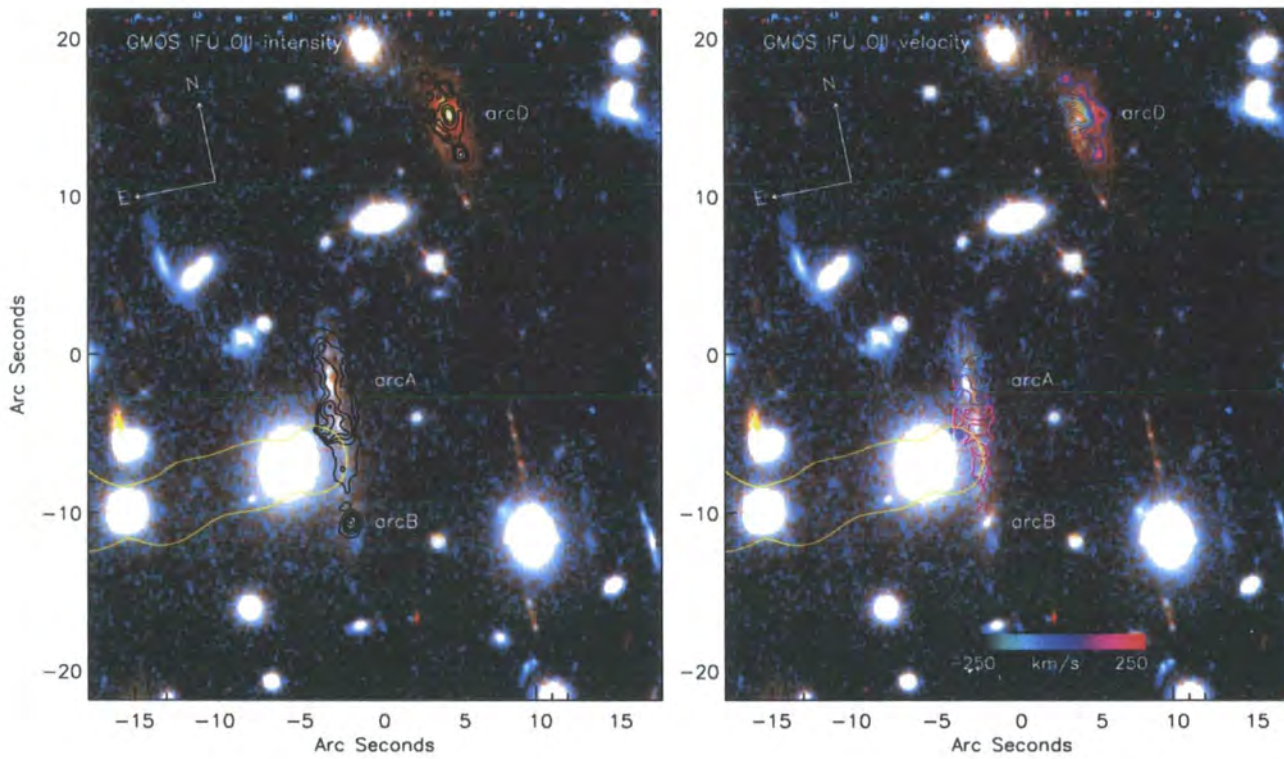

Figure 4.2: True colour VI image of the lensing cluster A2390 at z=0.228 with the GMOS IFU data overlaid. In both panels we show the critical line and caustic line for z=0.912, z=1.033. *Left:* The intensity distribution of the [OII] emission line overlaid on the arcs. *Right:* The velocity field of the arcs derived from the [OII] emission line. The straight arc has an observed peak-to-peak velocity gradient of $175 \pm 20\,\mathrm{km\,s^{-1}}$, but also appears to be multiply imaged at the southern end. This is confirmed by both the *HST* imaging and IFU observations. The smaller $z = 1.033$ arc has no detectable velocity structure and we place a limit of $\sim 60\,\mathrm{km\,s^{-1}}$ across the system. Arc D appears to be morphologically complex, with several components which may be indicative of a recent tidal interaction or merger.

makes this cluster an ideal gravitational telescope with which to study (and reconstruct) the detailed properties of high redshift galaxies.

To compute the magnification (μ) of the galaxies in our sample, we exploit the fact that gravitational lensing conserves surface brightness, and compute the luminosity weighted magnification in each band by using the transformation between the sky-plane and source-plane coordinates and compare the flux in the (reconstructed) source and (observed) sky frames. The statistical error bars on μ are derived from the family of lens models which adequately reproduce the multiply images arcs in the cluster. We estimate the 1-σ uncertainty by perturbing the parameters of the best fit lens model such that $\Delta\chi^2 = 1$. For each model we recompute the magnification of each arc. The error corresponds to the largest variation in magnification that we found and is converted into a magnitude estimate in the source plane photometry.

Having reconstructed the source mophology of the galaxies, we can determine the inclination. We fit ellipses to an isophote of the galaxy image in the source plane using the IDL GAUSS2DFIT routine (and assuming an intrinsically circular disk). The ellipticity is then $e = 1 - b/a$ (where a and b are the major and minor axis of the ellipse) and the inclination, i, is $\cos i = b/a$. The average axis ratios of the ellipses from the various passband are translated into inclinations and are given in Table 4.3.1.

Abell 2390 arcA

The straight arc at $z = 0.912$ was first studied in detail by Pelló et al. (1999) and is approximately 40″ away from the central galaxy. This arc is over 10″ in length and appears highly sheared at the southern end. To cover the large spatial extent we obtained two IFU pointings. The intrinsic peak-to-peak velocity difference in this galaxy is $420 \pm 20\,\mathrm{km\,s^{-1}}$. However, the most striking result is that both the mass model and our IFU observations support the claim that the arc is multiply imaged at the southern end. In Fig. 4.2 we show the field around the arcs in our sample and overlay the GMOS results. We also overlay the z=0.912 critical curves which show that the southern end of straight arc crosses the critical lines predicting that the southern end of the galaxy disk should be multiply imaged. The velocity field of the galaxy strongly agrees with this interpretation: the southern end of the galaxy (S0) has an observed velocity (with respect to the center of the galaxy) of $\sim 120\,\mathrm{km\,s^{-1}}$. Moreover, components S1 and S2 have exactly the same velocity as S0 and are located spatially in exactly the same position as the lens model predicts the multiple images should be. Using the transformations between source- and sky- planes we reconstruct the source mophology of the galaxy, (Fig. 4.3), which (combined with the velocity field) shows that this galaxy appears to be a disk-like spiral galaxy with stable disk-kinematics. Using the techniques described above, we compute the luminosity weighted magnification of this galaxy to be 13 ± 2, with a source frame inclination of $70 \pm 5°$.

Abell 2390 arcB

The second pointing of the straight arc also covered the slightly higher redshift (z=1.033) arc (Frye and Broadhurst, 1998). This galaxy has a compact morphology ($\lesssim 1.5$″FWHM) in the sky plane and $\sim$5 kpc in the source frame and has an magnification of 17 ± 1. We detect no coherent velocity gradient across the galaxy, and we place a limt of $60 \pm 15\,\mathrm{km\,s^{-1}}$ on a possible shear. The [OII] emission doublet is well resolved and has width of $50\,\mathrm{km\,s^{-1}}$ (FWHM) (deconvolved for instrumental resolution). The colours of this galaxy predict

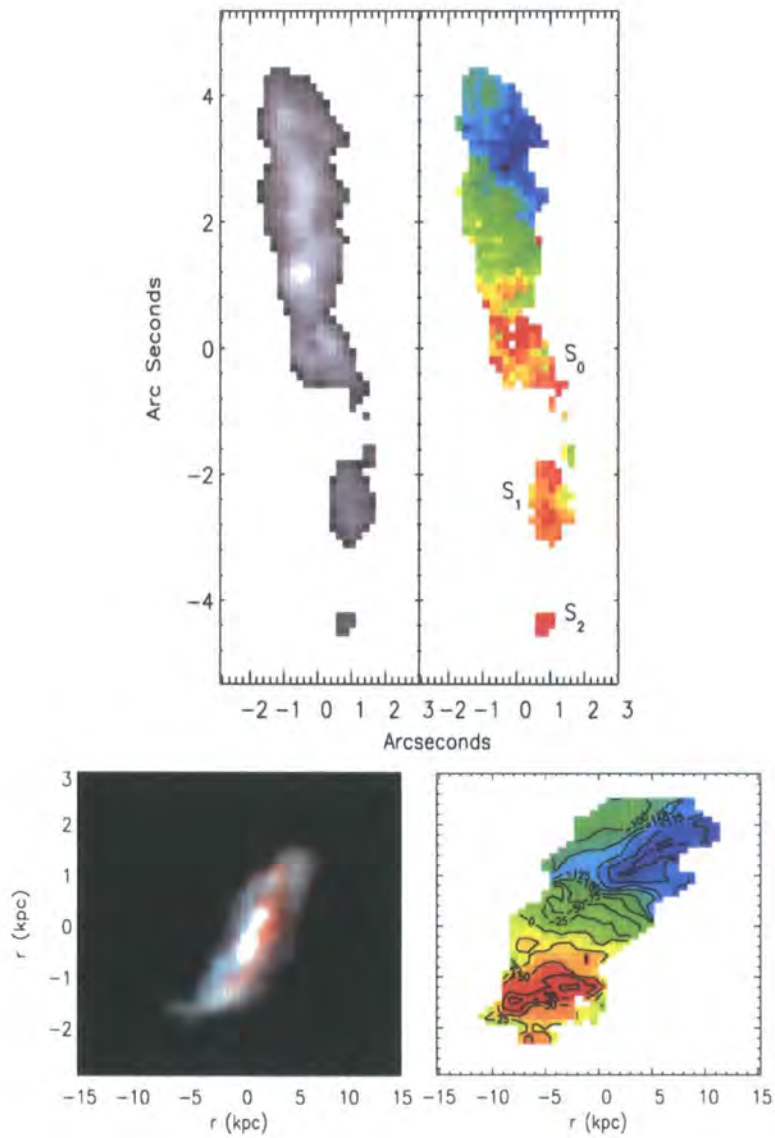

Figure 4.3: *Top Left:* [OII] emission line intensity map of the z=0.912 "straight" arc in A 2390 from the GMOS IFU observations. *Top Right:* Velocity field of the arc derived from the [OII] emission line. *Bottom Left:* Reconstructed image of the arc from HST V- and I-band observations. *Right:* Reconstructed velocity field of the arc. Components S1 and S2 are multiple images of S0. The colours, morphology and kinematics of this galaxy resemble a disk-like galaxy.

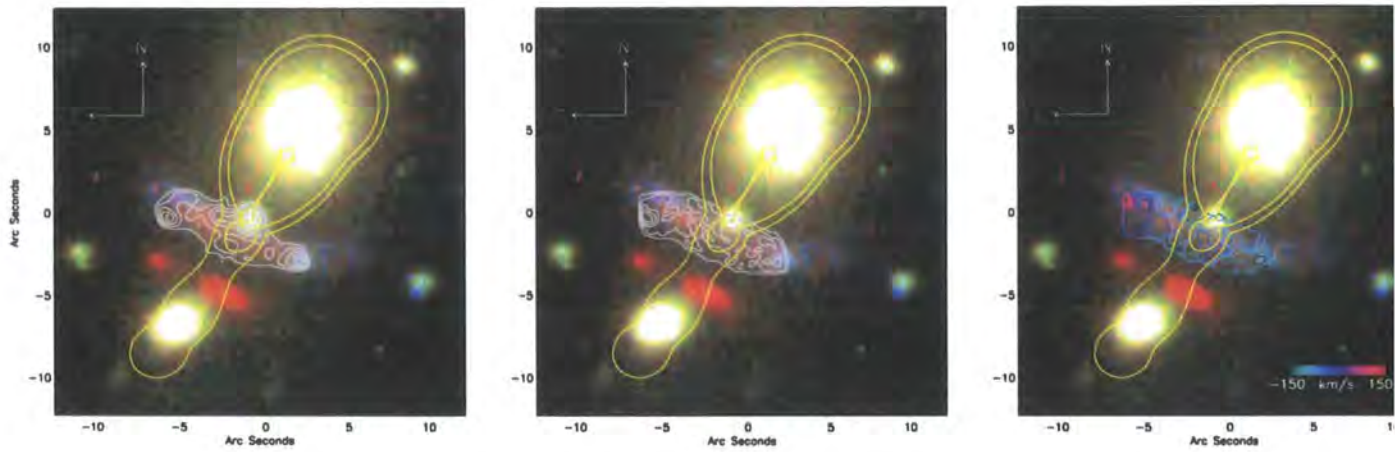

Figure 4.4: True colour *BRK* image of the lensing cluster RGB1745 at z=0.267 with the GMOS IFU observations overlaid. In all three diagrams we show the brightest cluster galaxies, as well as the $z = 1.056$ radial critical line and caustic line. We also overlay the z=1.2 critical line which we use to infer a redshift of z=1.2±0.1 of the triply imaged ERO ($R - K$=6) to the SE of the z=1.056 arc. *Left:* We have overlaid a wavelength collapsed (λ7600–7800) image which includes the [OII] emission (and also continuum from the foreground galaxy). *Middle:* The intensity distribution of the [OII] emission line overlaid on the arc. *Right:* The velocity field of the $z = 1.056$ arc derived from the [OII] emission line which (along with the cluster mass model) shows that the central component of the arc is multiply imaged.

a past-to-present star formation history consistent with a young starburst galaxy. The small intrinsic size of this galaxy argue it may be a HII region undergoing its first major star-formation episode.

Abell 2390 arcD

This $z = 0.912$ arc lies only 125 kpc away from the $z = 0.912$ straight arc in the source plane, and suggests that this cluster may be lensing a high redshift group of galaxies (Pello et al., 1991). The imaging observations of this galaxy shows a disturbed morphology, with multiple components and colours consistent with an evolved stellar population. The IFU observations show that the galaxy has a disturbed velocity field, which are compounded by large (FWHM$\sim 300\,\mathrm{km\,s^{-1}}$) emission lines widths. There is evidence for some rotational motion across the short axis of the galaxy (with peak-to-peak velocity of $\sim 500\,\mathrm{km\,s^{-1}}$). The bright knot (located $1''$ to the south) is offset by $\sim 480 \pm 60\,\mathrm{km\,s^{-1}}$ and 2 kpc in projection (in the source frame) and has an [OII] line width of $800 \pm 200\,\mathrm{km\,s^{-1}}$ (FWHM). The magnification of this source is a factor 3.0±0.5 (corresponding to a boost in magnitude of Δm=1.4).

This galaxy is not detected in the Chandra 9.1 ks image to a flux limt of $\sim 1 \times 10^{-15}\mathrm{erg\,cm^{-2}\,s^{-1}}$ in the in the 0.5-7 KeV-band (which corresponds to a maximum source luminosity (accounting for lensing) of $\sim 4 \times 10^{42}\mathrm{erg\,s^{-1}}$), ruling out that this galaxy has a high luminosity AGN (Allen et al., 2001). However, this galaxy is detected in a deep ISOCAM survey of this cluster at 7μm and 15μm with corresponding fluxes of 0.132±0.042mJy and 0.276±0.93mJy resectively (Metcalfe et al., 2003), furthering the evidence for an evolved population. The complex morphology and residual motion in the chaotic velocity field suggest that this galaxy may recently have undergone a tidal interaction or merger. Assuming the velocity offsets across the galaxy arise from merging

components across ~12 kpc (corrected for lensing) we estimate a dynamical mass of ~ 10^{11} $M_{\odot}$ (although clearly there are uncertainties about whether this galaxy is relaxed).

4.4.3 Cl2236

A cluster mass model for the cluster Cl2236 (z_{cl} = 0.56) was originally developed by Kneib et al. (1994). The cluster contains two bright elliptical galaxies (labelled A and B in Fig. 4.1). The giant elliptical galaxy, A (with an extended envelope) is a radio emitter and is the central galaxy of the cluster. The arc at z = 1.116 lies between these two galaxies, but is closer to B. It is almost straight, with a length of ~ 8″ but with a slight curvature towards galaxy B. This suggests that there is a clump of mass around A but with a perturber around B. A slightly higher redshift arc (z = 1.334) lies to the East (labelled C). Previous longslit observations showed that the z = 1.116 arc has a velocity gradient of ~ 120 km s^{-1}. Kneib et al. (1994) suggest that this velocity gradient probably arises due to interacting galaxies seperated by ~2 kpc in the source frame. Our IFU observations of this arc therefore provide a powerful tool for testing this hypothesis, since we can decouple the spatial and velocity information which is often mixed in longslit observations.

In Fig. 4.1 we show the field around the arc, and overlay the [OII] intensity (as measured from our GMOS IFU observations) on the image. We also show the velocity field derived from the [OII] emission line. In the observed frame, the z = 1.116 arc shows a peak velocity gradient of 110 ± 15 km s^{-1} across the galaxy. However, it is not clear that this system comprises of two interacting galaxies. Instead, our IFU observations suggest that this galaxy is either a multiply imaged or highly sheared image of a single background galaxy. Using the velocity field of the z=1.116 arc and the same lensing constraints as (Kneib et al., 1994) we compute a family of models which adeqeutely reproduce the positions and shapes of the arcs. We construct nine such models, all of which have a dark matter halo centered on the BCG (galaxy "A"), and seven of which have a dark-matter sub-halo around the perturber (galaxy "B"). The lowest mass versions (σ_A=930 km s^{-1}, σ_B=0 km s^{-1}) of the models shear the galaxy sufficiently to reproduce a symmetric source-plane morphology with respect to the position where the observed velocity field changes sign. The highest mass versions of the models (σ_A=750 km s^{-1}, σ_B=500 km s^{-1}) multiply image the receeding part of the galaxy, but do not have quite sufficient mass to multiply image the aproaching part of the galaxy.

Fig. 4.1 shows the field around the arc and we overlay the z = 1.116 critical lines. Using the best fit lens model (σ_A=875 km s^{-1}, σ_B=300 km s^{-1}), we compute the magnification (μ) of the arc, obtaining a mean luminosity weighted magnification of μ = 11.2, with an associated error (from the family of lens models) of ±2.5. This corresponds to a boost in magnitude of Δm=2.6±0.2) across the whole galaxy image. By reconstructing the galaxy with each model and in each band, we also determine a source frame inclination of i=45±10°.

4.4.4 RGB1745

The z = 1.056 arc in RGB1745+39 was originally discovered by Nilsson et al. (1999). The cluster lies at z = 0.267 and comprises of a giant elliptical galaxy at its center (which is also a strong radio emitor). A second subclump of galaxies lie to the SE of the central galaxy and the giant blue arc lies directly between these, lying directly beneath a third (smaller) perturber. The *BVRI* imaging data of this field comes from Nilsson et al.

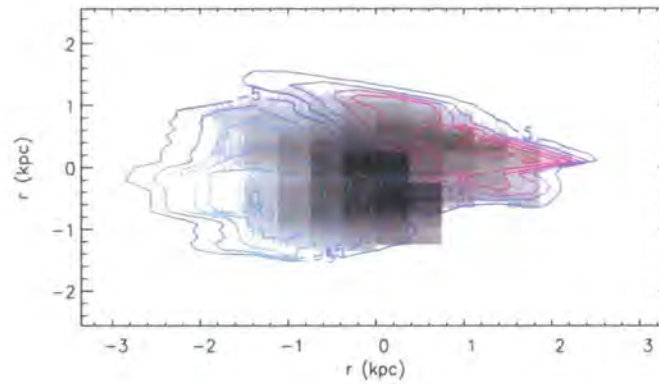

Figure 4.5: Combined reconstructed BRK image of the arc in Cl2236 with the reconstructed velocity field overlaid as contours. Whilst it is very difficult to constrain the morphology from ground based imaging, the best fit SED suggests a current-to-past star formation rate consistent with an Sab or Sbc galaxy. Furthermore, the velocity field of the galaxy clearly resembles that of a disk with stable disk kinematics.

(1999), but we also complement this data with $J-$ and $K-$band imaging from UIST on UKIRT.

Before we discuss the IFU observations of the $z = 1.056$ arc, we note that the most striking feature from the JK imaging is the presence of a triply imaged galaxy $4''$ to the SE of the $z = 1.056$ arc. This galaxy is barely detected in the optical imaging, but is very bright in the near-infared ($J = 18.27 \pm 0.06$ and $K = 16.32 \pm 0.04$) and an $R - K$ colour of 6.4 ± 0.2. Using LRIS on Keck we obtained a 1 hour z-band spectrum on March 03 2005. The spectrum shows no emission lines, but we identify a continuum discontinuity as 8440Å which we interpret as the 4000Å break for z=1.11±0.05. Using this redshift and the obvious triple image configuration, we obtain a tight constraint on the lens model for this cluster.

Returning to the z=1.056 arc, traditional longslit spectroscopy of this arc from Nilsson et al. (1999) showed a velocity gradient of $\sim 200\,\mathrm{km\,s^{-1}}$ across the long axis, making it an ideal target for IFU spectroscopy.

By extracting a spectrum from the IFU datacube we confirm that the bright galaxy $1''$ to the NW of the arc is a foreground galaxy, and isn't the bulge of the background galaxy. We use the continuum image of this foreground galaxy to align the IFU observation with the imaging. Using the velocity field of the arc, we identify three features which appear to have a triple image configuration and use this data to constrain the lens model. From our data, it appears that in the source plane, the center of the galaxy lies directly between the critical lines, with either side of the spiral arms lying outside the caustic (Fig 4.4). Thus in the image plane, the center of the galaxy appears triply imaged, with the outer edges of the galaxy being singly imaged. The source-frame peak-to-peak velocity field of the galaxy is $190 \pm 20\,\mathrm{km\,s^{-1}}$ and we compute the magnification to be 10.4 ± 1.0. The extracted one-dimensional rotation curve from this galaxy exibits a strong velocity shear but doesn't show any sign of turning over. This may arise if the IFU only covered the central regions of the galaxy (with some of the galaxy disk lying outside our field of view), or the galaxy may not yet have regular disk kinematics. However, since the velocity field (and rotation curve) is smooth we do not believe that this galaxy is a merging/interacting system, indeed the colours of this galaxy suggest a past-to-present star formation history

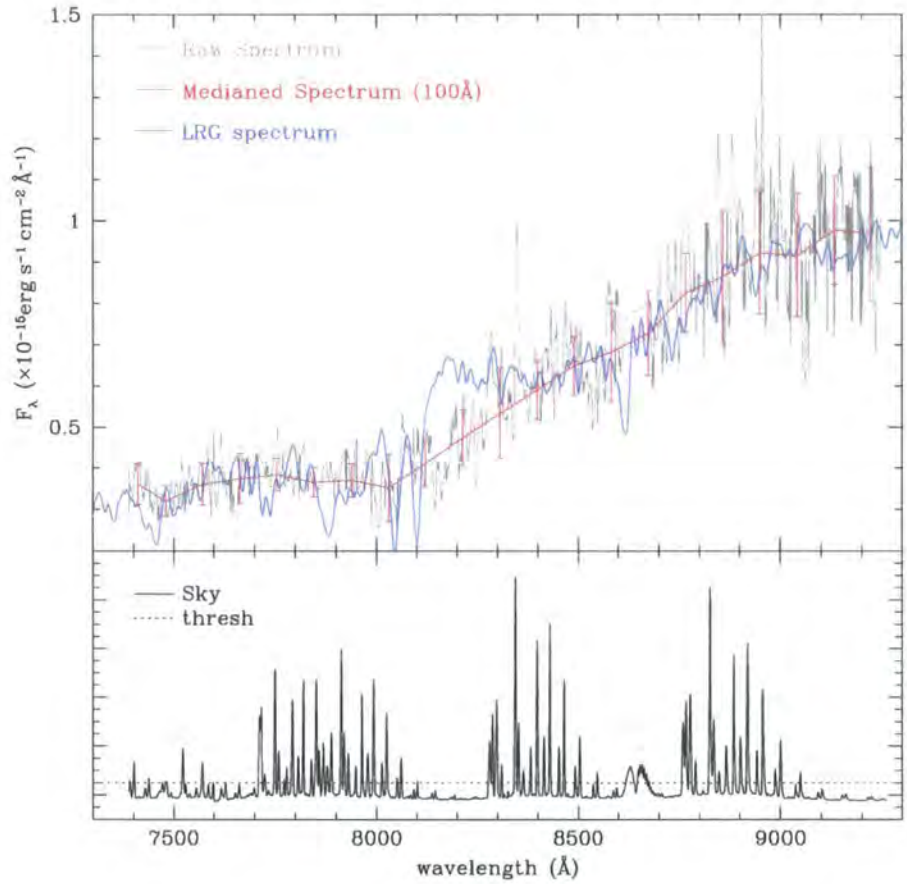

Figure 4.6: LRIS z-band spectra of the multiply imaged ERO in RGB1745+39. The spectrum is produced by rejecting pixels dominated by the strong night sky emission i.e. those regions above the horizontal line in the lower spectrum which shows the night sky spectrum (offset and scaled for clarity). The smoothed spectrum is produced by median filtering the raw spectrum with a boxcar width of 100Å and the error bars represent 1σ errors in each boxcar window. We identify the discontinuity in the spectral shape at λ8440Å as the 4000Å break which yields a redshift of z=1.11±0.05. The blue line shows an LRG galaxy template from the SDSS, redshifted to the same redshift as the ERO.

consistent with a late type spiral galaxy.

4.5 Discussion

The tight correlation between luminosity and rotation velocity for spiral galaxies in the local universe is known as the Tully-Fisher (TF) relation (Tully and Fisher, 1977). By observing the distant ($z > 1$) universe, we sample cosmic history at a time before many present-day stars had formed. The "classical" galaxy formation model, where the formation of a dark halo precedes the formation of the galaxy's disk (with the disk subsequently growing over an extended period of time through the gradual accretion of gas from the halo, (e.g. Eggen et al., 1962; Larson et al., 1980; Sandage, 1990), predicts that the stellar masses at a given circular velocity will be much lower at $z = 1$ (by about a factor of 2) than at the present-day. In contrast, CDM hierarchical models predict that galaxies would follow a similar stellar mass versus circular velocity correlation at all redshifts (Cole et al., 2000). Previous work in this area has, by necessity, concentrated on galaxies which are intrinsically bright and mostly at $z < 0.5$ (Vogt et al., 1997; Verheijen, 2001; Ziegler et al., 2002; Böhm et al., 2003), with only a few galaxies being studied at higher redshift (Vogt et al., 1996; Milvang-Jensen et al., 2003; Barden et al., 2003). The results suggest an increase in B-band luminosity for a given circular velocity (Vogt et al., 2002; Kannappan et al., 2002) – suggesting a preference for hierarchical formation models. However, even massive galaxies at these high redshifts only span 1–2″ on the sky, and therefore these studies usually preferentially select high-luminosity (and therefore high mass) and spatially extended galaxies in order to attempt to identify the turn over in the rotation curve.

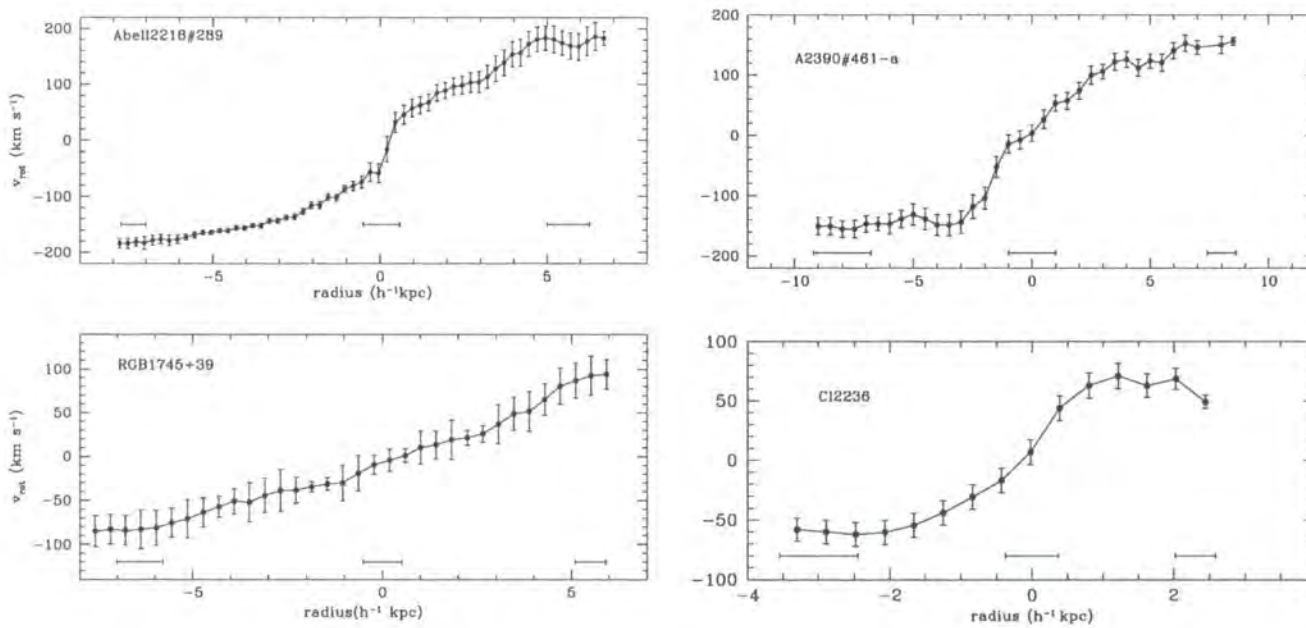

Figure 4.7: One-dimensional rotation curves from the galaxies in our sample. These are extracted from the two-dimensional source plane major axis cross section. The solid bars represent 0.7″ seeing (transformed to the source plane) of each galaxy.

In this study, we have targeted six $z \sim 1$ gravitationally lensed galaxies with IFU spectroscopy. Using detailed mass models for the clusters we have reconstructed the

source morphologies of these galaxies. The typical boost in magnitude for these galaxies is $\Delta m = 2$, which means the typical (unlensed) R-band magnitude of our sample of $m_R \gtrsim 22$. Using the IFU on GMOS-North we have mapped the two-dimensional velocity fields of these galaxies. IFU spectroscopy is preferential to traditional longslit spectroscopy which often mixes spatial and spectral resolution, leading to primary uncertanties about the true asymptotic rotational velocity field of galaxies. Such studies usually have to deconvolve the seeing from the rising rotation curve in order to infer the true rotational velocity. In contrast, our IFU data decouples the spectral and spatial information allowing us to clearly resolve the turn over in the rotation curves in our sample.

With a small sample of high redshift galaxies which show stable (disk-like) kinematics we can measure the evolution of the offset in the TF relation under the assumption that the slope remains fixed. In Fig. 4.8, we compare the rotation velocities and source brightness of the arcs which resemble stable disks with that of local and other high redshift galaxies in rest frame B and I. We also include the Abell 2390 arcB and arcD in this analysis. Whilst these two galaxies do not resemble rotating disks (and therefore inclination corrections are uncertain), we view it as more reliable to include them in this analysis than to exclude them. Whilst the current high redshift data are concentrated in rest frame B-band, rest frame I-band observations will prove a more rigorous test of evolution of the TF relation since the corrections for dust and on-going star formation are much smaller at longer wavelengths. The rest frame I-band TF therefore gives a clearer indication of the true stellar luminosity and hence the ratio of stellar mass to total halo mass. The position of the galaxies on the TF relation in both the B and I bands shows good agreement with local data (Pierce and Tully, 1992; Mathewson et al., 1992; Haynes et al., 1999; Verheijen, 2001). This data is in agreement with existing intermediate ($z \sim 0.5$) redshift studies, (Vogt et al., 1997; Milvang-Jensen et al., 2003; Böhm et al., 2003; Ziegler et al., 2002) and also high redshift ($z \sim 1$) studies, (Vogt et al., 2002; Barden et al., 2003). Whist the small number of galaxies in our sample means it is difficult to draw strong conclusions, our observations suggest a ~ 0.5mag of brightening in the B-band TF from the local ($z = 0$) correlation, whilst in the I-band we place a limit of < 0.1mag between our $z = 1$ sample and the local $z = 0$ correlation.

Clearly, it would be dangerous to draw far reaching conclusions from a small number of high-redshift galaxies, but the following comparison illustrates the sensitivity that can be expected if this level of evolution is confirmed by further observations (Flores et al. 2004). The theoretical evolution of the I-band TF relation from hierarchical models of galaxy formation from Cole et al. (2000) predict that for any given disk circular velocity, the I band luminosity should decrease by ~ 0.1 magnitudes from $z = 0$ to $z = 1$, whilst in the B-band such models predict an increase in luminosity of ~ 0.5 magnitude for the same redshift change. In contrast, we would expect a decrease in luminosity of ~ 0.7 magnitudes from $z = 0$ to $z = 1$ (in the I-band) if all of the galaxy's mass were already in place at $z = 1$, but only half of the stars had yet formed. The small scatter around the local I-band TF relation shown by our galaxies suggests a preference for hierarchical rather than the "classical" formation model. Furthermore, the 0.5 magnitude evolution in the rest-frame B-band suggests increased star formation activity at $z = 1$.

For those galaxies with well defined rotation curves, we can also compare the shapes of the rotation curves with those of local ($z \lesssim 0.03$) spiral galaxies by Courteau and Rix (1997). We fit the observed source-plane 1-D rotation curve with the ARCTAN and multi-fit parameter models from Courteau and Rix (1997). Using a χ^2 fit the observed rotation curves are best fit with models with high values of γ and r_t/r_{opt} (where r_t describes the transition radius between the rising and flattening of the curve and r_{opt} is the radius enclosing 83% of the light in the source plane photometry). Such models indicate slowly

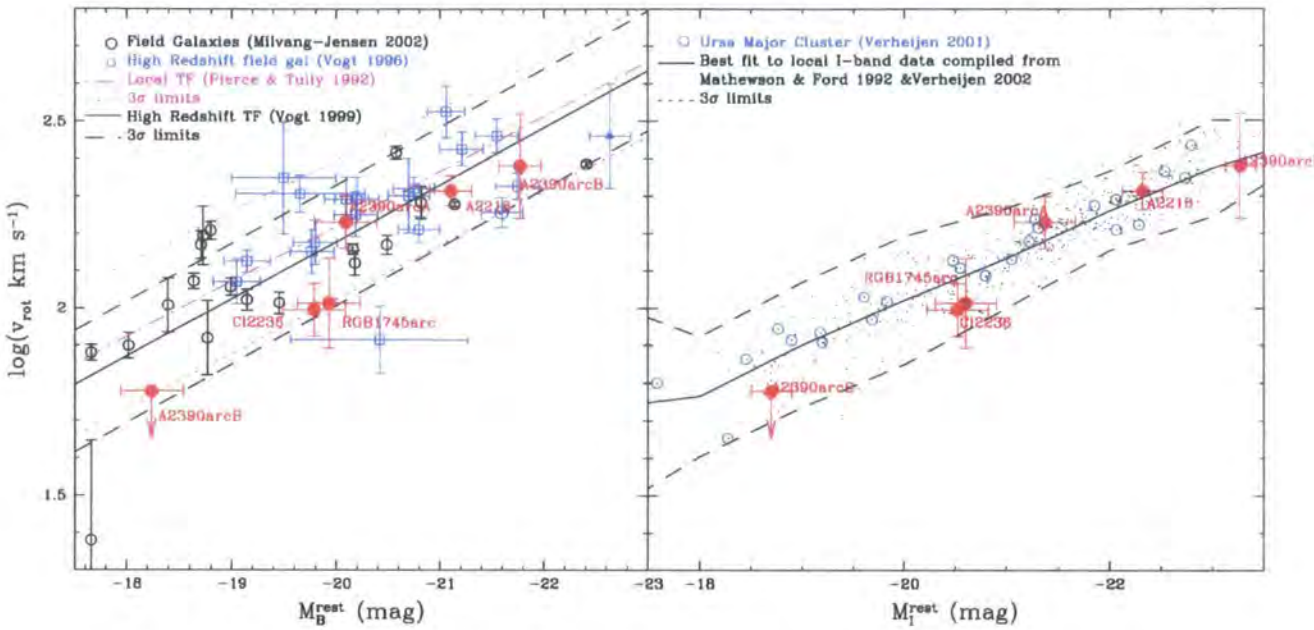

Figure 4.8: Left: The arcs from our survey on the Tully-Fisher relation in rest frame B-band compared to high redshift ($z \sim 0.83$) field galaxies (Milvang-Jensen et al. 2003) and the high redshift sample from Vogt et al. (1999). For comparison we show the low redshift local fit from Pierce & Tully (1992). The solid triangle shows a massive disk galaxy (L451) at $z = 1.34$ (van Dokkum & Stanford 2001). Right: The rest frame I-band Tully-Fisher relation compiled from Mathewson & Ford (1992) and from the Ursa-Major Cluster (Verheijen 2001). The arcs are shown by the solid points.

rising rotation curves and usually favour fainter (or low-surface brightness) galaxies, yet the source frame surface brightnesses of the four galaxies are consistent with high surface brightness (HSB) galaxies ($\mu_{b,o}$=21.5, 21.2, 20.6 and 21.0 for A2390arcA, Cl2236arc, A2218arc#289 and RGB1745arc respectively). In order to investigate how sensitive these estimates are to the seeing, we convolve the rotation curves with a further $0.7''$ seeing (transformed to the source plane of the galaxies) and refit the rotation curves. The result is only modest, at best and we find that the inner rotation typically curve flattens the transition radius by $\Delta r_t = 0.5$ and $\Delta r_t = 0.6$, $\gamma = 0.18$ in the ARCTAN and multiparamater fits respectively. We therefore feel confident that the slow rise we see is real and not simply an artifact of the seeing FWHM. In the local galaxy population, only about 10% of galaxies have similarly shaped rotation curves.

The dynamics of two of the galaxies in our sample do not resemble galaxies with stable disk kinematics. The first, Abell 2390arcB appears to be a highly magnified HII region, with a velocity dispersion of $\sim 50\,\mathrm{km\,s^{-1}}$ and a (source frame) radius of $\sim$5 kpc. The other galaxy in our sample which does not appear to have regular disk kinematics is Abell 2390 arcD. This galaxy has a disturbed morphology, and appears to have several components. When combined with the velocity field from the [OII] emission, we find some evidence for rotation, although this is compounded by the large line widths ($\sim 300\,\mathrm{km\,s^{-1}}$ FWHM). We identify a bright knot, or companion, offset by 2 kpc and $300\pm50\,\mathrm{km\,s^{-1}}$ in projection, indicating that this galaxy has recently undergone a tidal interaction/merger which has promoted the complex morpholgy.

Our observations clearly show the power of using integral field spectroscopy of gravitationally lensed galaxies to study the evolution of galaxy mass. Whilst only four of the six

galaxies in our sample appear to have regular disk kinematics, the high redshift Universe is clearly a much more violent place than today, and therefore to find merging/interacting or starburst galaxies is also a useful probe of galaxy formation models.

Chapter 5

The Rest Frame Optical Spectra of SCUBA Galaxies

Motivation

The processes by which the dense, gravitationally bound galaxies formed in the early Universe can be investigated by studying both "normal" galaxies (which we can observe due to the boost of gravitational lensing) and by comparing these with galaxies which are already luminous/massive systems at similar epochs. One important population of galaxies has recently been identified using the SCUBA camera on the JCMT (which operates in atmospheric windows around 450μm and 850μm). Discovery of these galaxies nearly 10 years ago lead to excitement, however this quickly turned to pecisism as the large beamsize of the JCMT (8″) conspired with the optical faintness to render source identifications rare and therefore investigating their source properties incredibly difficult. However, sub-arcsecond resolution radio maps were able to pin-point the optical counterparts of SCUBA galaxies and as a result, these far-infrared luminous galaxies appear to be a diverse population – some quasar like with broad lines and X-ray detections, some ERO like, some morphologically complex and some with unmistakeable signatures of obscured AGN and/or superwind activity. Furthermore, the intense bolometric luminosity displayed by these galaxies suggests large star-formation rates ($\gtrsim$1000M$_\odot$yr^{-1}) and these galaxies may therefore be responsible for much of the cosmic star-formation rate at z$\sim$2. As a result these galaxies have therefore been proposed to be the progenitors of the most luminous cluster ellipticals at the present day. However, little is understood about the intrinsic properties of SCUBA galaxies, such as masses, dust and AGN content and metallicities, all of which are important diagnostics for untangling the processes which drive the immense star formation activity in this diverse population. In this chapter we use near-infrared longslit spectroscopy and narrow-band imaging around redshifted Hα emission to probe the properties of a sample of SCUBA galaxies (Swinbank et al., 2004). These diagnostics can be used to compare this galaxy population with their proposed low redshift counterparts (massive, luminous ellipticals) in order to understand how local galaxies evolve from their high redshift progenitors.

Abstract

We present near-infrared spectroscopy and narrow-band imaging at the wavelength of redshifted Hα for a sample of 30 high-redshift, far-infrared luminous galaxies. This sample is selected from surveys in the sub-millimeter, millimeter and radio wavebands and has complete redshift coverage with a median redshift of $z \sim 2.4$. We use our data to measure the Hα properties of these systems and to gauge the prevalence of AGN in these galaxies through their [NII]/Hα ratios and Hα line widths. Removing obvious AGN, we

find that the Hα star formation rates in this diverse population are suppressed (by a factor of ~ 10) compared to those derived from their far-infrared luminosities. Using the AGN indicators provided by our near-infrared spectra we estimate that AGN are present in at least 40% of the galaxies in our sample. To further investigate this we construct a composite rest-frame spectrum for both the entire sample and for those galaxies which individually show no signs of nuclear activity. We find [NII]/Hα ratios for both composite spectra which suggest that the energy output of the galaxies is star-formation- rather than AGN-dominated. However, we also find that the Hα line in the composite non-AGN spectrum is best fit with an underlying broad line component with a narrow/broad flux ratio of 0.45 ± 0.20. The median Hα line width for our sample (removing obvious AGN) is $400 \pm 70\,\mathrm{km\,s^{-1}}$ (FWHM) and the typical spatial extent of the Hα emission in our narrow-band observations is $\lesssim$ 4–8 kpc which indicates a dynamical mass of $1\text{–}2\times10^{11}\,M_{\odot}$ with corresponding dynamical times of 10–20 Myrs. Using both high-resolution imaging and spectroscopically identified velocity offsets we find that seven of the far-infrared luminous galaxies have companions, suggesting that they are undergoing interactions/mergers and from their relative velocities we can determine a dynamical mass of $1.5 \pm 0.9 \times 10^{11}\,M_{\odot}$. These measurements are comparable to millimetre CO estimates for the dynamical masses of these systems on similar scales, and larger than recent estimates of the dynamical masses of UV-selected galaxies at similar redshifts derived in an identical manner. Using the [NII]/Hα index to predict abundances we investigate the Luminosity–Metallicity relation for these galaxies and find that many have metallicities consistent with UV selected high-redshift galaxies and slightly lower than local luminous infrared galaxies and ellipticals (although we caution that our metallicity estimates have possible systematic uncertainties). We also compared our Hα and far-infrared luminosities with deep *Chandra* observations of a subset of our survey fields and use these data to further assess their AGN content. We conclude that these high-redshift, far-infrared luminous galaxies represent a population of massive, metal-rich, merging systems with high instantaneous star formation rates, strong dust obscuration and actively-fuelled AGN which are likely to be the progenitors of massive local ellipticals.

5.1 Introduction

Recent surveys in the submillimeter (sub-mm), millimeter (mm) and radio wavebands suggest that the star formation density detectable by these dust-independent tracers has evolved strongly with redshift. Indeed, this evolution appears to out strip that found using tracers which are more sensitive to dust obscuration, suggesting that an increasing proportion of activity in more distant galaxies may be highly obscured (Blain et al., 1999). The populations resolved in these wavebands appear to be responsible for much of the energy density in the extragalactic far-infrared/sub-mm background (Smail et al., 2002; Cowie et al., 2002; Chapman et al., 2004a). However, the extreme faintness of optical counterparts to these obscured galaxies has made it very difficult to obtain accurate redshifts and measure intrinsic properties (e.g. Simpson et al., 2004).

The best-studied examples of the high-redshift, far-infrared luminous galaxy population are those identified in the sub-mm waveband using the SCUBA camera on the JCMT. The median redshift for this population is $< z > \sim 2.4$ (Chapman et al., 2003a, 2005) and their sub-mm fluxes suggest they have bolometric luminosities $> 10^{12} L_{\odot}$ – implying that they are Ultraluminous Infrared Galaxies (ULIRGs). The nature of this population and their relevance to models of galaxy formation models and evolution is particularly important (e.g. Genzel et al., 2003; Baugh et al., 2005). If they are powered purely by star-formation then these galaxies form about half of the stars seen locally (Lilly et al., 2003). However, both AGN activity and star-formation could contribute to their immense far-infrared luminosities, and without further information it is impossible to disentangle the precise energy source (Alexander et al., 2003a).

Rest-frame optical emission line properties provide a powerful tool to investigate star formation rates (SFR), power sources and metallicity of galaxies. In particular, the Hydrogen Balmer emission line series is one of the primary diagnostics of the SFR in nearby galaxies, with the strength of Hα and its relative insensitivity to extinction making it the line of choice. The nebular recombination lines are a direct probe of the young, massive stellar population, since only stars with masses $\gtrsim 10 M_{\odot}$ and lifetimes $\lesssim 20$ Myr contribute significantly to the integrated ionising flux. Hence the strength of these emission lines provide a nearly instantaneous measure of the SFR, independent of the previous star formation history. Moreover, by combining the SFR inferred from this diagnostic line with the far-infrared emission (which comes from reprocessed radiation which has been absorbed and re-emitted by dust in the far-infrared at wavelengths of 10–300μm) we can gauge the prevalence of dust obscuration. The width of the Hα line and its intensity relative to other rest-frame optical lines can also give important information about the presence and luminosity of an AGN within a galaxy (Veilleux and Osterbrock, 1987; Veilleux et al., 1995).

Hα is visible in the near-infrared waveband out to $z \sim 2.6$ and projects exploiting the Hα emission at these high redshifts have provide unique insights into the star formation properties of distant galaxies (e.g. Yan et al., 1999; Erb et al., 2003; Shapley et al., 2004; van Dokkum et al., 2004). With precise redshifts for the far-infrared luminous population from the work of Chapman et al. (2003a, 2005), we can efficiently target the Hα emission from the galaxies to understand the formation and evolution of this population, identify the power sources, star formation rates, metallicities (which are accessible through the [NII]/Hα (N2) index (Pettini and Pagel, 2004) and masses as well as more general issues such as their relation to other classes of high redshift sources such as Lyman Break Galaxies (LBGs Pettini et al., 2001; Erb et al., 2003; Shapley et al., 2003).

As well as measuring the star formation rate from Hα, it is also possible to measure dynamics of these systems from the same spectra. Far-infrared luminous galaxies at $z \sim 2$ appear morphologically complex (Chapman et al., 2003b; Smail et al., 2004). By mea-

suring the internal dynamics of the galaxies, or the velocity offsets between companions we can also place limits on their masses and so test if these galaxies are truly massive systems (Genzel et al., 2003).

In this paper we present the results from a near-infrared study of a sample of far-infrared detected galaxies at z=1.4–2.7. We use the Hα emission line to derive their star formation rates and dynamics. We investigate the metallicity of these galaxies through their [NII]/Hα emission, and dynamics as traced by velocity structures visible in Hα emission in a subset of galaxies. Using *Chandra* data we also compare our Hα and far-infrared luminosities with X-ray luminosities in several of our survey fields.

In §5.2 we present the data reduction and results from the spectroscopic survey and narrow-band imaging; in §5.3 we discuss the Hα properties of the far-infrared luminous galaxies and present a discussion of the star formation rates estimated from their Hα and far-infrared emission, and present a discussion of their dynamics, metallicities and X-ray counterparts. We present our conclusions in §5.4. We use a cosmology with $H_0 = 72\,\mathrm{km\,s^{-1}}$, $\Omega_0 = 0.3$ and $\Lambda_0 = 0.7$ in which $1''$ corresponds to 8.2 kpc at $z = 2.4$.

5.2 Observations and Analysis

Our target sample comes from two catalogues of far-infrared luminous galaxies by Chapman et al. (2003a, 2005). The majority of our sample comprises sub-mm detected, radio identified galaxies (SMGs). These galaxies have precise positions from the μJy radio emission and are confirmed to be far-infrared luminous from their detection in the sub-mm/mm wavebands with SCUBA or MAMBO. The radio-detected subset of the SMG population represent ~60–70% of all SMGs brighter than $\gtrsim 5\,\mathrm{mJy}$ (Ivison et al., 2002; Chapman et al., 2001; Wang et al., 2004). In addition we have also included a small number of optical and sub-mm faint radio galaxies (OFRGs) at similar redshifts which have been proposed to be similarly luminous far-infrared galaxies, but with somewhat hotter dust temperatures resulting in them having comparatively faint submm fluxes (Chapman et al., 2004a; Blain et al., 2004). The median redshift of the combined sample is $<z>= 2.4 \pm 0.2$. For the purposes of this study we chose targets whose redshifts place Hα in spectral regions which are relatively free from strong atmospheric absorption and emission.

We have explored two routes to investigate the Hα emission from SMG/OFRGs. Firstly, we used narrow-band imaging to assess the Hα fluxes of galaxies in our sample – from both a tunable filter (NSFCAM on IRTF) and more traditional narrow-band filters (with the UFTI near-infrared imager on UKIRT) for galaxies whose redshifts serendipitously place Hα into the filter bandwidth. These narrow-band observations provide the opportunity to determine the total Hα emission from the SMG/OFRGs, and search for any extended emission or spatial companions.

Secondly we used classical long-slit near-infrared spectroscopy with the NIRSPEC spectrograph on Keck and the ISAAC spectrograph on the VLT. These observations allow us to measure precise systemic redshifts for these SMG/OFRGs, with much higher reliability than that available from their rest-frame UV emission – which frequently show velocity shifts of 100's of $\mathrm{km\,s^{-1}}$. These precise redshifts are necessary for interferometric CO follow-up of these galaxies (Neri et al., 2003; Greve et al., 2004). The longslit spectroscopic observations also allow us to measure the Hα luminosities and SFR(Hα), as well as allowing us to gauge the prevalence of AGN in these galaxies – through the detection of broad lines and extreme [NII]/Hα flux ratios.

These two approaches therefore provide complementary information on the Hα emission properties of the SMG/OFRG population.

TABLE 1: SUMMARY OF NARROW BAND IMAGING

Object	λ_{cen} (μm)	t_{exp} (ks) K	Hα
IRTF Tunable Filter			
SMM J105230.73+572209.5	2.3692	2.5	12.6
SMM J123635.59+621424.1	1.9721	1.4	9.0
SMM J131215.27+423900.9	2.3396	1.4	7.2
SMM J140104.96+025223.5	2.3396	0.7	9.0
SMM J163631.47+405556.9	2.1544	4.5	14.4
UKIRT Narrow-band			
SMM J105226.61+572113.0	2.248	5.6	22.7
SMM J131232.31+423949.5	2.166	4.0	15.0

Table 5.1: Notes: λ_{cen} denotes the central position of the narrow-band filter for the observations.

5.2.1 Narrow-band Imaging

IRTF

Narrow-band imaging of five targets was carried out using the NASA Infra-Red Telescope Facility[1](IRTF) 3-m Telescope between 2003 April 28 and May 02. The observations were made in generally photometric conditions and $\sim 1''$ seeing. We used the NSFCAM camera (Shure et al., 1993) which employs a 256×256 InSb detector at $0.15''$ pixel^{-1} to give a $38''$ field of view (which probes roughly 300 kpc at $z \sim 2.4$). The continuously variable tunable narrow-band filter (CVF) in NSFCAM provides an $R = 90$ passband which was tuned to the galaxy redshifts measured from the UV spectra from (Chapman et al., 2003a, 2005). Shorter, matched broad-band imaging were interspersed between the narrow-band exposures to provide continuum subtraction.

The observations were taken in a standard 9-point dither pattern and reduced using a running flat field of the six nearest temporally adjacent frames, masking bright objects before creating the flat-field frame. The final image was made by averaging the flat-fielded frames with a 3σ clip to reject cosmic rays. To calibrate our data, we observed UKIRT faint photometric standards (Hawarden et al., 2001). These standards were observed at similar air masses and using the same instrumental configuration as the target galaxies. As well as providing good flux calibrations, these observations also allow us to calculate the relative throughput of the narrow-band and broad-band filters. This allows precise subtraction of the continuum contribution from the Hα emission in the narrow-band filter. The NSFCAM CVF filter is wide enough that it contains both the Hα and [NII] emission lines (with the [NII] emission line included at 95% of peak transmission assuming Hα falls at the peak of the filter trace). The median [NII]/Hα ratio in our spectroscopic sample is 0.25, and we therefore apply a 24% correction to the narrow-band flux to account for the [NII] emission line. Exposure times, central wavelengths and measured Hα fluxes from these observations are given in Tables 5.2.1 & 5.2.3. We illustrate the Hα morphology for one of the more unusual galaxies in our sample in Fig. 5.5 and discuss this in more detail in §5.3.1.

[1]The Infrared Telescope Facility is operated by the University of Hawaii under Cooperative Agreement no. NCC 5-538 with the National Aeronautics and Space Administration, Office of Space Science, Planetary Astronomy Program.

UFTI

We obtained classical narrow-band imaging of two SMGs, SMM J105226.61 and SMM J131232.31, whose redshifts should place Hα emission in the Brγ and H_2 S1 filters respectively. These data were taken with the UFTI near-infrared camera (Roche et al., 2003) on UKIRT[2]on 2003 February 25–27 in $\lesssim 0.7''$ seeing and photometric conditions. The UFTI camera has a 1024 x 1024 HgCdTe array and a plate scale of 0.091 arcsecond per pixel, giving a field of view of $92''\times92''$ (which probes roughly 0.75Mpc in our adopted cosmology). To provide continuum subtraction we interspersed the narrow-band observations with K-band imaging. The data was reduced using the ORAC-DR pipeline. The relative throughputs of the broad and narrow band filters and flux calibration was determined using 2MASS K-band photometry on bright ($K \sim 12$) stars within the $92''$ field of view.

All of our narrow-band observations were taken based on the rest-frame UV redshifts and assuming that the rest-frame optical redshifts were in agreement. However a velocity offset of $\sim 500\,\mathrm{km\,s^{-1}}$ between the rest-frame UV and optical emission lines can redshift the Hα out of the narrow-band filter. Shifts of this amplitude are relatively rare and so we assume that our observations have sampled the bulk of the Hα emission in these galaxies.

5.2.2 Keck Spectroscopy

We obtained near-infrared spectra of 24 SMG/OFRGs using NIRSPEC (McLean et al., 1998) on the 10-m Keck telescope[3]. These observations were obtained on the nights of 2003 August 3, in non-photometric conditions; in somewhat better conditions on 2004 February 1 and in $0.5''$ seeing and in photometric condition between 2004 April 6–9 and 2004 July 31. In all four instances, observations were made using the low-resolution, longslit mode with a 4-pixel wide ($0.76''$) slit. Spectra were obtained in the K-band using the N7 or K' filters. In this configuration the resolution is $R \sim 1500$. To subtract sky emission the observations were made in a standard ABBA sequence, where the object is nodded along the slit by $10–20''$. The total integration times are listed in Table 5.2.3 (the integration times of individual exposures were typically $\sim$ 600s). One goal of these observations was to provide precise systemic redshifts of the SMG/OFRGs to compare to those measured in the UV and also to provide a precise redshift for our on-going CO mapping programme on the Plateau de Bure interferometer (Neri et al., 2003; Greve et al., 2004). To maximise the sample size, the exposure times were therefore kept short and so the Hα lines are rarely detected with sufficient signal-to-noise to measure more than their most basic characteristics. We note that the success rate for detecting Hα emission in the SMG/OFRGs in the near-infrared is $\sim$ 70%. This estimate is based on the results from the third observing run which was largely photometric since the first two observing runs were plagued by cloud. In cases where there was no detection of either continuum or Hα emission, we have assumed that the target was not on the slit (either due to an offset error, or loss of guiding during the offset from a nearby bright star). In two cases we detected continuum from the target but could not detect any emission lines. In these cases we have quoted upper limits for the Hα luminosity and SFR.

The spectroscopic observations were reduced using the WMKONSPEC package in IRAF. We remap the 2-D spectra using linear interpolation to rectify the spatial and spectral dimensions. After subtracting pairs of nod-positions, residual sky features were removed

[2]The United Kingdom Infrared Telescope is operated by the Joint Astronomy Centre on behalf of the U.K. Particle Physics and Astronomy Research Council.

[3]Obtained at the W.M. Keck Observatory, which is operated as a scientific partnership among the California Institute of Technology, the University of California and the National Aeronautics and Space Administration. The Observatory was made possible by the generous financial support of the W.M. Keck Foundation.

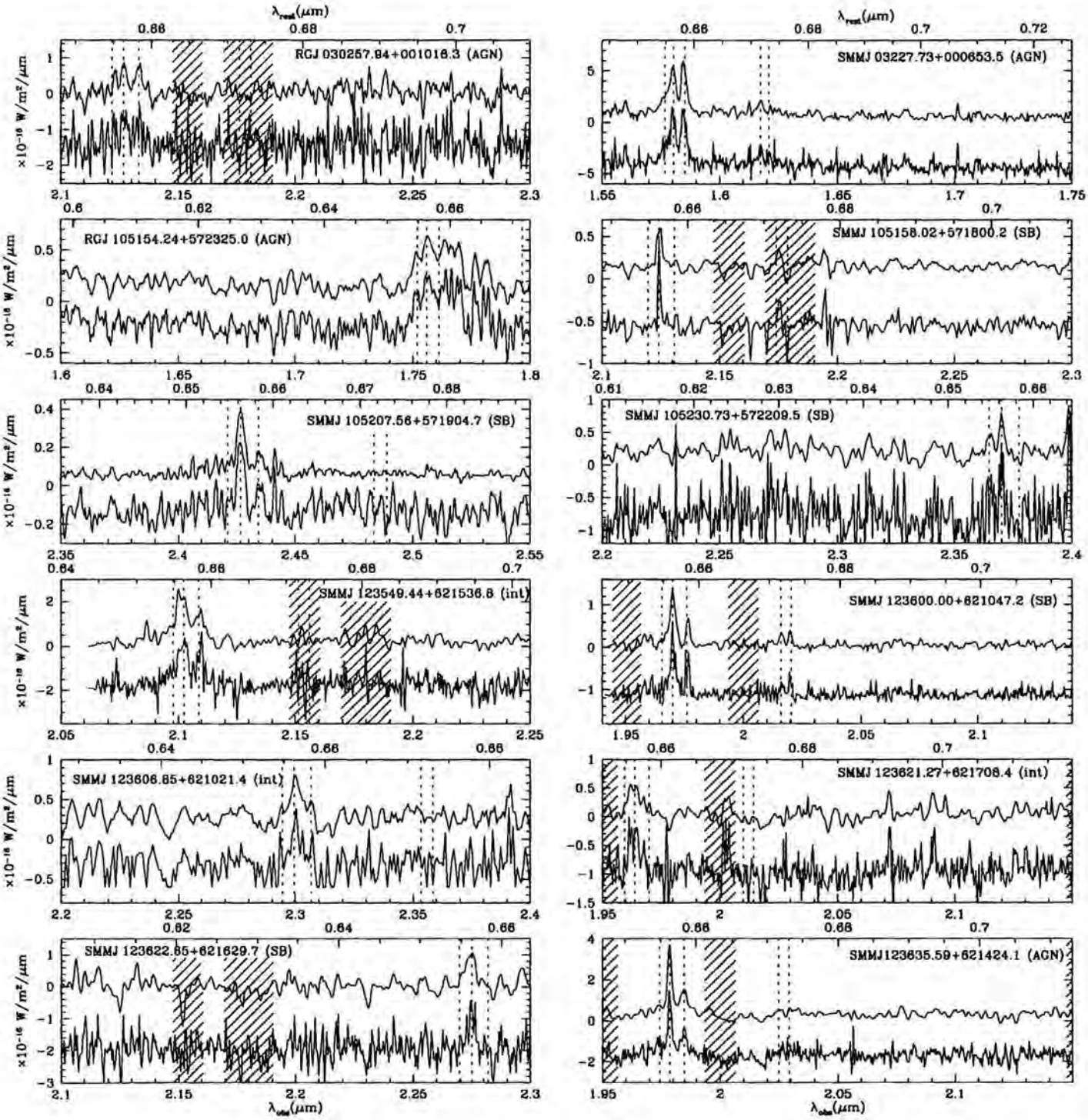

Figure 5.1: Hα spectra for the SMG/OFRGs in our sample. The bottom spectra in each panel is the raw spectrum (offset in flux scale for clarity). The upper spectra is smoothed to the instrumental resolution. The dashed vertical lines show the positions of the Hαλ6562.8Å, [NII]λλ6548.1,6583.0Å, and [SII]λλ6717,6731Å emission lines. The lower axis scale shows the observed wavelength, whilst the upper scale displays the rest-frame wavelength. The shaded areas are regions of strong sky emission. The spectra are ordered in RA range as in Table 2 and we label each galaxy with its spectral classification from §5.2.4. Note that we identify two Hα emission lines from SMMJ123707.21 rather than Hα + [NII] (see §5.3.1). The final spectra are higher resolution ISAAC/VLT spectra (Table 2).

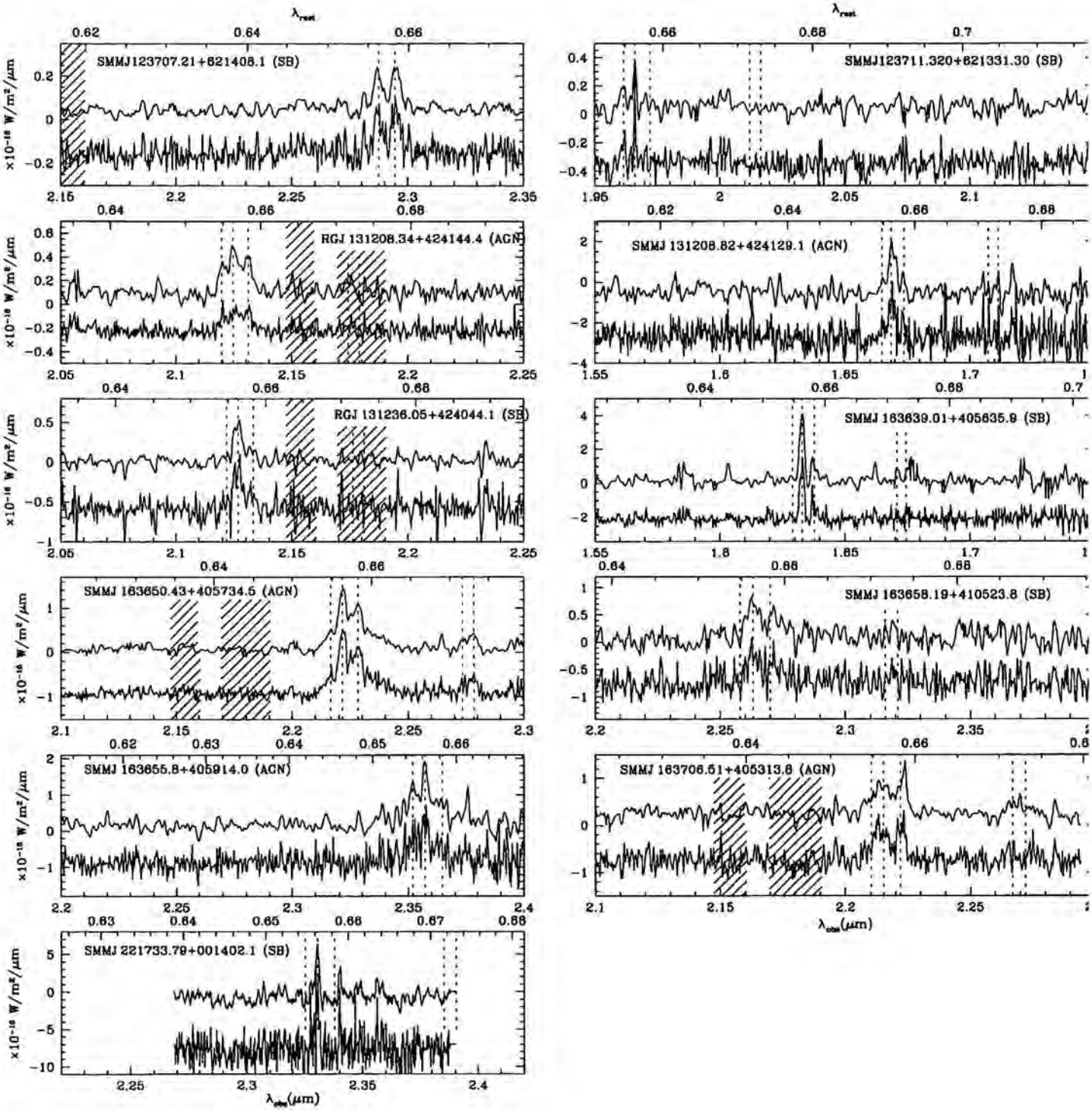
SMMJ123707.21+621408.1 (SB)
SMMJ123711.320+621331.30 (SB)
RGJ 131208.34+424144.4 (AGN)
SMMJ 131208.82+424129.1 (AGN)
RGJ 131236.05+424044.1 (SB)
SMMJ 163639.01+405635.9 (SB)
SMMJ 163650.43+405734.5 (AGN)
SMMJ 163658.19+410523.8 (SB)
SMMJ 163655.8+405914.0 (AGN)
SMMJ 163706.51+405313.6 (AGN)
SMMJ 221733.79+001402.1 (SB)
λrest
λobs(μm)
×10⁻¹⁸ W/m²/μm

in IDL using sky regions on either side of the object spectrum. The wavelength calibration from the 2003 run used the night sky lines, whilst for the 2004 observing runs we used an argon arc lamp. The output pixel scale is 4.3 Å pixel^{-1} and the instrumental profile has a FWHM of 15Å (measured from the widths of the sky-lines). In all line widths quoted in the following sections we have deconvolved the instrumental profile from the FWHM of the galaxies.

The redshifts of our targets have been relatively well constrained from rest-frame UV spectroscopy carried out with LRIS on the Keck telescope. Although, again we stress that the rest-frame UV and optical emission lines can show velocity offsets of a few 100's km s^{-1} (which are largely attributed to galactic winds) (Pettini et al., 2001; Erb et al., 2003; Shapley et al., 2003). With knowledge of the UV redshift we were able to identify the Hα and [NII] emission in each spectrum and ensure the correct line identification.

As the first two and final observing runs were non-photometric we calibrate the integrated Hα fluxes onto an absolute flux scale by careful comparison of the spectra with the K-band photometry of the galaxies (Smail et al., 2004). We convolve the galaxy spectra with the normalised K-band filter response curve to obtain the mean flux conversion factor for each galaxy spectrum. We also note that the atmospheric transmission at the wavelength of redshifted Hα is $\sim$ 1 for all targets except SMM J123621.27, where the transmission is 0.75 ± 0.02. For the third observing run we used a standard star (FS27) to flux calibrate the data. We also use the broadband photometry to flux calibrate these data in order to verify that the process applied to calibrate the previous observations is reliable and obtain a mean ratio of calibration factors of 1.05 ± 0.10. This gives us confidence that using the photometry to flux calibrate gives consistent results. All of the objects included here have detectable continuum emission. Where the continuum or emission lines are faint, we binned the reduced 2-D frames by a factor of two in both the spatial and spectral dimension to improve the contrast prior to extraction. We show the extracted spectra for the whole sample in Fig. 5.1.

5.2.3 ISAAC VLT Spectroscopy

During the night of 2003 October 21 observations of SMM J221733.79 were obtained in queue mode with the ISAAC spectrograph on the VLT[4](Moorwood, 1997). The data were taken using the medium resolution ($R = 3000$) grating and a 1″ slit (with an instrumental FWHM of ~6.7Å) and in 0.8″ seeing. In this configuration the output pixel scale is 1.2Å/pixel. The total integration time was 3.0 ks with the data taken in 4×750s exposures in the standard ABBA sequence where the object is nodded along the slit by 10–20″ to achieve sky subtraction. We reduced the data using the ISAAC data-reduction pipeline which rectifies, flat-fields and wavelength calibrates the 2D-frames. Prior to extraction the data was binned by a factor of two in the spectral direction to boost the contrast of the object. We observed the standard star HIP032007 for flux calibration. The derived Hα fluxes and redshifts are listed in Table 5.2.3 and the spectra are shown in Fig. 5.1.

5.2.4 Spectral Analysis

To accurately determine the redshift for each galaxy, we fit both the continuum level and emission lines: H$\alpha\lambda$6562.8Å and [NII]$\lambda\lambda$6548.1,6583.0Å simultaneously with a flat continuum plus Gaussian profiles using a χ^2 fit and taking into account the greater noise in regions of strong sky emission. As well as fitting the narrow line Hα and [NII] emission, we also attempt to identify any underlying broad line Hα (AGN) component by fitting a broad Gaussian profile at the same redshift as the narrow-line Hα emission but only

[4]Based on observations collected with the ESO VLT-UT1 Antu Telescope (072.A-0156)

TABLE 2: SUMMARY OF RESULTS

Object	t_{exp} (ks)	z	Hα Flux (10^{-19} W m^{-2})	FWHM$_{rest}$ (km s^{-1})	EW$_{rest}$ (Å)	SFR(Hα) ($M_\odot$ yr^{-1})	[NII]/Hα	L_{FIR} ($10^{12} L/L_\odot$)	Class (UV / Hα)
Spectroscopy									
NIRSPEC Keck									
SMM J030227.73+000653.5	3.0	1.4076[2]	15.2 ± 2.0	420 ± 15	85 ± 10	140 ± 18	1.38 ± 0.07	$5.78^{+2.44}_{-0.82}$	SB / AGN
RGJ 030258.94+001016.3	2.0	2.2404[8]	1.8 ± 0.5	327 ± 22	360 ± 110	51 ± 15	1.13 ± 0.40	$7.74^{+1.41}_{-1.41}$	int / AGN
RGJ 105154.24+572325.0	4.8	1.681[8]	2.7 ± 1.9	1565 ± 250	91 ± 6	61 ± 40	< 0.2	$2.80^{+0.35}_{-0.35}$	SB / AGN
SMM J105158.02+571800.3	2.4	2.2390[4]	2.4 ± 1.2	257 ± 44	21 ± 5	57 ± 15	< 0.1	$10.40^{+1.90}_{-1.90}$	SB / SB
SMM J105207.56+571904.7	4.8	2.692[2]	1.3 ± 0.4	285 ± 20	21 ± 4	217 ± 64	0.18 ± 0.10	$9.46^{+2.70}_{-2.70}$	SB / SB
SMM J105230.73+572209.5	2.4	2.6100[3]	1.2 ± 0.3	171 ± 40	10 ± 3	42 ± 15	< 0.05	$10.29^{+0.75}_{-1.12}$	SB / SB
SMM J123549.44+621536.8	2.4	2.2032[3]	15 ± 1	536 ± 33	184 ± 9	239 ± 18	0.50 ± 0.10	$6.76^{+1.50}_{-1.12}$	SB / int
SMM J123600.15+621047.2	1.2	2.0017[2]	3.7 ± 0.3	305 ± 12	91 ± 8	126 ± 8	0.20 ± 0.10	$10.50^{+1.50}_{-1.50}$	SB / SB
SMM J123606.85+621021.4	2.4	2.5054[8]	2.0 ± 0.3	612 ± 35	28 ± 5	78 ± 12	< 0.2	$8.70^{+1.80}_{-1.20}$	SB / int
SMM J123621.27+621708.4	2.4	1.9924[7]	2.0 ± 0.6	586 ± 92	212 ± 25	56 ± 16	0.20 ± 0.15	$12.76^{+1.50}_{-2.25}$	SB / int
SMM J123622.65+621629.7	2.4	2.4662[5]	3.4 ± 0.6	434 ± 25	137 ± 40	125 ± 20	< 0.05	$9.01^{+1.88}_{-2.03}$	SB / SB
SMM J123635.59+621424.1	1.8	2.0150[2]	4.2 ± 0.3	240 ± 33	45 ± 10	130 ± 30	0.67 ± 0.27	$7.47^{+1.50}_{-1.50}$	AGN / AGN
			6.9 ± 0.9	1623 ± 213	73 ± 10				Broad line cmpt
SMM J123707.21+621408.1	3.6	2.490[5]	1.6 ± 0.5	348 ± 40	35 ± 8	88 ± 24	...	$5.48^{+2.03}_{-1.58}$	SB /SB
SMM J123711.32+621331.3	2.4	1.9958[4]	0.4 ± 0.3	112 ± 18	10 ± 5	16 ± 9	< 0.05	$5.48^{+2.03}_{-1.58}$	int / SB
SMM J123711.98+621325.7	2.4	...	< 0.25	...	< 5	< 6	...	$3.88^{+1.05}_{-0.82}$	SB / ...
SMM J131205.60+423946.0	2.4	...	< 0.3	...	< 6	< 8	...	$5.50^{+2.00}_{-2.00}$	SB / ...
RGJ 131208.34+424144.4	2.4	2.2372[18]	0.9 ± 0.2	448 ± 60	24 ± 5	32 ± 18	1.20 ± 0.60	$5.13^{+1.05}_{-1.05}$	SB / AGN
			0.9 ± 0.8	959 ± 100	26 ± 5				Broad line cmpt
SMM J131208.82+424129.1	2.4	1.5439[6]	6.1 ± 2.3	387 ± 60	103 ± 15	111 ± 32	0.20 ± 0.15	$3.23^{+0.15}_{-0.19}$	SB / AGN
			2.1 ± 1.0	450 ± 80	120 ± 20				Broad line cmpt
RGJ 131236.05+424044.1	2.4	2.2402[8]	2.3 ± 1.2	447 ± 75	20 ± 6	106 ± 40	0.22 ± 0.08	$6.69^{+0.59}_{-0.59}$	SB / SB
SMM J163639.01+405635.9	2.4	1.4880[6]	8.9 ± 3.0	248 ± 25	188 ± 35	147 ± 48	0.30 ± 0.20	$5.47^{+1.88}_{-1.50}$	SB / SB
SMM J163650.43+405734.5	4.8	2.3850[5]	2.2 ± 0.5	306 ± 47	105 ± 20	58 ± 19	0.41 ± 0.10	$50.5^{+15.0}_{-15.8}$	int / AGN
			12.0 ± 1.0	1753 ± 238	1236 ± 200				Broad line cmpt
SMM J163655.80+405914.0	2.4	2.5918[6]	2.4 ± 0.4	225 ± 29	336 ± 60	102 ± 15	0.45 ± 0.10	$10.9^{+2.25}_{-3.76}$	AGN / AGN
			16 ± 2	2962 ± 402	254 ± 40				Broad line cmpt
SMM J163658.19+410523.8	2.4	2.4482[6]	1.9 ± 0.4	364 ± 77	76 ± 15	71 ± 35	0.65 ± 0.3	$10.90^{+2.25}_{-3.76}$	SB / SB
SMM J163706.51+405313.8	2.4	2.3745[9]	4.7 ± 0.6	225 ± 29	96 ± 15	160 ± 20	0.27 ± 0.04	$7.17^{+4.21}_{-3.00}$	AGN / AGN
			2.7 ± 0.8	3317 ± 987	125 ± 15				Broad line cmpt
SAAC VLT									
SMM J221733.79+001402.1	3.0	2.5510[7]	8.5 ± 3.5	198 ± 98	30 ± 10	254 ± 128	...	$4.94^{+1.88}_{-2.63}$	SB / SB
Narrow-band imaging									
UFSFCAM IRTF									
SMM J105230.73+572209.5	12.6	2.610[5]	1.2 ± 0.5	...	...	21 ± 8	...	$10.3^{+0.75}_{-1.13}$	SB / ...
SMM J123635.59+621424.1	9.0	2.005[5]	8.1 ± 1.0	...	...	181 ± 20	...	$7.47^{+1.50}_{-1.50}$	AGN / ...
SMM J131215.27+423900.9	7.2	2.565[5]	11.8 ± 1.0	...	...	493 ± 41	...	$13.90^{+0.53}_{-2.48}$	AGN / ...
SMM J140104.96+025223.5	9.0	2.565[5]	1.2 ± 0.2	...	...	47 ± 10	...	$6.76^{+2.50}_{-2.50}$	AGN / ...
SMM J163631.47+405546.9	14.4	2.283[5]	0.30 ± 0.19	...	...	10 ± 6	...	$10.97^{+6.79}_{-4.73}$	AGN / ...
UFTI UKIRT									
SMM J105226.61+572113.0	22.7	2.425[5]	0.78 ± 0.1	...	...	27 ± 4	...	$2.40^{+1.40}_{-1.40}$	SB / ...
SMM J131232.31+423949.5	15.0	2.300[5]	1.9 ± 0.1	...	...	58 ± 5	...	$14.80^{+0.98}_{-2.93}$	SB / ...

Table 5.2: Note the value given in the [] z column is the error in the last decimal place. The Hα flux given in column 4 is the narrow line Hα flux unless otherwise stated. The Hα fluxes are the observed flux (not corrected for slit flux losses or atmospheric transmission), but the SFR's have had both corrections applied (where applicable). The Hα star-formation rates are uncorrected for extinction. Hα classifications are described in §5.2.4 (SB=star burst; int=intermediate, AGN=AGN).

accepting the result if the χ^2 fit is significantly better (with >90% confidence limit) than with no broad line component. This allows us to deconvolve the narrow-line Hα flux, which may arise from star-formation, from the broad-line Hα flux from an AGN. For the observations which were flux calibrated using the K-band photometry we estimate the errors in the Hα flux and continuum levels using both the uncertainty in the K-band magnitude and the errors on the best fit to the emission line, evaluated by varying the fit by $\Delta\chi^2 = 1$. The error bars on the emission line fluxes and equivalent widths are therefore conservative errors which take into account the error in using the K-band photometry and the uncertainty which arises from the signal-to-noise in the data. This flux error is propagated through to the star formation rate. We list the parameters for the fits for narrow (and where relevant broad) components in Table 5.2.3, along with their uncertainties. We note that the [SII]$\lambda\lambda$6716,6731Å doublet are detected in at least three individual spectra: SMM J123600.00, SMM J163650.43 and SMM J163639.01.

The ratio of [NII] to Hα line fluxes from our spectra, as well as the presence of a broad component can all be used to identify luminous AGN in these galaxies Veilleux and Osterbrock (e.g. 1987); Armus et al. (e.g. 1989).

Spectral Classification of Narrow-Emission-Line Galaxies

Before we classify the galaxies from our observations, we briefly review the physical distinction and diagnostics used to differentiate between HII regions, AGN and LINER galaxies.

An important fraction of galaxies have emission lines in their spectra. The physical difference that distinguishes a narrow-line AGN from an HII region is the photo-ionising continuum. In narrow-line AGNs the ionising radiation is well approximated by a (non-thermal) power-law continuum, $\nu^{-\alpha}$ (with spectroscopic index $\alpha \sim 1.0 - 1.5$; Ferland and Osterbrock (1986)). In HII regions the ionisation is due to UV photons emitted by hot OB stars. Therefore, in contrast with HII region-like objects, narrow-line AGNs have a significant fraction of their energy in the X-ray regime and have more photons capable of ionising heavy ions such as O^+. These X-ray photons penetrate deeply into neutral regions, producing a large, partly ionised hydrogen region ($H^+/H \sim 0.2$-0.4; e.g. Osterbrock 1984)

The hot free electrons produced in the region by X-ray photo-ionisation can have a positive effect on the collisional excitation of [OI]λ6300, [OIII]λ5007, [SII]$\lambda\lambda$6716,6731, [NI]λ5199 and [NII]λ6583. In contrast, the intensities of these emission lines are weaker in HII regions with respect to Hα than in narrow-line AGNs because collisional excitation of these lines is more important in regions with a mix of Hydrogen and ionised Hydrogen. In Fig. 5.2 we show the [OIII]λ5007/Hβ vs. [NII]λ6583/Hα emission line intensities for a sample of 265 objects: 105 HII regions in external galaxies, 37 HII region-like galaxies, 41 Seyfert 2 galaxies and 30 LINERS from Veilleux and Osterbrock (1987). The dashed line is the proposed dividing line used to classify galaxies from Baldwin et al. (1981).

On the basis of the boundries between HII regions and AGN we can attempt to classify the galaxies in our sample. However, in trying to decide whether an object is an HII region galaxy or a narrow-line AGN, ideally the spectral lines of [OIII], Hβ, Hα and [NII] are required. Unfortunately, our spectra do not cover the wavelength range around [OIII] and Hβ and therefore we choose a canonical value of [NII]/Hα with which we can approximately separate HII regions from AGN. We note that without the [OIII] and Hβ emission line, it is possible to mis-classify HII region-like galaxies as AGN and therefore we look forward to future studies which include these emission lines (Takata et al. 2005 in prep.).

We measure all of these observables from our spectra and use them to flag galaxies

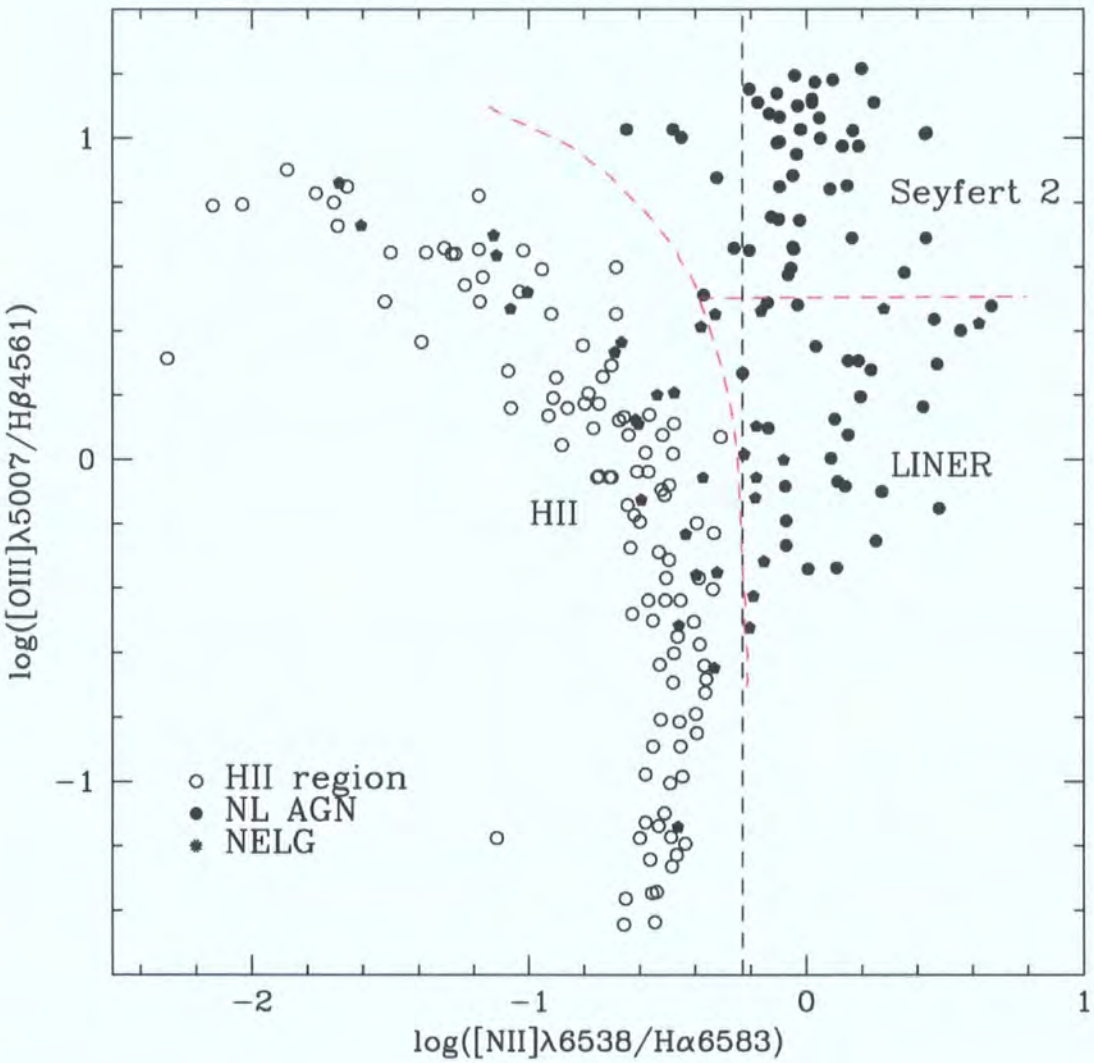

Figure 5.2: [OIII]/Hβ vs. [NII]/Hα emission line intensity ratios for a sample of HII regions and AGN from Veilleux et al. (1987). The red dashed line divides the AGN from the HII region-like objects from the models of Baldwin et al. (1981). Since our spectroscopy of SMGs/OFRGs only cover [NII] and Hα we choose a canonical value of [NII]/Hα>0.7 as the dividing line between AGN and HII regions and mark this on the plot (vertical dashed line).

whose Hα and far-infrared luminosities could be affected by emission from an AGN, rather than being star-formation dominated (Table 5.2.3). Using the [NII]/Hα emission line ratio and Hα line width as diagnostics we separate our sample into three classes: AGN dominated, intermediate, and systems whose properties are consistent with star-formation (but may still contain some AGN). In a later section we test the reliability of these classes through the use of deep X-ray observations. We classify galaxies whose near-infrared spectra show [NII]/Hα<0.7 (below the dashed line on Fig 5.2) and FWHM$_{\rm rest}$<500km s^{-1} as star-bursts (SB). Galaxies with FWHM$_{\rm rest}$ between 500 and 1000km s^{-1} are classified as intermediate, whilst galaxies with [NII]/Hα>0.7 (above the dashed line on fig 5.2) and/or FWHM$_{\rm rest}$>1000km s^{-1} are classified as AGN. Using this classification, ~40% (9/24) of our detected spectroscopic sample have some indication of an AGN (most classifications are based on Hα line widths, with only one AGN changing classification if we remove the limits on [NII]/Hα). This is similar to the rate estimated from UV spectroscopy and high-resolution radio imaging (Chapman et al., 2003a, 2004b, 2005). By comparing the rest-frame UV and optical spectral classifications (Table 5.2.3) we find that the fifteen galaxies identified as SB in the rest-frame UV are classified as SB[9], AGN[3] and intermediate[3] from their rest-frame optical spectra. Likewise, the three AGN identified in the rest-frame UV are all classified as AGN from their rest-frame optical spectra. We conclude that these classifications are in reasonable agreement. However, we note that their AGN could be easily hidden from view in both wavebands (e.g., see §5.3.7). Looking at the far-infrared luminosities of the three spectral classes we find median values of $5.2 \pm 3.0 \times 10^{12}$ L$_\odot$ for the SMG/OFRGs classed as AGN, $6.6 \pm 0.7 \times 10^{12}$ L$_\odot$ and $5.4 \pm 1.4 \times 10^{12}$ L$_\odot$ for the star-bursts and intermediate respectively. We thus find no strong evidence for a strong luminosity dependence of the different spectral classes.

To determine total Hα fluxes we have also corrected for slit losses based on the average K-band light distribution of the galaxies. As we know the position, width and orientation of the spectroscopic aperture for each galaxy, we use the K-band images to calculate the fraction of the total K-band light that enters the spectroscopic aperture. The galaxies are frequently extended and disturbed (e.g. Smail et al., 2004), and while this correction is uncertain, we view it as more reliable to apply this factor before comparing Hα to far-infrared star formation rates, rather than to ignore it. However, we note that using a single factor for correcting slit losses may contribute some scatter when comparing the Hα and far-infrared star formation rates. By careful comparison of a simulated slit for each galaxy in our sample the K-band imaging, we estimate that the fraction of the flux entering the slit compared to the total K-band flux of the galaxy, f, and obtain a mean value of $f = 0.62 \pm 0.06$. We assume that the equivalent width of the Hα emission line is constant across the galaxy and so only those galaxies with spectra taken in photometric conditions, whose flux calibration was carried out using the standard star observations, require this correction to their Hα flux.

Finally, we note that there are two repeated observations of targets between the spectroscopic and narrow-band imaging samples: SMM J105230.60 and SMM J123635.59 — as well as narrow-band imaging of SMM J140104.96 for which an Hα spectrum exists in the literature ($0.56 \pm 0.08 \times 10^{-18}$ W m^{-2}, Ivison et al. (2000)). The agreement between the Hα fluxes from the two techniques is very good (Table 5.2.3), with a median ratio of spectroscopic to imaging fluxes of 0.96 ± 0.04. On the basis of this good agreement we feel confident in combining the spectroscopic and narrow-band imaging data to discuss the Hα luminosities of SMG/OFRGs in the following sections.

5.2.5 Star Formation Rates

For solar abundances and adopting a Salpeter IMF, the conversion between Hα flux and SFR is SFR($M_\odot yr^{-1}$) = 7.9×10^{-35}L(Hα) W (Kennicutt, 1998). This calibration assumes that all of the ionising photons are reprocessed into nebular lines (i.e. they are neither absorbed by dust before they can ionise the gas, nor do they escape the galaxy).

We also have a second SFR indicator for our sample of SMG/OFRGs – their far-infrared (FIR) luminosities. A significant fraction of the bolometric luminosity of the most active dusty galaxies is absorbed by interstellar dust and re-emitted in the thermal IR, at wavelengths 10–300μm. If young stars dominate the radiation output in the UV-visible waveband and the dust opacity is high everywhere, then the far-infrared luminosity measures the bolometric luminosity of the star-burst and this in turn provides an excellent tracer of the SFR of the galaxy. Adopting the models of Leitherer and Heckman (1995) for continuous bursts of age 10–100 Myr and using the same IMF as in the Hα calculation, yields: SFR($M_\odot$ yr^{-1}) = 4.5×10^{-37}L(FIR) W (Kennicutt, 1998). We stress that this relation only holds if the age of the star-burst is less than 100 Myr.

We list the SFR and Hα fluxes measurements from our sample in Table 5.2.3. We also give the far-infrared luminosities of these galaxies from Chapman et al. (2003a, 2005a). These values are derived from fitting model spectral energy distributions to the observed 850 μm and 1.4-GHz fluxes of the galaxies at their known redshifts, assuming the local far-infrared–radio correlation holds (Condon et al., 1991; Garrett, 2002).

5.3 Results and Discussion

5.3.1 Notes on Individual Galaxies

Observations of six of the galaxies in our sample are particularly noteworthy and so we discuss these in more detail here:

SMM J123635.59+621424.1:

Dawson et al. (2003) identified this object as a z=2.015 spiral galaxy, but their near-infrared spectroscopy around the Hα emission line shows a 2500±250 km s^{-1} broad line Hα component and [NII]/Hα emission line flux ratio 0.45±0.1. The presence of the broad line component and detection of hard (Γ = 0.3) X-ray emission from *Chandra* imaging indicate an obscured type II AGN (Dawson et al., 2003). Our spectroscopic and narrow-band observations of this galaxy produce comparable Hα fluxes, which along with the compact morphology of the galaxy in the IRTF narrow-band image, suggests that the spectroscopic slit is sampling the bulk of the emission from this system (the slightly lower flux in the narrow-band observation arises because the narrow-filter only samples the narrow line Hα, $\sim$ 20% of the broad line flux is missed). Our spectroscopic observations of this target shows clear velocity structure in the Hα and [NII] emission lines (Fig. 5.3). We aligned the slit with the center of the galaxy and the bright knot (labelled A2 in Fig. 5.3), and our resulting Keck spectroscopic observations indicate either a velocity shear or rotation in the Hα emission line with an amplitude of $\sim$ 100 km s^{-1} within $\sim$ 2″ (17 kpc in projection) along the slit (Fig. 5.3). By collapsing down the Hα and [NII] emission lines in the spectral direction, we find an offset of 0.3″ (3 kpc) along the slit between the maximum intensities of these two lines – and an associated variation in the [NII]/Hα ratio from $\sim 0.2 \pm 0.1$ up to $\sim 0.60 \pm 0.15$ (which is consistent with the results of Dawson et al. (2003)). We also find a similar broad line component to the Hα emission, confirming the presence of an AGN. The high resolution *Hubble Space Telescope*[5] (*HST*) ACS image of this galaxy (Fig. 5.3), from the GOODS imaging of this region, (Giavalisco et al., 2004; Dawson et al., 2003; Smail et al., 2004) shows an apparently face-on spiral

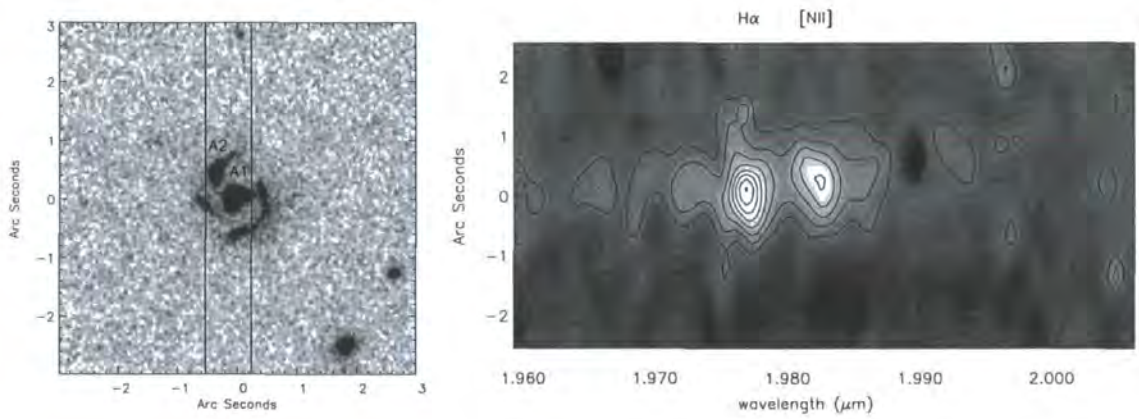

Figure 5.3: On the left we show the combined B, V and I-band *HST* ACS observations of SMM J123635.59+621424.1 with the slit position overlaid. On the right we give the position-velocity diagram around the Hα line from the NIRSPEC near-infrared spectrum of the galaxy. This shows an apparent $\sim$100 km s^{-1} velocity gradient in the Hα emission line and a somewhat larger velocity gradient, $\sim$150 km s^{-1}, in [NII]. The central component of the galaxy (labelled A1) has an [NII]/Hα ratio of 0.60 ± 0.15 and hosts a bright, unresolved radio source (Chapman et al. 2004a): both features suggest it contains an AGN. A1 is offset from A2 by $\sim$150 km s^{-1} in velocity and around 3 kpc in projection on the sky. A2 has an [NII]/Hα ratio of 0.2 ± 0.1, suggesting that this is a star forming knot or close companion. 1″ corresponds to 8.4 kpc at the redshift of this galaxy and the image has been rotated to match the PA of the spectrum.

galaxy with a bright nucleus (A1) and a prominent companion or knot in one of the spiral arms (A2), the optical extent of the galaxy is 13 kpc (1.5″). The separation between the nucleus (A1) and knot (A2) in the image is $\sim$ 0.5″ (5 kpc) – comparable to the apparent offset in the emission line peaks. The high-resolution 1.4-GHz MERLIN map of this galaxy in (Chapman et al., 2004b) shows an unresolved radio source coincident with the nuclear component, which is also where the [NII]/Hα is the strongest ($\sim$ 0.6), providing further support for the classification of this component as an AGN. The face-on aspect of this system, combined with the modest velocity difference between A1 and A2 suggests to us that the latter may be a dynamically-distinct component (rather than a star-forming knot inside a spiral arm), an interaction which has prompted the activity we see. We note that it is possible for intensity gradients between separate components to mimic velocity gradients due to the way in which long-slit spectroscopy mixes spatial and spectral domains. However, the spatial offset between A1 and A2 in the dispersion direction is $\sim$ 0.4″, corresponding to 10Å, which is much less than the apparent velocity gradient. We therefore suggest that the velocity offset most likely arises from motions within the galaxy, rather than as an artifact of the observation.

SMM J123707.21+621408.1:

We observed this target with a position angle such that the NIRSPEC slit passes through the two components shown in the *HST* ACS imaging in Smail et al. (2004). This galaxy consists of a red component and a much bluer object separated by 0.2″ (1.7 kpc) (labelled B1 and B2 in Fig 5.4). The resulting NIRSPEC spectrum shows two strong, spatially-extended lines separated by $\sim$ 600 km s^{-1}. We identify both of these emission lines as Hα (rather than Hα and [NII]) from two separate components for two reasons:

[5]Based on observations made with the NASA/ESA *Hubble Space Telescope* which is operated by STSCI for the Assosciate of Universities for Research in Astronomy, Inc., under NASA contract NAS5-26555

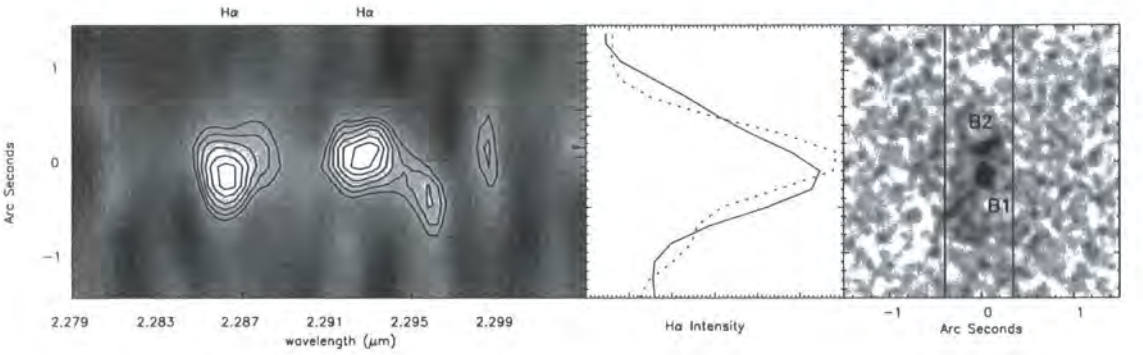

Figure 5.4: On the left we show the position-velocity diagram around the Hα line from the near-infrared spectrum of SMM J123707.21 and on right we show the combined B, V and I-band *HST* ACS observations of this galaxy with the slit position overlaid. In the middle we show the intensity distribution of the Hα emission collapsed over the central 200 km s^{-1} of each of the two Hα emission lines. This shows an apparent spatial offset of 0.2″ (and 600 km s^{-1} velocity offset) between the two galaxies. This matches the apparent separation of the central component of the galaxy (labelled B1) from the much redder second component (labelled B2) which are offset by 2 kpc in projection. (For a color version of this image, see Smail et al. 2004).

1) the spatial separation between the two components in the spectra is matched almost exactly by the separation in the *HST* ACS image (Fig. 5.4); 2) if the higher velocity component was identified as strong [NII]λ6583 then the line ratio would be [NII]/Hα $\sim$ 1 and yet we see no signs of the [SII] emission line which has a ratio of [SII]/[NII]$\sim$ 0.5 for AGN (Ferland & Ostenbrock 1986).

SMM J123711.32+621331.3: This target was known to consist of two radio sources, both of which may contribute to the far-infrared emission. Aligning the slit along both components, we detect only faint continuum and no lines from the UV-identified component, SMM J123711.98+621325.7, for which Chapman et al. (2004a) measured the redshift of the system. However, we do detect Hα emission from the second radio source, SMM J123711.32+621331.3. This allowed us to derive a redshift of 1.9958$\pm$0.0004, giving an offset of 400$\pm$50 km s^{-1} and 8″ ($\sim$70 kpc) in projection from SMM J123711.98+621325.7.

RGJ 131236.05+424044.1:

The ground-based K-band imaging of this galaxy from Smail et al. (2004) shows a bright nucleus surrounded by a diffuse halo approximately 2″ (16 kpc) in extent. The two components seen in the near-infrared spectrum are separated by $\sim$ 185 $\pm$ 45 km s^{-1} in velocity and 0.4″ (3.4 kpc) in projection. The two dimensional near-infrared spectrum suggests that one of the sources (labelled C1) displays signs of a velocity shear in Hα across $\sim$ 0.5″. The [NII]/Hα ratio shows marginal evidence for variation from 0.45 $\pm$ 0.10 to 0.35 $\pm$ 0.10 between C1 and C2, and also mimics the velocity offset between C1 and C2. These modest [NII]/Hα emission line ratios indicate that both components are likely to be star-burst, rather than AGN-, dominated.

SMM J140104.96+025223.5:

This z = 2.56 sub-mm selected galaxy (SMM J14011+0252) is discussed in detail by Ivison et al. (2001). It lies in the field of the z = 0.25 cluster A 1835 and is expected to be amplified by a factor of 2.75$\times$ by the foreground cluster potential. The morphology of this galaxy is complex (Fig. 5.6). Ivison et al. (2001) identify three main components: J1, a blue relatively smooth and regular object; J2, a bluer and more compact object about

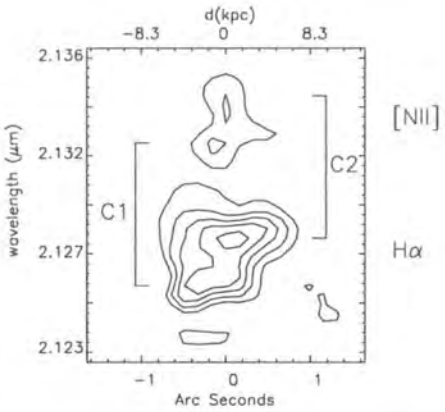

Figure 5.5: The 2-D near-infrared spectrum of RGJ J131236.05, showing the velocity structure seen in Hα and [NII]. We identify two components (labelled C1 and C2), offset by $185 \pm 40\,\mathrm{km\,s^{-1}}$ and 3.4 kpc in projection along the slit.

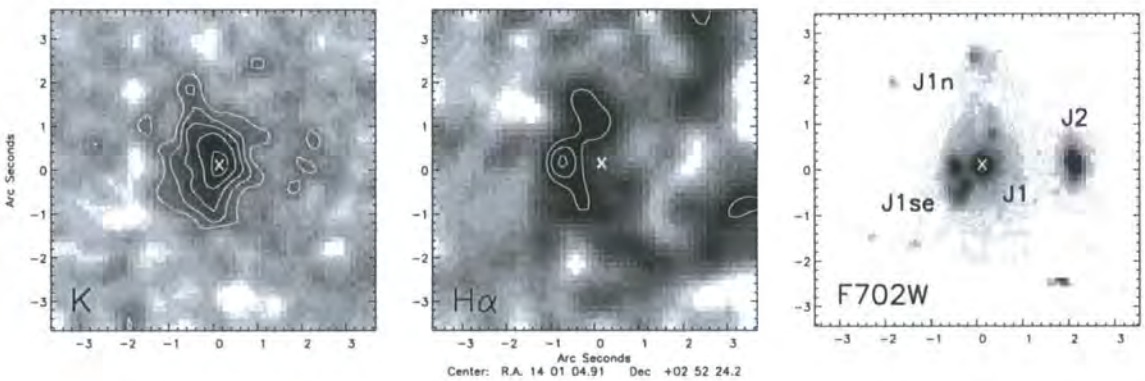

Figure 5.6: Three views of SMM J140104.96, from left to right: Broadband K image from IRTF; Hα continuum-subtracted, narrow-band image from IRTF and the *HST* R_{702}-band of the system which illustrates its very complex morphology. We identify on the *HST* image the three main components of this galaxy as defined by Ivison et al. (2001) and in each panel we also mark the position of the peak of component J1. It is clear that the optical-near-infrared colors and Hα surface brightness of component J2 is much different from that of J1n and J1se – ruling out the suggestion that J2 represents a lensed counter-image of J1n or J1se (Downes & Solomon 2003). Moreover, the Hα emission extending south from J1n and wrapping around J1 traces the morphology of the clumps visible in the R-band, J1se, and has no significant contribution from the smooth component, J1.

2″ to the west of J1; and J1n an extremely red, diffuse structure which extends 2–3″ to the north of J1.

The interpretation of this multi-component system is contentious, Ivison et al. (2001) suggest that the gas reservoir and source of the far-infrared emission from this galaxy reside in J1n – with J2 and J1 simply being less-obscured components within the same system. However, Downes and Solomon (2003) suggest that the clumpy features to the south-west of J1 (called J1se), as well as J1n and J2 are all images of a single, highly-amplified background sub-mm source – which is being lensed by both the regular component of J1 (which they identify as a foreground ($z \sim 0.20$) galaxy) and the cluster potential.

Our IRTF continuum-subtracted Hα image provides a powerful tool for testing these competing suggestions (e.g. Tecza et al., 2004). We compare the morphology of the Hα emission with the R_{702}- and K-band images in Fig. 5.6. It is clear that the bulk of the emission traces the components J1 and J1se, with the regular J1 and compact J2 being undetected. This immediately rules out the possibility that J2 is a lensed counter-image of J1n or J1se. However, the absence of Hα emission from the smooth component of J1 is a concern – suggesting that Downes and Solomon (2003) claim that it is a foreground lens may be correct. To further test this we have returned to the optical spectrum of J1 presented by Barger et al. (1999) and claimed by them to represent a classical Lyman-break galaxy. More careful study of this spectrum leads us to re-examine this interpretation: there are strong absorption features at 4745, 4784, 4912, 4957, 5374 and 6070Å, which are unidentifiable at the redshift claimed by Barger et al. (1999), $z = 2.55$, but correspond exactly to Balmer Hζ, Hη, Ca H&K, G-band and Hβ absorption at $z = 0.248$. This is an unfortunate conjunction – J1 is an ~ 0.1L*, post-starburst member of the A 1835 cluster. The absence of any strong emission lines in this galaxy and broadband colours which are much bluer than the typical passive E/S0 cluster member mean that its nature is not immediately obvious from either the published spectrum or the true colour images of the cluster (Ivison et al., 2000, 2001).

How does this effect the interpretations of SMM J140104.96 by Downes and Solomon (2003) and Ivison et al. (2001)? We confirm that J1 is a foreground lens as stated by Downes and Solomon (2003). However, our observations disprove their central claim that J1n/J1se/J2 are highly-amplified multiple images of an intrinsically low-luminosity sub-mm source. In fact, J1n/J1se and J2 are probably single images of three background galaxies at $z = 2.56$ (see Tecza et al., 2004), with the Hα emission from this system arising entirely from very red J1n/J1se – which is also the site of a massive gas reservoir and hence most likely the far-infrared source (Frayer et al., 2003; Ivison et al., 2001). The addition of J1 to the foreground lens model does increase the estimate of the area-averaged amplification for J1n/Jse from 2.5 to ~ 5, however, this does not significantly alter any of the conclusions in Ivison et al. (2001).

SMM J163650.43+405734.5: We also observed of SMM J163650.43 (ELAIS N2 850.4 Smail et al., 2003a) using NIRSPEC for a total of 4.8 ks at two orthogonal position angles. The detailed kinematics of this complex merging system using 3-D near-infrared spectroscopy is discussed in a later chapter. However, we note that the broad Hα component is apparently offset from the narrow Hα component by $\sim 800\,\mathrm{km\,s^{-1}}$. The redshift quoted in Table 5.2.3. is that of the narrow line Hα.

5.3.2 Hα Properties of SMGs

We show near-infrared spectra of the 23 detected galaxies from our Keck and VLT observations in Fig. 5.1 marked with the expected redshifts of lines based on the best-fit Hα

redshift (Table 5.2.3). As these were short exposures, primarily meant to derive redshifts, the signal-to-noise on the individual galaxies is generally modest. To overcome this we have also combined all of the spectra to provide a composite near-infrared spectrum for a representative far-infrared luminous galaxy at $z \sim 2.4$.

We create the composite spectrum by de-redshifting and summing all of the spectra (normalised by Hα flux) for our galaxies (we note that stacking the spectra based on their individual signal-to-noise or an unweighted stack does not alter any of the conclusions below). We also derive a composite spectrum for those galaxies which individually show no signs of an AGN (i.e. those with small [NII]/Hα ratios (<0.7) and line widths (<700 km s^{-1} FWHM$_{rest}$)). The resulting composite spectra are shown in Fig. 5.7. The restframe composite spectrum from the entire sample is best fit (> 99% confidence level) with an underlying broad-line region with a narrow-to-broad line flux ratio of 0.6 ± 0.1 and FWHM$_{\rm rest}$ of 1300 ± 210 km s^{-1} for the broad-line Hα and FWHM$_{\rm rest}$ of 325 ± 30 km s^{-1} for the narrow-line Hα.

The [SII]/Hα ratio can be used to classify the spectral type of galaxies (Veilleux et al., 1995). The wavelengths of the [SII]$\lambda\lambda$6716, 6731 lines in the composite spectra are 6722 ± 6Å and 6729 ± 5Å – indicating no detectable velocity offset between the Hα and [SII] emission lines. From the strengths of the lines we estimate a ratio of [SII]/Hα = 0.10 ± 0.04 – placing the composite SMG/OFRG within either the LINER or HII region of the classification space (Veilleux and Osterbrock, 1987; Veilleux et al., 1995). This is similar to the typical optical spectral classification of local ULIRGs, for which mid-infrared observations (Lutz et al., 1999) and spatially-resolved spectroscopy (Heckman et al., 2000) both suggest that star-formation is the dominant power source (see Lutz et al., 1999).

The composite spectrum also shows an absorption feature at a wavelength close to that expected for the Na doublet which is seen from cool stars and from the warm neutral (T$\sim 10^4$ K) phase of the ISM (Phillips, 1993). This has been used to map the velocity structure of large scale outflows from nearby ULIRGs (Heckman et al., 2000; Rupke et al., 2002). For a galaxy whose light is dominated by a young star-burst, as we believe is the case for these SMG/OFRGs, the warm ISM is expected to be the primary source of this absorption feature. We fit the Na absorption line with two Gaussian profiles with a fixed separation and variable width and derive a central wavelength of 5889±5Å, which is entirely consistent with the rest-frame wavelength of the resolved doublet (λ5889.95, 5895.92Å). We thus place a limit of <150 km s^{-1} on the possible velocity offset of this feature from the Hα redshift. The FWHM$_{\rm rest}$ of the Na lines is 292 ± 192 km s^{-1} which is also consistent with the FWHM of the Hα emission in the rest-frame composite.

The composite spectrum thus shows no signs of an offset in velocity between Na or [SII] and Hα. This is slightly surprising since many local luminous/ultra-luminous infrared galaxies display velocity offsets of several 100's km s^{-1} between these lines (Heckman et al., 2000; Rupke et al., 2002).

Turning to the rest-frame composite from those galaxies which individually show no signs of an AGN component (i.e. those with low [NII]/Hα emission line ratios and small Hα line widths): we fit this spectrum with both [NII]λ6548,6583 emission lines and also attempt to fit a broad line Hα component. When the broad component is included in the fit, the total χ^2 is marginally better than when the broad component is excluded, with a change in the total $\chi^2 = 4$ which corresponds to $\sim 2\sigma$ (or $\sim 87\%$ confidence). The resulting best-fit model for the SB composite has underlying broad-line Hα component with a ratio of broad/narrow line Hα = 0.45 ± 0.20 and a broad line FWHM$_{\rm rest}$ = 890 ± 210 km s^{-1}, suggesting that even the SMG/OFRGs which are identified individually as star-bursts may contain at least some level of underlying non-thermal

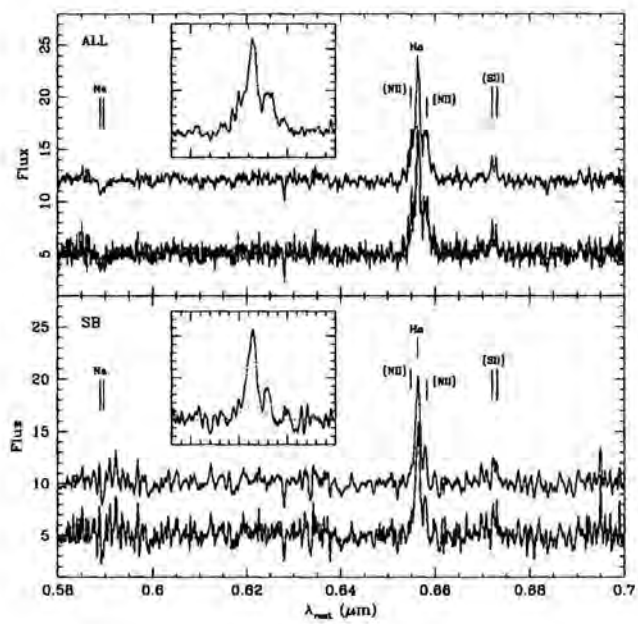

Figure 5.7: The rest-frame composite spectrum of all of the galaxies in our sample (top) as well as the composite from the (individually spectroscopically classified) star-forming galaxies (bottom) (we have not included SMMJ123707.21 in either composite as we believe the spectra displays two Hα components coming from two interacting galaxies rather than Hα and [NII]). The insets show the region around the Hα emission line with the best fit to the emission line using four Gaussian profiles overlaid. We also show the broad line component of the best-fit. The average [NII]/Hα ratio is 0.42 ± 0.05 for the entire sample and 0.19 ± 0.05 for the star forming galaxies. Both are consistent with star-forming galaxies rather than an AGN. We also detect the [SII]$\lambda\lambda$6716,6731Å emission doublet (marginally detected in the SB sample) and the (unresolved) stellar Na$\lambda\lambda$5889.95,5895.92Å absorption doublet. By fitting the Na absorption and [SII] doublets we find no velocity offset from Hα. The [SII]/Hα ratio can be used to classify the SMG/ORFG's optical emission line properties as LINER- or HII-region-like. Whilst the SMG/OFRGs which are individually classified as star-forming galaxies show no signs of an underlying broad Hα line, the composite from this subsample of galaxies are best fit with a narrow/broad Hα emission line ratio of 0.45 ± 0.20.

activity. Nevertheless, the [NII]/Hα emission line ratio is 0.19 ± 0.05, which along with the limit of [SII]/H$\alpha \lesssim 0.14$, still suggests that the energy output is star-formation-, rather than AGN- dominated.

5.3.3 Kinematics of Hα emission

The narrow Hα emission line of the SB composite has a rest-frame FWHM$_{\rm rest}$, after correcting for the instrumental resolution of the observations, of FWHM$_{\rm rest}$ = $400 \pm 70\,{\rm km\,s^{-1}}$ – in agreement with the average Hα line width from the SMG/OFRGs which make up this composite spectrum ($350 \pm 50\,{\rm km\,s^{-1}}$). This is somewhat larger than the Hα line widths of UV-selected galaxies at $z \sim 2$ identified by Erb et al. (2003) who derive a mean FWHM$_{\rm rest}$ = $242 \pm 65\,{\rm km\,s^{-1}}$ for their sample. We compare the distribution of line widths for these two populations (as a function of their Hα luminosities) in Fig. 5.8. We see that the SMG/OFRGs are typically 6× brighter in Hα (*before* any correction for reddening) than the UV-selected population at their epoch. More interestingly, the emission line widths of the SMG/OFRG are on average $\sim$50% larger than those measured for the UV-selected systems, although the two distributions overlap substantially. This difference could either reflect: 1) different halo masses; 2) different dynamical states; 3) a contribution from a broad AGN component in some SMG/OFRGs, 4) starburst driven superwinds contributing to the line widths. The composite spectra from §5.3.2 certainly suggest that an unidentified broad component to the Hα emission may be present in some SMG/OFRGs – however, as we show below we do not believe this is the chief cause of the difference in the line widths of the two populations.

We first compare our Hα-derived line widths with those obtained from the dynamics of cold gas as traced by interferometric maps of the CO distributions in a small number of SMGs (Frayer et al., 1999; Neri et al., 2003; Genzel et al., 2003). The sample of five galaxies compiled by Neri et al. (2003) have a FWHM$_{\rm rest}$ for the CO of $420\pm35\,{\rm km\,s^{-1}}$ and a mean ratio of Hα to CO FWHM consistent with unity (1.27 ± 0.24) for the four galaxies in common with our sample. The CO line widths are unaffected by the presence of any AGN or large scale winds and so this suggests that the AGN or superwind contribution to the Hα line widths for SMG/OFRGs may not be responsible for the comparatively large Hα line widths.

We can therefore combine the emission line widths for our sample with the typical physical extent of the Hα emission from our narrow-band imaging of the SMG/OFRGs to place limits on their masses. The spatial extent of the Hα in the galaxies has a wide distribution: $\lesssim 0.5$–$1.0''$ (corrected for seeing) or $\lesssim$ 4–8 kpc (c.f. Smail et al., 2004). Assuming the Hα emission arises from virialised clouds in the galaxy's potential well, then we estimate a typical mass of 1–2×10^{11} M$_\odot$ for the SMG/OFRG in our sample (Erb et al., 2003), with corresponding dynamical times of 10–20 Myrs. Using the limits on the spatial extent of the CO emission, Neri et al. (2003) determine a median dynamical mass of $\sim 6 \times 10^{10} M_\odot$ assuming the CO gas is in bound orbits. Thus the masses derived from the dynamics of the cold gas in a small sample of these galaxies support those estimated from the emission line kinematics.

The masses of UV-selected galaxies at $z \sim 2$ derived in an identical manner by Erb et al. (2003) have a median of $3.3 \pm 1.1 \times 10^{10} M_\odot$, around 5× lower than our estimates for the SMG/OFRGs. This is due to a combination of smaller estimated sizes and lower Hα line widths. Clearly both of these estimates have large systematic errors, yet they are suggestive of a real difference in the characteristic masses (or dynamical states) of rest-frame UV- and far-infrared selected galaxies at $z \gtrsim 2$.

An independent estimate of the mass can also be obtained for those galaxies for which we confirmed spatial and velocity offsets in Hα emission in the slit spectroscopy.

For any individual galaxy, the mass estimate is highly uncertain since we must assume that the projected velocity and spatial offsets reflect the overall dynamics of the system. However, for a sample of seven SMG/OFRGs for which we have estimates of the velocity differences between the components we can assume random orientations on the sky and that the components are bound/merging. Clearly this will reduce the uncertainties in the projection effects seen in individual systems, and therefore will give a much fairer mass estimate. Using this technique we derive a dynamical mass of $\sim 1.5 \pm 0.9 \times 10^{11} M_{\odot}$. This is comparable to the earlier estimates and gives us confidence that the SMG/OFRGs are indeed massive galaxies.

We also note that recent mid-infrared observations with the Spitzer Space Telescope have been used to infer the stellar mass in these galaxies (at $z \sim 2.5$, rest-frame K-band is shifted to observed $\sim 7\mu$m; Borys et al. 2005).

5.3.4 Magnitude – Line Width correlations

Correlations between rest-frame luminosity and kinematics (as measured by the widths of the emission lines) at high redshift have had only limited success. Pettini et al. (2001) and van Dokkum et al. (2004) have attempted to study the Tully-Fisher or Faber-Jacskon (Tully and Fisher, 1977; Faber and Jackson, 1976) like correlation for LBGs and DRGs at $z \gtrsim 2$, however no correlations have been found over the range $\mathrm{FWHM_{rest}} \sim 120 - 300\,\mathrm{km\,s^{-1}}$. This may in part be due to the small sample sizes involved. To search for such a correlation, the SMGs for which we have well defined narrow-line Hα line width measurements can be added to this sample. We compute the de-reddened rest-frame V-band magnitudes for the SMGs in our sample by using HYPER-Z (Bolzonella et al., 2000) to compute the best fit SED to the observed IJK photometry from Smail et al. (2004). We also convert $\mathrm{FWHM_{rest}}$ to σ by assuming $\mathrm{FWHM} = 2.35 \times \sigma$.

Fig. 5.8 shows the resulting luminosity–linewidth correlation for the combined sample of SMGs LBGs and DRGs (the latter two from Pettini et al. (2001) and van Dokkum et al. (2004) are corrected for reddening using their estimates of A_V). We also overlay the local Faber–Jackson relation from (Jorgensen et al., 1995; Jørgensen et al., 1999) (assuming $V - R = 0.3$), and fit the zero-point of the same correlation so that it passes through the median of the SMG sample – resulting in an offset of 2.5 magnitudes. This offset is comparable to the $\Delta_{\mathrm{fade}} V$ found in Smail et al. (2004) and suggests that the descendants of these high redshift populations are likely to lie on or around the local Faber–Jackson relation.

5.3.5 SFR Comparisons

Next, we compare the far-infrared and Hα luminosities of the galaxies in our sample to investigate the influence of AGN and star formation power-sources and the possible effects of dust extinction on the Hα emission from this population.

Fig. 5.9 compares the Hα and far-infrared luminosities of the galaxies in our sample. We have also include measurements from the literature from five well-studied dusty, high-redshift galaxies: SMM J02399−0136 (Ivison et al., 1998, 2000), SMM J17142+5016 (Smail et al., 2003b), ERO J164502+4626 (Dey et al., 1999), SMM J04431+0210 (Frayer et al., 2003) and SMM J16359+6612 (Kneib et al., 2004b).

The star formation rate derived from the far-infrared and Hα should be correlated if the effects of dust and any contributions from AGN are uniform across the sample. The SMG/OFRGs in our sample show only a weak correlation between SFR(FIR) and SFR(Hα), with comparable scatter in the Hα-derived SFR and that estimated from the far-infrared (Δ(FIR)/FIR$= 0.30 \pm 0.18$ versus $\Delta(\mathrm{H}\alpha)/\mathrm{H}\alpha = 0.37 \pm 0.20$). Reassuringly,

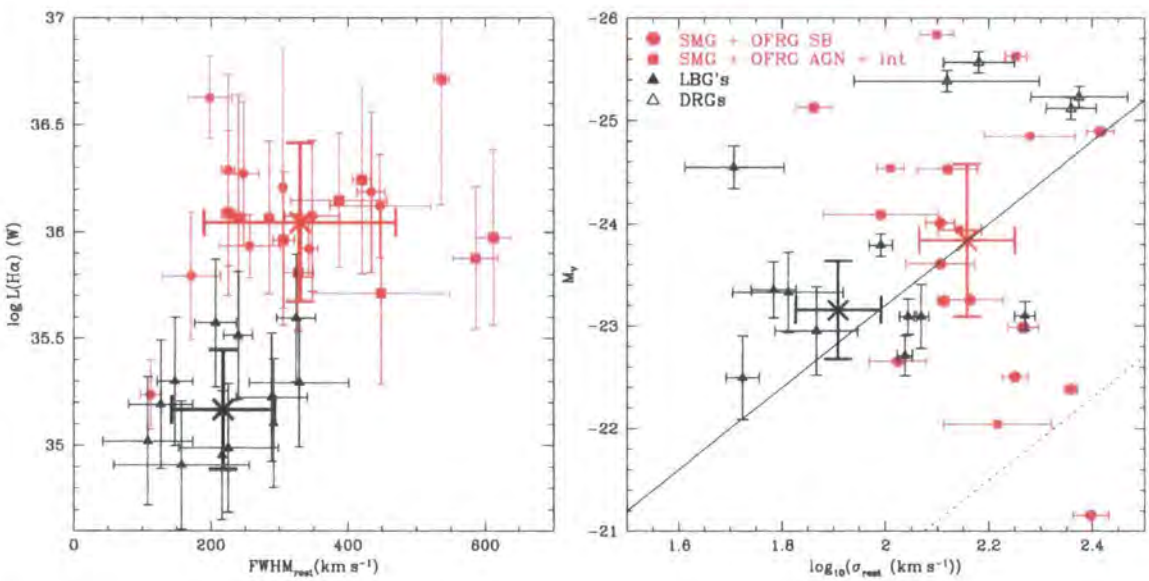

Figure 5.8: Left: Comparison of the Hα luminosity versus FWHM$_{\rm rest}$ for the narrow Hα components (deconvolved for instrumental resolution) in our sample compared to those found in UV-selected galaxies by Erb et al. (2003) (we have conservatively assumed a factor of two uncertainty in the Hα luminosities for this sample). We also include those galaxies which show single broad lines (no narrow component). The crosses mark the positions of the median luminosity and FWHM$_{\rm rest}$ for the two populations. The line widths in the SMG/OFRGs has a median of 330 km s^{-1} and have a long tail out to $\sim$ 600 km s^{-1}. In comparison to the UV-selected galaxies studied by Erb et al. (2003) (which have a median of $\sim$ 210 km s^{-1}), SMG/OFRGs appear to be typically more massive systems, with a wider distribution of line widths (although some of the broadest lines may come from unresolved companions or AGN). Right: Correlation between rest-frame optical emission line width verses rest-frame V-band luminosity (the Faber–Jackson relation) for the SMG/OFRGs compared to the LBGs and DRGs from Pettini et al. (2001) and van Dokkum et al. (2004). The crosses mark the positions of the median luminosity and $\sigma_{\rm rest}$ for the SMG/OFRGs and LBGs. We overlay the local Faber–Jackson relation as the dotted line (assuming $V - R$=0.3) and also the same line offset by a further 2.5 magnitudes in order to pass through the median of the SMG sample (solid line).

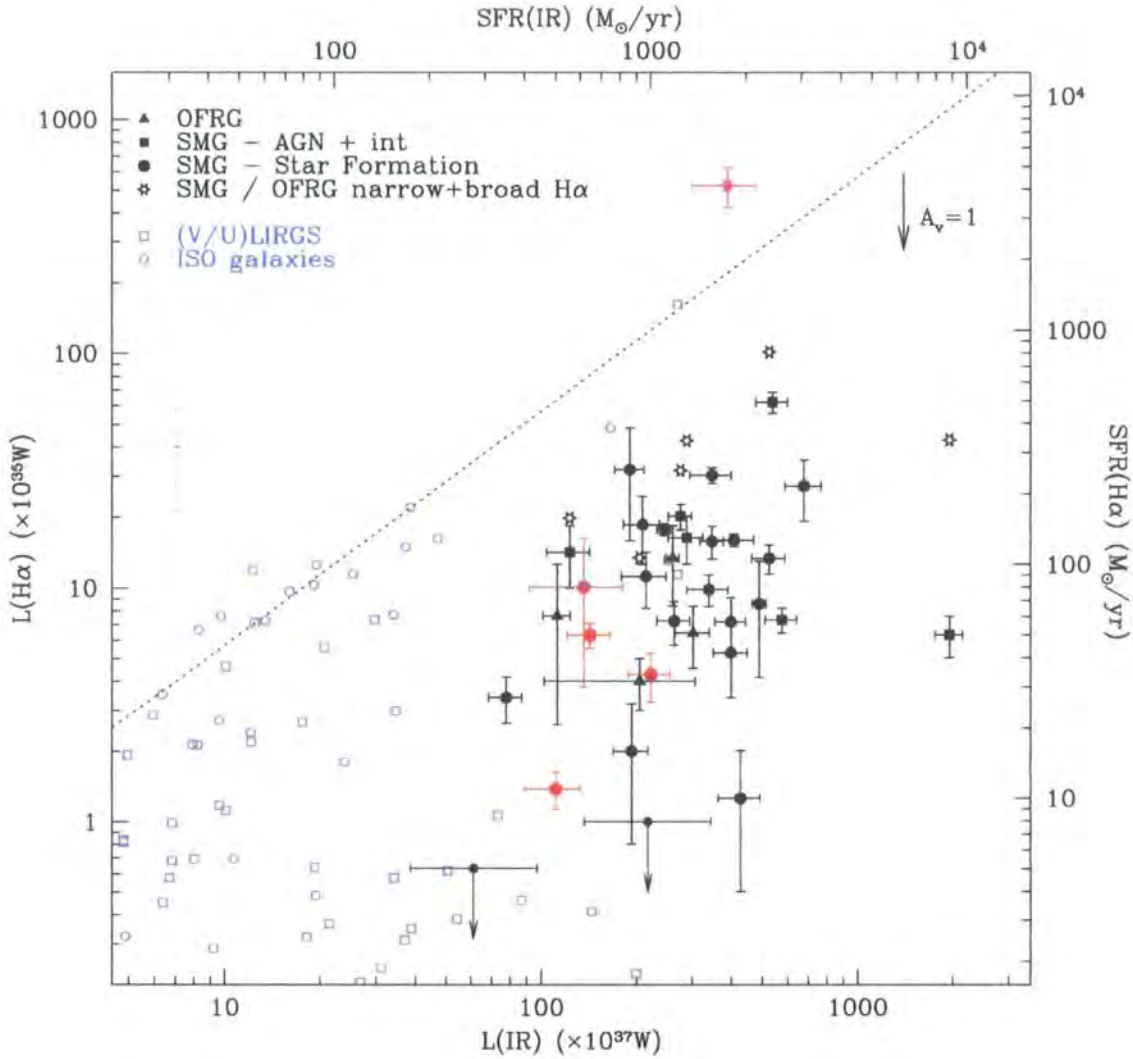

Figure 5.9: Comparison of the far-infrared versus narrow-line Hα luminosities and star formation rates in our data compared to local samples. We include in the plot the SFR's for the SMG/OFRGs when the broad line Hα flux is included in the estimate (the galaxies classified as intermediate in §2.4 are included with the AGN classification). This is more comparable to the quantities calculated for local samples. We also include the previously published SMGs (Kneib et al. 2004; Dey et al. 1999; Smail et al. 2003; Frayer et al. 2003; Ivison et al. 1998) as red points ordered from lowest to highest Hα luminosity respectively. The dotted line represents identical estimated SFR from Hα and far-infrared. The sample is compared to the results from ISOCAM, including the z = 0.2–1.5 galaxies in the HDF-S by Franceschini et al. (2003); the local luminous infrared galaxy sample (z = 0.2–0.7) by Flores et al. (2004). We also compare the data to the Very Luminous and Ultra-Luminous infrared galaxy sample of local *IRAS* >2Jy sources by Dopita et al. (2002) and Poggianti & Wu (2000). We include a representative error bar from the comparison samples on the left hand side of the plot.

the two galaxies for which we failed to obtain Hα detections in good conditions are also two of the least luminous galaxies when ranked on their far-infrared emission.

We have also included on Fig. 5.9 samples of similar and less luminous far-infrared galaxies from surveys of the $z < 1$ Universe. These come from ISOCAM-selected galaxy surveys (Franceschini et al., 2003; Flores et al., 2004) and studies of local Very- and Ultra-Luminous infrared galaxies by Poggianti and Wu (2000) and Dopita et al. (2002). Comparing to these samples we see a similar wide dispersion in the ratio of far-infrared to Hα luminosities across a factor of nearly 100 in far-infrared luminosity. This is suggestive of a similar diversity in the energy sources and obscuration for galaxies with far-infrared luminosities spanning 10^{10}–$\gtrsim 10^{12}$ $L_{\odot}$. In support of this, we note that the distribution of Hα equivalent widths (EW, Table 5.2.3) for the SMG sample peaks at about $\sim$ 20–40Å and has a long tail out to $\gtrsim$ 100Å, with a median EW(Hα) = 75 ± 25Å. The shape of the distribution is very similar to that seen for the rest-frame Hα EW's of local ULIRGs from (Veilleux et al., 1999), which have a median EW(Hα) = 73 ± 8Å suggesting that the unobscured/partially observed mix of emission line gas and stellar continuum is comparable to local ULIRGs (although we note that the projected size of the spectroscopy apertures in the local ULIRGs is <1 kpc, whereas for the SMG/OFRGs the projected size is $\sim$ 10 kpc, thus some caution should be taken when comparing the two samples).

Our SMG/OFRG sample are intrinsically luminous in the far-infrared, but their Hα flux (and estimated SFR) is much less than expected with a median SFR(Hα) compared to SFR(IR) of 94 ± 20 and 1380 ± 190$M_{\odot}yr^{-1}$ respectively. Overall, the Hα SFR's are suppressed by at least a factor of ten relative to that suggested by the far-infrared. In comparison to other far-infrared selected samples, we see that the SMG/OFRG extend the trend for proportionally less Hα luminosity in more far-infrared luminous galaxies. As we have shown there is no detectable difference between the far-infrared luminosities of the starburst- and AGN-classed galaxies in our sample – suggesting that this declining ratio of Hα to far-infrared emission is unlikely to be caused by an increasing AGN contribution. Hence, we attribute the variation to copious and increasing amounts of dust enshrouding the galaxy and extinguishing Hα emission.

Unfortunately, the wavelength coverage of our spectroscopic observations does not extend to Hβ, and thus the reddening in these galaxies cannot be estimated directly from the Balmer decrement to confirm this suggestion: although attempts at estimating the reddening in this manner are underway for a subsample of galaxies. The only target with a $H\beta$ measurement in the literature is SMM J123707.21+621408.1 (Simpson et al., 2004) with a Hβ flux of $2.1\pm0.9\times10^{-20}$ W m^{-2}. The Hα/Hβ flux ratio is 8±6 which corresponds to a reddening of $A_V = 1.4 \pm 1.0$ (Calzetti et al., 1994), the large uncertainties arise from the modest signal-to-noise detections of both Hα and Hβ emission lines. For the rest of the sample, we have attempted to derive the reddening for these galaxies from their broadband optical/near-infrared colours (Smail et al., 2004). These are derived by using the HYPER-Z photometric redshift code (Bolzonella et al., 2000) to fit young continuous star formation models with variable reddening and age to the galaxy photometry at their known redshifts. We find a median reddening of $A_V = 3.0 \pm 1.0$. Accounting for the contribution of Hα to the K-band photometry may decrease this estimate slightly but the reddening estimated from the continuum colours indicates substantial extinction at the wavelength of Hα (assuming the continuum and line emission arise from the same regions in the galaxy). The scatter of a factor of 2.5× is more than sufficient to explain the dispersion in the strength of the Hα emission at a fixed far-infrared luminosity. We conclude therefore that the large scatter in SFR(FIR)/SFR(Hα) probably arises from two main factors: first, there is a range in the continuum extinction in the more far-infrared luminous population and secondly the morphological diversity of sub-mm-selected

galaxies – which includes a large fraction of interacting or merging systems, sometimes with highly-obscured components may lead to a large variation in the in-slit Hα fluxes for these systems (Chapman et al., 2003b; Smail et al., 2004).

5.3.6 Metallicities

Before discussing the abundance measurements which we derive from our data, we briefly review some of the principles and limitations of using emission lines as abundance measurements in high redshift galaxies.

Rest-frame optical emission lines from extra-galactic HII regions provide an important diagnostic of the chemical evolution of galaxies since their properties reflect the make up of the interstellar medium (ISM). The most widely used abundance indicator, the R_{23} index relates the abundance of oxygen to the ratio of ([OII]+[OIII]) to Hβ and have been calibrated onto more secure abundance determinations based on auroral measurements or on detailed photoionisation models (e.g. McGaugh 1991). However, systematic differences of up to 0.5dex remain between oxygen abundances derived from the R_{23} index and those deduced from other methods (such as the 'direct' T_e method, which measures the ratios of auroral to nebular emission lines intensities). When combined with the double-valued nature behaviour of (O/H) versus R_{23}, this can lead to order of magnitude uncertainties in (O/H) in galaxies at $z \sim 2$. Despite the uncertainties in these calibrations, the measured abundances of star-forming galaxies at high redshift is still an important diagnostic for galaxy formation and evolution, and with the advent of 8-10m telescopes, it has been made it possible observe these lines in a few high redshift galaxies (e.g. Teplitz et al. 2000; Steidel et al. 2004).

However, at high redshift (e.g. $z \gtrsim 2$), these observations encounter new practical obstacles. The first is that, given large distances involved, the line fluxes are reduced dramatically. This is compounded by the fact that the rest-frame optical emission lines are redshifted into the near-infrared, where the sky background is orders of magnitude higher than in the optical. Second, at a given redshift, only a subset of the strong lines will fall within an atmospheric window and thus be accessible from the ground. Even at particularly favourable redshifts, such as $z \sim 2.3$ (which shifts [OII], [OIII], Hβ, Hα and [NII] into the middle of the J, H, and $K-$ bands respectively), it is not possible to record all of these lines in a single exposure, but rather different spectrograph settings are normally required, introducing errors in the relative flux calibrations. Therefore, there is high incentive to develop abundance measurements based on only a few emission lines (preferably close in wavelength). Whilst, admittedly this may be less reliable than the full treatments mentioned above, it may overcome some of the practical limitations mentioned above and may still lead to an adequate characterisation of the chemical enrichment of distant galaxies.

For star-forming and irregular galaxies the correlation between metallicity (traced by Oxygen abundances, O/H) and rest-frame luminosity is well established in the local Universe and spans a factor of over 100 in (O/H) and at least eight magnitudes in M_V. The correlation is in the sense that more massive (and luminous) galaxies exhibit a higher degree of metal enrichment (Zaritsky et al., 1994; Garnett et al., 1997; Lilly et al., 2003; Lamareille et al., 2004). If such a correlation exists at high redshift then it may be more important for understanding the present distribution of metals in the Universe, since the bulk of the star-formation activity in the most massive and active galaxies is thought to occur at $z > 1$ (Blain et al., 1999).

Since we lack the observations necessary to calculate the R_{23} index (Zaritsky et al., 1994) for our sample, we turn to the $N2$ index described by Storchi-Bergmann et al. (1994) and discussed more recently by Denicoló et al. (2002) and Pettini and Pagel (2004). This

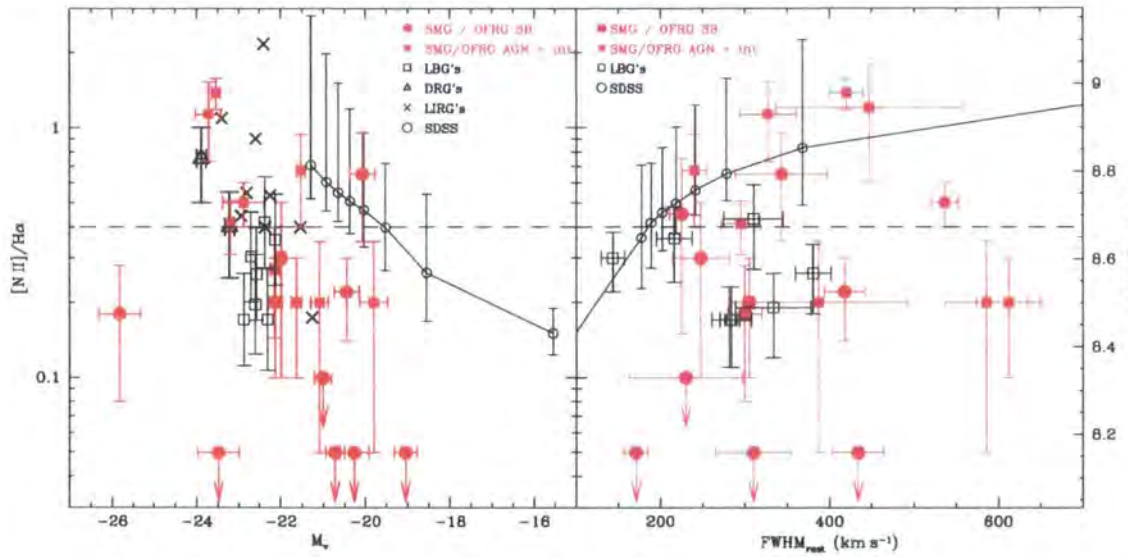

Figure 5.10: Left: The Metallicity-Luminosity relationship for SMG/OFRGs. Right: The line width versus metallicity relation for the SMG/OFRGs. The abundance is derived using the N2 index calibration given by Pettini et al. (2004). We show two low-redshift samples for comparison, one from the SDSS DR2 (Abazajian et al. 2003) and one for local luminous infrared galaxies (Armus 1989). For a higher redshift comparison sample, we show the metallicities for the $z \sim 2$ UV-selected galaxies from Shapley et al. (2004) and for an near-infrared selected sample of luminous, $z \sim 2$ galaxies from van Dokkum et al. (2004). The horizontal dashed line represents solar metallicity. The SMG/OFRGs exhibit a large range in M_V and $\mathrm{FWHM_{rest}}$, and many have slightly sub-solar or solar abundances. Note that these are the observed V-band luminosities (uncorrected for reddening, c.f. Fig. 5.7).

indicator is defined at $N2 = log([\mathrm{N\,II}]\lambda6584/\mathrm{H}\alpha)$ and is calibrated to the oxygen abundance (O/H) via $12 + log(\mathrm{O/H}) = 8.90 + 0.57 \times N2$ (Pettini and Pagel, 2004). This calibration has the advantage that, even at high spectral resolution, the [NII] and Hα are only 20Å apart (in the rest-frame) and can therefore be observed in a single observation. However, this calibration is used as an abundance measurement in extragalactic HII regions (i.e. star-forming galaxies), and although remains uncertain, there are obvious drawbacks to using this index for young galaxies in which AGN may play a role in defining the emission line characteristics. One way to overcome this is to measure the ratios of [OIII]/Hβ **and** [NII]/Hα and place the galaxies on Fig. 5.2 (proving they resemble HII regions before measuring their abundances). However, since we currently lack the observations required to measure [OIII]/Hβ, we are forced to use the $N2$ ratio alone. We therefore caution that there remain uncertainties in the following analysis since AGN activity in some the sub-mm galaxies may effect the $N2$ index.

For this reason, we chose to compare populations directly using their $N2$ measurements (as opposed to (O/H) measured from a range of indicators) to minimise systematic uncertainties arising from the calibration from $N2$ to (O/H). We therefore determine the $N2$ index for all of the galaxies in our sample and give upper limits where the [NII] emission line is not detected with sufficient significance to measure accurately.

In Fig. 5.10 we show the distribution of M_V–$N2$ for SMG/OFRGs as a proxy for their Luminosity–Metallicity relation and compare this with similar observations of both local and high redshift galaxy populations. To calculate the observed rest-frame V-band lumi-

nosities of the SMGs we use the photometry from Smail et al. (2004) and fit SED's based on their observed broad-band IJK magnitudes which, at $z \sim 2.4$, corresponds to rest-frame UBR, bracketing the V-band. As Smail et al. (2004) show, the competing effects of dust reddening and fading of the young stellar populations almost cancel each other ($\Delta_{\rm dust}V \sim 3$–$4$, $\Delta_{\rm fade}V \sim 4$ based on fitting the broadband colors of this population). Thus we expect that the present-day descendants of these galaxies would have absolute luminosities not very dissimilar to those we have estimated (see also Fig. 5.10). For the comparison samples we convert the rest-frame B-band magnitudes for the UV-selected $z \sim 2$ sample from Shapley et al. (2004) using their $(R-K)$ colors topredict the rest-frame V-band magnitudes. We also convert the median, 10 and 90 percentile trend lines from a volume limited ($z < 0.1$) local emission line galaxy sample from the SDSS DR2 ((The SDSS collaboration), 2003) (although we stress that the Sloan aperture only samples the central ~ 3 kpc of a galaxy at $z = 0.05$ whereas the NIRSPEC slit will sample ~ 10 kpc at $z = 2.3$). We see at least an order of magnitude range in $N2$ for the SMG/OFRGs (discounting obvious AGN), with little correlation between the line index and rest-frame luminosity. The implied median metallicity is slightly below solar, and appears to be similar to that inferred for bright, UV-selected galaxies at $z \sim 2$ (Shapley et al., 2004).

To address the competing and uncertain effects of dust reddening and passive fading of the stellar populations on the M_V–[NII]/Hα plot we have also constructed a FWHM$_{\rm H\alpha}$–[NII]/Hα diagram, adopting the FWHM$_{\rm H\alpha}$ as a crude proxy for the dynamical mass of the galaxies. As can be seen the large dynamical masses we inferred for the SMG/OFRG population suggests that their present-day descendants are likely to be luminous and metal-rich (super-solar) systems (as shown by the trends seen in the SDSS dataset plotted in Fig. 5.10). The apparently modest metallicities we measure would then indicate that these systems are seen during an early phase of enrichment – suggesting that they are relatively youthful galaxies and arguing against them undergoing a cycle of repeated short (~ 10 Myrs) bursts of star-formation over a relatively extended period ($\gtrsim 1$ Gyr; Smail et al., 2003a). However, there are other possible explanations for the apparently low metallicities of these galaxies. Firstly, we note that star-formation can usually only act to increase a galaxy's metallicity (and therefore $N2$), and in particular star-burst driven feedback mechanisms are unlikely to preferentially expel large quantities of metals without entraining and expelling associated gas. Only an infall of unenriched material into the galaxy could cause the metallicity and effective heavy element yield to decrease (e.g. Garrett, 2002). Alternatively, if these systems are very young and the halos of the SMG/OFRG have yet to coalesce (as suggested by the clear merger/interacting morphologies of many systems), then the metallicities we measure may reflect those of the progenitor components. The similarity of the $N2$ estimates with those for the UV-selected population at this epoch could also then be interpreted as indicating that the SMG/OFRGs arise from mergers amongst the UV population. The slightly more evolved descendants of these mergers will be able to retain their enriched gas and so produce a super-solar stellar population. We stress that local calibrations of the $N2$ index from HII regions can show super-solar metallicities which may not reflect the global abundance in a galaxy. However, since our spectroscopic slit covers most of the area of our galaxies, and the measured Hα fluxes suggest substantial star-formation, we suggest that the $N2$ index should provide a fair estimate of the metallicity of the gas in the galaxy as a whole.

It is also interesting to note that local N/O versus O/H relations suggest that, for metal rich systems the nitrogen is secondary in origin (produced from intermediate mass stars far removed from the first generation). The fact that we measure metallicities close to solar in the SMGs/OFRGs therefore suggests that the nitrogen is also secondary in nature (rather than being primary enrichment produced from high mass (2-7M$_\odot$) first

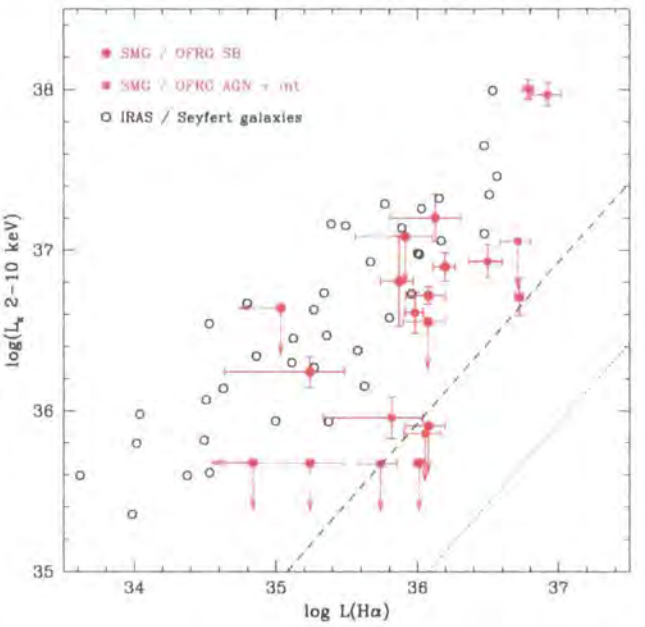

Figure 5.11: The distribution of Hα and X-ray luminosities for the SMG/OFRGs in our sample as compared to the local *IRAS*-selected Seyfert galaxies from Ward et al. (1988). For the SMG/OFRGs sample we plot the total Hα luminosity from both narrow and broad components (if present). We also compare the data to a sample of nearby star-forming galaxies by Ranalli et al. (2003) as a dotted line (converting their L(FIR) to L(Hα) assuming the correlation in §5.2.5 holds) and also include the same line but assuming a 10× suppression of the Hα emission (relative to the far-infrared) as indicated in Fig. 5.8 as a dashed line. The plot shows that some SMG/OFRGs which are identified as star-forming in the near-infrared (with FWHM $\leq 500\,\mathrm{km\,s^{-1}}$ and [NII]/H$\alpha \lesssim 0.7$) show 2–10 KeV X-ray fluxes consistent with AGN luminosities. It is also interesting to note that some of the SMG/OFRGs which are spectroscopically-classified as AGN from their near-infrared spectra are not detected in the hard X-ray band.

generation stars).

5.3.7 X-ray comparisons

Using deep *Chandra* observations of the HDF, ELAIS N2, and SSA13 fields (Alexander et al., 2003a,b; Manners et al., 2003; Mushotzky et al., 2000) it is possible to compare the X-ray and Hα properties of the SMG/OFRGs which overlap with the *Chandra* coverage. Of the 18 sources which were covered by *Chandra*, nine were detected in the 2–8 KeV hard X-ray band, mostly in the HDF due to the much deeper X-ray observations available for that field. We convert the observed 2–8 KeV flux to a rest-frame 2–10 KeV luminosity using $L_X = 4\pi d_L^2 f_X (1+z)^{\Gamma-2}$, which takes into account the k-correction (Alexander et al., 2003b), assuming a spectral index $\Gamma = 2$.

In Fig 5.11 we compare the Hα luminosities from the SMG/OFRGs to their X-ray luminosities and contrast these with a local sample of *IRAS*-selected Seyfert galaxies analysed by Ward et al. (1988). We also overlay two lines showing the correlation of $L_{(2-10\mathrm{KeV})}$ versus L(FIR) from Ranalli et al. (2003). The first line simply converts their L(FIR) to L(Hα) assuming the relation in §2 holds, the second line assumes a further 10× suppression of the Hα emission (relative to the far-infrared) as indicated by Fig. 5.9.

The distribution of the SMG/OFRGs in Fig. 5.11 roughly follows that seen for the Ward et al. (1988) sample – *irrespective* of the spectral classification of the SMG/OFRG. However, we note that the correlation for local star-forming galaxies from Ranalli et al. (2003) – if scaled for the relative underluminosity of Hα in the SMG/OFRGs – can explain the properties of the least X-ray luminous galaxies, these comprise roughly half of our sample.

The most intriguing galaxies in Fig. 5.11 are those which have high X-ray luminosities ($\log L_x \gtrsim 36.5$) but have restframe optical spectral classifications of star-formation – the X-ray luminosity in these galaxies probably arises from an AGN which is either so highly obscured that it is hidden in the restframe optical spectra (given their modest signal to noise), or that we missed the AGN component with our spectroscopic slit in these systems. The presence of a broad-line component in the composite star-forming spectrum in §5.3.2 would support the former interpretation.

We also point out that there are six SMG/OFRGs which are not detected to a flux limit of 1.4×10^{-19} W m^{-2} in the 2-Ms *Chandra* observations of the HDF(2) or 2.2×10^{-18} W m^{-2} in the ELAIS N2(4) field. Whilst three of these are classified as SB from their restframe optical spectra, three others show some signs of AGN in the near-infrared spectra (with broad Hα or large [NII]/Hα ratio's). The X-ray limits on two of these (SMM J163650.43 and SMM J163706.51) are particularly stringent – yet they show clear AGN signatures in their near-infrared spectra. The detection of broad Hα and lack of X-ray emission is difficult to understand – with these galaxies being almost an order of magnitude fainter in the X-ray waveband than expected from their Hα luminosities. Given the amount of gas available to fuel and AGN in these systems, we conclude that they are likely to be intrinsically low luminosity and probably have low mass central black holes.

5.4 Conclusions

We present the results of near-infrared spectroscopic and narrow-band detections or limits on the Hα emission from a sample of 30 ultraluminous, dusty galaxies at $z \sim 1.4$–2.7. The majority of these galaxies come from sub-mm/mm-surveys, with a small number identified as probable hot, luminous far-infrared sources from their radio emission. We see no difference between the properties of these two samples in any of our diagnostic diagrams – supporting the claimed similarity of the two populations (Chapman et al., 2004a). We identify the Hα emission in the near-infrared spectra and use the spectra to classify AGN by flagging galaxies with large [NII]/Hα ratio's (≥ 0.7) and/or large Hα FWHM ($> 500\,\mathrm{km\,s^{-1}}$). We find that the ratio of AGN- to star formation- dominated galaxies from the restframe optical spectroscopy is roughly 40%:60% – similar to the proportions estimated from their UV spectra by Chapman et al. (2005). By constructing a restframe composite spectrum for the entire sample we find the average [NII]/Hα ratio is 0.42 ± 0.05 and also has an underlying broad line component. Furthermore the composite spectra shows both NaD absorption and [SII] emission features, although we find no evidence of velocity offsets between these features and the Hα emission. The [SII]/Hα emission ratio in the composite spectrum is 0.10 ± 0.04 – indicating that the spectral properties of our sample are comparable to a LINER or HII region – similar results are found from the spectral classifications of local ULIRGs (Veilleux and Osterbrock, 1987; Veilleux et al., 1995).

We also derive the composite spectrum for those galaxies which, individually, show no signs of an AGN in their near-infrared spectra. This composite has an average [NII]/Hα flux ratio of 0.19 ± 0.05 and $\mathrm{FWHM_{rest}}$ of $400\pm70\,\mathrm{km\,s^{-1}}$. However, the most striking result is that the composite spectrum appears to show an underlying broad Hα line with

a broad/narrow Hα flux ratio of 0.45 ± 0.20 suggesting that even these galaxies may host a low luminosity AGN which is undetectable in our modest signal-to-noise spectroscopy.

In seven of the systems with spectroscopic observations we find velocity structure in the Hα emission line. By comparison with high-resolution broadband imaging we identify these galaxies as multi-component (probably interacting) systems with typical velocity offsets between components of 100–600 km s^{-1}. This is not surprising since locally many far-infrared luminous galaxies appear to be disturbed/interacting systems. Assuming that these are merging systems with random orientations of their orbits on the sky, we estimate a typical mass of $1.5 \pm 0.9 \times 10^{11} M_{\odot}$. We obtain a similar estimate from the Hα line widths of the whole sample. These estimates are comparable to the dynamical mass estimates from CO observations of a subset of these systems.

In all of the galaxies we have attempted to deconvolve any broad component to the Hα line (which comes from an accretion disk around a central super-massive black hole) from the narrow-line Hα flux (which comes from the star-forming regions). Using the narrow-line Hα flux we compare the SFR's of the SMG/OFRGs to the SFR derived from the far-infrared emission. The SFR(Hα) versus SFR(FIR) correlation shows a large scatter, with the SFR(Hα) typically a factor of ten less that we would expect from their far-infrared luminosities. Most of this scatter however can be explained by the reddening in these systems (estimated from their broad-band photometry in Smail et al. (2004)). The suppression of the Hα flux is therefore attributed to both heavily obscured galaxies and a diverse range of morphologies. The average SFR derived from Hα for the SMG/OFRGs in our sample is $94 \pm 20 M_{\odot} yr^{-1}$ (uncorrected for extinction). Since the continuum extinction correction at 6563Å is ~2.5 magnitudes the total inferred SFR of these galaxies is expected to be $\sim 1000 M_{\odot} yr^{-1}$ – comparable to that seen in the far-infrared. We also compare the SFR properties for our high redshift sample to local Very/Ultra-Luminous galaxy samples and find that the scatter within our high redshift SMG/OFRG and the distribution of equivalent widths are comparable to those of local Ultra/Very luminous galaxy samples. This suggest a similar range of obscured/unobscured activity in the distant population to that seen locally, although with a higher proportion of the star formation completely obscured from view.

Using the $N2$ index we have investigated the chemical abundances of these galaxies and find that the $N2$ indices for the SMG/OFRGs suggest they have slightly sub-solar metallicities, similar to recent results from UV selected galaxies at these early epochs (Shapley et al., 2004). However, we note that the $N2$ indicator may not be a reliable metallicity indicator for this population – especially in the presence of an AGN. We find that the SMG/OFRGs in our sample display a large range in [NII]/Hα versus M_V or $FWHM_{rest}$ (which we use as a proxy for their dynamical masses).

For the galaxies which are in the HDF, ELAIS N2 and SSA13 fields we use their X-ray properties in order to further classify the galaxies. The SMG/OFRGs classified as AGN on the basis of their near-infrared spectra broadly follow the correlation seen between X-ray and Hα luminosities for local Seyfert 2's (Ward et al., 1988). We find that a subset of galaxies which are spectroscopically-classified as star-forming in the near-infrared have high X-ray luminosities, suggesting they host highly obscured AGN. Likewise, a small number of near-infrared spectroscopically-classified AGN are undetected in deep *Chandra* observations. We conclude that these galaxies are likely to be intrinsically low luminosity and probably have low mass central black holes.

With observations of the Hα emission from these SMG/OFRGs at $z \sim 2$ we can at last start to directly compare these galaxies to similarly distant UV-selected systems. We find that as expected the SFR(Hα) for our sample is nearly an order of magnitude higher than that found in $z \sim 2$ UV-selected galaxies by Erb et al. (2003) (who find an

average SFR(Hα) of $21 \pm 3 M_{\odot} yr^{-1}$ – even after their sample is corrected for extinction). Similarly, the line widths and dynamical information suggest that the halos of a typical SMG/OFRGs may be up to 5× more massive than the UV-selected population. We also find a higher rate of AGN activity in the SMG/OFRGs – suggesting the presence of actively fuelled and growing super-massive black holes in these galaxies. However, somewhat surprisingly we find similar metallicities for the UV-selected and the more massive far-infrared luminous populations. We suggest that this may be explained if the SMG/OFRGs are relatively youthful, with their deepening potential wells not yet sufficiently organised to retain a larger fraction of the enriched material from their star formation activity.

Overall our observations suggest that the high redshift SMG/OFRG population shares many of the characteristics of similar (but somewhat less luminous) far-infrared galaxies identified in the local Universe. This includes the Hα equivalent widths, the proportion of obvious AGN and the typical optical spectral classification. Previous work has demonstrated the preponderance of merger-like morphologies in the two populations and the similarity of their restframe optical luminosities. Yet there remain differences, with proportionally more highly-obscured activity in the high-redshift population, apparently larger dynamical mass, lower metallicities and higher gas fractions on 10-kpc scales.

We conclude that the SMG/OFRGs in our sample represent a population of young, massive merging/interacting systems, the results of which cause high instantaneous bursts of (highly obscured) star-formation and actively fuelled AGN activity. Although these bursts are brief, they can form all of the stars in an L^* galaxy and in doing so will raise the metallicity of these systems closer to that required by observations of their likely present-day descendants: luminous elliptical galaxies.

Chapter 6

Optical and Near-Infrared Integral Field Spectroscopy of the SCUBA Galaxy N2-850.4

Motivation

With the sample of submm galaxies in § 5 in hand, we can address critical issues in understanding the rapid evolution of the SCUBA galaxy population. One powerful route to relating the apparantly disparate high-redshift galaxy populations is to spatially resolve and compare the kinematics, metallicities and structural information from rest-frame optical emission lines. In the next two chapters, we use integral field spectroscopy of powerful far-infrared luminous galaxies to address these issues. In particular, in this chapter we also investigate how the AGN and starburst feedback regulate galaxy formation by combining optical and near-infrared integral field spectroscopy (Swinbank et al., 2005b).

Abstract

We present optical and near-infrared integral field spectroscopy of the SCUBA galaxy SMM J163650.43+405734.5 (ELAIS N2 850.4) at z=2.385. We combine Lyα and Hα emission line maps and velocity structure with high resolution *HST* ACS and NICMOS imaging to probe the complex dynamics of this vigorous star-burst galaxy. The imaging data shows a complex morphology, consisting of at least three components separated by $\sim$1″ (8 kpc) in projection. When combined with the Hα velocity field from UKIRT UIST IFU observations we identify two components whose redshifts are coincident with the systemic redshift, measured from previous CO observations, one of which shows signs of AGN activity. A third component is offset by $220 \pm 50\,\mathrm{km\,s^{-1}}$ from the systemic velocity. The total star formation rate of the whole system (estimated from the narrow-line Hα and uncorrected for reddening) is $340 \pm 50 M_{\odot} \mathrm{yr}^{-1}$. The Ly$\alpha$ emission mapped by the GMOS IFU covers the complete galaxy and is offset by $+270 \pm 40\,\mathrm{km\,s^{-1}}$ from the systemic velocity. This velocity offset is comparable to that seen in rest-frame UV-selected galaxies at similar redshifts and usually interpreted as a star-burst driven wind. The extended structure of the Lyα emission suggests that this wind is not a nuclear phenomenon, but is instead a galactic scale outflow. Our observations suggest that the vigorous activity in N2 850.4 is arising as a result of an interaction between at least two dynamically-distinct components, resulting in a strong starburst, a starburst-driven wind and actively-fuelled AGN activity. Whilst these observations are based on a single object, our results clearly

show the power of combining optical and near-infrared integral field spectroscopy to probe the power sources, masses and metallicities of far-infrared luminous galaxies, as well as understanding the role of AGN- and star-burst driven feedback processes in these high redshift systems.

6.1 Introduction

Recent surveys have concluded that a substantial fraction of the high redshift submillimetre (sub-mm) selected galaxy population comprises morphologically complex systems with high instantaneous star formation rates and actively fuelled AGN (Smail et al., 1997; Barger et al., 1999; Scott et al., 2002; Smail et al., 2002; Ivison et al., 2002; Alexander et al., 2003a; Chapman et al., 2003b; Webb et al., 2003; Dannerbauer et al., 2004; Swinbank et al., 2004; Chapman et al., 2004b; Pope et al., 2005). Understanding the importance of this population requires identifying their power source (e.g. to determine whether star formation- or AGN- activity dominate the luminosity output) and, perhaps more importantly, masses for these galaxies. Although they have only moderate space densities, their apparantly high star formation rates mean their contribution to the cosmic star formation rate could be significant (e.g. Chapman et al., 2004b). Moreover, the star formation activity suggests *a priori* that these galaxies should house starburst-driven superwinds – outflows which expel gas from the galaxy potential (e.g. Pettini et al., 2001; Shapley et al., 2003) and which are believed to play an important role in regulating galaxy formation, preventing the bulk of baryons cooling into stars (the "cosmic cooling crisis" White and Rees, 1978; Cen and Ostriker, 1999; Balogh et al., 2001). However, to study the energetics and dynamics of these frequently complex systems (e.g. Smail et al., 2004) we must trace the distribution of the velocity and intensity of emission lines on sub-arcsecond scales. Ideally, this should be achieved in 2-D to untangle the complex morphologies of these systems and, in addition to search for signatures of lensing, which might provide a more mundane explanation of the apparently intense luminosities of these galaxies (Tecza et al., 2004).

In this paper we demonstrate the power of combining optical and near-infrared integral field spectroscopy with high resolution *Hubble Space Telescope (HST)* imaging to study the dynamics, morphologies, masses and outflows of SCUBA galaxies. Using the Integral Field Units (IFUs) on GMOS (optical) and UIST (near-infrared) we have studied the SCUBA galaxy SMM J163650.43+405734.5 (ELAIS N2 850.4 Scott et al., 2002; Ivison et al., 2002; Smail et al., 2003a). In §2 we present the data reduction and results from the spectroscopic and imaging data. In §3 and §4 we present our analysis and conclusions respectively. We use a cosmology with $H_0 = 70\,\mathrm{km\,s^{-1}}$, $\Omega_M = 0.3$ and $\Omega_\Lambda = 0.7$ in which $1''$ corresponds to 8.2 kpc at $z = 2.4$.

6.2 Observations and Analysis

N2 850.4 was first catalogued as a bright (8.2 ± 1.7mJy) sub-mm source by Scott et al. (2002) and identified through its radio counterpart by Ivison et al. (2002). A spectroscopic redshift of $z = 2.38$ for the radio counterpart was measured by Chapman et al. (2005). N2 850.4 has a far-infrared bolometric luminosity of $L_{FIR}=3.1\times10^{13}L_\odot$ (Chapman et al. 2005a) which corresponds to a star formation rate of $\sim 5400 M_\odot yr^{-1}$, (Kennicutt, 1998); (although the far-infrared luminosity may have a contribution from a non-thermal (AGN) component). Interferometric observations of the molecular CO emission in this system by Neri et al. (2003) have tied down the systemic redshift as $z = 2.384 \pm 0.001$ and indicate a gas mass of 5.5×10^{10} $M_\odot$. The system was studied in detail by (Smail et al., 2003a)

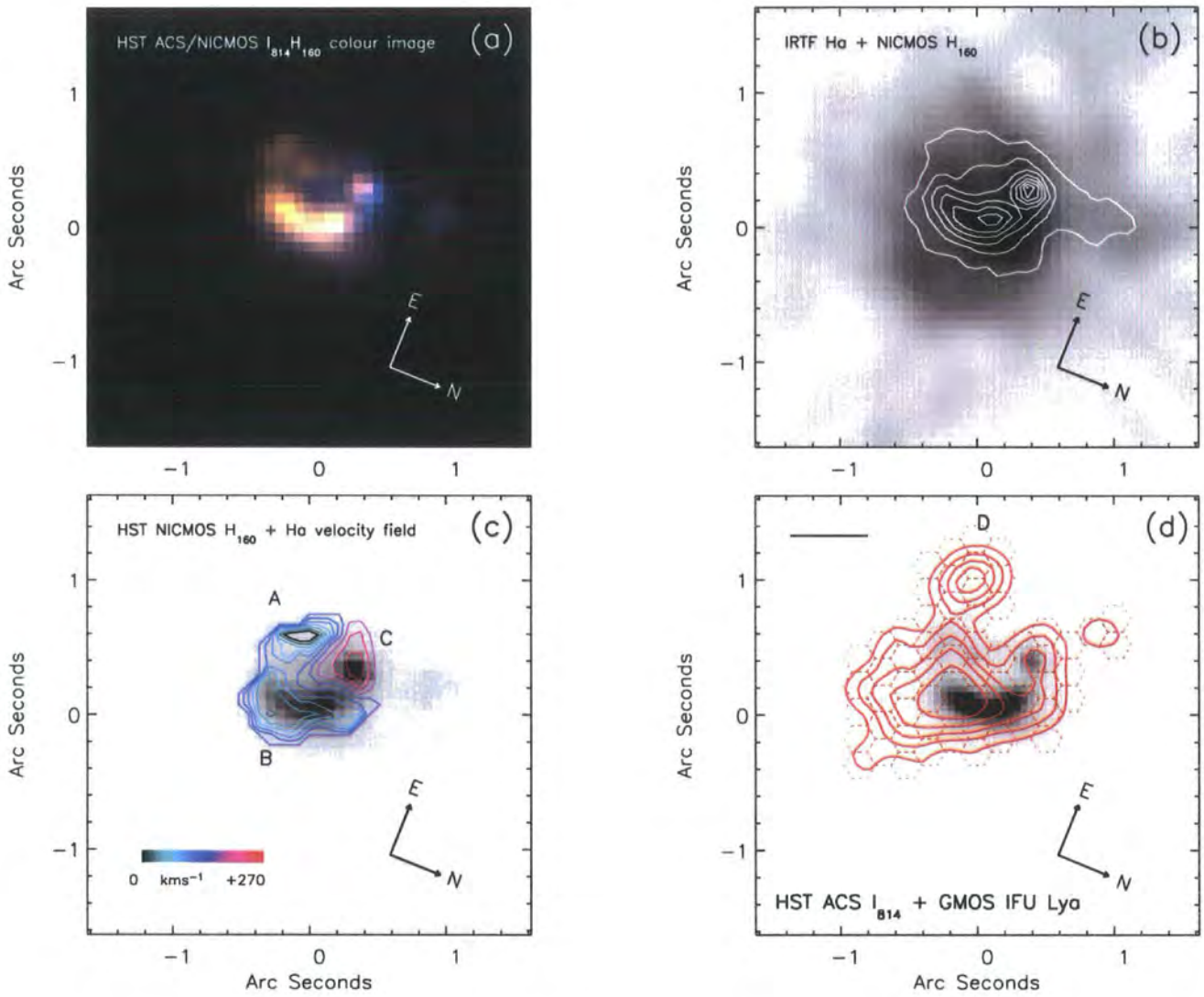

Figure 6.1: (a) True colour $I_{814}H_{160}$ image of N2 850.4 from the *HST* ACS and NICMOS imaging. The image shows a complex morphology, with at least three distinct components separated by $\sim 1''$ ($\sim$8 kpc) in projection. (b) IRTF Hα narrow-band image of N2 850.4 with the contours from the NICMOS H_{160}-band image overlaid. This Hα narrow-band image shows a diffuse halo of material distributed asymmetrically around the galaxy [seeing $\sim$0.7″]. (c) The velocity field of N2 850.4 derived from UIST IFU observations of the Hα emission line overlaid on the NICMOS H_{160}-band image. The redshift of component A is in excellent agreement with previous CO observations (Neri et al., 2003). Components A and B are separated by $50 \pm 50\,\mathrm{km\,s^{-1}}$ whilst there is a velocity difference of $+270 \pm 50\,\mathrm{km\,s^{-1}}$ between components A and C [the 0.6″ seeing is marked by the solid bar in the top left hand corner of panel d]. (d) *HST* ACS I_{814}-band (F814) image of N2 850.4 with the Lyα intensity from the GMOS IFU overlaid as contours (the contours mark 3,4,5,6 and 7σ). We also overlay the footprint of the GMOS IFU fibers which have $> 3\sigma$ emission line detections. The solid bar in the top left hand corner of this panel represent 0.6″ seeing. The Lyα contours match the high surface brightness emission traced by the I_{814}-band imaging data, although there is Lyα emission to the East (labelled D) which is not seen in the $I_{814}-$band morphology. The Lyα is redshifted from the systemic by $+270 \pm 40\,\mathrm{km\,s^{-1}}$, indicating of a galactic-scale outflow.

whose multi-wavelength longslit observations suggest that this system comprises at least two components, one of which has a Seyfert-like AGN and the other maybe a UV-bright starburst with an outflow. These observations show extended [OIII]λ5007 emission as well as strong UV stellar absorption features.

However, due to the multi-component nature of this system and the way in which longslit observations mix spatial and spectral resolution, the observations of this galaxy have been difficult to interpret (Smail et al., 2003a). By targeting N2 850.4 with an IFU we are able to decouple the spatial and spectral resolution and cleanly probe the dynamics and power sources of this hyper-luminous SCUBA galaxy.

6.2.1 HST Optical and Near-Infrared Imaging

HST Advanced Camera for Surveys (ACS) observations were obtained from the *HST* public archive[1] (Program ID #9761). The data consist of dithered exposures with the F814W filter, taken in LOWSKY conditions using the default four-point ACS-WFC-DITHER-BOX configuration. This pattern ensures optimal half-pixel sampling along both coordinates. The total integration time was 4.8 ks. We reduced the data using the latest version of the MULTIDRIZZLE software (Koekemoer et al., 2002) using the default parameters with PIXFRAC=1 and SCALE=1. The resulting image has 0.05″ pixels and is free from artifacts (Fig. 6.1).

The NICMOS data were obtained in Cycle 12, and the target was observed using the NIC2 camera in the F160W filter for a total of 2.3 ks (Program ID #9856). We employed the standard four point spiral dither pattern, LOWSKY conditions and used the MULTIACCUM readmode. Each exposure was corrected for a pedastal offset, and then mosaiced using the CALNICB task in IRAF. Unfortunately the observation was effected by the South Atlantic Anomaly (SAA), and extra processing steps were required[2]. The final images appear very flat and have very low cosmic ray contamination. Absolute astrometry of the NICMOS images is accurate to only $\leq 2''$, so we cross-correlated the full image against the high resolution ACS data to align the near-infrared image with the optical image. Both are aligned to the FK5 coordinate system of our deep radio map of this field (Ivison et al., 2002) which has an absolute astrometry precision of 0.3″. A complete discussion of the optical and near-infrared observations and data-reduction is given in Borys et al. (2005).

We degrade the *HST* ACS data to the same resolution as the NICMOS observations and make a true colour ($I_{814}H_{160}$) image of N2 850.4. An inspection of this imaging data (Fig. 6.1) reveals a complex system made up of several components. In particular, the brightest features have similar colours and an apparent geometry which is reminiscent of a triply-imaged, strongly lensed system. Could the immense luminosity of N2 850.4 be due to strong lensing? (e.g. Chapman et al., 2002). Our IFU observations of this system provide a powerful tool for testing this suggestion, since the redshifts and spectral features should be the same for all three components if they are all images of a single background galaxy.

[1] Obtained from the Multimission Archive at the Space Telescope Science Institute (MAST). STScI is operated by the Association of Universities for Research in Astronomy, Inc., under NASA contract NAS5-26555. Support for MAST for non-*HST* data is provided by the NASA Office of Space Science via grant NAG5-7584 and by other grants and contracts.

[2] For a full description, see
http://www.stsci.edu/hst/nicmos/tools/post_SAA_tools.html

6.2.2 IRTF Narrow-band Imaging

Narrow-band imaging of N2 850.4 was carried out using the 3-m NASA Infra-Red Telescope Facility[3](IRTF) Telescope between 2003 April 28 and May 02. The observations were made in generally photometric conditions and $\sim 0.7''$ seeing. We used the NSFCAM camera (Shure et al., 1993) which employs a 256×256 InSb detector at $0.15''$ pixel^{-1} to give a $38''$ field of view (which probes roughly 300 kpc at $z \sim 2.4$). The continuously variable tunable narrow-band filter (CVF) in NSFCAM provides an $R = 90$ passband which was tuned to target the Hα emission at the systemic galaxy redshift measured ($z = 2.384$) from CO and UV spectrum of Neri et al. (2003) and Smail et al. (2003a) respectively. Shorter, matched broad-band imaging were interspersed between the narrow-band exposures to provide continuum subtraction. The total narrow-band integration time was 19.8 ks and the total broad band integration time was 2.2 ks. These observations, their reduction and analysis are discussed in detail in (Swinbank et al., 2004).

6.2.3 Spectroscopic Imaging

UIST Near-Infrared Integral Field Spectroscopy

Observations of N2 850.4 were made in queue mode with the UKIRT Image-Spectrometer (UIST) IFU between 2003 March 27 and April 04 in $<0.6''$ seeing and photometric conditions[4]. The UIST IFU uses an image slicer and re-imaging mirrors to reformat a square array of 14-slices of the sky, (each $0.24''\times0.12''$) into a pseudo-longslit. The resulting field of view is $3.4''\times6.0''$ (Ramsay Howat et al., 1998). We used the HK grism which has a spectral resolution of $\lambda/\Delta\lambda = 1000$ and covers a wavelength range of 1.4–2.4μm. Observations were carried out in the standard ABBA configuration in which we chopped away to sky by $12''$ to achieve good sky subtraction. Individual exposures were 240s seconds and each observing block was 7.2 ks which was repeated four times, thus the total integration time was 28.8 ks.

To reduce the data we used the relevant ORAC-DR pipeline (Cavanagh et al., 2003) which sky-subtracts, extracts, wavelength calibrates, flatfields, and forms the datacube. To accurately align and mosaic the four datacubes we created white light (wavelength collapsed) images around the redshifted Hα emission line from each observing block and used the peak intensity to centroid the object in the IFU datacube. We then spatially aligned and co-added the four individual data-cubes (weighted by Hα signal-to-noise) using MOSAIC in KAPPA.

To search for velocity structure we attempt to identify Hα emission on a pixel-by-pixel basis by averaging over a $0.48''\times0.48''$ region (4×2 pixels), increasing to $0.6''\times0.72''$ (5×3 pixels) if no emission line could initially be identified. At $z = 2.385$, H$\alpha\lambda$6562.8 emission falls at 2.221μm, which is away from any strong OH emission or absorption. We attempt to fit a single Gaussian to the Hα emission line, but also attempt to identify an [NII]λ6583 emission line, only accepting the fit if the χ^2 is significantly better than without the [NII] line. We checked the wavelength calibration of each IFU pixel by fitting a nearby sky line with a Gaussian profile. The errors in the velocity field are calculated by building two independent data-cubes, each of 14.4 ks and recomputing the velocity field in an identical manner to that described above. Using the same fitting techniques as above we estimate

[3]The Infrared Telescope Facility is operated by the University of Hawaii under Cooperative Agreement no. NCC 5-538 with the National Aeronautics and Space Administration, Office of Space Science, Planetary Astronomy Program.

[4]The United Kingdom Infrared Telescope is operated by the Joint Astronomy Center on behalf on the UK Particle Physics and Astronomy Research Council.

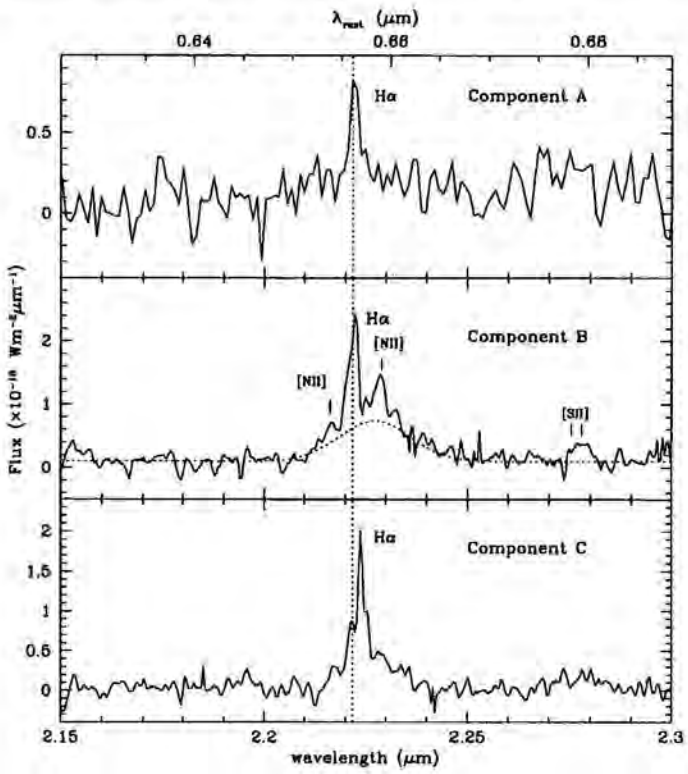

Figure 6.2: *Top:* Near-infrared spectrum of component A around the Hα emission line. This component is at the same redshift as the systemic redshift ($z = 2.384$) as measured from the molecular CO emission by Neri et al. (2003). *Middle:* Near-infrared spectrum of component B from which shows a $+50 \pm 50\,\mathrm{km\,s^{-1}}$ velocity shift from the systemic. This component also has a broad Hα regions offset by $+800 \pm 150\,\mathrm{km\,s^{-1}}$ which indicates AGN activity. The FWHM of the broad line is $2300 \pm 250\,\mathrm{km\,s^{-1}}$. *Lower:* Near-infrared spectrum of component C which shows a $220 \pm 50\,\mathrm{km\,s^{-1}}$ velocity offset from the systemic. Component C also displays a broad line component ($FWHM = 1800 \pm 300\,\mathrm{km\,s^{-1}}$) which is at a similar redshift to the broad line seen in component B and may arise due to the same scattering seen in [OIII] by Smail et al. (2003). The top panel has been binned by a factor of two in the spectral direction to boost the contrast of the Hα emission. The dotted line shows the systemic redshift of 2.384 (Neri et al. 2003; Smail et al. 2003).

that the average velocity error to be $\simeq 50\,\mathrm{km\,s^{-1}}$. Spectra from the three components identified in the UIST IFU observations are shown in Fig. 6.2.

To confirm the velocity gradients seen in the UIST IFU data (Fig. 6.1) we also obtained a 4.8 ks exposure around the Hα emission lines with the Keck near-infrared longslit spectrograph. We aligned the slit along components A and B in Fig. 1 and derive the same velocity offsets between components as in our the IFU data (the spectra and line fluxes are shown and discussed in Swinbank et al. (2004).

GMOS Optical Integral Field Spectroscopy

N2 850.4 was observed with the GMOS-IFU on Gemini North on 2002 June 12 during Science Demonstration time for a total of 7.2 ks in 0.6″ seeing and photometric conditions[5]. The GMOS IFU uses a lensed fibre system to reformat a 7″ × 5″ field into two long slits (Allington-Smith et al., 2002). Using a B-band filter in conjunction with the B600 grating results in two tiers of spectra recording the maximum field of view. The spectral resolution

of this configuration is $\lambda/\Delta\lambda_{\rm FWHM} = 2000$. For the galaxy at $z = 2.385$, the Lyα emission falls at 4112Å which is in a region of low sky emission, but also low throughput.

The GMOS data reduction pipeline was modified such that the extracted spectra included the blue edge of the CCD (where the Lyα emission falls) and then used to extract and wavelength calibrate the spectra of each IFU element. The variations in fibre-to-fibre response were removed using the continuum around the expected range of Lyα emission. To check the wavelength calibration around 4100Å we wavelength calibrated the CuAr arc observations and fit the arc lines between 4000 and 4200Å with Gaussian profiles. We measured the rms offset between the observed arc line centroids and the arc line list to be less than 0.02Å (which corresponds to less than $8\,{\rm km\,s^{-1}}$ in the rest frame of the galaxy). This gives us confidence that any velocity structures or offsets in the GMOS IFU data are real and not simply an artifact of the observations. To search for velocity structure the spectra were averaged over a 3×3 pixel ($0.6'' \times 0.6''$) spatial region, except where the signal was too low to give a significant detection of the line, in which case the smoothing area was increased to 4×4 pixels. In regions where this averaging process still failed to give an adequate χ^2 (i.e. the inclusion of an emission line component does not improve the fit), no fit was made. In order to detect and fit the line we required a minimum S/N of 3 and checked every fit by eye. In the inner regions of the galaxy all of the Gaussian profile fits are accepted, while in the outer regions we reject fits if the line centroid is greater than $3000\,{\rm km\,s^{-1}}$ away from the systemic, or the best fit Gaussian profile has a width greater than FWHM$>3000\,{\rm km\,s^{-1}}$. Although the Lyα emission is resolved (FWHM$\sim 700\,{\rm km\,s^{-1}}$), we detect no significant coherent velocity gradient across the system and place a limit of $100\,{\rm km\,s^{-1}}$ on possible velocity structure (Table 6.3.). We construct a *Lyα intensity map* from the emission line and overlay this on the *HST* ACS image in Fig. 6.1.

6.3 Analysis

To spatially align the imaging and spectroscopy observations we begin by constructing a Hα image from the UIST IFU and align this with the IRFT Hα and continuum images (which are also aligned to the NICMOS and ACS images using stars in the field of view). Furthemore, to tie these to the GMOS data, we construct a Lyα and continuum image from the GMOS IFU and align these with the galaxy in an observed V-band image from Ivison et al. (2002). This V-band image is then aligned to the near-infrared imaging and results accurate alignment between the GMOS, UIST, IRTF and HST observations. We estimate that the uncertainty in the astrometry between any two frame to be $\lesssim 0.2''$. Having combined the *HST* H_{160} and I_{814}-band NICMOS and ACS imaging with the velocity structure of the Hα emission, we find at least three dynamically distinct components (labelled *A*, *B*, and *C* in Fig. 6.1) and we show the near-infrared spectra around the Hα emission from these components in Fig. 6.2. The redshift of components *A* and *B* are in excellent agreement with previous CO(4–3) observations which measured the systemic redshift to be 2.384 ± 0.001 (Neri et al., 2003; Greve et al., 2004). The other component, labelled *C* is dynamically distinct from the systemic redshift. Component *B* has an [NII]/Hα emission line ratio of 0.37 ± 0.05, which is indicative of star-formation, although the presence of an underlying ($2300 \pm 250\,{\rm km\,s^{-1}}$) H$\alpha$ broad line region suggests

[5]Programme ID: GN-2002A-DD-4. Obtained at the Gemini Observatory, which is operated by the Association of Universities for Research in Astronomy, Inc., under a cooperative agreement with the NSF on behalf of the Gemini partnership: the National Science Foundation (United States), the Particle Physics and Astronomy Research Council (United Kingdom), the National Research Council (Canada), CONICYT (Chile), the Australian Research Council (Australia), CNPq (Brazil) and CONICET (Argentina)

AGN activity or scattered light from an AGN. The velocity offset of the narrow line Hα from the systemic galaxy is $+50 \pm 50\,\mathrm{km\,s^{-1}}$ and has a width of $360 \pm 25\,\mathrm{km\,s^{-1}}$ whilst the broad line Hα is redshifted by $+800 \pm 150\,\mathrm{km\,s^{-1}}$ (all line widths are deconvolved for the instrumental resolution).

Turning to the Lyα emission line map from the GMOS IFU observations (Fig. 6.1), we find an an extended, diffuse Lyα halo. Whilst the Lyα seems to roughly follow the I_{814}-band morphology, we also identify Lyα emission lying outside the optical extent of the galaxy (labelled *D* in Fig. 6.1). The spatial extent of the Lyα is $\sim 16\,\mathrm{kpc}$, however, most interestingly the velocity of the emission line is placed $+270 \pm 40\,\mathrm{km\,s^{-1}}$ redward of the systemic velocity of this system. We detect no significant velocity structure in the Lyα emission across the system (see Table 1).

Using a deep, 1.44″ resolution 1.4-GHz map of the field from the VLA, Ivison et al. (2002) identified a compact radio source with a centroid which corresponds exactly to the location of component *B* in Fig. 6.1. This gives us confidence that this component is responsible for the far-infrared activity. The third component (labelled *C*) is offset from *A*/*B* by $+220 \pm 50\,\mathrm{km\,s^{-1}}$ and has an upper limit of [NII]/H$\alpha \lesssim 0.05$ and a width of $320 \pm 30\,\mathrm{km\,s^{-1}}$. This indicates star-formation rather than AGN activity, although there is also evidence for a broad-line Hα component which is at the same redshift as the broad line seen in component *B* (Fig. 6.2). This broad line Hα may arise as part of the same scattered emission seen in the [OIII]λ5007 emission in Smail et al. (2003a). To attempt to identify which component hosts the AGN activity, we construct a (wavelength collapsed) white light image from the datacube between 2.23μm and 2.25μm (i.e. the broad-line Hα emission) and compare this with the white light image generated by collapsing the datacube between 2.215μm and 2.225μm (which includes the narrow-line Hα emission). Unfortunately these two images look very similar and it is not possible to identify which component hosts the AGN.

The velocity offsets and spectral differences seen among the various morphological components immediately rules out the possibility that all are gravitationall lensed images of a single background source. Instead, it appears that N2-850.4 is a multi-component and complex merger. Assuming the velocity offsets arises due to merging components in the potential well, we estimate a dynamical mass of $\gtrsim 2 \times 10^{11}\,\mathrm{M_\odot}$.

The velocity offsets from the Hα emission can be compared directly to the dynamics from the CO(4–3) and CO(7–6) observations from Neri et al. (2003). It appears that the broad CO(4–3) emission arises from two components (a bright component at z=2.383, and a fainter component at slightly higher redshift (at z$\sim$2.388) which is located $\gtrsim 0.3''$ to the NE of the first component). Narrow CO(7–6) emission is also detected at the same position and redshift as the lower redshift CO(4–3) emission. Assuming the CO(7–6) and the lower redshift CO(4–3) emission arise from warm, dense gas associated with *A* and/or *B* and the higher redshift CO(4–3) emission arises from component *C*, the velocity and spatial offsets are in excellent agreement with our IFU observations. Furthermore, this suggests that *A*/*B* and *C* all host gas reservoirs, with *B* being the most massive. The implied molecular gas mass from the CO observations is $\sim 5.5 \times 10^{10}\,\mathrm{M_\odot}$, thus the dynamical mass ($\sim 2 \times 10^{10}\,\mathrm{M_\odot}$) for N2 850.4 is approximately four times greater than gas mass estimate suggesting that this system has a high baryonic fraction in the central regions.

Using the Hα emission line as a star-formation rate indicator we can calculate the star formation rate in each of the three components. For solar abundances and adopting a Salpeter IMF, the conversion between Hα flux and star formation rate is $\mathrm{SFR(M_\odot yr^{-1})}=7.9\times 10^{-35}\mathrm{L(H\alpha)}W$ (Kennicutt 1998). This calibration assumes that all of the ionising photons are reprocessed into nebular lines (i.e. they are neither absorbed by dust before they can

TABLE 1.
VELOCITIES OF REST FRAME UV AND OPTICAL EMISSION

Component	$z_{H\alpha}$	FWHM$_{H\alpha}$ ($\mathrm{km\,s^{-1}}$)	Hα Flux ($10^{-19}\,\mathrm{W\,m^{-2}}$)	$z_{Ly\alpha}$	$v_{H\alpha}$ ($\mathrm{km\,s^{-1}}$)	$v_{Ly\alpha}$ ($\mathrm{km\,s^{-1}}$)
A	2.3841[4]	330±40	0.9 ± 0.2	...	0±50	...
B	2.3847[3]	360±25	4.4 ± 0.9	2.3870[4]	+50±50	+260±40
B_{broad}	2.3930[10]	2300±250	16.7 ± 2.0	...	+800±150	...
C	2.3866[3]	320±30	4.0 ± 1.0	2.3872[4]	+220±50	+275±40
C_{broad}	2.3900[12]	1800±300	8.0 ± 1.5	...	+550±200	...
D	...	...	...	2.3860[6]	...	+170±50

Table 6.1: Notes: The value given in the [] z column is the error in the last decimal place. The quoted velocities are with respect to the systemic redshift from Neri et al. 2003.

ionise the gas, nor do they escape the galaxy). Using the narrow-line Hα emission line fluxes with this calibration we find that the star formation rates of components A, B and C (uncorrected for reddening) are $\lesssim 30$, 150±30 and 140±30$\mathrm{M_\odot yr^{-1}}$respectively. The total star formation rate is a factor of $\gtrsim 10$ less than the star formation rate implied from the far-infrared luminosity, and implies aproximately three magnitudes of dust extinction (e.g. Smail et al., 2004).

6.4 Discussion & Conclusions

The colours and morphology of N2 850.4 from our *HST* ACS and NICMOS imaging resemble those of a strongly lensed galaxy, however the lens interpretation is quickly ruled out from the Hα emission maps which show that this system is made up of at least three dynamically distinct components separated by $\sim 1''$ (8 kpc) in projection and up to $220 \pm 50\,\mathrm{km\,s^{-1}}$ in velocity. The ground- and space-based imaging data also shows a diffuse and asymmetric halo of material surrounding the galaxy. The Hα redshift of components A/B in Fig. 6.1 are in excellent agreement with previous CO and rest-frame UV longslit observations which have measured the systemic redshift to be 2.384 (Neri et al., 2003; Smail et al., 2003a). The presence of an underlying broad ($\sim 2000\,\mathrm{km\,s^{-1}}$) emission line (offset by $\sim +800\,\mathrm{km\,s^{-1}}$) in components B and C suggests AGN activity. Comparable narrow-line to broad-line velocity offsets are frequently seen in local Seyfert nuclei (e.g. Osterbrock and Shuder, 1982; Corbin and Boroson, 1996; Storchi-Bergmann et al., 2003)as well as high-redshift radio galaxies (e.g. Simpson et al., 1999). The third component detected in narrow-line Hα emission C is redshifted from the systemic by $220 \pm 50\,\mathrm{km\,s^{-1}}$. Combined with the high resolution imaging, the complex morphology and dynamics of this system suggests a massive merger event which has presumably triggered a strong, obscured star-burst and AGN activity.

The GMOS IFU observations show that N2 850.4 has an extended halo of Lyα emission. The Lyα halo has a spatial extent of ~ 16 kpc and is redshifted relative to the systemic velocity by $+270 \pm 40\,\mathrm{km\,s^{-1}}$. It is interesting to compare the Lyα emission from N2 850.4 with the giant sub-mm detected Lyα haloes LAB1 and LAB2 in the SSA22 field (Steidel et al., 2000; Chapman et al., 2000; Bower et al., 2004). From our observations, N2 850.4 has a slightly lower integrated Lyα luminosity ($\gtrsim 3\times10^{43}\mathrm{erg\,s^{-1}}$) compared to LAB1 and LAB2 ($1\times10^{44}\mathrm{erg\,s^{-1}}$ and $9\times10^{43}\mathrm{erg\,s^{-1}}$ respectively), but is much more compact (LAB1 and LAB2 have areas of over 100arcsec^2 (5000 kpc^2)), however the limiting surface brightness of the GMOS observations are $\sim 5\times10^{-16}\mathrm{erg\,s^{-1}cm^{-2}arcsec^{-2}}$ (signif-

icantly less than the surface brightness limit of LAB1 and LAB2 narrow-band imaging observations), and it is therefore possible that N2 850.4 is surrounded by a large-scale diffuse emission halo below the sensitivity limit of the GMOS IFU observations. Nevertheless, the Lyα emission from N2 850.4 is much more peaked than LAB1 and therefore this halo may represent a different evolutionary phase. Unfortunately, due to the very different surface brightnesses of the systems and the large pixel scale of the SAURON IFU (which has 1.0″ fibres), it is very difficult to directly compare the dynamics of the two systems (Bower et al., 2004). In terms of the wider environment, it is interesting to note that a second sub-mm detected galaxy has recently been detected in the same structure as N2 850.4 (at a distance of 2.5 Mpc; Chapman et al., 2005).

The observed velocity offset between Hα and Lyα emission is comparable to those seen in the spectra of rest-frame UV selected galaxies at $z \gtrsim 2$ (Teplitz et al., 2000; Pettini et al., 2001; Shapley et al., 2003) where they have been attributed to galactic scale outflows produced by the collective effects of heating and outflows from supernovae. In this scenario, the Lyα appears redshifted due to resonant scattering of photons from the inner surface of a receding shell of material. Such flows have been termed "superwinds" by analogy to the wind seen in the spectra of local ultra-luminous infrared galaxies and local star-burst galaxies (Martin, 2005; Keel, 2005). If such winds can escape from the potential well, they can carry metals to large distances from the galaxy and deposit large amounts of energy in the intergalactic medium. These winds thus have important consequences for the metal enrichment of the Universe (Aguirre et al., 2001) and galaxy formation models (Benson et al., 2003). The key issue, however, is whether the wind material is localised within individual HII regions (in which case, it may not escape the galaxy potential), or whether the expelled shell already envelops the complete galaxy. The latter interpretation is supported by Adelberger et al. (2003) observation of a small scale anti-correlation between galaxies and Lyα absorption in QSO spectra (although as those authors quote, the statistical significance of this result is modest). If it can be demonstrated that the superwind shell had already escaped from the galaxy disk, then it may have enough energy to escape the gravitational potential to distribute its energy metals widely across the Universe.

To distinguishing between these scenarios, we must examine the spatial variation of the velocity offset between Hα and Lyα. Our data show no correlation between the emission wavelength of Lyα and the velocity variations clearly seen in Hα. This argues that the Lyα emission originates outside the individual components. If we were seeing the inner surface of a shell located well outside the galaxy we would expect a negligible velocity shear and indeed our observations place a limit on the shear of $\lesssim 100\,\mathrm{km\,s^{-1}}$.

We can also investigate how closely the morphology of the Lyα emission traces the star-forming regions of the galaxy. While the Lyα intensity map generally traces the I_{814}-band morphology, the diffuse extension labelled D in Fig. 6.1, has no counterpart in the I_{814}-band image. This component may be a dense knot in an outflowing shell and would be compatible with a model in which scattered Lyα photons are observed from the outflowing shell.

The data presented here support that idea that we are seeing wind material that has already escaped from the galaxy. It is interesting to compare the velocity offset in Lyα with the escape velocity of the galaxy. Using the dynamical mass estimate ($\sim 2\times10^{11}\,\mathrm{M_\odot}$) enclosed in a radius of $\sim$8 kpc we estimate escape velocity to be $\gtrsim 500\,\mathrm{km\,s^{-1}}$ (assuming a central concentration of $c = 7$ for $z = 2.4$); (Navarro, Frenk & White 1997). Whilst this escape velocity exceeds that of the outflowing material, the fate of the outflow will depend on its present location (or equivalently, its initial velocity). For example, if the outflow originated in the galaxy with an initial speed of $\sim 270\,\mathrm{km\,s^{-1}}$, then it will surely rain back

down on the galaxy. However, if, as we have argued, the shell is currently located outside the galaxy (i.e. $\gtrsim$10kpc), then the escape velocity will be a factor of $\sim$ 2 less, in which case the outflow will probably escape the gravitational potential and distribute the gas much more widely in the environment. We also note that the UV-bright starburst in N2 850.4 is still relatively young ($\sim$10 Myr; Smail et al., 2003a) and therefore this material may still be accelerating into the inter-galactic medium. Future observations of a larger sample of these galaxies (at various evolutionary stages) may yield further information about the origin of the outflows and the size of the regions which they affect around them.

Our observations suggest that the vigorous activity in N2-850.4 is arising due to an interaction between at least two distinct components. One of these contains warm, dense molecular gas and hosts an AGN, while the second appeard to be less massive, but still contains substantial amounts of cold gas. The resulting gravitational tides resulted in a starburst and (actively fuelled) AGN activity. This activity has produced a wind that maybe driving enriched gas out into the inter-galactic medium. Whilst these observations are based on a single galaxy, our results clearly show the power of combining optical and near-infrared observations to probe the power sources, masses and feedback processes in high redshift, far-infrared luminous selected galaxies. The next step is to generate a statistically useful sample to gauge the prevalence outflows from these massive galaxies which may explain the processes which shape the galaxy luminosity function and explain why only 10% of baryons cool to form stars.

Chapter 7

Near-Infrared Integral Field Spectroscopy of SCUBA Galaxies

We now expand this sample to include two more powerful, high redshift, far-infrared luminous galaxies. We primarily target the Hα emission line from these galaxies with the near-infrared UIST IFU on UKIRT (Swinbank et al. 2005c, MNRAS submitted).

Abstract

We present two-dimensional spectroscopy around the rest-frame optical emission lines of two luminous sub-millimetre selected galaxies at high redshift. Using the UIST near-infrared integral field spectrograph on UKIRT together with *Hubble Space Telescope* ACS and NICMOS imaging we map the dynamics and morphologies of N2 850.7 (z=1.488) and N2 1200.18 (z=2.592). Both sub-millimetre galaxies show multiple mergers in their spatially resolved spectra. N2 850.7 appears to consist of at least three dynamically distinct components with velocity offsets of up to $\sim$430 km s^{-1} and $\sim$13 kpc in projection, whilst N2 1200.18 comprises two components separated by 350$\pm$80 km s^{-1} and $\sim$7 kpc in projection. While the line widths and ratios of all of the components in N2 850.7 are consistent with star-formation, the [OIII]/Hα emission line flux ratio and spatial distribution of [OIII] in N2 1200.18 suggest one component of this system houses a high luminosity AGN. The multi-component mergers in these sub-millimetre galaxies are further evidence that these systems represent high redshift analogs of the most luminous ULIRGs in the local Universe. The measure line widths and velocity offsets are consistent with the velocity dispersions of local luminous ellipticals and therefore we suggest that these galaxies have deep potential wells in which these starburst galaxies are forming most of the stars which eventually make up the most massive local luminous ellipticals at the present day.

7.1 Introduction

Deep optical and near-infrared imaging with the superlative resolution of the NICMOS and ACS cameras onboard *HST* has made it possible to study the morphologies and colours of sub-mm selected (SCUBA) galaxies in unprecedented levels of detail (Smail et al., 2004; Pope et al., 2005). By combining this data with spectroscopically confirmed redshifts (Chapman et al., 2005), we are beginning to understand the processes which drive the immense bolometric luminosity output in these galaxies, allowing us to address issues such as their true contribution to the star-formation rate history of the Universe (e.g. Chapman et al., 2004b). Sub-mm galaxies are amongst the most bolometrically luminous galaxies in the universe (with a median redshift of $< z > \sim 2.4$ and $L_{bol} \gtrsim 10^{12}$–$10^{13} L_{\odot}$), however, in contrast to quasars at the same early epochs, their bolometric output appears to be dominated by star-formation rather than AGN activity (Alexander et al., 2005). It is clearly important to firmly establish the masses for these galaxies in order

to understand the rapid evolution of the sub-mm population, and so determine how they relate to present day galaxy populations and in particular test whether they represent the formation phase of the most massive elliptical galaxies at the present day, as many suspect.

To probe the structures of these complex systems requires a reliable separation of the spatial and spectral information. One particularly powerful approach to achieve this is using high resolution millimetric CO emission line maps to trace the distribution and kinematics of dense gas within these galaxies (Greve et al., 2005). Unfortunately, prior to the commissioning of the Atacana Large Millimetric Array (ALMA), this approach remains observationally demanding, requiring 30 hours per source with the (Institute for Radio and Millimeter Astronomy) IRAM interferometer, and can only be applied to the most massive and gas rich sub-mm galaxies. An alternative tool which is less demanding in terms of telescope time and can provide spatially resolved spectroscopy of sub-mm galaxies with sufficient spatial and velocity resolution to study their internal structures is near-infrared integral field spectroscopy (Swinbank et al., 2005b; Tecza et al., 2004). The spectroscopic maps so produced allow us to trace the dynamical and structural properties of sub-mm galaxies on scales of a few kpc, pin-point the location of sites of active star formation and identify non-thermal emission from active galactic nuclei (AGN) in components within these systems. However, they are also subject to potential biases due to extreme extinction within some regions of the sub-mm galaxies and from outflows in the emission line gas which is being observed.

In the previous chapter we used optical and near-infrared integral field spectroscopy to probe the dynamics and power-sources in a SCUBA galaxy at z=2.38. We now expand that sample by adding two more SCUBA galaxies at z=1.48 and z=2.59. Using the UIST Integral Field Unit (IFU) on UKIRT we have studied the rest-frame optical emission line properties of two SCUBA galaxies: SMM J163655.80 +405914.0 at z=2.5918 (N2 1200.18) and SMM J163639.01 +405635.9 at z=1.488 (N2 850.7). These observations, together with high resolution imaging from *HST* allow us to directly understand the rapid evolution of SCUBA galaxies, allowing us to test claims that far-infrared luminous galaxies comprise merging systems which are likely to be the progenitors of local massive ellipticals, or whether instead they are simply high-luminosity episodes in the history of more mundane galaxies. This chapter is laid out as follows: in § 7.2 we present the data reduction and results from the spectroscopic and imaging data. In § 7.3 and § 7.4 we present our analysis and conclusions respectively. We use a cosmology with $H_0 = 70\,\mathrm{km\,s^{-1}}$, $\Omega_M = 0.3$ and $\Omega_\Lambda = 0.7$ in which 1″ corresponds to 8.2 kpc at z=2.5 and 8.5 kpc at z=1.5.

7.2 Observations

The sub-mm galaxies N2 850.7 and N2 1200.18 were identified as bright sub-mm/mm sources in the surveys of the ELAIS-N2 field at 850μm by Scott et al. (2002) and at 1.2mm by Greve et al. (2004) respectively. Radio counterparts for both sources (Chapman et al., 2004b) provide precise positions which enabled spectroscopic redshifts to be measured for the sub-mm sources by Chapman et al. (2005) and Swinbank et al. (2004). N2 850.7, which has $S_{850\mu m}$=9.0±2.4mJy has a far-infrared bolometric luminosity of L_{FIR}=6.4±1.7×$10^{12}L_\odot$. The existing optical and near-infrared spectroscopy of this source suggests that the bolometric luminosity of this galaxy is dominated by a starburst, with low [NII]/Hα and CIV/Lyα emission line ratios (Chapman et al., 2005; Swinbank et al., 2004). Interferometric observations of the molecular CO emission in this system by Greve et al. (2005) failed to detect the CO(2-1) emission. If the gas reservoir within this galaxies is close to the systemic redshift indicated by the Hα emission, then this

non-detection implies an upper limit of $<1.8\times10^{10}M_{\odot}$ on the H_2 gas mass.

The near-infrared spectroscopy of N2 1200.18 indicates a redshift of 2.592 (Swinbank et al., 2004), and its 1.2mm flux of $S_{1200\mu m}=2.2\pm0.6\mu$Jy by Greve et al. (2004) suggests the far-infrared luminosity of N2 1200.18 is $L_{FIR}=10.9\pm3.0\times10^{12}L_{\odot}$. Both optical and near-infrared spectroscopy of N2 1200.18 suggests strong AGN activity, with high [NII]/Hα and CIV/Lyα emission line ratios as well as a broad-line underlying Hα emission ($2900\pm400\,km\,s^{-1}$) from a partially obscured AGN.

Deconvolving the exact contributions from the star-forming regions and AGN activity within these galaxies is difficult using just the rest-frame UV spectroscopy from Chapman et al. (2005). Ideally we need to use the well-developed spectral line indicators based on rest-frame optical emission lines (Veilleux and Osterbrock, 1987) which fall in the near-infrared for these high-redshift galaxies. Coupling the spatial coverage from an IFU with coverage around the rest-frame optical emission lines allows us to locate and isolate the components hosting the AGN in these systems, determine dynamical masses, as well as searching for extended halos and/or companions.

7.2.1 *HST* Optical and Near-Infrared Imaging

HST Advanced Camera for Surveys (ACS) observations of both targets were obtained from the *HST* public archive[1](Program ID #9761). The data consist of dithered exposures with the F814W filter, taken in LOWSKY conditions using the default four-point ACS-WFC-DITHER-BOX configuration. This pattern ensures optimal half-pixel sampling along both coordinates. The total integration time was 4.8 ks. We reduced the data using the latest version of the MULTIDRIZZLE software (Koekemoer et al., 2002) using the default parameters with PIXFRAC=1 and SCALE=1. The resulting image has 0.05″ pixels and is free from artifacts.

HST NICMOS observations of N2 850.7 were obtained in Cycle 12, and the target was observed using the NIC2 camera in the F160W filter for a total of 2.3 ks (Program ID #9856). We employed the standard four point spiral dither pattern, LOWSKY conditions and used the MULTIACCUM read-mode. Each exposure was corrected for a pedestal offset, and then mosaiced using the CALNICB task in IRAF. Unfortunately the observation was effected by the South Atlantic Anomaly (SAA), and extra processing steps were required[2]. The final images appear very flat and have very low cosmic ray contamination.

7.2.2 UIST Near-Infrared Integral Field Spectroscopy

Observations of N2 850.7 and N2 1200.18 were made in queue mode with the UKIRT Image-Spectrometer (UIST) IFU between 2004 July 13 and September 11 in <0.6″ seeing and photometric conditions[3]. We used the *HK* grism which has a spectral resolution of $\lambda/\Delta\lambda = 1000$ and covers a wavelength range of 1.4–2.4μm. Observations were carried out in the standard ABBA configuration in which we chopped away to sky by 12″ to achieve good sky subtraction. Individual exposures were 240s seconds and each observing block was 7.2 ks which was repeated three times, thus the total integration time for each object was 21.6 ks.

[1]Obtained from the Multimission Archive at the Space Telescope Science Institute (MAST). STScI is operated by the Association of Universities for Research in Astronomy, Inc., under NASA contract NAS5-26555. Support for MAST for non-*HST* data is provided by the NASA Office of Space Science via grant NAG5-7584 and by other grants and contracts.

[2]For a full description, see
http://www.stsci.edu/hst/nicmos/tools/post_SAA_tools.html

[3]The United Kingdom Infrared Telescope is operated by the Joint Astronomy Center on behalf on the UK Particle Physics and Astronomy Research Council.

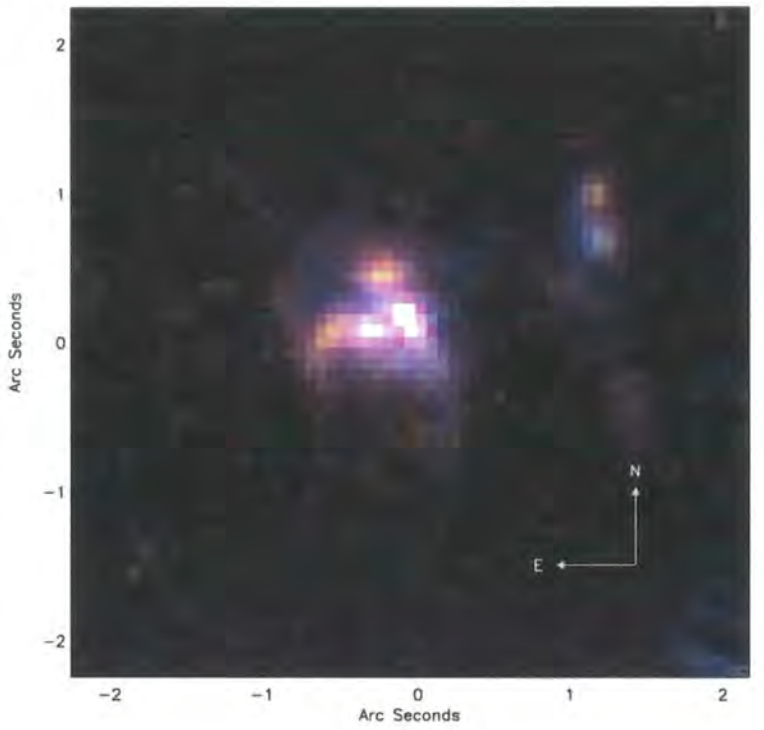

Figure 7.1: True colour $I_{814}H_{160}$ image of N2 850.7 from the *HST* ACS and NICMOS imaging. The image shows a complex morphology; the nucleus comprising at least two distinct components separated by $\sim 1''$ (~8 kpc) in projection. There is also a component to the North-West which may be associated with the same structure.

To reduce the data we used the relevant ORAC-DR pipeline (Cavanagh et al., 2003) which sky-subtracts, extracts, wavelength calibrates, flat-fields, and forms the datacube. To accurately align and mosaic the four datacubes we created white light (wavelength collapsed) images around the redshifted Hα emission line from each observing block and used the peak intensity to centroid the object in the IFU datacube. We then spatially aligned and co-added the four individual data-cubes to create the final mosaic.

7.3 Analysis

The *HST* imaging of both galaxies shows they have complex morphologies (Fig. 7.2 & Fig. 7.4), with companions or extended halos. N2 850.7 appears to consist of at least two high surface brightness regions with a low-surface brightness halo distributed asymmetrically around the system and another potentially related source lying approximately ~1.5″ to the West. While N2 1200.18 comprises a bright, nucleated component, with an extended lower surface brightness region to the north.

7.3.1 N2 850.7

We construct an Hα image of N2 850.7 by collapsing the datacube between 1.620 and 1.64μm. In Fig 7.2 we show the *HST* NICMOS image of N2 850.7 and align and overlay the Hα image from the IFU observations. The H-band continuum morphology is well matched by the Hα morphology, and we confirm that the component ~1.5″ (~14 kpc) to the North-West is associated with the same structure as N2 850.7 itself. The Hα morphology of the central galaxy is elongated both in the continuum and Hα image and

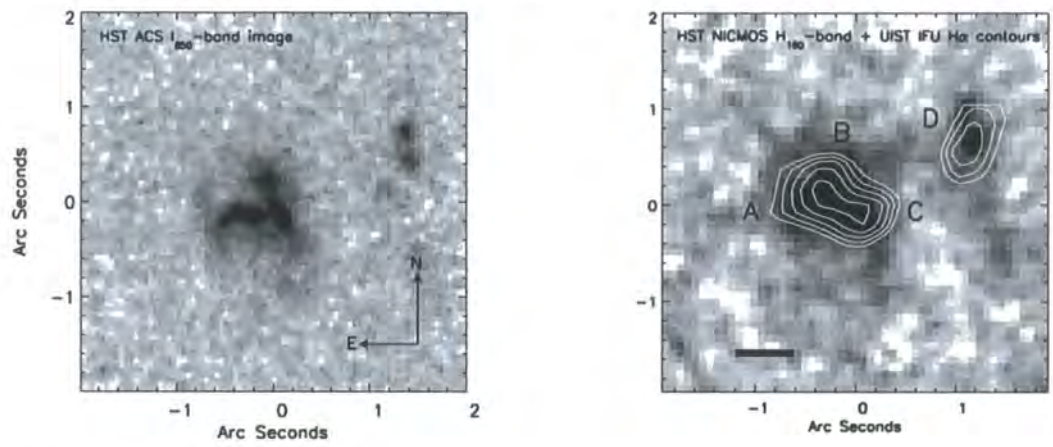

Figure 7.2: We show the *HST* ACS I_{850}-band and NICMOS H_{160}-band images of N2 850.7 in the left- and right-hand panels respectively. We overlay on the NICMOS image the Hα emission line intensity (produced by collapsing the datacube between 1.620 and 1.640μ). The ACS image is displayed in log scale to emphasize the multiple components within this system. The galaxy is morphologically complex, comprising at least three components, marked as A, C and D and possibly a fourth: B. The continuum colours of C are bluer than the other components The intensity of the Hα emission traces the H_{160}-band morphology. Each panel is 4 arcsec square (34 kpc at z=1.49) and has East left and North top. The solid bar represents 0.6″ seeing.

therefore to search for velocity structures, we extract a series of spectra from the regions around the densest components seen in the *HST* imaging from the IFU datacube. From each individual component, the signal-to-noise is only modest at best, nevertheless, we centroid the Hα emission lines and find a velocity offsets between components A and B of 215±80 km s^{-1} in projection. Furthermore the velocity offset between A and C is 135±100 km s^{-1}. The *HST* imaging and velocity offsets suggest that two galaxies are undergoing an interaction, although whether component C belongs the same structure as A or B will have to wait for higher resolution (adaptive optics) IFU observations (we note that the colours of A, B and C are very similar; Borys et al. 2005). The IFU observations also show that component D is redshifted by ∼430±150 km s^{-1} with respect to component A.

Using the Hα as a star-formation rate indicator, we derive Hα star-formation rates of 90±20, 70±20, 60±20 and 50±20M$_\odot yr^{-1}$ from components A, B, C and D respectively (Kennicutt 1998). In comparison, the star-formation rate implied from the far-infrared luminosity is 1100±300M$_\odot yr^{-1}$, implying ∼2 magnitudes of extinction (q.v. Smail et al., 2004). We reiterate that neither the emission line flux ratios from our IFU observations nor the rest-frame UV spectroscopy from Chapman et al. (2005) show signs of AGN signatures.

7.3.2 N2 1200.18

The *HST* I_{850}-band ACS image of this galaxy also appears complex with a bright knot and low-surface extension distributed to the North (Fig. 7.4). Since the IFU observations of N2 1200.18 cover Hβ,[OIII] and Hα, we construct white light images around the [OIII]λ5007 and Hα emission lines and overlay these on the K-band image in Fig. 7.4. The strongest [OIII]λ5007 appears to come from an unresolved (point) source in the center of the bright I_{850}-band continuum component. In contrast the Hα is much more extended and has

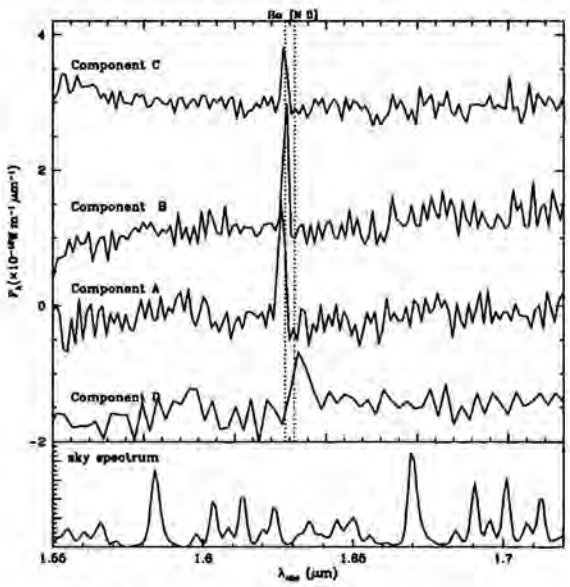

Figure 7.3: Spectra covering the redshifted Hα emission in the four components of N2 850.7 from the UIST IFU observations. The spectra have been offset in flux scale for clarity, and the spectrum for Component D has been binned by a factor of four in the spectral direction to improve the contrast of the emission line. The dotted lines show the expected position of the H$\alpha\lambda$6562.8 and [NII]λ6583 emission lines for a redshift of z=1.488. The lower panel shows a sky spectrum. By centroiding the emission lines, we find velocity offsets between components A & B and A & C of $215 \pm 80\,\mathrm{km\,s^{-1}}$ and $135 \pm 90\,\mathrm{km\,s^{-1}}$ in projection respectively, whilst component D is redshifted by $\sim +430\,\mathrm{km\,s^{-1}}$ from A

TABLE 1.
EMISSION LINE PROPERTIES OF THE TWO COMPONENTS IN N2 1200.18

Component	z	Hα/Hβ	[OIII]/Hα	N[II]/Hα	FWHM(Hα) ($\mathrm{km\,s^{-1}}$)	FWHM([OIII]) ($\mathrm{km\,s^{-1}}$)
North	2.588[1]	-	0.4±0.2	0.6±0.1	375±120	400±200
Nucleus	2.592[1]	6±2	2.0±0.5	0.7±0.1	880±200	630±180

Table 7.1: Notes: The value given in the [] z column is the error in the last decimal place.

features which match the extended northern component seen in the I_{850}-band image. This suggests that the compact continuum source may host an AGN and indeed,both the strong, spatially unresolved [OIII] and high [OIII]/Hα and [NII]/Hα emission line ratios indicate AGN activity in this component.

Using the velocity derived from the narrow-line Hα emission, we find that the central component appears redshifted from the northern component with a velocity offset of $250\pm75\,\mathrm{km\,s^{-1}}$ across $0.8''$ ($\sim$7 kpc) in projection.

We can use the emission line flux ratios of [OIII]/Hβ and [NII]/Hα to classify the two components seen in the UIST IFU data (Baldwin et al., 1981). The northern component has an [NII]/Hα emission line flux ratio of 0.6±0.1 and [OIII]/Hβ emission line flux ratio of 0.5±0.2, together these place this component in the LINER region of the diagnostic diagrams of Baldwin et al. (1981). The high [OIII]/Hα and high [NII]/Hα emission line flux ratio from the unresolved component indicate a Seyfert type 2 AGN (Fig. 7.6).

Using deep *Chandra* observations of the ELAIS N2 field it is possible to compare the X-ray and spectral properties of N2 1200.18. This galaxy is detected in the hard

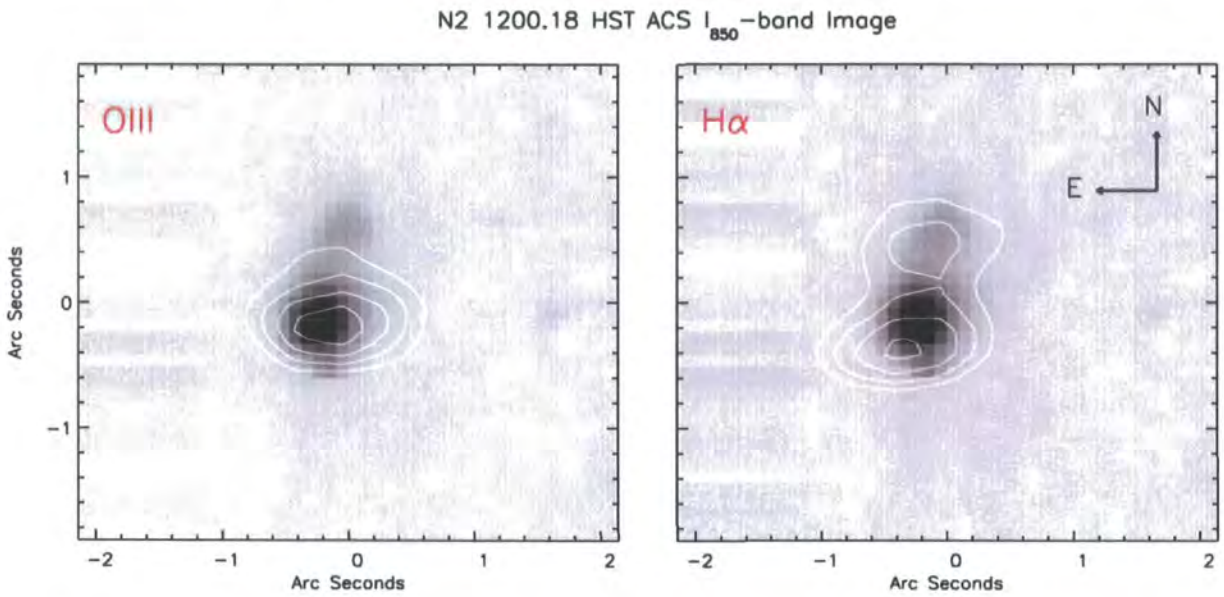

Figure 7.4: *HST* I_{850}-band image of N2 1200.18 with the [OIII]λ5007 and Hα emission line intensity maps from the UIST IFU observations overlaid as contours. The *HST* image shows a complex morphology, with a bright, dense component and a lower-surface brightness component to the North. The [OIII]λ5007 and Hα also have different morphologies, with the strong [OIII]λ5007 probably arising from (unresolved) AGN activity, whilst the Hα morphology appears resolved and probably arises in part from star-formation activity in dense knots outside the nucleus. (The *HST* image is displayed in *log* scale to emphasis the morphology)

(2-8 keV) X-ray image with a flux of $14.72\pm2.12\times10^{-15}\,\mathrm{erg\,s^{-1}\,cm^{-2}}$ (Manners et al., 2003). We convert the observed 2-8keV flux to a rest frame 2-10keV luminosity using $L_x = 4\pi d_L^2 f_x (1+z)^{\Gamma-2}$ which takes into account the k-correction (Alexander et al., 2003b) assuming a spectral index Γ=2. We derive L_x=9.1$\pm$1.3$\times10^{44}$erg. Under the assumption that the [OIII] emission line and the hard X-ray fluxes are isotropic, they can be used to investigate the intrinsic power of Seyfert galaxies (Mulchaey et al., 1994; Alonso-Herrero et al., 1997). N2 1200.18 sits comfortably in the scatter of the $L_{[OIII]}$-L_X plot for local Seyferts from Mulchaey et al. (1994), although it lies at the high luminosity end, suggesting N2 1200.18 is a high luminosity Seyfert 2 type AGN, and also suggesting that increase AGN activity results in increased photo-ionisation of the surrounding material.

7.4 Discussion

One of the outstanding issues regarding the distant far-infrared luminous galaxy population is to understanding their rapid evolution. The first step in this study is to understand what process causes the immense star-formation activity in SCUBA galaxies: is it associated with merger activity (as in comparably luminous galaxies in the local Universe; Veilleux et al. 1999) or is there another mechanism which is responsible for triggering this activity.

One powerful route to relate the apparently disparate high-redshift galaxy populations is to spatially resolve the dynamics and compare the kinematic and structural information from rest-frame optical rotation curves/line-widths. Rest-frame optical spectroscopy therefore provides crucial diagnostics of the physical mechanism generating their huge

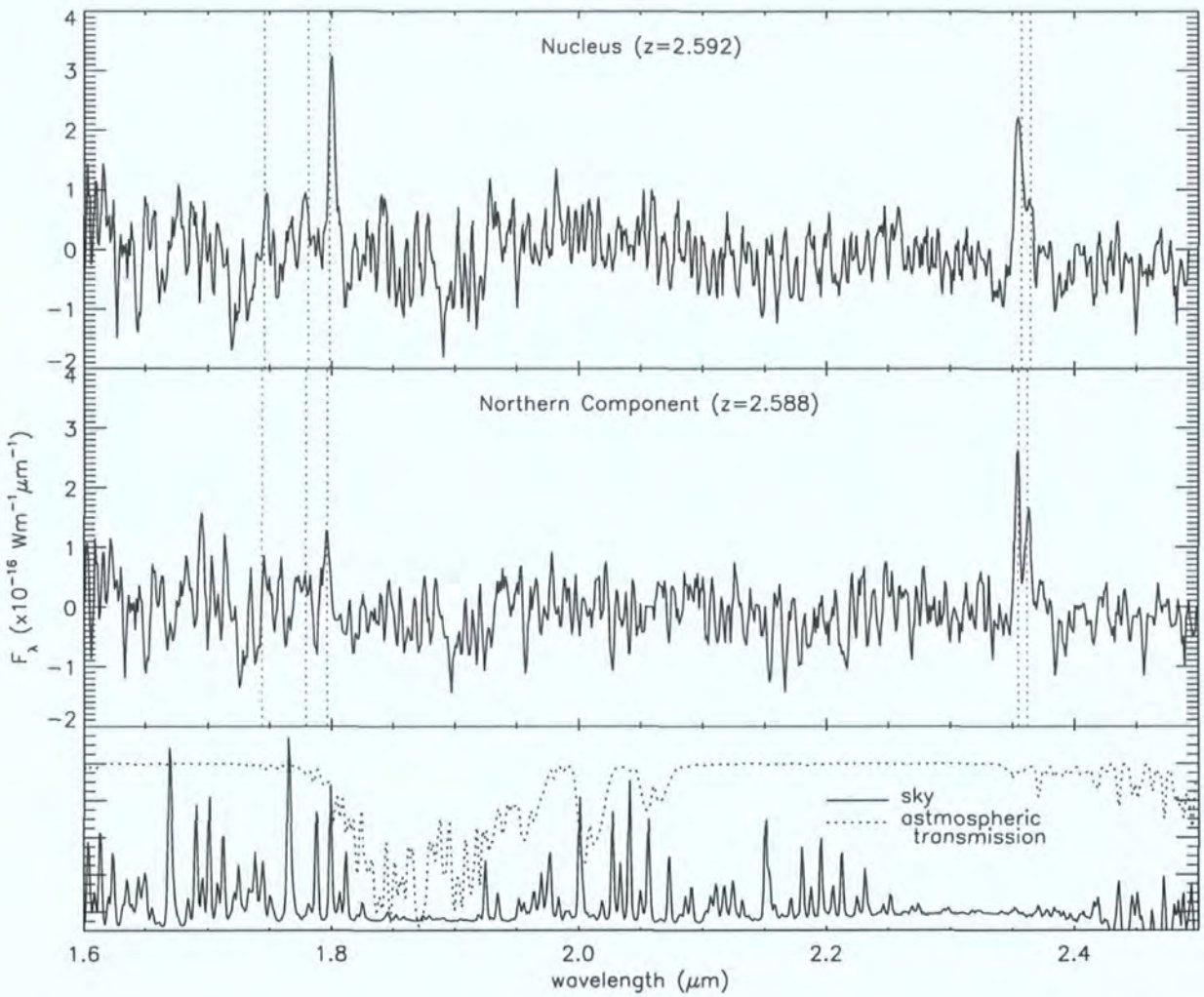

Figure 7.5: *Top:* Spectrum from the central component of N2 1200.18 around the [OIII] and Hα emission lines from the UIST IFU observations. This spectrum has an [OIII]λ5007/Hα emission line flux ratio of 2.0±0.5 which, combined with the unresolved [OIII] emission in Fig. 7.4 suggests AGN activity. The dotted lines show the positions of the H$\beta\lambda$4861, [OIII]λ4949,5007, H$\alpha\lambda$6562.8 and [NII]λ6583 emission lines for a redshift of z=2.592. *Middle:* Spectrum of the northern component of N2 1200.18. The dotted lines show the positions of the expected Hβ, [OIII], Hα and [NII] emission lines (as above) for a redshift of 2.588, giving a velocity offset of $\sim$350 km s^{-1} between the two components. This northern component has star-burst (rather than AGN) characteristics, with a small [OIII]/Hα and [NII]/Hα emission line flux ratios. *Bottom:* The sky OH airglow emission (continuous line), as well as the Mauna Kea atmospheric transmission (dotted line).

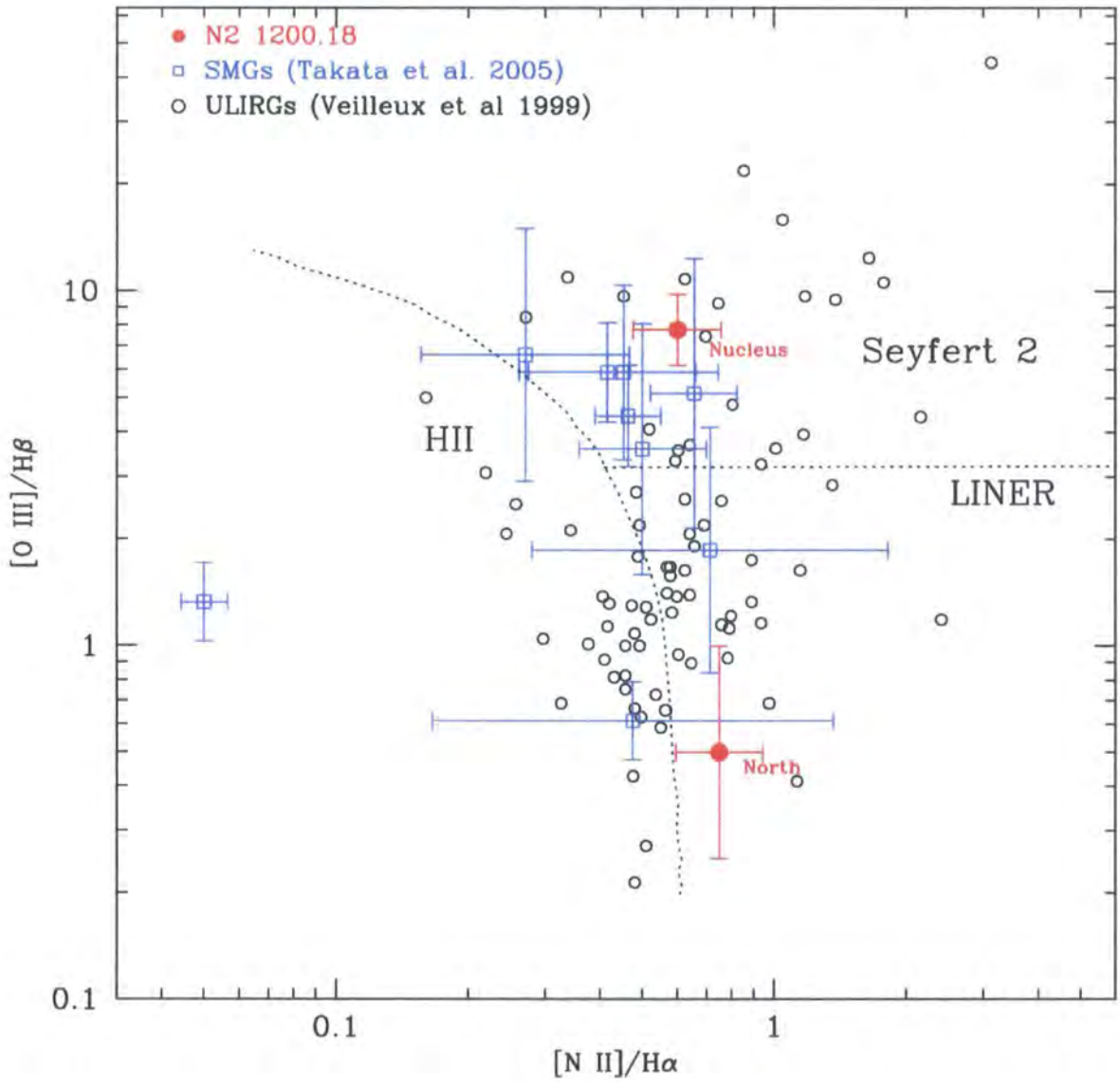

Figure 7.6: Emission line flux ratios of the two components in N2 1800.18. The nucleus has characteristics of AGN activity, whilst the northern component has [NII]/Hα and [OIII]/Hβ emission line flux ratios of a LINER (Baldwin et al. 1988).

luminosity through emission line widths and ratios.

Using the near-infrared IFU on UIST/UKIRT we have studied the Hα and [OIII], Hβ and Hα emission line properties from two SCUBA galaxies at z=1.48 and z=2.59.

From *HST* imaging and IFU observations, the central regions of N2 850.7 comprise at least three components, separated by up to 215±80 km s^{-1} and 1″ (8.5 kpc) in projection, although the associations of each structure with each other is difficult to determine due to the small angular size of the galaxy. However, the complex morphology of this galaxy from high resolution *HST* imaging suggests that these velocity offsets arise due to merger activity (rather than a simple disk kinematics). A fourth component component is tentatively detected redshifted by ~430 km s^{-1} and ~1.5″ (~14 kpc) in projection away from the galaxy, indicating that this system may be a multi-component, massive merger. Assuming the velocity offsets arise from merging components in a deep potential well, we determine a merging mass of $\sim 7 \times 10^9 M_\odot$ withing 8 kpc and $\sim 3 \times 10^{10} M_\odot$ within ~16 kpc. The integrated star-formation rate, estimated from the Hα emission is $\sim 310 M_\odot yr^{-1}$, whilst the star-formation rate estimated from the far-infrared luminosity is $960 \pm 150 M_\odot yr^{-1}$, indicating aproximately 1.2 magnitudes of dust extinction (q.v. Smail et al., 2004).

Interferometric CO(2-1) observations around components *A* & *B* of this galaxy from Greve et al. (2005) have placed a limit on the H_2 mass of $<1.8 \times 10^{10} M_\odot$, indicating a baryonic to non-baryonic mass fraction in the central regions of <0.36.

Turning to N2 1800.18, the unresolved [OIII] emission and high [OIII]/Hα emission line ratio from the nucleus indicate AGN- activity, however, to the north, the extended Hα emission suggest star-formation activity. The northern component has emission line flux ratios which resembles a LINER. The velocity offsets between these two components is 350±80 km s^{-1} across 7 kpc in projection.

7.4.1 Multi-Component Mergers and the Comparison Between Local ULIRGs

Although intrinsically luminous, obtaining high quality integral field spectroscopy of sub-mm galaxies is expensive, usually requiring four to eight hours per source. Including the galaxies published here, we now have a sample of only four systems with resolved spectroscopy. The first, SMM J163650+4057 (aka. N2 850.4 Smail et al. 2003a; Swinbank et al. 2005b) appears to be a multi-component merger, comprising at least three dynamically distinct components separated by up to 250 km s^{-1} and 8.2 kpc in projection. This galaxy has a Hα halo which is asymmetrically distributed around the galaxy. Secondly, SMM J14011+0252 (aka. J1/J2 Tecza et al. 2004; Swinbank et al. 2004) is a bright sub-mm source behind the lensing cluster Abell 1835. The exact nature of this sub-mm galaxy has been contentious, although Smail et al. (2005) recently derived an amplification for this galaxy of μ ~3-5 which arises due to a super-position of the cluster potential and a dwarf, early type member of the galaxy cluster. Having removed the foreground galaxy (J1c; Smail et al. 2005) from their analysis, J1/J2 appears to comprise two dynamically distinct components separated by ~300 km s^{-1} and 20 kpc in projection.

Although there are only four galaxies with spatially resolved spectroscopy, two of these appear to be multiple component in nature (N2 850.4 and N2 850.7), the other two comprising binary galaxy interactions (N2 1200.18 and J1/J2). Overall, observations of high-redshift SCUBA galaxies share many of the characteristics of similar (but somewhat less luminous) far-infrared galaxies (ULIRGs) in the local Universe; this includes Hα equivalent widths, proportion of obvious AGN and typical spectral classification. In comparison to local ULIRGs (which are less bolometrically luminous galaxies), 85% of the most luminous ULIRGs are those which are composed of two or more interacting

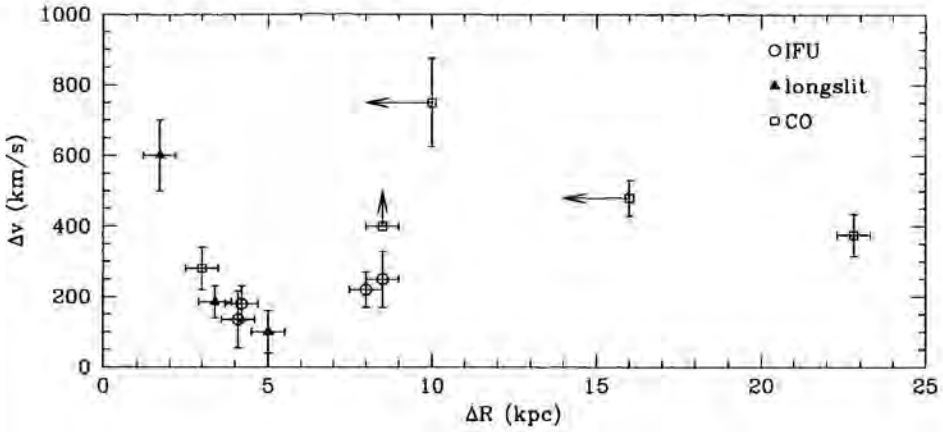

Figure 7.7: Spatial and Velocity offsets between multi-component SMGs from longslit and IFU spectroscopy and resolved PdB (CO) interferometry.

systems (Bushouse et al., 2002), and therefore our observations provide complementary evidence that the multi-component nature of local ULIRGs is mirrored in high redshift SCUBA galaxies.

7.4.2 Velocity Offsets and Potential Well Depths

Combined with the low numbers of galaxies involved and their large contribution to the far-infrared background, these high redshift SCUBA galaxies have been interpreted as the formation phase of the most massive stellar systems in the local Universe. In contrast to the optical UV background, which arises from a large density of low luminosity galaxies, the sub-mm background arises from a population of much more luminous galaxies with implied star formation rates of $\gtrsim 1000 M_{\odot} yr^{-1}$.

The typical velocity offsets between components from the IFU observations is $\sim 270\,km\,s^{-1}$ (this rises to $310 \pm 80\,km\,s^{-1}$ if we include the velocity offsets between components as observed through resolved CO spectroscopy and longslit spectroscopy from Greve et al. 2005, Tacconi et al. 2005 and Swinbank et al. 2004). In order to plausibly develop into giant ellipticals at the present day, these galaxies must reside in halos with average line widths of $\sim$300-400 $km\,s^{-1}$ (Tacconi et al., 2002). Thus, if these measured velocity offsets are those of merging galaxies then they may eventually develop into velocity dispersions in elliptical galaxies. We caution, however that there are uncertainties in turning a measured velocity offset between merging systems into a velocity dispersion since a significant amount of energy will be lost during the interaction (e.g. due to dynamical friction). The amount of energy dissipated will depend on several things, including the geometry of the interaction (or the inclination of the encounter), the mass ratio of the two progenitors and the velocity of the encounter (e.g. Bournaud et al., 2005). However, even if half of the energy is lost during the interaction, the final velocity dispersions only will be a factor of $\sim\sqrt{2}$ lower. Nevertheless, given the large velocity offsets we measure (and the likely hood that these galaxies will undergo further merger activity) the resulting galaxies are likely to have velocity dispersions close to that required for giant ellipticals at the present day.

In Table 7.4.2 we list the velocity and spatial offsets (and illustrate this is Fig. 7.7 between known multi-component sub-mm galaxies from IFU and slit spectroscopy as well as resolved CO maps of SMGs.

TABLE 1.
Known SMGs with velocity offsets between two or more components

Name	Emission Line	dv ($\mathrm{km\,s^{-1}}$)	dR (kpc)	ref
N2 850.7	Hα(6562.8)	-180±80	5.1	[1]
N2 850.7	Hα(6562.8)	+135±80	4.1	[1]
N2 850.7	Hα(6562.8)	+430±150	11.5	[1]
N2 1200.18	Hα(6562.8)	250±80	8.5	[1]
N2 850.4	Hα(6562.8)	220±50	8.0	[2]
N2 850.4	Hα(6562.8)	50±50	8.0	[2]
J1/J2	Hα(6562.8)	180±50	4.2	[2,4]
SMMJ 12363+6214	Hα(6562.8)	100±60	5.0	[2]
SMMJ 12370+6214	Hα(6562.8)	600±100	1.7	[2]
SMMJ 12371+6213	Hα(6562.8)	400±50	70	[2]
RGJ 131236+4240	Hα(6562.8)	185±45	3.4	[2]
SMM J02396-0134	CO(2-1)	375±60	22.8	[5]
SMM J02399-0136	CO(3-2)	750±125	<10	[5,6,9]
SMM J04431+0210	CO(3-2)	≳400	8.5	[5,8]
SMM J16359+6612	CO(3-2)	220±60	3	[5,7]
SMMJ 16366+4105	CO(3-2)	480±50	<16	[5]

Table 7.2: [1] This work; [2] Swinbank et al. (2004); [3] Swinbank et al. (2005); [4] Tecza et al. (2004); [5] Greve et al. (2005); [6] Frayer et al. (1998); [7] Kneib et al. (2004); [8] Neri et al. (2003); [9] Genzel et al. (2003)

7.5 Conclusions

In this chapter we have studied the rest-frame optical emission line structures and dynamics of two powerful SCUBA galaxies at z=1.488 and z=2.592. In one of the SCUBA galaxies we find evidence for a multi-component merger, with velocity offsets of upto $\sim$430 $\mathrm{km\,s^{-1}}$ and $\sim$13 kpc in projection. Of the four SCUBA galaxies which now have resolved spectroscopy (N2 850.4, N2 850.7, N2 1200.18 and J1/J2) two appear to be multi-component in nature and therefore these systems may be analogous to the multi-component nature of (less bolometrically luminous) ULIRGs in the local Universe. The second galaxy in this sample also appears morphologically complex with two components separated by 250±80 $\mathrm{km\,s^{-1}}$ and 0.8″ (7 kpc) in projection. The rest-frame optical emission line ratios and strong X-ray detection suggests that the nucleus houses a high luminosity type 2 Seyfert AGN. Combined with previously published IFU observations of SCUBA galaxies, we find merging masses of 1–2×$10^{11}\mathrm{M}_{\odot}$, which is similar to that found using Hα line widths (Swinbank et al., 2004) and resolved CO spectroscopy (Greve et al. 2005, Tacconi et al. 2005). Furthermore, recent fundamental plane surveys suggest that most of the stars in the most massive ellipticals (i.e., those with velocity dispersions between 250 and 400 $\mathrm{km\,s^{-1}}$) were in place 4±1 Gyr after the Big Bang (Nelan et al. 2005, ApJ in press). Thus, if these galaxies represent a 'maximum starburst' phase (in which most of the available cold gas is consumed in a starburst on timescales of 6-15 Myr; Tacconi et al. 2005), we may be seeing the formation of the majority of the stars now seen in local, massive ellipticals.

Overall, our observations further the evidence that SCUBA galaxies represent merging/interacting systems with high instantaneous star formation rates and actively fuelled AGN. The multiple component nature in these galaxies indicates they may be analogous (but scaled up) versions of local ULIRGs. Furthermore, the velocity offsets and line widths from the resolved components in these galaxies are consistent with those seen

in local luminous ellipticals, furthering support that these galaxies represent their most active formation phase.

Chapter 8

Near-Infrared Integral Field Spectroscopy of Two Powerful Radio Galaxies at z∼2.4

Motivation

We have demonstrated the feasibility of using integral field spectroscopy to probe the dynamical and power sources of powerful, high redshift galaxies. In this chapter, we further expand this sample to investigate the dynamical structures of two powerful radio galaxies at $z \sim 2.4$. Some authors have suggested that radio galaxies undergo a SCUBA phase at early times and therefore by investigating the dynamics it may be possible to provide links between the two populations. Moreover, the AGN and starburst characteristics displayed in radio galaxies provides us with an important laboratory in which we can study how feedback mechanisms regulate galaxy formation and enrich the IGM.

Abstract

In this chapter we present the two-dimensional dynamics of two powerful radio galaxies at z=2.23 and z=2.52. We use the [OIII]λ5007 emission line to constrain the dynamics of these systems and find that the direction of the strongest velocity gradients are in the same direction as the radio lobes, suggesting that the feedback mechanisms in these galaxies are dominated by the AGN activity. Furthermore, by comparing the [OIII]λ5007 emission line profile with high resolution Lyα spectroscopy we investigate models in which high column density absorbing halos are thought to play an important role in resonantly scattering and asymmetrically shaping the Lyα emission from these active galaxies.

8.1 Introduction

Powerful Radio Galaxies are some of the most distant luminous galaxies known. Since these galaxies can be seen to large redshifts, and they are spatially extended, they are useful probes of the early Universe and important laboratories for testing models for galaxy formation. One of the most remarkable properties of high redshift radio galaxies (HzRGs) is the initially unexpected alignment between the UV/optical emission morphology and the radio structures (McCarthy et al., 1987; Chambers et al., 1987), and the presence of gaint (≳100 kpc) ionised gas halos which emit powerful Lyα emission.

In Chapter 6 we investigated the feedback processes which arise in a powerful starburst SCUBA galaxy. However, it is generally accepted that both star formation and accretion onto black holes have a role in feedback in massive galaxies (e.g. Silk & Rees 1998). As we

have seen, this feedback mechanism is thought to regulate galaxy formation, preventing 'over-cooling' of gas into stars (e.g. Balogh et al., 2001). HzRGs harbour powerful radio jets and provide an important laboratory for studying feedback processes (Rawlings and Jarvis, 2004). First, the radio source activity appears to be common during the formation phase in most (massive) high redshift galaxies. Second, the outflows which are induced by the powerful radio source heat the gas that ultimately forms the intra-cluster medium, and therefore we may be seeing an important phase in the formation and metal enrichment of galaxy clusters. Finally, the radio properties reflect the processes which first triggered the AGN, and therefore it is possible to test models in which star-formation and black-hole growth are an intimately linked.

Until recently, most work has concentrated on the rest-frame UV emission lines from HzRGs. In particular, high resolution spectra of the Lyα emission lines from young radio galaxies suggests that the gas in the halo is kinematically active ($v \gtrsim 1000\,\mathrm{km\,s^{-1}}$) with much more quiescent absorbing halos (or shells) seen against the Lyα emission (van Ojik et al. 1997; Jarvis et al. 2003; Wilman et al. 2004). These shells are thought to be very smooth and ubiquitous in young HzRGs, with HI column densities of the order 10^{18}–$10^{19.5}\mathrm{cm}^{-2}$, however, a short time after the radio source has been triggered, outflows introduce metals into these shells as the radio source propagates through these low density environments, causing them to become metal enriched. These galaxies typically have moderately large star-formation rates (upto several tens or even hundreds of solar mass per year; Archibald et al. (2001)), which in turn suggests that they may house starburst driven superwinds. The key question, however, is to test which mechanism dominates the feedback processes. If the dominant feedback mechanism arises as a result of AGN activity, then we would expect the outflow to be collimated along the same axis as the radio jet, whereas in the case of a starburst, the direction of the outflow and the radio jet will not necessarily be linked. However, attempts to measure the velocity structure of HzRGs using traditional longslit spectroscopy have only had limited success since the two dimensional dynamics are required to reliably decouple the spatial and dynamical information in these complex structures.

In this chapter we show the power of using IFS to probe the two-dimensional velocity structure of two powerful radio galaxies. In § 8.2 we describe the observations and data-reduction, in § 8.3 we present our results and analysis and in § 8.4 we present the discussion and conclusions. We use a cosmology with $H_0 = 70\,\mathrm{km\,s^{-1}}$, $\Omega_M = 0.3$ and $\Omega_\Lambda = 0.7$.

8.2 Observations and Analysis

TX0200+015 (z=2.23, RA: 02:02:42.99, Dec: +01:49:10.3) and TX0828+193 (z=2.52, RA: 08:30:35.48, Dec: +19.13:15.5 (J2000)) were catalogued as bright radio emitting galaxies by Carilli et al. (1997). Spectroscopic redshifts have been measured using both optical and near-infrared spectroscopy for both sources (van Ojik et al., 1997; Evans, 1998; Iwamuro et al., 2003). Both galaxies have been studied in detail by van Ojik et al. (1997) and Wilman et al. (2004) using high-resolution spectroscopy around the Lyα emission line, and both show complex asymmetric line profiles which are attributed to foreground neutral material.

8.2.1 Optical and Near-Infrared Imaging

HST WFPC2 observations of TX0828+193 were obtained from the *HST* public archive[1]. The data consist of dithered exposures with the F675W filter, and total integration time of 1.0 ks. We reduced the data using the standard STSDAS packages in IRAF. The resulting

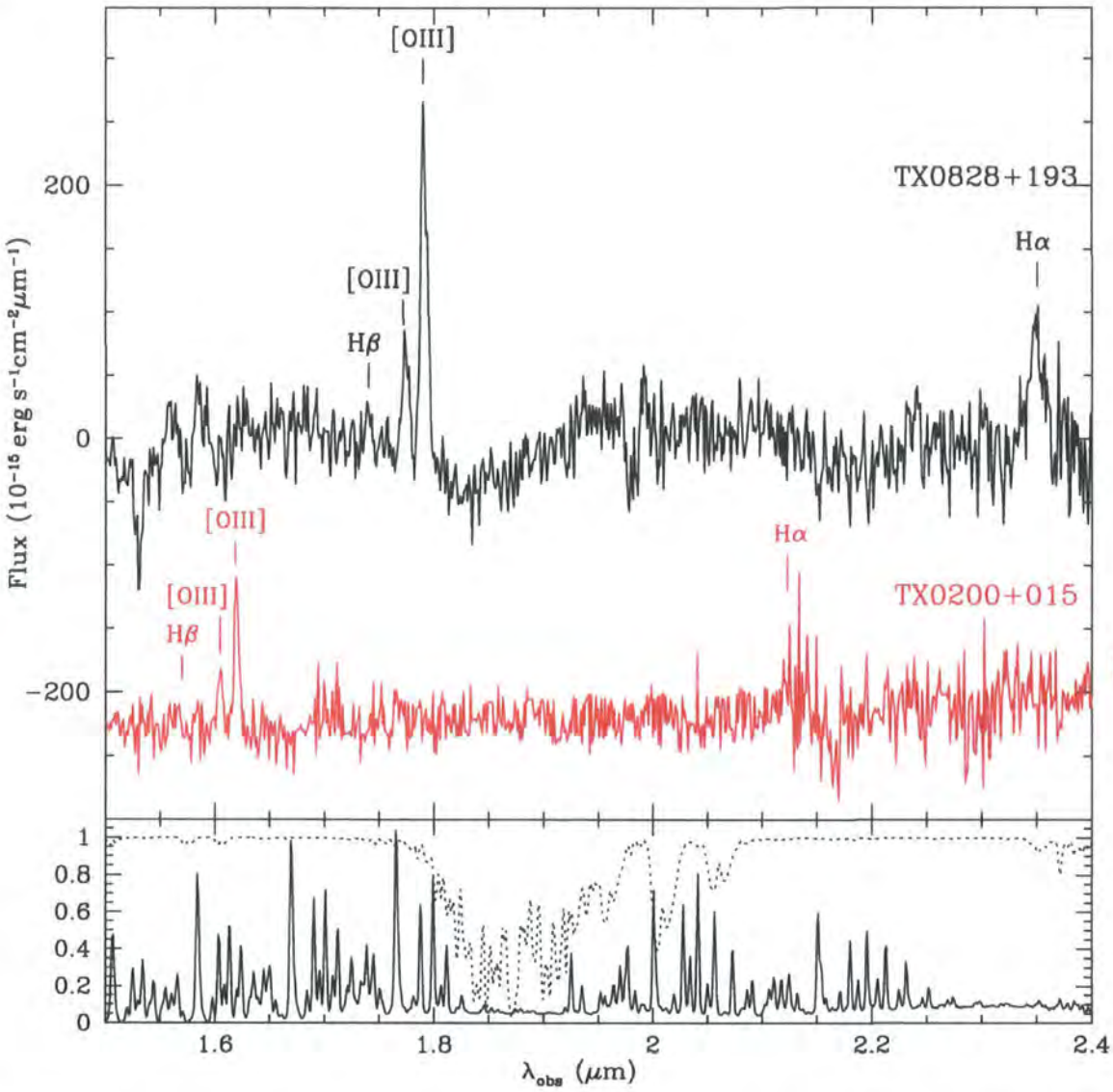

Figure 8.1: Collapsed spectra of both radio galaxies in our sample from the UIST IFU observations. TX0200+015 is offset in flux scale for clarity. We mark the positions of the strongest emission features. We also show a (scaled) sky spectrum (bottom pannel), as well as the Mauna Kea atmospheric transmission (dashed line).

image has 0.0996″ pixels and is free from artifacts.

Near-infrared imaging of TX0200+015 was kindly provided by Dr. Kentaro Motohara. The data consists of a K′ image of the field taken with the ISAAC imaging spectrograph on the VLT for a total of 540 seconds.

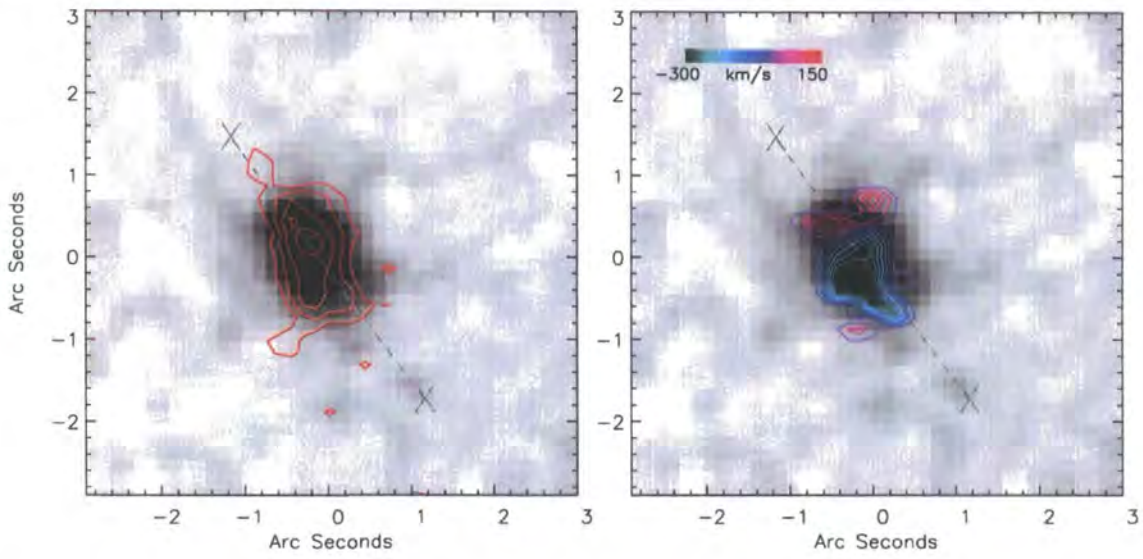

Figure 8.2: *Left:* The ISAAC K′ image of TX0200+015 (z=2.23) with the [OIII]λ5007 emission line intensity overlaid as contours. *Right:* The ISAAC K′ image of TX0200+015 with the velocity field derived from the [OIII]λ5007 emission line overlaid. The dashed line shows the orientation of the radio lobes and the crosses mark their location (Carilli et al., 1997). It is clear that the velocity field follows the direction of the radio jet

8.2.2 Spectroscopic Imaging

UIST Near-Infrared Integral Field Spectroscopy

Observations of the two radio galaxies were made with the UIST IFU on UKIRT between 2003 October 25 and 28 in <0.7″ seeing and photometric conditions[2]. We used the *HK* grism which has a spectral resolution of $\lambda/\Delta\lambda \sim 1000$ and covers a wavelength range of 1.4–2.4μm. Observations were carried out in the standard ABBA configuration in which we chopped away to sky by 12″ to achieve good sky subtraction. Individual exposures were 240 seconds and each observing block was 7.2 ks which was repeated three times, thus the total integration times (for each source) was then 21.6 ks.

To reduce the data we used the relevant ORAC-DR pipeline (Cavanagh et al., 2003) which sky-subtracts, extracts, flat-fields, wavelength and flux calibrates the data and forms the datacube. To accurately align and mosaic the four datacubes we created white light (wavelength collapsed) images around the redshifted [OIII] emission line from each observing block and used the peak intensity in [OIII] to centroid the object in the IFU datacube. We then spatially aligned and co-added the four individual data-cubes (weighted by [OIII] signal-to-noise). We show the reduced, collapsed spectra from both targets in Fig. 8.1 and mark the positions of the strongest emission features. We also plot the sky spectrum (scaled) as well as the atmospheric transmission.

To search for velocity structure in TX0828+193 we attempt to identify the [OIII]λλ4959,5007 emission lines (with a fixed seperation and a fixed intensity ratio of $\frac{I_{\lambda 5007}}{\lambda 4959} = 3$) on a pixel-by-pixel basis by averaging over 0.48″×0.48″ pixels, increasing to 0.6″×0.72″ if no emission

[1]Obtained from the Multimission Archive at the Space Telescope Science Institute (MAST). STScI is operated by the Association of Universities for Research in Astronomy, Inc., under NASA contract NAS5-26555. Support for MAST for non-HST data is provided by the NASA Office of Space Science via grant NAG5-7584 and by other grants and contracts.

[2]The United Kingdom Infrared Telescope is operated by the Joint Astronomy Center on behalf on the UK Particle Physics and Astronomy Research Council.

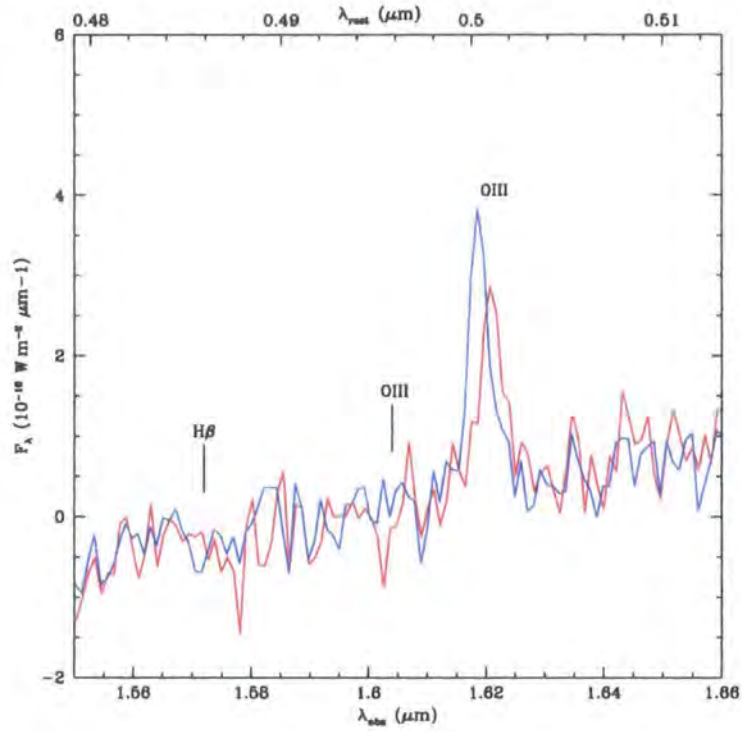

Figure 8.3: Extracted one dimensional spectra from the red and blue-shifted [OIII] emission line from TX0200+105. The spectra clearly show the velocity offsets between the red and blue-shifted parts of the galaxy

line could initially be identified. At $z = 2.23$ and $z = 2.52$, [OIII] emission falls at 1.62μm and 1.74μm, which is away from any strong OH emission or absorption. Due to the modest signal-to-noise in TX0200+015 we only attempt to identify the [OIII]λ5007 emission line. We use a series of reduced sky frames to check the wavelength calibration by fitting a nearby sky line with a Gaussian profile. The errors in the velocity field are calculated by building two independent data-cubes, each of 10.8 ks and recomputing the velocity field in an identical manner to that described above. Using the same fitting techniques as above we estimate that the average velocity error to be $\simeq 40\,\mathrm{km\,s^{-1}}$.

8.3 Analysis

8.3.1 TX0200+015

Like most HzRGs above $z \sim 0.6$, TX0200+015 has its radio and optical axis aligned along the same direction. The [OIII]λ5007 emission is double peaked along the same long axis (Fig. 8.2). The radio lobes of this galaxy extend $\sim$1.5″ ($\sim$10 kpc) from the centre of the galaxy. The velocity field of the [OIII]λ5007 emission appears to comprise of at least two components separated by $450 \pm 50\,\mathrm{km\,s^{-1}}$ and $\sim$2″($\sim$16 kpc) in projection (Fig. 8.2).

High resolution (R=35,000) Lyα spectroscopy was taken from two independent components of this galaxy (Wilman et al., 2004). These observations consist of a spectrum from the centre of the galaxy, and from a region offset 1″ to the North (Fig. 8.4). Both of the spectra show complex line profiles which Wilman et al. (2004) attribute to high column density neutral gas.

We transform both the high resolution Lyα spectra and the [OIII]λ5007 emission line

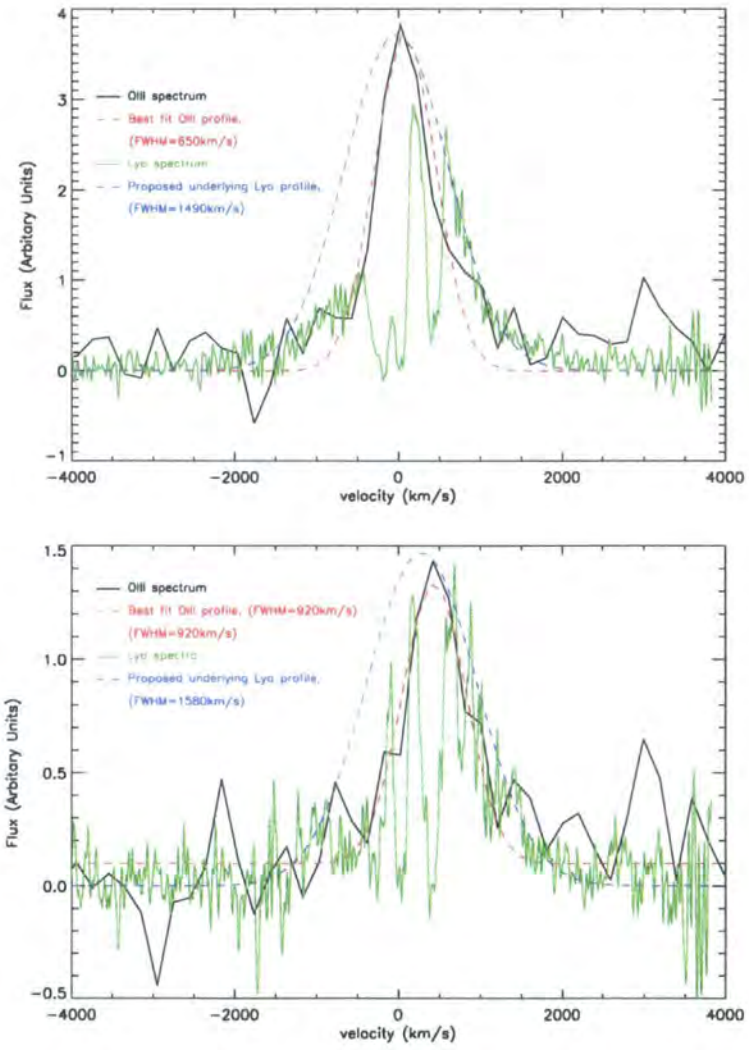

Figure 8.4: Comparison of the two emission line regions in [OIII]λ5007 and Lyα emission in TX0200+015. *Top:* The Lyα and [OIII] emission lines from the central 2.5 arcsec of the galaxy with the proposed underlying Lyα profile from Wilman et al. (2004) also overlaid. *Bottom:* A comparison of the Lyα and [OIII]λ5007 emission from the redshifted component of the galaxy (offset by 1.25-2.5 arcsec to the North-West). Both panels show that the model for the underlying Lyα emission is much broader than the [OIII]λ5007 emission. All line widths are deconvolved for instrumental resolution. (Lyα emission line observations and models were kindly provided by Dr. Richard Wilman)

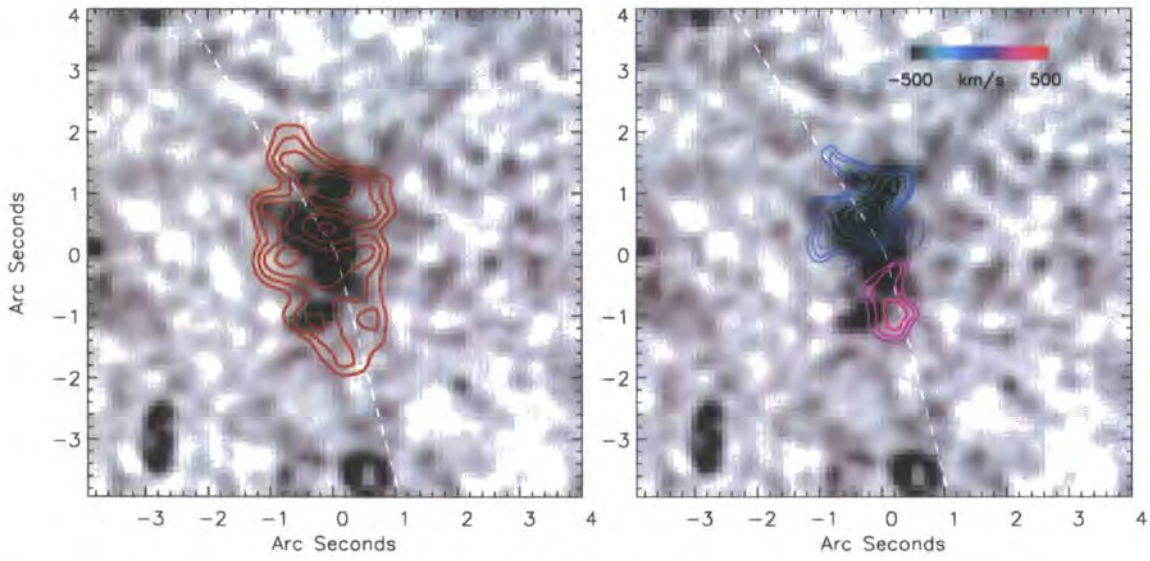

Figure 8.5: *Left:* The HST WFPC2 V-band image of TX0828+193 with the [OIII]λ5007 emission line intensity overlaid as contours. *Right:* The velocity field of the galaxy derived from the [OIII]λ5007 emission line overlaid on the *HST* image. The dashed line shows the orientation of the radio lobes (Carilli et al., 1997).

to rest-frame velocity (assuming a redshift of z=2.230). The central peak of the proposed underlying Lyα emission from the center of the galaxy is at 3925Å which indicates a redshift identical to that observed [OIII]λ5007 emission from the same region. Furthermore, Lyα observations of the proposed underlying Lyα emission in the northern component is centred at 3935Å (an offset of $\sim$400 km s^{-1}) which is also in excellent agreement with our observations of the relative velocity offset of the [OIII]λ5007 emission. In Fig. 8.4 we show the [OIII] emission line profile compared to the Lyα emission from Wilman et al. (2004) for both the redshifted and blue-shifted components. We also overlay the proposed underlying Lyα emission line profile from Wilman et al. (2004). This is derived assuming the underlying Lyα emission has a Gaussian profile with four absorbers (each of which also has a Gaussian profile) which act against the Lyα emission. We also fit and overlay the best Gaussian profile fit to the [OIII]λ5007 emission. In both the nuclear and spatially offset components of the galaxy, the velocity centroids of the proposed Lyα emission line profile and [OIII] emission lines are in excellent agreement, however it is clear that the [OIII] emission is much narrower than the Lyα, indicating that a simple model in which the underlying Lyα emission has a Gaussian profile which is absorbed by foreground neutral gas may be incomplete. Instead, our observations suggest that the resonant scattering of the Lyα within the emitting region may be responsible for broadening the emission line profile over and above that caused by the bulk motion of the gas.

8.3.2 TX0828+193

In Fig. 8.5 we show the *HST* image of TX0828+193 with the intensity and velocity information from the [OIII]λ5007 emission line overlaid as contours. Both the *HST* image and the [OIII]λ5007 emission line intensity appear morphologically complex with several spatial components. The radio lobes from this galaxy extend along the major axis of the rest-frame UV emission from the galaxy (marked by dashed lines in Fig. 8.5). The velocity field from the [OIII] emission shows that the gas has two distinct velocities separated by $\sim$ 1000 km s^{-1} and $\sim$2″($\sim$16 kpc) in projection. The direction of the strongest velocity

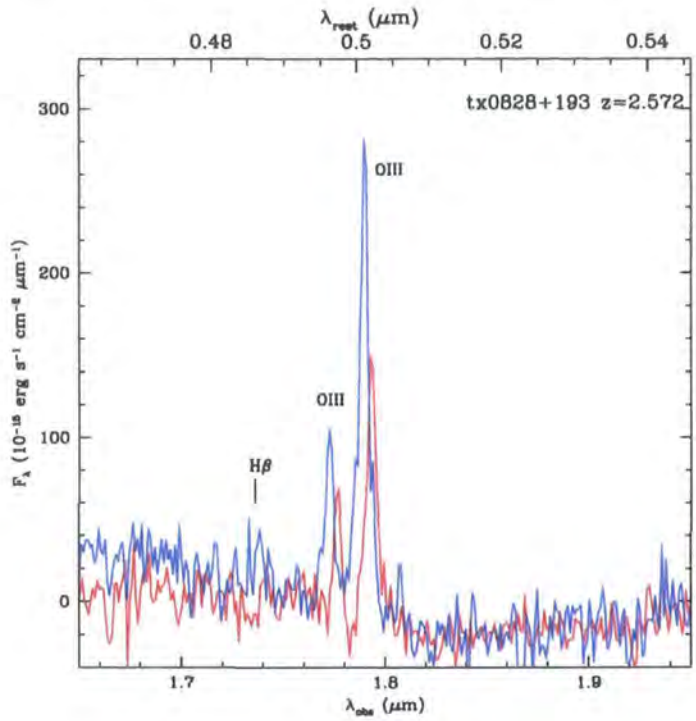

Figure 8.6: Extracted one dimensional spectra from the red and blue-shifted [OIII]λ5007 emission line from TX0828+193. The spectra clearly show the velocity offsets between the red and blue-shifted parts of the galaxy

gradient also follows the same axis as the radio emission (the radio lobes extend ~9″ (~70 kpc) from the centre of the galaxy). The large velocity offsets across the galaxy must either arise from outflowing material (or material which has been swept up by the radio jet).

The morphology of the [OIII]λ5007 emission also shows a cavity near the centre of the galaxy which may by due to the radio jet either highly ionising or evacuating the gas and/or dust. It is interesting to note that the angle between the two radio jets is not 180°. This may arise if the galaxy has a high velocity across the line of sight. However, the emission line morphology shows a strong component to the North West which may also be acting to bend the radio jet.

Fig. 8.6 shows the [OIII]λ5007 emission from both the high and low redshift components. We note that the Hα emission falls on a part of the chip with relatively low throughput, and is also is much weaker than the [OIII]λ5007 emission, and therefore it was not possible to derive any velocity information from this emission line. Instead we collapse the datacube around the Hα emission line and make a Hα intensity map and overlay this on the *HST* image (Fig. 8.7). Whilst there is lower signal-to-noise in the Hα emission, it appears that the morphology is more nucleated than the [OIII]λ5007 emission. This may partly arise due to a strong underlying broad-line Hα region from the AGN in the central regions of the galaxy.

From high resolution rest-frame UV spectroscopy of this source, van Ojik et al. (1997) propose that the Lyα emission is absorbed by neutral foreground material which asymmetrically shapes the Lyα emission. The observed Lyα emission line profile is well fit by a single Gaussian profile with four absorbers (van Ojik et al. 1995). Since rest-frame optical emission lines do not suffer the absorption by neutral material, comparing the Lyα with

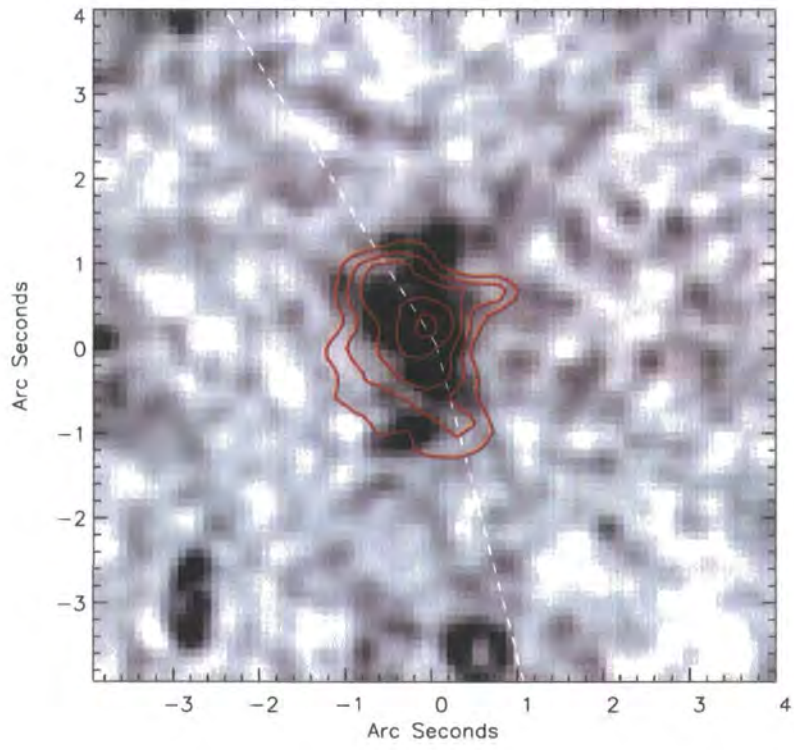

Figure 8.7: The HST WFPC2 V-band image of TX0828+193 with the Hα emission line intensity overlaid as contours.

other emission lines is useful for testing of the proposed resonant scattering model.

In Fig. 8.8 we show the collapsed [OIII]λ5007 emission line profile and overlay the collapsed Lyα emission line observations from van Ojik et al. (1997). The slit in the Lyα observations was placed along the long axis of the galaxy, however, van Ojik et al. (1997) only consider the collapsed spectra and therefore we can only compare the collapsed spectra from our observations rather than individual components as in § 8.3.1. It is clear that in TX0828+193 the centroid and width of the model for the underlying Lyα emission line and the observed [OIII] emission line are in excellent agreement. We stress, however, that we have to compare the collapsed spectra from both Lyα and [OIII]λ5007 emission and therefore some caution should be taken when comparing two collapsed spectral profiles which have 1000 km s^{-1} velocity gradient between them. We also note that in the collapsed spectra, both the Lyα emission and the [OIII]λ5007 emission appear double peaked (in the case of [OIII]λ5007 this is due to the velocity offset between the northern and southern ends of the galaxy). Since the double peak structure arises in both components, and without two-dimensional information about the Lyα emission it is not possible to rule out the possibility that the Lyα emission line profile arises due to two discrete velocity components, which would then match the observed [OIII]λ5007 velocity field. Nevertheless, the fact that the agreement is so good strongly supports van Ojik's suggestion that a model in which neutral gas shapes an underlying Gaussian emission line profile is a good fit to the data.

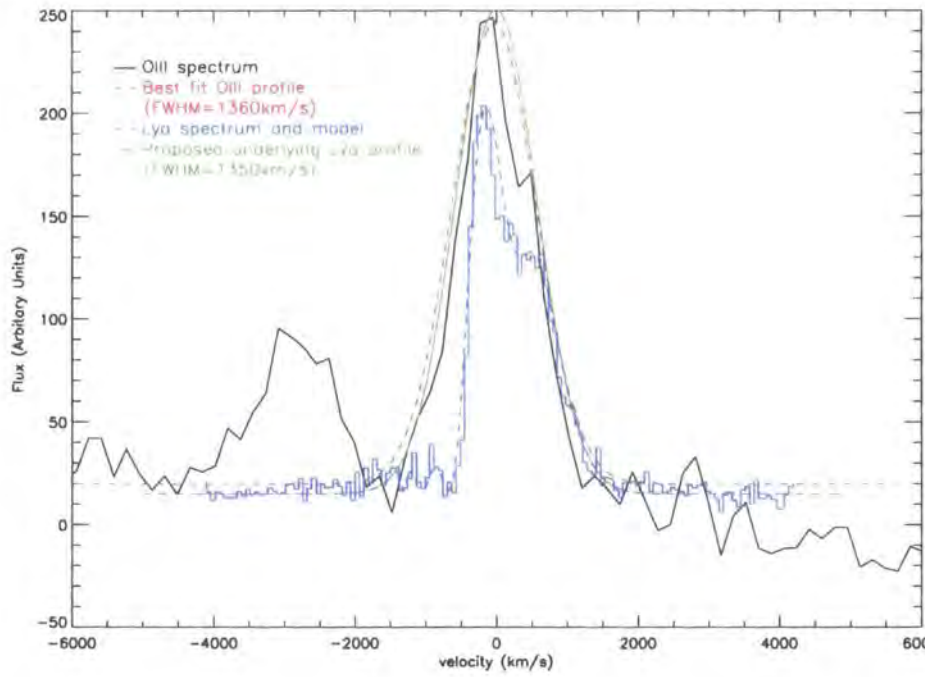

Figure 8.8: Comparison of the Lyα and [OIII] emission line profiles in TX0828+193. The line widths of the proposed underlying Lyα emission and the [OIII] (which does not suffer absorption by foreground neutral material) are in excellent agreement. (Lyα observations and model are taken from van Ojik et al. (1997).

8.4 Discussion & Conclusions

One of the key outstanding issues in understanding the formation and evolution of radio galaxies are the effects of feedback both the host galaxy and the surrounding environment. For example, starburst driven winds may be responsible for regulating galaxy formation, yet in radio galaxies strong radio jets provide a massive energy injection system with which to dump energy into the galaxy and surrounding environment. But which of these processes has the strongest effect on the galaxy and its environment? For example, since we know that the radio jets are relativistic and highly collimated, they may quickly escape the gravitational potential of the galaxy, and whilst energy may be expelled along a jet, it may have little effect on the host galaxy. On the other hand, starburst driven superwinds are not necessarily collimated (they may have "bubble"-like structures which surround the galaxy) which can fragment and fall back down on the galaxy, disrupting the disk and causing further bursts of star-formation. To disentangle these processes and understand their effects requires analysis of the two-dimensional dynamics of HzRGs.

We have targeted two HzRGs with IFS in order to probe the velocity structure of the galaxy. We find that the dynamics of the [OIII]λ5007 emission from both HzRGs show that the strongest velocity gradient is along the same axis as the radio lobes, arguing that the AGN jet is driving the bulk motion of the gas in the galaxy.

Furthermore, the majority of HzRGs show complex and asymmetric Lyα emission line profiles which are usually attributed to neutral gas clouds with high column densities (10^{18}–$10^{19.5}$ cm^{-2}) resonantly scattering and absorbing the Lyα emission. Rest-frame optical emission lines do not suffer the same absorption properties as Lyα, and therefore a comparison of the Lyα and rest-frame optical emission lines (such as) [OIII]λ5007 emission may offer insight into this model.

By comparing the high resolution Lyα emission line profile of these galaxies with that of the [OIII]λ5007 emission we find differing results. In both radio galaxies we have studied we find excellent agreement between the redshifts of [OIII]λ5007 and Lyα emission. However, the line widths produce differing results. In TX0828+193 (z=2.52) we find excellent agreement between the [OIII] emission line width and the proposed underlying Lyα emission line profile, however, the double peaked profile of both Lyα and [OIII]λ5007 may arise entirely from the bulk kinematics, and may not result of a resonant scattering of Lyα photons. In the second radio galaxy in this sample, TX0200+015 (z=2.23) we have spatially resolved spectroscopy from two regions within the galaxy. We find that the [OIII]λ5007 is much narrower (FWHM=650$\pm$40 km s^{-1} for the nuclear component and FWHM=920$\pm$50 km s^{-1} for the spatially offset region), whereas the proposed underlying Lyα emission line from Wilman et al. (2004) has FWHM=1490 km s^{-1} and 1580 km s^{-1} respectively. This is a problem for models in which the Lyα emission line profile was shaped solely by neutral material, where the line widths should be in good agreement. The fact that they disagree (by a factor of $\sim$2) suggests that the photons within the emitting regions may be responsible for broadening the emission profile to a profile greater than that caused by the bulk gas motion.

These differing results are difficult to reconcile. Both targets show a strong velocity gradient in the same direction as the radio lobes, indeed one galaxy shows a 1000 km s^{-1} velocity gradient across the galaxy which probably arises due to outflowing material. These results suggest that the feedback processes in the most luminous HzRGs is dominated by AGN (rather than starburst) driven mechanisms. Moreover, models in which an underlying Lyα emission line is resonantly scattered by neutral gas in the galaxy halo may be an incomplete description of how complex Lyα profiles are generated. However, clearly IFU observations of a larger sample of HzRGs are required to further generalise these conclusions.

Chapter 9 | *Conclusions*

Major advances in the development of instruments for eight and ten meter class telescopes are revolutionising our understanding of galaxy formation. In particular, Integral Field Spectrographs allow us to spatially resolve the two dimensional velocity structures of distant galaxies. These observations can be used to investigate masses, power-sources and metallicities of galaxies and compare the results with local counterparts in order to identify evolutionary trends. In this thesis we have exploited these integral field spectrographs to address questions regarding the physics of galaxy formation, such as the evolution of galaxy mass and the star formation activity in high redshift galaxies. We have addressed issues such as the links between massive high redshift galaxies (such as SCUBA galaxies) and their present day descendants. In this final section, we summarise our results.

9.1 E+A Galaxies

In Chapter 2 we have mapped the absorption line spectra using *Nod and Shuffle* Integral Field Spectroscopy to study the dynamics and distribution of the A-stars and nebular emission in a local (z=0.1) post-starburst (E+A) galaxy. These galaxies represent the short-lived but potentially important transition of galaxies from star-forming, rotationally-supported disks to passive, pressure-supported spheroidals.

We selected one field galaxy from the SDSS which shows strong Balmer absorption lines (which are indicative of a strong A- star population), but has only a small ongoing star-formation rate. This galaxy has a disturbed morphology, with a halo of diffuse material distributed asymmetrically toward the north. Using the [OII] emission line (W_o[OII]=4.1Å) we find that the gas and hot OB stars are offset from the older stars in the system. The gas also has a spatially extended and elongated morphology with a velocity gradient of $100 \pm 20\,\mathrm{km\,s^{-1}}$ across 6 kpc in projection. Using the strong $H\gamma$ and $H\delta$ absorption lines we find that the A- stars are widely distributed across the system and are not centrally concentrated arguing that the A-star population has formed in molecular clouds outside the nucleus. The disturbed morphology, strong colour gradients and strong Hδ and Hγ absorption lines in SDSSJ 101345.39 argue that this is a recent tidal interaction/merger between a passive elliptical and star-forming galaxy.

Our observations suggest that the activity in SDSS J102145.39 may be the result of a strong tidal interaction between a passive (possibly elliptical) galaxy (giving rise to the old stellar population), and a gas-rich, star-forming (spiral or irregular?) galaxy (giving rise to the spatially offset of hot stars and nebular emission). The interaction between the two components is likely to have been responsible for the production of the A-star population in a burst of star formation. In our pilot study we have shown that the A-stars are widely distributed across the galaxy, which coupled with the spatially extended morphology of the gas suggests a clear preference for the *squeezed cloud* model for E+A galaxy formation.

9.2 The Evolution of Galaxy Mass – Gravitational Telescopes:

We have targeted a series of highly magnified, high-redshift galaxies with integral field spectroscopy to probe the evolution of galaxy mass. We have proved that galaxy clusters can be effectively used to study the dynamics of lensed galaxies at $z \sim 1$ through the Tully-Fisher relation. The amplification caused by this natural magnification causes the brightness of the background galaxy to be increased by up-to a factor 30 and the gain in spatial resolution allows us to resolve component parts (on sub kilo-parsec scales) from the ground. By comparing the maximal circular velocity–luminosity relation of these galaxies with the local Tully-Fisher relation we find evidence for 0.5 magnitudes of brightening in the rest-frame B-band, and negligible evolution in the rest-frame I-band. This suggests both that galaxies build up via hierachical merging and that the star-formation activity was higher at $z \sim 1$. We also compare the shapes of the extracted one-dimensional rotation curves of these galaxies and find that they rise much more slowly than we would expect from similarly luminous galaxies in our local neighbourhood. This may be suggestive of a real difference in the organisation of the potential wells at these early times.

Using integral field spectroscopy of gravitationally lensed galaxies we have also demonstrated that multiply-imaged background galaxies can be used to tie down the cluster potential in unprecedented detail by kinematically locating the exact position of the critical lines.

9.3 Far-infrared Luminous Galaxies:

By targeting SCUBA galaxies with near-infrared spectroscopy and narrow-band imaging around redshifted Hα emission we have found that the high redshift sub-mm population share many characteristics with the somewhat less luminous far-infrared galaxies identified in the local Universe. This includes the Hα equivalent widths, the proportion of obvious AGN and the typical spectral classification. Yet there remain important differences, with proportionally more highly-obscured activity in the high-redshift population, apparently larger dynamical mass, lower metallicities and much higher gas fractions on 10-kpc scales. We have shown that SCUBA galaxies are morphologically complex, dusty, metal-rich, merging systems with high instantaneous star formation rates and actively fuelled AGN. Using the near-infrared spectroscopy we have attempted to identify power sources (to determine whether star formation- or AGN- activity dominate the luminosity output) and (more importantly) masses for these galaxies.

Using both optical and near-infrared wavelength Integral Field Spectroscopy, we have also studied the emission line structure of a small number of these galaxies in order to further understand their intrinsic properties. In particular, by combining the Hα and Lyα emission maps from UIST and GMOS IFU observations of N2 850.4 (z=2.38) we find that the Lyα covers the complete galaxy and is offset by $+270 \pm 40\,\mathrm{km\,s^{-1}}$ from the systemic velocity. This velocity offset is comparable to that seen in rest-frame UV-selected galaxies at similar redshifts and usually interpreted as a star-burst driven wind. The extended structure of the Lyα emission suggests that this wind is not a nuclear phenomenon, but is instead a galactic scale outflow. Our observations suggest that the vigorous activity in SMGs arises as a result of interactions between (at least two) dynamically-distinct components, resulting in a strong starburst activity and actively-fuelled AGN activity.

Whilst starburst driven outflows seem to dominate the feedback processes in SCUBA galaxies, we also investigate the velocity structures of two powerful radio galaxies at similar redshifts. We use the [OIII]λ5007 emission line to constrain the dynamics of these

systems and find that the strongest velocity gradients are in the same direction as the radio lobes, suggesting that the feedback mechanisms in these galaxies are dominated by the AGN activity. Furthermore, by comparing the [OIII]λ5007 emission line profile with high resolution Lyα spectroscopy we investigate models in which high column density absorbing halos are thought to play an important role in resonantly scattering and asymmetrically shaping the Lyα emission from these active galaxies.

9.4 Evolutionary Links

We have effectively shown that integral field spectroscopy can be used to investigate galaxy formation, but what have we learned about galaxy formation itself? Most of the results presented here suggest that galaxies are built up over cosmic time by the merging of smaller (sub-galactic) units. E+A galaxies appear to be in the final stages of transforming from late type (spiral) galaxies to (early type) spheroidals with the post-starburst characteristics suggesting that an intense starburst occurs during the initial encounter. Since the local universe is mainly an inert place, these galaxies are also responsible for most of the local cosmic star formation rate density.

Whilst local E+A's appear to be the remnants of merging systems which dominate the star formation rate density locally, we have identified a population of galaxies which account for the bulk of the star formation activity at high (z$\sim$2). These SCUBA galaxies also appear to be dusty merging systems, with high masses and star-formation rates and are believed to be the progenitors of local massive ellipticals at the present day.

E+A's and SMGs are at very different redshifts, but share the characteristics that they are star-burst galaxies, induced by merger activity and therefore represent the extreme ends of the galaxy populations at their given epoch. "Freaky" galaxies are useful tests of galaxy formation, but in order to understand how galaxies evolve, we also need to observe distant "normal" galaxies in order to fully understand the processes which drive galaxy evolution. By investigating the Tully Fisher relation of "normal" distant galaxies (which we can observe due to the boost of gravitational lensing), we find no evidence for evolution in the I-band TF, but 0.5mag of brightening in the B-band TF relation (from our small sample) suggesting increased star formation activity towards $z = 1$, but also strong evidence that the typical dynamical masses of "normal" galaxies at $z \sim 1$ are about a factor of two smaller than the present day.

9.5 What Next?

The next step in this programme is to expand these high redshift samples to more statistically significant numbers. Integral field spectroscopy is only now reaching maturity on large aperture telescopes and therefore it is becoming feasible to build reasonably large samples with modest investments of time. We have demonstrated that galaxy evolution can be understood by mapping the intrinsic properties of galaxies: by observing galaxies as they transform from one type to another, the effects of galaxy-galaxy mergers/interactions (at all epochs) and the evolution of galaxy mass (both baryonic and dark).

One particular problem with current galaxy formation models which is ideally suited to IFU studies of high redshift galaxies is to understand how *feedback* regulates galaxy formation. Galaxy formation models with simple cooling prescriptions predict that more than 50% of baryons should condense into stars (e.g. White & Frenk 1991). This is an unfortunate conjecture: observations have tied down the fraction of baryons locked up into stars as <10% (Balogh et al. 2001, Cole et al. 2001). This problem remains unresolved, but may arise as a result of starburst-driven winds expelling gas and regulating the number

of baryons allowed to cool to form stars. Since the star formation activity of galaxies was more efficient at high redshift, these feedback processes mainly occur in young galaxies between 1 Gyr and 8 Gyr after the Big Bang (i.e. between redshifts $z = 5$ and $z = 1$ respectively). Compounded by the fact that galaxies at $z > 1$ are intrinsically small and faint, attempts to observationally identify the consequences of star-bursts on the galaxy and its environment have only had limited success, even with ten meter class telescopes.

As we have seen, nature provides us with a *natural telescope* with which to study the high redshift universe. This natural phenomenon allows studies which would otherwise require the light grasp of thirty or one-hundred meter telescopes, advancing research perhaps fifteen years ahead of its time. By coupling this lensing phenomenon with integral field spectroscopy we can address the following fundamental questions:

- **What are the masses of these very high redshift galaxies?** It is important to firmly establish whether high redshift galaxies have regular disk kinematics, or whether they are so perturbed by bursts of star formation that they lie outside of the low redshift morphological classification scheme. Constraining the structure of any disk and the nature of the dark matter halo will allow us to measure their masses and determine whether galaxies at $z > 2$ are massive galaxies, or whether their luminosity comes from a burst of star formation in an intrinsically low mass sub-galactic system.

- **What is the nature of outflowing gas from high redshift galaxies?** The gain in spatial resolution provided by the gravitational lens allows us to resolve the structure of star-burst driven superwinds which are thought to regulate cooling. The discovery of these winds is a recent observation breakthrough, however the geometry and dynamics of the outflowing material remain largely unstudied, yet have serious implications for the evolution of the galaxy and enrichment of the inter-galactic medium (IGM). For example, if outflowing gas has sufficient energy to escape the gravitational potential, then it will be expelled from the galaxy and play no further role in galaxy formation. This may explain the ubiquitous presence of metals in the lowest density regions of the IGM. However, if the gas does not escape the galaxy, it may stall, fragment and drain back down on the disk (a more energetic version of a galactic fountain). This reprocessed material may trigger further star-formation, disrupt or enrich the galaxy disk. Using integral field spectroscopy, we can faithfully decouple the spatial and spectral resolution, which are usually mixed in traditional longslit observations. Furthermore, by targeting rest-frame UV and optical emission lines (which are redshifted into the near-infrared at $z \gtrsim 2$), we can investigate the structure of the wind and how it relates to the underlying galaxy.

- **Probing the Fossil Records of Star Formation: Are Chemical Abundance Gradients Weaker or Stronger than those in present-day Spirals?** The distribution of chemical elements is a powerful diagnostic of galaxy formation models. By observing whether chemical abundance gradients are weaker or stronger than those found in present-day spirals, we can determine if disks have formed *outside in* or *inside out*. The metallicities of high redshift galaxies can also place powerful constraints on how galaxy populations at the present day have evolved from their high redshift progenitors.

Furthermore, we can also draw distinctions between these *normal* galaxies (which we can observe due to the boost from the gravitational lens) and galaxies which (identified from SCUBA and Spitzer) are strong star-bursts at similar redshifts. Such galaxies

are frequently bright enough to study individually. By comparing and contrasting the differences in metals, masses and dynamics we can provide a link between the galaxy populations and investigate how galaxies evolve from high redshift proto-galaxies to their present day descendants.

9.6 The Future

We have laid out some important questions which can be adressed using current state-of-the-art instrumentation on large aperture telescopes, but with 30m, and even 100m telescopes (extremely large telescopes; ELT), Next Generation Space Telescope (NGST) and the next generation of instrumentation right around the corner, where could this subject go in the next 10 years? We have already seen that gravitational lensing allows us to perform science that would otherwise require the light grasp of an ELT and therefore we may be in a privileged position to steer the science in this area. Of course, with an ELT we no longer need the boost of a gravitational lens to study "normal" galaxies out to $z \sim 5$ – the light grasp of an ELT and adaptive optics will resolve these galaxies in enough detail to carry out studies in as much detail as current studies of galaxies at $z = 0.1$. However, gravitational lensing has allowed us to perform science years ahead of its time, so why not simply shift the focus to *even higher* redshifts and do the same thing? By using large area IFUs (e.g. MUSE) on an ELT we could obtain an ultra-deep observation of an entire cluster core in one observation. This would allow us to probe all of the critical lines and search for the first stars and proto-galaxies which were active (and responsible for?) reionisation. Whilst there are conflicts between theorists, the first stars and galaxies are predicted to have formed as early at $z \sim 35$ and therefore one of the goals of future surveys will be to probe the power sources, star formation rates, and masses of the galaxies responsible. Of course, from the cluster core we also glean all of the information on the cluster and all of the lensed galaxies down to some ridiculous sub-L_* limit.

9.7 Summary

In this thesis, we have used Integral Field Spectroscopy to investigate the star-formation properties, kinematics and chemical properties of distant galaxies. By observing *normal* galaxies (which are observable thanks to the boost from gravitational lensing) and comparing the metallicities, dynamics and chemical abundances with SCUBA and Spitzer selected galaxies at similar redshifts, we have identified power sources and traced the evolution of galaxy mass from high redshift to their present day descendants. Moreover, by observing the geometry and kinematics of starburst and AGN- driven outflows from these galaxies we have begun to address key issues such as how outflows – high energy blast waves which expel gas from the galaxy and into the IGM – regulate baryon cooling and prevent galaxy formation from involving more that 10% of baryons.

The next step is to generate statistically useful samples. This can be best achieved by investigating the dynamical interplay of stars and gas using Integral Field Spectroscopy to deconvolve spatial and velocity information. With many new IFU's coming on line now or in the near future (e.g. GNIRS and NIFS (Gemini), VIMOS & SINFONI (ESO), OSIRIS (Keck)) there will be no shortage of instruments to carry on this research over the next few years.

Appendix A

GMOS Integral Field Spectroscopy of the Small Scale Triply Imaged Arc in Abell 1201

In this appendix we briefly discuss the power of using gravitational lensing to probe the structure (and sub-structure) of galaxy clusters. In particular, we show that IFU observations of multiply imaged background galaxies can effectively be used to constrain the mass distribution in the cores of galaxy clusters. The observations in this appendix will form part of a paper which combines the IFU data with forthcoming *Chandra* spectro-imaging (Smith et al. in prep).

Abstract

In this chapter we present integral field spectroscopy of the multiply imaged lensed galaxy behind Abell 1201. We demonstrate the feasibility of constraining a mass model by kinematically locating the fold in the velocity field of a lensed galaxy. The lensed galaxy lies at z=0.451 and has a peak-to-peak velocity gradient of 40 km s^{-1}, however, due to the high signal-to-noise we demonstrate that the line centroid is good to $\sim$4 km s^{-1}, allowing extremely accurate positioning of the critical lines. Follow-up spectro-imaging of this cluster with *Chandra* are required to confirm the elongation of the dark matter halo which appears in the *HST* imaging.

A.1 Introduction

Galaxy clusters are important laboratories in which to study physical processes that are generally inaccessible in other environments. For example the radial density profile and the projected ellipticity of clusters on the sky may offer valuable clues into the nature of dark matter (e.g., Spergel and Steinhardt, 2000; Sand et al., 2002, 2004; Miralda-Escudé, 2002; Arabadjis et al., 2002). Complications often arise in cluster–based studies of dark matter due to the presence of baryons (e.g., Allen, 1998; Smith et al., 2001a; Lewis et al., 2003). However, from a broader perspective such complications provide us with important clues into the physics of gas cooling, and inter–play between baryons and dark matter, both of which are central to attempts to understand the physics of galaxy formation (e.g., Cole et al., 2000).

Progress towards these goals requires detailed study of the distribution of mass in clusters. Strong gravitational lensing offers the most direct and precise probe of cluster mass distributions (e.g., Kneib et al., 1996; Smith, 2003; Smith et al., 2003), however

complementary constraints from X–ray observations (e.g., Allen et al., 2002), weak lensing (e.g., Kneib et al., 2003) and the three–dimensional distribution of cluster galaxies (e.g., Czoske et al., 2001) are necessary for a comprehensive understanding of mass in clusters. Armed with the results from such multi–wavelength studies, robust constraints on the dark matter particle and gas cooling may ultimately flow.

A recent snapshot survey of 55 X–ray luminous galaxy clusters with the WFPC2 camera on HST (PID's 8301 & 8719; PI Edge) uncovered new cluster lenses with which to explore these questions. The snapshot observing strategy is well–suited to identifying clusters containing rare and powerful constraints such as radial arcs (e.g. RXJ,1133 – Sand et al. 2003).

During this program we have uncovered a remarkable gravitational arc in A1201. The extremely tight radius of curvature of the lensed galaxy ($\lesssim 2''$) is unparalled and means that we can probe the inner structure ($\lesssim$10 kpc) of the cD cluster galaxy dark matter halo. The apparant multiple image morphology in the imaging observations of this background galaxy makes it an ideal candidate with which to constrain the central mass profile of the galaxy cluster.

A.2 Observations, Analysis & Results

A.2.1 HST Observations

Abell 1201 was observed through the F606W filter with *HST* using the WFPC2 camera on 2001 April 7th. We combine the 2×400-second exposures into a single mosaic using the standard IRAF tasks and present the region around the central galaxy and arc in Fig. A.1 (see Edge et al. 2003 for a complete description of the *HST* observations).

A.2.2 GMOS Spectroscopic Imaging

The z=0.451 arc in Abell 1201 was observed with the GMOS-IFU on Gemini South on 2004 February 25th U.T. during Science Demonstration time for a total of 10.8 ks in 0.6″ seeing and photometric conditions. The IFU uses a lensed fiber system to reformat the $7'' \times 5''$ field into two long slits (Allington-Smith et al., 2002). Using an B-band filter in conjunction with the B600 grating results in two tiers of spectra recording a maximum field of view. The spectral resolution of this configuration is $\lambda/\Delta\lambda = 2000$. For the galaxy at z=0.451, the emission for the [OII] doublet falls at a wavelength of 5320$\AA$, in a region of low sky emission.

The GMOS data reduction pipeline was used to extract and wavelength calibrate the spectra of each IFU element. The variations in fiber-to-fiber response were removed in IDL by using continuum regions either side of the expected range of [OII] emission. The [OII] doublet is clearly resolved in the GMOS spectra. The emission line doublet was fitted using a χ^2 minimisation procedure, taking into account the greater noise at the position of the sky lines. The spectra were averaged over a 3×3 spatial pixel region, increasing this region to 4×4 pixels if the signal was too low to give a sufficiently high χ^2 improvement over a fit without the line. In regions where this averaging process still failed to give an adequate χ^2, no fit was made. We required a minimum χ^2 of 25 (S/N of 5) to detect the line, and allow the signal to drop by a χ^2 of 9 to calculate the error in the velocity. This corresponds to a formal 3σ error.

In Fig. A.1 we show the HST image of the central galaxy which also shows the multiply imaged arc. Our GMOS IFU observations show that there are two arcs in the field of view. The first is a singly imaged z=0.273. The second is the multiply imaged galaxy at z=0.451. In the left hand panel of Fig. A.1 we show the intensity of the [OII] emission

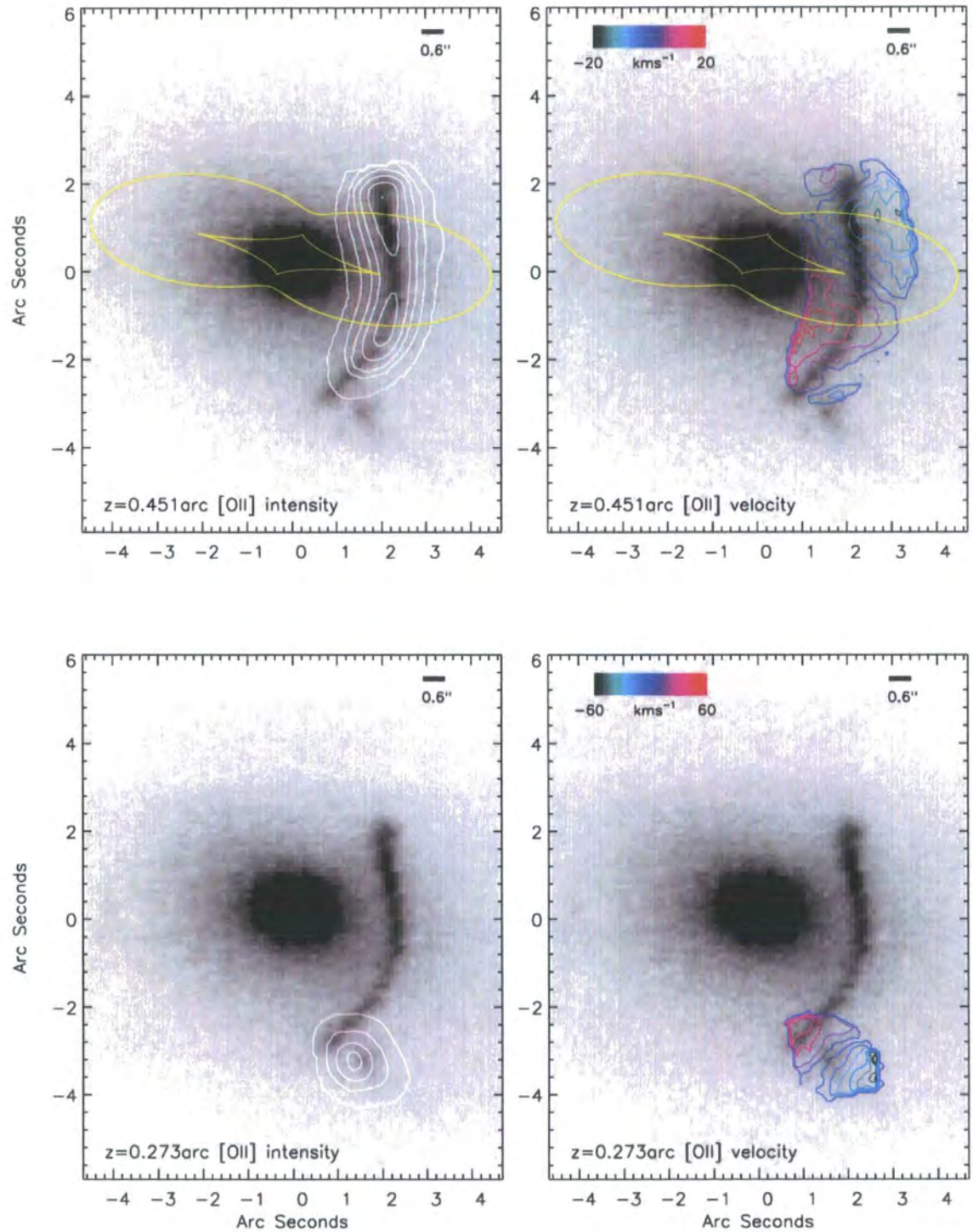

Figure A.1: HST image of the lensing cluster Abell 1201 with the intensity and velocity contours of the z=0.451 and z=0.273 arc overlaid as contours. The contours in the [OII] emission line intensity map are at 5,6,7,8,9 and 10–σ. The contours in the velocity field are spaced by average 1–σ errors. The folding of the velocity field in the z=0.451 arc can clearly be seen, and we overlay the resulting z=0.451 critical curves. The solid bar in the top right hand corner of each panel marks the size of the seeing disk.

(contours mark 5,6,7,8,9 and 10σ). In the right hand panel we show the velocity field derived from the [OII] emission. The contours spaced by average 1σ errors (which are aproximately 4 km s^{-1}). The velocity field shows a peak-to-peak velocity gradient of 40 km s^{-1}, but most strikingly, the multiple image configuration manifests itself through the the folded velocity field of the z=0.451 arc.

Updating the mass model from Edge et al. (2003), we kinematically locate and identify the positions of the critical lines. We overlay the z=0.451 critical curves on the image.

A.2.3 Velocity Errors

The accuracy to which the positions of the critical lines can be constrained depends on two things: the observed peak-to-peak velocity field of the galaxy, and the signal-to-noise of the data. These (multiply imaged), strongly lensed, galaxies are highly sheared, and usually are barely resolved in both dimensions, making it difficult to infer the inclination before an IFU observation is taken, thus high signal-to-noise IFU observations are required to ensure any form of rotating disk (even at high inclinations) can be identified. The average signal-to-noise of the data in any indiviual pixel in our GMOS IFU observations is $\sim$ 8. To test the line centroid accuracy, we generate fake [OII] doublets and add noise. We then fit and measure the line centroid of the [OII] doublet using an identical procedure to that in A.2.2 (we use an [OII] emission line width comparable to that of the galaxy which has a FWHM$\sim$75 km s^{-1}). In Fig. A.2 we show the precision of the line centroid for the GMOS spectrograph as a function of signal-to-noise for a galaxy at z=0.451. It is clear that at low signal-to-noise, the line centroid accuracy is poor, however above a signal-to-noise of $\sim$8, the line centroid is good to $\sim$4 km s^{-1} (at this resolution, 1 pixel corresponds to 50.6 km s^{-1} at this redshift).

A.3 Discussion & Conclusions

A 1201 is drawn from a sample of 55 X-ray luminous clusters observed with *HST* snapshot of BCGs. Among the 100 or so clusters observed with either ACS of WFPC2, A 1201 is the only galaxy cluster with a tangential arc on scales as small as R$\sim$2″. The rarity of this arc therefore makes it an important target with which to probe the small-scale mass distribution in clusters.

The peak-to-peak velocity gradient of the galaxy is 40 ± 4 km s^{-1}. From the current (relatively shallow) *HST* imaging it is not possible to infer a source-frame inclination for the lensed galaxy, however the velocity field suggests that it has regular rotation and therefore is probably a sub-L$_*$ spiral. Further (deeper) multi-colour *HST* ACS observations may allow us to constrain the morphology and past-to-present star-formation history further. However, more crucially, our GMOS IFU observations of this arc provide conclusive evidence that this galaxy lies in the super-critical region of the galaxy cluster, resulting in it being multiply imaged. By kinematically locating the positions of the "folds" in the velocity field, we can constrain the position of the critical lines, thus constraining the mass model (Fig. A.1). The resulting gravitational lens model is significantly more elongated ($\epsilon_{total} \geq 0.5$) than the light distribution of the BCG on 2″ scales (ϵ_{BCG}=0.23$\pm$0.03). However, with the current data we are unable to determine whether the matter distribution really is more elongated than the stellar distribution, or whether the matter and stellar distributions are significantly offset, which may indicate the cluster is not dyanamically relaxed as the optical data suggest.

To resolve this issue requires coupling our IFU observations, and mass model with forthcoming *Chandra* observations which will probe the distribution of hot gas in the

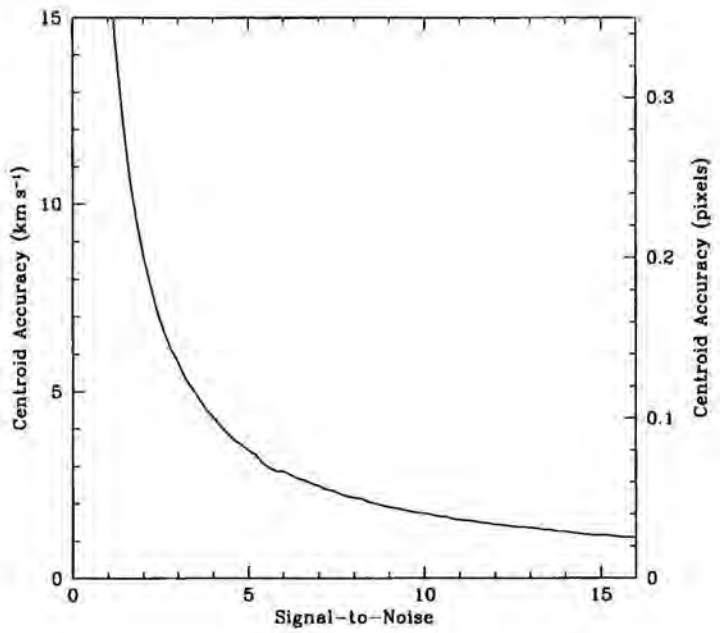

Figure A.2: The velocity error of the [OII] emission line doublet as a function of signal-to-noise for a galaxy at z=0.451 with a FWHM$\sim$75 km s^{-1}. This plot shows that the typical velocity centroid error for a S/N$\sim$8 is less than 5 km s^{-1}

cluster to larger ($\sim$50–500 kpc) scales. This will allow us to constrain some of the physics at work in the cores of galaxy clusters.

Bibliography

G. O. Abell. The Distribution of Rich Clusters of Galaxies. ApJS, 3:211–+, May 1958.

K. L. Adelberger and C. C. Steidel. Multiwavelength Observations of Dusty Star Formation at Low and High Redshift. ApJ, 544:218–241, Nov 2000.

K. L. Adelberger, C. C. Steidel, A. E. Shapley, and M. Pettini. Galaxies and Intergalactic Matter at Redshift z˜3: Overview. ApJ, 584:45–75, Feb 2003.

A. Aguirre, L. Hernquist, J. Schaye, N. Katz, D. H. Weinberg, and J. Gardner. Metal Enrichment of the Intergalactic Medium in Cosmological Simulations. ApJ, 561:521–549, Nov 2001.

D. M. Alexander, F. E. Bauer, A. E. Brandt, W. N. Hornschemeier, C. Vignali, G. P. Garmire, D. P. Schneider, G. Chartas, and S. C. Gallagher. The Chandra Deep Field North Survey. XIV. X-Ray-Detected Obscured AGNs and Starburst Galaxies in the Bright Submillimeter Source Population. AJ, 125:383–397, Feb 2003a.

D. M. Alexander, F. E. Bauer, W. N. Brandt, D. P. Schneider, A. E. Hornschemeier, C. Vignali, A. J. Barger, P. S. Broos, L. L. Cowie, G. P. Garmire, L. K. Townsley, M. W. Bautz, G. Chartas, and W. L. W. Sargent. The Chandra Deep Field North Survey. XIII. 2 Ms Point-Source Catalogs. AJ, 126:539–574, Aug 2003b.

D. M. Alexander, I. Smail, F. E. Bauer, S. C. Chapman, A. W. Blain, W. N. Brandt, and R. J. Ivison. Rapid growth of black holes in massive star-forming galaxies. Nature, 434:738–740, March 2005.

S. W. Allen. Resolving the discrepancy between X-ray and gravitational lensing mass measurements for clusters of galaxies. MNRAS, 296:392–406, May 1998.

S. W. Allen, S. Ettori, and A. C. Fabian. Chandra measurements of the distribution of mass in the luminous lensing cluster Abell 2390. MNRAS, 324:877–890, July 2001.

S. W. Allen, R. W. Schmidt, and A. C. Fabian. Chandra observations of RX J1347.5-1145: the distribution of mass in the most X-ray-luminous galaxy cluster known. MNRAS, 335:256–266, Sept 2002.

J. Allington-Smith, G. Murray, R. Content, G. Dodsworth, R. Davies, B. W. Miller, I. Jorgensen, I. Hook, D. Crampton, and R. Murowinski. Integral Field Spectroscopy with the Gemini Multiobject Spectrograph. I. Design, Construction, and Testing. PASP, 114:892–912, Aug 2002.

J. R. Allington-Smith, C. M. Dubbeldam, R. Content, C. J. Dunlop, D. J. Robertson, J. Elias, B. Rodgers, and J. E. Turner. Integral field spectroscopy with the Gemini Near-Infrared Spectrograph. In *UV and Gamma-Ray Space Telescope Systems. Edited by Hasinger, Günther; Turner, Martin J. L. Proceedings of the SPIE, Volume 5492, pp. 701-710 (2004).*, pages 701–710, Sept 2004.

A. Alonso-Herrero, M. J. Ward, and J. K. Kotilainen. [OIII]lambda5007, near-IR and X-ray properties of Seyfert 2 galaxies. MNRAS, 288:977–987, July 1997.

J. S. Arabadjis, M. W. Bautz, and G. P. Garmire. Chandra Observations of the Lensing Cluster EMSS 1358+6245: Implications for Self-interacting Dark Matter. ApJ, 572: 66–78, June 2002.

E. N. Archibald, J. S. Dunlop, D. H. Hughes, S. Rawlings, S. A. Eales, and R. J. Ivison. A submillimetre survey of the star formation history of radio galaxies. MNRAS, 323: 417–444, May 2001.

L. Armus, T. M. Heckman, and G. K. Miley. Long-slit optical spectroscopy of powerful far-infrared galaxies - The nature of the nuclear energy source. ApJ, 347:727–742, Dec 1989.

A. Böhm, B. L. Ziegler, K. J. Fricke, and t. FDF Team. Scaling relations of field spirals at intermediate redshift. Ap&SS, 284:689–692, 2003.

J. A. Baldwin, M. M. Phillips, and R. Terlevich. Classification parameters for the emission-line spectra of extragalactic objects. PASP, 93:5–19, Feb 1981.

M. L. Balogh, C. Miller, R. Nichol, A. Zabludoff, and T. Goto. Near-infrared imaging of 222 nearby Hdelta-strong galaxies from the SDSS. *ArXiv Astrophysics e-prints*, March 2005.

M. L. Balogh, S. L. Morris, H. K. C. Yee, R. G. Carlberg, and E. Ellingson. Differential Galaxy Evolution in Cluster and Field Galaxies at z˜0.3. ApJ, 527:54–79, Dec 1999.

M. L. Balogh, F. R. Pearce, R. G. Bower, and S. T. Kay. Revisiting the cosmic cooling crisis. MNRAS, 326:1228–1234, Oct 2001.

M. Barden, M. D. Lehnert, L. Tacconi, R. Genzel, S. D. White, and A. Franchesini. Tully Fisher Relation. *astro-ph/0302392*, 2003.

A. J. Barger, L. L. Cowie, I. Smail, R. J. Ivison, A. W. Blain, and J.-P. Kneib. Redshift Distribution of the Faint Submillimeter Galaxy Population. AJ, 117:2656–2665, June 1999.

C. M. Baugh, C. G. Lacey, C. S. Frenk, G. L. Granato, L. Silva, A. Bressan, A. J. Benson, and S. Cole. Can the faint submillimetre galaxies be explained in the Λ cold dark matter model? MNRAS, 356:1191–1200, Jan 2005.

A. J. Benson, R. G. Bower, C. S. Frenk, C. G. Lacey, C. M. Baugh, and S. Cole. What Shapes the Luminosity Function of Galaxies? ApJ, 599:38–49, Dec 2003.

G. Bertelli, A. Bressan, C. Chiosi, F. Fagotto, and E. Nasi. Theoretical isochrones from models with new radiative opacities. A&AS, 106:275–302, Aug 1994.

E. Bertin and S. Arnouts. SExtractor: Software for source extraction. A&AS, 117: 393–404, June 1996.

A. W. Blain, S. C. Chapman, I. Smail, and R. Ivison. Accurate Spectral Energy Distributions and Selection Effects for High-Redshift Dusty Galaxies: A New Hot Population to Discover with the Spitzer Space Telescope? ApJ, 611:52–58, Aug 2004.

A. W. Blain, I. Smail, R. J. Ivison, and J.-P. Kneib. The history of star formation in dusty galaxies. MNRAS, 302:632–648, Feb 1999.

M. Bolzonella, J.-M. Miralles, and R. Pelló. Photometric redshifts based on standard SED fitting procedures. A&A, 363:476–492, Nov 2000.

G. D. Bothun and A. Dressler. Blue disk galaxies in the Coma Cluster - Analogs to Z = 0.5 cluster members? ApJ, 301:57–64, Feb 1986.

F. Bournaud, C. J. Jog, and F. Combes. Galaxy mergers with various mass ratios: Properties of remnants. A&A, 437:69–85, July 2005.

R. G. Bower, S. L. Morris, R. Bacon, R. J. Wilman, M. Sullivan, S. Chapman, R. L. Davies, P. T. de Zeeuw, and E. Emsellem. Deep SAURON spectral imaging of the diffuse Lyman α halo LAB1 in SSA 22. MNRAS, 351:63–69, June 2004.

G. Bruzual and S. Charlot. Stellar population synthesis at the resolution of 2003. MNRAS, 344:1000–1028, Oct 2003.

A. J. Bunker, L. A. Moustakas, and M. Davis. Resolving the Stellar Populations in a z=4 Lensed Galaxy. ApJ, 531:95–117, March 2000.

H. A. Bushouse, K. D. Borne, L. Colina, R. A. Lucas, M. Rowan-Robinson, A. C. Baker, D. L. Clements, A. Lawrence, and S. Oliver. Ultraluminous Infrared Galaxies: Atlas of Near-Infrared Images. ApJS, 138:1–18, Jan 2002.

D. Calzetti, A. L. Kinney, and T. Storchi-Bergmann. Dust extinction of the stellar continua in starburst galaxies: The ultraviolet and optical extinction law. ApJ, 429: 582–601, July 1994.

L. E. Campusano, R. Pelló, J.-P. Kneib, J.-F. Le Borgne, B. Fort, R. Ellis, Y. Mellier, and I. Smail. VLT spectroscopy of galaxies lensed by the AC 114 cluster:. Implications for the mass model and the study of low-luminosity galaxies at high-redshift. A&A, 378:394–407, Nov 2001.

C. L. Carilli, H. J. A. Roettgering, R. van Ojik, G. K. Miley, and W. J. M. van Breugel. Radio Continuum Imaging of High-Redshift Radio Galaxies. ApJS, 109:1–+, March 1997.

B. Cavanagh, P. Hirst, T. Jenness, F. Economou, M. J. Currie, S. Todd, and S. D. Ryder. ORAC-DR: One Pipeline for Multiple Telescopes. In *ASP Conf. Ser. 295: Astronomical Data Analysis Software and Systems XII*, pages 237–+, 2003.

R. Cen and J. P. Ostriker. Where Are the Baryons? ApJ, 514:1–6, March 1999.

K. C. Chambers, G. K. Miley, and W. van Breugel. Alignment of radio and optical orientations in high-redshift radio galaxies. Nature, 329:604–606, Oct 1987.

S. C. Chapman, A. W. Blain, R. J. Ivison, and I. R. Smail. A median redshift of 2.4 for galaxies bright at submillimetre wavelengths. Nature, 422:695–698, Apr 2003a.

S. C. Chapman, A. W. Blain, I. Smail, and R. J. Ivison. A Redshift Survey of the Submillimeter Galaxy Population. ApJ, 622:772–796, Apr 2005.

S. C. Chapman, E. A. Richards, G. F. Lewis, G. Wilson, and A. J. Barger. The Nature of the Bright Submillimeter Galaxy Population: A Radio-preselected Sample with I¿˜25. ApJ, 548:L147–L151, Feb 2001.

S. C. Chapman, D. Scott, C. C. Steidel, C. Borys, M. Halpern, S. L. Morris, K. L. Adelberger, M. Dickinson, M. Giavalisco, and M. Pettini. A search for the submillimetre counterparts to Lyman break galaxies. MNRAS, 319:318–330, Nov 2000.

S. C. Chapman, I. Smail, A. W. Blain, and R. J. Ivison. A Population of Hot, Dusty Ultraluminous Galaxies at z ˜ 2. ApJ, 614:671–678, Oct 2004a.

S. C. Chapman, I. Smail, R. J. Ivison, and A. W. Blain. The effect of lensing on the identification of SCUBA galaxies. MNRAS, 335:L17–L21, Sept 2002.

S. C. Chapman, I. Smail, R. Windhorst, T. Muxlow, and R. J. Ivison. Evidence for Extended, Obscured Starbursts in Submillimeter Galaxies. ApJ, 611:732–738, Aug 2004b.

S. C. Chapman, R. Windhorst, S. Odewahn, H. Yan, and C. Conselice. Hubble Space Telescope Images of Submillimeter Sources: Large Irregular Galaxies at High Redshift. ApJ, 599:92–104, Dec 2003b.

S. Cole, C. G. Lacey, C. M. Baugh, and C. S. Frenk. Hierarchical galaxy formation. MNRAS, 319:168–204, Nov 2000.

S. Cole, P. Norberg, C. M. Baugh, C. S. Frenk, J. Bland-Hawthorn, T. Bridges, and R. Cannon. The 2dF galaxy redshift survey: near-infrared galaxy luminosity functions. MNRAS, 326:255–273, Sept 2001.

J. J. Condon, M. L. Anderson, and G. Helou. Correlations between the far-infrared, radio, and blue luminosities of spiral galaxies. ApJ, 376:95–103, July 1991.

M. R. Corbin and T. A. Boroson. Combined Ultraviolet and Optical Spectra of 48 Low-Redshift QSOs and the Relation of the Continuum and Emission-Line Properties. ApJS, 107:69–+, Nov 1996.

W. J. Couch and R. M. Sharples. A spectroscopic study of three rich galaxy clusters at Z = 0.31. MNRAS, 229:423–456, Dec 1987.

S. Courteau and H.-W. Rix. Maximal Disks and the Tully-Fisher Relation. *Bulletin of the American Astronomical Society*, 29:1332–+, Dec 1997.

L. L. Cowie, A. J. Barger, and J.-P. Kneib. Faint Submillimeter Counts from Deep 850 Micron Observations of the Lensing Clusters A370, A851, and A2390. AJ, 123: 2197–2205, May 2002.

O. Czoske, J.-P. Kneib, G. Soucail, T. J. Bridges, Y. Mellier, and J.-C. Cuillandre. A wide-field spectroscopic survey of the cluster of galaxies Cl0024+1654. I. The catalogue. A&A, 372:391–405, June 2001.

E. Daddi, A. Cimatti, L. Pozzetti, H. Hoekstra, H. J. A. Röttgering, A. Renzini, G. Zamorani, and F. Mannucci. Detection of strong clustering of extremely red objects: implications for the density of z>1 ellipticals. A&A, 361:535–549, Sept 2000.

H. Dannerbauer, M. D. Lehnert, D. Lutz, L. Tacconi, F. Bertoldi, C. Carilli, R. Genzel, and K. M. Menten. The Faint Counterparts of MAMBO Millimeter Sources near the New Technology Telescope Deep Field. ApJ, 606:664–682, May 2004.

S. Dawson, N. McCrady, D. Stern, M. E. Eckart, H. Spinrad, M. C. Liu, and J. R. Graham. Optical and Near-Infrared Spectroscopy of a High-Redshift Hard X-Ray-emitting Spiral Galaxy. AJ, 125:1236–1246, March 2003.

G. Denicoló, R. Terlevich, and E. Terlevich. New light on the search for low-metallicity galaxies - I. The N2 calibrator. MNRAS, 330:69–74, Feb 2002.

A. Dey, J. R. Graham, R. J. Ivison, I. Smail, G. S. Wright, and M. C. Liu. Observations of a Z = 1.44 Dusty, Ultraluminous Galaxy and Implications for Deep Submillimeter Surveys. ApJ, 519:610–621, July 1999.

G. P. di Benedetto. Towards a fundamental calibration of stellar parameters of A, F, G, K dwarfs and giants. A&A, 339:858–871, Nov 1998.

M. A. Dopita, M. Pereira, L. J. Kewley, and M. Capaccioli. Star Formation Rates in Interacting Starburst Galaxies. ApJS, 143:47–72, Nov 2002.

D. Downes and P. M. Solomon. Molecular Gas and Dust at z=2.6 in SMM J14011+0252: A Strongly Lensed Ultraluminous Galaxy, Not a Huge Massive Disk. ApJ, 582:37–48, Jan 2003.

A. Dressler and J. E. Gunn. Spectroscopy of galaxies in distant clusters. I - First results for 3C 295 and 0024 + 1654. ApJ, 263:533–545, Dec 1982.

A. Dressler and J. E. Gunn. Spectroscopy of galaxies in distant clusters. IV - A catalog of photometry and spectroscopy for galaxies in seven clusters with Z in the range of 0.35 to 0.55. ApJS, 78:1–60, Jan 1992.

J. Dunlop. Sub-mm Clues to Elliptical Galaxy Formation. In *Deep Millimeter Surveys: Implications for Galaxy Formation and Evolution*, pages 11–+, 2001.

F. W. Dyson and A. S. Eddington. Astrographic Catalogue, Greenwich, Analysis of the proper motions of the reference stars. MNRAS, 62:291, May 1920.

T. Ebbels, R. Ellis, J. Kneib, J. Leborgne, R. Pello, I. Smail, and B. Sanahuja. Spectroscopic confirmation of redshifts predicted by gravitational lensing. MNRAS, 295:75–+, March 1998.

A. C. Edge, G. P. Smith, D. J. Sand, T. Treu, H. Ebeling, S. W. Allen, and P. G. van Dokkum. A Unique Small-Scale Gravitational Arc in A1201. ApJ, 599:L69–L72, Dec 2003.

O. J. Eggen, D. Lynden-Bell, and A. R. Sandage. Evidence from the motions of old stars that the Galaxy collapsed. ApJ, 136:748–+, Nov 1962.

A. Einstein. Sitzungsber. *Sitzungsber.*, PreuB:Akad, Dec 1915.

A. Einstein. Lens-Like Action of a Star by the Deviation of Light in the Gravitational Field. *Science*, 84:506–507, Dec 1936.

F. Eisenhauer, M. Tecza, S. Mengel, N. A. Thatte, C. Roehrle, K. Bickert, and J. Schreiber. Imaging the universe in 3D with the VLT: the next-generation field spectrometer SPIFFI. In *Proc. SPIE Vol. 4008, p. 289-297, Optical and IR Telescope Instrumentation and Detectors, Masanori Iye; Alan F. Moorwood; Eds.*, pages 289–297, Aug 2000.

R. Ellis, M. R. Santos, J. Kneib, and K. Kuijken. A Faint Star-forming System Viewed through the Lensing Cluster Abell 2218: First Light at z~=5.6? ApJ, 560:L119–L122, Oct 2001.

D. K. Erb, A. E. Shapley, C. C. Steidel, M. Pettini, K. L. Adelberger, M. P. Hunt, A. F. M. Moorwood, and J. Cuby. Hα Spectroscopy of Galaxies at z>2: Kinematics and Star Formation. ApJ, 591:101–118, July 2003.

A. S. Evans. Near-Infrared Spectroscopy of Powerful Radio Galaxies at Z = 2.2-2.6. ApJ, 498:553–+, May 1998.

S. M. Faber and J. S. Gallagher. Masses and mass-to-light ratios of galaxies. ARA&A, 17:135–187, 1979.

S. M. Faber and R. E. Jackson. Velocity dispersions and mass-to-light ratios for elliptical galaxies. ApJ, 204:668–683, March 1976.

G. J. Ferland and D. E. Osterbrock. IUE spectra and a resulting model of Seyfert 2 galaxies. ApJ, 300:658–668, Jan 1986.

H. Flores, F. Hammer, D. Elbaz, C. J. Cesarsky, Y. C. Liang, D. Fadda, and N. Gruel. Star formation rates of distant luminous infrared galaxies derived from Hα and IR luminosities. A&A, 415:885–888, March 2004.

B. Fort, J. L. Prieur, G. Mathez, Y. Mellier, and G. Soucail. Faint distorted structures in the core of A 370 - Are they gravitationally lensed galaxies at Z about 1? A&A, 200: L17–L20, July 1988.

A. Franceschini, S. Berta, D. Rigopoulou, H. Aussel, C. J. Cesarsky, D. Elbaz, R. Genzel, E. Moy, S. Oliver, M. Rowan-Robinson, and P. P. Van der Werf. Infrared spectroscopy of faint 15 mu m sources in the Hubble Deep Field South: First hints at the properties of the sources of the IR background. A&A, 403:501–522, May 2003.

M. Franx, G. D. Illingworth, D. D. Kelson, P. G. van Dokkum, and K. Tran. A Pair of Lensed Galaxies at z=4.92 in the Field of CL 1358+62. ApJ, 486:L75+, Sept 1997.

D. T. Frayer, L. Armus, N. Z. Scoville, A. W. Blain, N. A. Reddy, R. J. Ivison, and I. Smail. The ¡ITAL¿z¡/ITAL¿=2.51 Extremely Red Submillimeter Galaxy SMM J04431+0210. AJ, 126:73–80, July 2003.

D. T. Frayer, R. J. Ivison, N. Z. Scoville, A. S. Evans, M. S. Yun, I. Smail, A. J. Barger, A. W. Blain, and J.-P. Kneib. Molecular Gas in the Z = 2.565 Submillimeter Galaxy SMM J14011+0252. ApJ, 514:L13–L16, March 1999.

A. Fritz, B. L. Ziegler, R. G. Bower, I. Smail, and R. L. Davies. The Evolutionary Status of Early-type Galaxies in Abell 2390. Ap&SS, 285:61–66, 2003.

B. Frye and T. Broadhurst. Discovery of Red Selected Arcs at Z = 4.04 behind Abell 2390. ApJ, 499:L115+, June 1998.

J. Gallego, J. Zamorano, A. Aragon-Salamanca, and M. Rego. The Current Star Formation Rate of the Local Universe. ApJ, 455:L1+, Dec 1995.

D. R. Garnett, G. A. Shields, E. D. Skillman, S. P. Sagan, and R. J. Dufour. Interstellar Abundance Gradients in NGC 2403: Comparison to M33. ApJ, 489:63–+, Nov 1997.

M. A. Garrett. The FIR/Radio correlation of high redshift galaxies in the region of the HDF-N. A&A, 384:L19–L22, March 2002.

R. Genzel, A. J. Baker, L. J. Tacconi, D. Lutz, P. Cox, S. Guilloteau, and A. Omont. Spatially Resolved Millimeter Interferometry of SMM J02399-0136: AVery Massive Galaxy at z = 2.8. ApJ, 584:633–642, Feb 2003.

M. Giavalisco, H. C. Ferguson, A. M. Koekemoer, M. Dickinson, D. M. Alexander, F. E. Bauer, J. Bergeron, C. Biagetti, W. N. Brandt, S. Casertano, C. Cesarsky, E. Chatzichristou, C. Conselice, S. Cristiani, L. Da Costa, T. Dahlen, D. de Mello, P. Eisenhardt, T. Erben, S. M. Fall, C. Fassnacht, R. Fosbury, A. Fruchter, J. P. Gardner, N. Grogin, R. N. Hook, A. E. Hornschemeier, R. Idzi, S. Jogee, C. Kretchmer, V. Laidler, K. S. Lee, M. Livio, R. Lucas, P. Madau, B. Mobasher, L. A. Moustakas, M. Nonino, P. Padovani, C. Papovich, Y. Park, S. Ravindranath, A. Renzini, M. Richardson, A. Riess, P. Rosati, M. Schirmer, E. Schreier, R. S. Somerville, H. Spinrad, D. Stern, M. Stiavelli, L. Strolger, C. M. Urry, B. Vandame, R. Williams, and C. Wolf. The Great Observatories Origins Deep Survey: Initial Results from Optical and Near-Infrared Imaging. ApJ, 600:L93–L98, Jan 2004.

G. Gilmore, R. F. G. Wyse, and K. Kuijken. Kinematics, chemistry, and structure of the Galaxy. ARA&A, 27:555–627, 1989.

M. D. Gladders, H. K. C. Yee, and E. Ellingson. Discovery of a z =0.77 Galaxy Cluster with Multiple, Bright, Strong-Lensing Arcs. AJ, 123:1–9, Jan 2002.

K. Glazebrook and J. Bland-Hawthorn. Microslit Nod-Shuffle Spectroscopy: A Technique for Achieving Very High Densities of Spectra. PASP, 113:197–214, Feb 2001.

T. Goto, R. C. Nichol, S. Okamura, M. Sekiguchi, C. J. Miller, M. Bernardi, A. Hopkins, C. Tremonti, A. Connolly, F. J. Castander, J. Brinkmann, M. Fukugita, M. Harvanek, Z. Ivezic, S. J. Kleinman, J. Krzesinski, D. Long, J. Loveday, E. H. Neilsen, P. R. Newman, A. Nitta, S. A. Snedden, and M. Subbarao. H-delta-Strong Galaxies in the Sloan Digital Sky Survey: I. The Catalog. PASJ, 55:771–787, June 2003.

T. R. Greve, F. Bertoldi, I. Smail, R. Neri, S. C. Chapman, A. W. Blain, R. J. Ivison, R. Genzel, A. Omont, P. Cox, L. Tacconi, and J.-P. Kneib. An interferometric CO survey of luminous submillimetre galaxies. MNRAS, 359:1165–1183, May 2005.

T. R. Greve, R. J. Ivison, F. Bertoldi, J. A. Stevens, J. S. Dunlop, D. Lutz, and C. L. Carilli. A 1200-μm MAMBO survey of ELAISN2 and the Lockman Hole - I. Maps, sources and number counts. MNRAS, 354:779–797, Nov 2004.

A. H. Guth. Inflationary universe: A possible solution to the horizon and flatness problems. Phys. Rev. D, 23:347–356, Jan 1981.

G. K. T. Hau, D. Carter, and M. Balcells. The shell elliptical galaxy NGC 2865: evolutionary population synthesis of a kinematically distinct core. MNRAS, 306:437–460, June 1999.

T. G. Hawarden, S. K. Leggett, M. B. Letawsky, D. R. Ballantyne, and M. M. Casali. JHK standard stars for large telescopes: the UKIRT Fundamental and Extended lists. MNRAS, 325:563–574, Aug 2001.

E. Hawkins, S. Maddox, S. Cole, O. Lahav, D. S. Madgwick, P. Norberg, J. A. Peacock, I. K. Baldry, C. M. Baugh, J. Bland-Hawthorn, T. Bridges, R. Cannon, M. Colless, C. Collins, W. Couch, G. Dalton, R. De Propris, S. P. Driver, G. Efstathiou, R. S. Ellis, C. S. Frenk, K. Glazebrook, C. Jackson, B. Jones, I. Lewis, S. Lumsden, W. Percival,

B. A. Peterson, W. Sutherland, and K. Taylor. The 2dF Galaxy Redshift Survey: correlation functions, peculiar velocities and the matter density of the Universe. MNRAS, 346:78–96, Nov 2003.

M. P. Haynes, R. Giovanelli, J. J. Salzer, G. Wegner, W. Freudling, L. N. da Costa, T. Herter, and N. P. Vogt. The I-Band Tully-Fisher Relation for SC Galaxies: Optical Imaging Data. AJ, 117:1668–1687, Apr 1999.

T. M. Heckman, M. D. Lehnert, D. K. Strickland, and L. Armus. Absorption-Line Probes of Gas and Dust in Galactic Superwinds. ApJS, 129:493–516, Aug 2000.

L. Hernquist and M. L. Weil. Starbursts in the nuclei of shell galaxies. Nature, 358: 734–736, Aug 1992.

F. W. Herschel. On the Construction of the Heavens. *Phil. Trans*, 78:213, 1785.

E. Hubble and M. L. Humason. The Velocity-Distance Relation among Extra-Galactic Nebulae. ApJ, 74:43–+, July 1931.

E. P. Hubble. A spiral nebula as a stellar system, Messier 31. ApJ, 69:103–158, March 1929.

R. J. Ivison, T. R. Greve, I. Smail, J. S. Dunlop, N. D. Roche, S. E. Scott, M. J. Page, J. A. Stevens, O. Almaini, A. W. Blain, C. J. Willott, M. J. Fox, D. G. Gilbank, S. Serjeant, and D. H. Hughes. Deep radio imaging of the SCUBA 8-mJy survey fields: submillimetre source identifications and redshift distribution. MNRAS, 337:1–25, Nov 2002.

R. J. Ivison, I. Smail, A. J. Barger, J.-P. Kneib, A. W. Blain, F. N. Owen, T. H. Kerr, and L. L. Cowie. The diversity of SCUBA-selected galaxies. MNRAS, 315:209–222, June 2000.

R. J. Ivison, I. Smail, D. T. Frayer, J.-P. Kneib, and A. W. Blain. Locating the Starburst in the SCUBA Galaxy SMM J14011+0252. ApJ, 561:L45–L49, Nov 2001.

R. J. Ivison, I. Smail, J.-F. Le Borgne, A. W. Blain, J.-P. Kneib, J. Bezecourt, T. H. Kerr, and J. K. Davies. A hyperluminous galaxy at z=2.8 found in a deep submillimetre survey. MNRAS, 298:583–593, Aug 1998.

F. Iwamuro, K. Motohara, T. Maihara, M. Kimura, S. Eto, T. Shima, D. Mochida, S. Wada, S. Imai, and K. Aoki. Infrared Spectroscopy of 15 Radio Galaxies at 2<z<2.6. ApJ, 598:178–189, Nov 2003.

G. H. Jacoby, D. A. Hunter, and C. A. Christian. A library of stellar spectra. ApJS, 56: 257–281, Oct 1984.

I. Jørgensen, M. Franx, J. Hjorth, and P. G. van Dokkum. The evolution of cluster E and S0 galaxies measured from the Fundamental Plane. MNRAS, 308:833–853, Sept 1999.

I. Jorgensen, M. Franx, and P. Kjaergaard. Multicolour CCD surface photometry for E and S0 galaxies in 10 clusters. MNRAS, 273:1097–1128, Apr 1995.

S. J. Kannappan, D. G. Fabricant, and M. Franx. Physical Sources of Scatter in the Tully-Fisher Relation. AJ, 123:2358–2386, May 2002.

W. C. Keel. Escape of Lyα Emission in the Starburst Galaxy Markarian 357: a Wind's Far Side. AJ, 129:1863–1872, Apr 2005.

R. C. Kennicutt. Star Formation in Galaxies Along the Hubble Sequence. ARA&A, 36: 189–232, 1998.

J. Kneib, R. S. Ellis, M. R. Santos, and J. Richard. A Probable z~7 Galaxy Strongly Lensed by the Rich Cluster A2218: Exploring the Dark Ages. ApJ, 607:697–703, June 2004a.

J. Kneib, P. Hudelot, R. S. Ellis, T. Treu, G. P. Smith, P. Marshall, O. Czoske, I. Smail, and P. Natarajan. A Wide-Field Hubble Space Telescope Study of the Cluster Cl 0024+1654 at z=0.4. II. The Cluster Mass Distribution. ApJ, 598:804–817, Dec 2003.

J. Kneib, P. P. van der Werf, K. Kraiberg Knudsen, I. Smail, A. Blain, D. Frayer, V. Barnard, and R. Ivison. A multiply imaged, submillimetre-selected ultraluminous infrared galaxy in a galaxy group at z~ 2.5. MNRAS, 349:1211–1217, Apr 2004b.

J.-P. Kneib, R. S. Ellis, I. Smail, W. J. Couch, and R. M. Sharples. Hubble Space Telescope Observations of the Lensing Cluster Abell 2218. ApJ, 471:643–+, Nov 1996.

J. P. Kneib, Y. Mellier, B. Fort, and G. Mathez. The Distribution of Dark Matter in Distant Cluster Lenses - Modelling A:370. A&A, 273:367–+, June 1993.

J. P. Kneib, Y. Mellier, R. Pello, J. Miralda-Escude, J.-F. Le Borgne, H. Boehringer, and J.-P. Picat. Dynamics of Abell 2218 from optical and near-IR imagery of arc(let)s and the ROSAT/HRI X-ray map. A&A, 303:27–+, Nov 1995.

J. P. Kneib, J. Melnick, and Gopal-Krishna. The Cl2236-04 lens cluster. Looking for a third gravitational image? A&A, 290:L25–L28, Oct 1994.

A. M. Koekemoer, A. S. Fruchter, R. N. Hook, and W. Hack. MultiDrizzle: An Integrated Pyraf Script for Registering, Cleaning and Combining Images. In *The 2002 HST Calibration Workshop : Hubble after the Installation of the ACS and the NICMOS Cooling System, Proceedings of a Workshop held at the Space Telescope Science Institute, Baltimore, Maryland, October 17 and 18, 2002. Edited by Santiago Arribas, Anton Koekemoer, and Brad Whitmore. Baltimore, MD: Space Telescope Science Institute, 2002., p.339*, pages 339–+, 2002.

M. Kojima and M. Noguchi. Sinking Satellite Disk Galaxies. I. Shell Formation Preceded by Cessation of Star Formation. ApJ, 481:132–+, May 1997.

A. V. Kravtsov, A. A. Klypin, J. S. Bullock, and J. R. Primack. The Cores of Dark Matter-dominated Galaxies: Theory versus Observations. ApJ, 502:48–+, July 1998.

F. Lamareille, M. Mouhcine, T. Contini, I. Lewis, and S. Maddox. The luminosity-metallicity relation in the local Universe from the 2dF Galaxy Redshift Survey. MNRAS, 350:396–406, May 2004.

R. B. Larson, B. M. Tinsley, and C. N. Caldwell. The evolution of disk galaxies and the origin of S0 galaxies. ApJ, 237:692–707, May 1980.

R. J. Lavery and J. P. Henry. Evidence for galaxy-galaxy interactions as an active agent of the 'Butcher-Oemler' effect at a redshift of 0.2. ApJ, 330:596–600, July 1988.

M. J. Ledlow, I. Smail, F. N. Owen, W. C. Keel, R. J. Ivison, and G. E. Morrison. Gemini Multi-Object Spectrograph Observations of SCUBA Galaxies behind A851. ApJ, 577: L79–L82, Oct 2002.

C. Leitherer and T. M. Heckman. Synthetic properties of starburst galaxies. ApJS, 96: 9–38, Jan 1995.

A. D. Lewis, D. A. Buote, and J. T. Stocke. Chandra Observations of A2029: The Dark Matter Profile Down to below 0.01rvir in an Unusually Relaxed Cluster. ApJ, 586: 135–142, March 2003.

S. J. Lilly, C. M. Carollo, and A. N. Stockton. The Metallicities of Star-forming Galaxies at Intermediate Redshifts 0.47<z<0.92. ApJ, 597:730–750, Nov 2003.

S. J. Lilly, S. A. Eales, W. K. P. Gear, F. Hammer, O. Le Fèvre, D. Crampton, J. R. Bond, and L. Dunne. The Canada-United Kingdom Deep Submillimeter Survey. II. First Identifications, Redshifts, and Implications for Galaxy Evolution. ApJ, 518:641–655, June 1999.

C. T. Liu and R. C. Kennicutt. A Spectrophotometric Survey of Merging Galaxies. ApJS, 100:325–+, Oct 1995.

D. Lutz, S. Veilleux, and R. Genzel. Mid-Infrared and Optical Spectroscopy of Ultraluminous Infrared Galaxies: A Comparison. ApJ, 517:L13–L17, May 1999.

P. Madau, H. C. Ferguson, M. E. Dickinson, M. Giavalisco, C. C. Steidel, and A. Fruchter. High-redshift galaxies in the Hubble Deep Field: colour selection and star formation history to z~4. MNRAS, 283:1388–1404, Dec 1996.

J. C. Manners, O. Johnson, O. Almaini, C. J. Willott, E. Gonzalez-Solares, A. Lawrence, R. G. Mann, I. Perez-Fournon, J. S. Dunlop, R. G. McMahon, S. J. Oliver, M. Rowan-Robinson, and S. Serjeant. The ELAIS deep X-ray survey - I. Chandra source catalogue and first results. MNRAS, 343:293–305, July 2003.

C. L. Martin. Mapping Large-Scale Gaseous Outflows in Ultraluminous Galaxies with Keck II ESI Spectra: Variations in Outflow Velocity with Galactic Mass. ApJ, 621: 227–245, March 2005.

D. S. Mathewson, V. L. Ford, and M. Buchhorn. A southern sky survey of the peculiar velocities of 1355 spiral galaxies. ApJS, 81:413–659, Aug 1992.

P. J. McCarthy, W. van Breugel, H. Spinrad, and S. Djorgovski. A correlation between the radio and optical morphologies of distant 3Cr radio galaxies. ApJ, 321:L29–L33, Oct 1987.

I. S. McLean, E. E. Becklin, O. Bendiksen, G. Brims, J. Canfield, D. F. Figer, J. R. Graham, J. Hare, F. Lacayanga, J. E. Larkin, S. B. Larson, N. Levenson, N. Magnone, H. Teplitz, and W. Wong. Design and development of NIRSPEC: a near-infrared echelle spectrograph for the Keck II telescope. In *Proc. SPIE Vol. 3354, p. 566-578, Infrared Astronomical Instrumentation, Albert M. Fowler; Ed.*, pages 566–578, Aug 1998.

Y. Mellier, B. Fort, G. Soucail, G. Mathez, and M. Cailloux. Spectroscopy of the gravitational arcs in CL 2244 - 02, A370 (arclet A5), and CL 0024 + 1654. ApJ, 380:334–343, Oct 1991.

M. Messier. . *Connaisance des Temps*, 1784.

L. Metcalfe, J.-P. Kneib, B. McBreen, B. Altieri, A. Biviano, M. Delaney, D. Elbaz, M. F. Kessler, K. Leech, K. Okumura, S. Ott, R. Perez-Martinez, C. Sanchez-Fernandez, and B. Schulz. An ISOCAM survey through gravitationally lensing galaxy clusters. I. Source lists and source counts for A370, A2218 and A2390. A&A, 407:791–822, Sept 2003.

J. C. Mihos and L. Hernquist. Gasdynamics and Starbursts in Major Mergers. ApJ, 464: 641–+, June 1996.

B. Milvang-Jensen, A. Aragón-Salamanca, G. K. T. Hau, I. Jørgensen, and J. Hjorth. The Tully-Fisher relation of cluster spirals at z= 0.83. MNRAS, 339:L1–L5, Feb 2003.

J. Miralda-Escudé. A Test of the Collisional Dark Matter Hypothesis from Cluster Lensing. ApJ, 564:60–64, Jan 2002.

A. F. Moorwood. ISAAC: a 1- to 5-um imager/spectrometer for the VLT. In *Proc. SPIE Vol. 2871, p. 1146-1151, Optical Telescopes of Today and Tomorrow, Arne L. Ardeberg; Ed.*, pages 1146–1151, March 1997.

J. S. Mulchaey, A. Koratkar, M. J. Ward, A. S. Wilson, M. Whittle, R. R. J. Antonucci, A. L. Kinney, and T. Hurt. Multiwavelength tests of the dusty torus model for Seyfert galaxies. ApJ, 436:586–598, Dec 1994.

R. F. Mushotzky, L. L. Cowie, A. J. Barger, and K. A. Arnaud. Resolving the extragalactic hard X-ray background. Nature, 404:459–464, March 2000.

R. Neri, R. Genzel, R. J. Ivison, F. Bertoldi, A. W. Blain, S. C. Chapman, P. Cox, T. R. Greve, A. Omont, and D. T. Frayer. Interferometric Observations of Powerful CO Emission from Three Submillimeter Galaxies at z=2.39, 2.51, and 3.35. ApJ, 597: L113–L116, Nov 2003.

I. Newton. Optiks: A Treastise of the reflexions, refractions, inflexions and colours of light. *The Royal Society London*, 1704.

K. Nilsson, L. O. Takalo, T. Pursimo, A. Sillanpää, J. Heidt, S. J. Wagner, S. A. Laurent-Muehleisen, and W. Brinkmann. Discovery of a blue arc near the BL Lacertae object RGB 1745+398. A&A, 343:81–85, March 1999.

S. A. Norton, K. Gebhardt, A. I. Zabludoff, and D. Zaritsky. The Spatial Distribution and Kinematics of Stellar Populations in E+A Galaxies. ApJ, 557:150–164, Aug 2001.

D. E. Osterbrock and J. M. Shuder. Emission-line profiles in Seyfert 1 galaxies. ApJS, 49:149–174, May 1982.

C. Packham, K. L. Thompson, A. Zurita, J. H. Knapen, I. Smail, R. Greimel, D. F. M. Folha, C. Benn, A. Humphrey, R. Rutten, D. Ciardi, M. Bec, R. Bingham, S. Craig, K. Dee, D. Ives, P. Jolley, P. Moore, M. Pi i Puig, S. Rees, G. Talbot, and S. Worswick. INGRID: A near-infrared camera for the William Herschel Telescope. MNRAS, 345: 395–405, Oct 2003.

R. Pelló, J. P. Kneib, J. F. Le Borgne, J. Bézecourt, T. M. Ebbels, I. Tijera, G. Bruzual, J. M. Miralles, I. Smail, G. Soucail, and T. J. Bridges. Two multiple-imaged Z = 4.05 galaxies in the cluster-lens Abell 2390. A&A, 346:359–368, June 1999.

R. Pello, J. F. Le Borgne, B. Sanahuja, G. Mathez, and B. Fort. The system of arcs in the cluster of galaxies Abell 2218 - Photometry, spectroscopy and geometry. A&A, 266: 6–14, Dec 1992.

R. Pello, B. Sanahuja, J. Le Borgne, G. Soucail, and Y. Mellier. A straight gravitational image in Abell 2390 - A striking case of lensing by a cluster of galaxies. ApJ, 366: 405–411, Jan 1991.

R. Pello-Descayre, B. Sanahuja, G. Soucail, G. Mathez, and E. Ojero. Detection and photometry of a complex system in the center of the A 2218 cluster of galaxies. A&A, 190:L11–L14, Jan 1988.

A. A. Penzias and R. W. Wilson. A Measurement of Excess Antenna Temperature at 4080 Mc/s. ApJ, 142:419–421, July 1965.

W. J. Percival, W. Sutherland, J. A. Peacock, C. M. Baugh, J. Bland-Hawthorn, T. Bridges, R. Cannon, S. Cole, M. Colless, C. Collins, W. Couch, G. Dalton, R. De Propris, S. P. Driver, G. Efstathiou, R. S. Ellis, C. S. Frenk, K. Glazebrook, C. Jackson, O. Lahav, I. Lewis, S. Lumsden, S. Maddox, S. Moody, P. Norberg, B. A. Peterson, and K. Taylor. Parameter constraints for flat cosmologies from cosmic microwave background and 2dFGRS power spectra. MNRAS, 337:1068–1080, Dec 2002.

M. Pettini and B. E. J. Pagel. [OIII]/[NII] as an abundance indicator at high redshift. MNRAS, 348:L59–L63, March 2004.

M. Pettini, A. E. Shapley, C. C. Steidel, J. Cuby, M. Dickinson, A. F. M. Moorwood, K. L. Adelberger, and M. Giavalisco. The Rest-Frame Optical Spectra of Lyman Break Galaxies: Star Formation, Extinction, Abundances, and Kinematics. ApJ, 554:981–1000, June 2001.

A. C. Phillips. Nuclear and large-scale outflow in NGC 1808. AJ, 105:486–498, Feb 1993.

M. J. Pierce and R. B. Tully. Luminosity-line width relations and the extragalactic distance scale. I - Absolute calibration. ApJ, 387:47–55, March 1992.

M. Pierre, C. Lidman, R. Hunstead, D. Alloin, M. Casali, C. Cesarsky, P. Chanial, P.-A. Duc, D. Fadda, H. Flores, S. Madden, and L. Vigroux. The first ISO ERO: A dusty quasar at z = 1.5. A&A, 372:L45–L49, June 2001.

B. M. Poggianti, I. Smail, A. Dressler, W. J. Couch, A. J. Barger, H. Butcher, R. S. Ellis, and A. J. Oemler. The Star Formation Histories of Galaxies in Distant Clusters. ApJ, 518:576–593, June 1999.

B. M. Poggianti and H. Wu. Optical Spectral Signatures of Dusty Starburst Galaxies. ApJ, 529:157–169, Jan 2000.

A. Pope, C. Borys, D. Scott, C. Conselice, M. Dickinson, and B. Mobasher. The Hubble Deep Field North SCUBA Super-map - III. Optical and near-infrared properties of submillimetre galaxies. MNRAS, 358:149–167, March 2005.

J. L. Puget, G. Lagache, D. L. Clements, W. T. Reach, H. Aussel, F. R. Bouchet, C. Cesarsky, F. X. Désert, H. Dole, D. Elbaz, A. Franceschini, B. Guiderdoni, and A. F. M. Moorwood. FIRBACK. I. A deep survey at 175 microns with ISO, preliminary results. A&A, 345:29–35, May 1999.

A. D. Quintero, D. W. Hogg, M. R. Blanton, D. J. Schlegel, D. J. Eisenstein, J. E. Gunn, J. Brinkmann, M. Fukugita, K. Glazebrook, and T. Goto. Selection and Photometric Properties of K+A Galaxies. ApJ, 602:190–199, Feb 2004.

S. K. Ramsay Howat, E. Ettedgui-Atad, R. J. Bennett, A. Bridger, R. Content, M. A. Ellis, P. R. Hastings, M. Strachan, R. Wall, and M. Wells. UIST: an imaging spectrometer for the UK Infrared Telescope. In *Proc. SPIE Vol. 3354, p. 456-467, Infrared Astronomical Instrumentation, Albert M. Fowler; Ed.*, pages 456–467, Aug 1998.

P. Ranalli, A. Comastri, and G. Setti. The 2-10 keV luminosity as a Star Formation Rate indicator. A&A, 399:39–50, Feb 2003.

S. Rawlings and M. J. Jarvis. Evidence that powerful radio jets have a profound influence on the evolution of galaxies. MNRAS, 355:L9–L12, Dec 2004.

E. A. Richards. The Nature of Radio Emission from Distant Galaxies: The 1.4 GHZ Observations. ApJ, 533:611–630, Apr 2000.

H. Rix, P. Guhathakurta, M. Colless, and K. Ing. Internal Kinematics of Distant Field Galaxies - I. Emission Linewidths for a Complete Sample of Faint Blue Galaxies at z 0.25. MNRAS, 285:779–792, March 1997.

P. F. Roche, P. W. Lucas, C. D. Mackay, E. Ettedgui-Atad, P. R. Hastings, A. Bridger, N. P. Rees, S. K. Leggett, C. Davis, A. R. Holmes, and T. Handford. UFTI: the 0.8 - 2.5 μm fast track imager for the UK infrared telescope. In *Instrument Design and Performance for Optical/Infrared Ground-based Telescopes. Edited by Iye, Masanori; Moorwood, Alan F. M. Proceedings of the SPIE, Volume 4841, pp. 901-912 (2003).*, pages 901–912, March 2003.

J. A. Rose. Constraints on stellar populations in elliptical galaxies. AJ, 90:1927–1956, Oct 1985.

D. S. Rupke, S. Veilleux, and D. B. Sanders. Keck Absorption-Line Spectroscopy of Galactic Winds in Ultraluminous Infrared Galaxies. ApJ, 570:588–609, May 2002.

E. E. Salpeter. The Luminosity Function and Stellar Evolution. ApJ, 121:161–+, Jan 1955.

D. J. Sand, T. Treu, and R. S. Ellis. The Dark Matter Density Profile of the Lensing Cluster MS 2137-23: A Test of the Cold Dark Matter Paradigm. ApJ, 574:L129–L133, Aug 2002.

D. J. Sand, T. Treu, G. P. Smith, and R. S. Ellis. The Dark Matter Distribution in the Central Regions of Galaxy Clusters: Implications for Cold Dark Matter. ApJ, 604: 88–107, March 2004.

A. Sandage. On the formation and age of the Galaxy. JRASC, 84:70–88, Apr 1990.

D. J. Schlegel. Full-Sky Mapping of the Peculiar Velocity Field with Tully-Fisher Distances to IRAS Galaxies. *Ph.D. Thesis*, Jan 1995.

P. Schneider, J. Ehlers, and E. E. Falco. *Gravitational Lenses.* Gravitational Lenses, XIV, 560 pp. 112 figs.. Springer-Verlag Berlin Heidelberg New York. Also Astronomy and Astrophysics Library, 1992.

S. E. Scott, M. J. Fox, J. S. Dunlop, S. Serjeant, J. A. Peacock, R. J. Ivison, S. Oliver, R. G. Mann, A. Lawrence, A. Efstathiou, M. Rowan-Robinson, D. H. Hughes, E. N. Archibald, A. Blain, and M. Longair. The SCUBA 8-mJy survey - I. Submillimetre maps, sources and number counts. MNRAS, 331:817–838, Apr 2002.

A. E. Shapley, D. K. Erb, M. Pettini, C. C. Steidel, and K. L. Adelberger. Evidence for Solar Metallicities in Massive Star-forming Galaxies at z>2. ApJ, 612:108–121, Sept 2004.

A. E. Shapley, C. C. Steidel, M. Pettini, and K. L. Adelberger. Rest-Frame Ultraviolet Spectra of z~3 Lyman Break Galaxies. ApJ, 588:65–89, May 2003.

Y. Shioya, K. Bekki, and W. J. Couch. Formation and Evolution of Red Hδ-strong Galaxies in Distant Clusters: Two Different Evolutionary Paths to S0 Galaxies? ApJ, 601:654–665, Feb 2004.

M. Shure, D. W. Toomey, J. Rayner, P. Onaka, A. Denault, W. Stahlberger, D. Watanabe, K. Criez, L. Robertson, and D. Cook. NSFCAM - A New Infrared Array Camera for the NASA Infrared Telescope Facility. *Bulletin of the American Astronomical Society*, 25:1468–+, Dec 1993.

C. Simpson, J. S. Dunlop, S. A. Eales, R. J. Ivison, S. E. Scott, S. J. Lilly, and T. M. A. Webb. Deep near-infrared spectroscopy of submillimetre-selected galaxies. MNRAS, 353:179–188, Sept 2004.

C. Simpson, S. Rawlings, and M. Lacy. Thermal-infrared imaging of 3C radio galaxies at z~1. MNRAS, 306:828–842, July 1999.

I. Smail, S. C. Chapman, A. W. Blain, and R. J. Ivison. The Rest-Frame Optical Properties of SCUBA Galaxies. ApJ, 616:71–85, Nov 2004.

I. Smail, S. C. Chapman, R. J. Ivison, A. W. Blain, T. Takata, T. M. Heckman, J. S. Dunlop, and K. Sekiguchi. A vigorous starburst in the SCUBA galaxy N2 850.4. MNRAS, 342:1185–1193, July 2003a.

I. Smail, A. Dressler, J. Kneib, R. S. Ellis, W. J. Couch, R. M. Sharples, and A. J. Oemler. Hubble Space Telescope Observations of Giant Arcs: High-Resolution Imaging of Distant Field Galaxies. ApJ, 469:508–+, Oct 1996.

I. Smail, R. J. Ivison, and A. W. Blain. A Deep Sub-millimeter Survey of Lensing Clusters: A New Window on Galaxy Formation and Evolution. ApJ, 490:L5+, Nov 1997.

I. Smail, R. J. Ivison, A. W. Blain, and J.-P. Kneib. The nature of faint submillimetre-selected galaxies. MNRAS, 331:495–520, March 2002.

I. Smail, R. J. Ivison, D. G. Gilbank, J. S. Dunlop, W. C. Keel, K. Motohara, and J. A. Stevens. A SCUBA Galaxy in the Protocluster around 53W002 at z=2.4. ApJ, 583: 551–558, Feb 2003b.

I. Smail, R. J. Ivison, J.-P. Kneib, L. L. Cowie, A. W. Blain, A. J. Barger, F. N. Owen, and G. Morrison. The discovery of ERO counterparts to faint submillimetre galaxies. MNRAS, 308:1061–1068, Oct 1999.

I. Smail, H. Kuntschner, T. Kodama, G. P. Smith, C. Packham, A. S. Fruchter, and R. N. Hook. A photometric study of the ages and metallicities of early-type galaxies in A 2218. MNRAS, 323:839–849, May 2001.

G. P. Smith. PhD Theseis. MNRAS, 000:000–000, Oct 2003.

G. P. Smith, A. C. Edge, V. R. Eke, R. C. Nichol, I. Smail, and J. Kneib. Measuring sigma-8 with Cluster Lensing: Biases from Unrelaxed Clusters. ApJ, 590:L79–L82, June 2003.

G. P. Smith, J. Kneib, H. Ebeling, O. Czoske, and I. Smail. A Hubble Space Telescope Lensing Survey of X-Ray Luminous Galaxy Clusters. I. A383. ApJ, 552:493–503, May 2001a.

G. P. Smith, I. Smail, J.-P. Kneib, C. J. Davis, M. Takamiya, H. Ebeling, and O. Czoske. A Hubble Space Telescope lensing survey of X-ray luminous galaxy clusters - III. A multiply imaged extremely red galaxy at z=1.6. MNRAS, 333:L16–L20, June 2002.

G. P. Smith, T. Treu, R. Ellis, I. Smail, J.-P. Kneib, and B. L. Frye. Near-Infrared Spectroscopy and Hubble Space Telescope Imaging of a Dusty Starburst Extremely Red Object. ApJ, 562:635–640, Dec 2001b.

J. Soldner. Uber die ablenkung eines lichtsahls von seiner geraldlinigen dewegung durch die attrsktion eines weltkorpers, an welchem er nahe vorbeigeht. *Berliner Astron. Jahrb*, 161:1804, 1804.

G. Soucail, B. Fort, Y. Mellier, and J. P. Picat. A blue ring-like structure, in the center of the A 370 cluster of galaxies. A&A, 172:L14–L16, Jan 1987.

G. Soucail, J. P. Kneib, J. P. Picat, and R. S. Ellis. Dynamics and Star Formation Properties of Giant Arcs Resolved by HST. In *ASP Conf. Ser. 146: The Young Universe: Galaxy Formation and Evolution at Intermediate and High Redshift*, pages 457–+, 1998.

D. N. Spergel and P. J. Steinhardt. Observational Evidence for Self-Interacting Cold Dark Matter. *Physical Review Letters*, 84:3760–3763, Apr 2000.

D. N. Spergel, L. Verde, H. V. Peiris, E. Komatsu, M. R. Nolta, C. L. Bennett, M. Halpern, G. Hinshaw, N. Jarosik, A. Kogut, M. Limon, S. S. Meyer, L. Page, G. S. Tucker, J. L. Weiland, E. Wollack, and E. L. Wright. First-Year Wilkinson Microwave Anisotropy Probe (WMAP) Observations: Determination of Cosmological Parameters. ApJS, 148: 175–194, Sept 2003.

V. Springel. Modelling star formation and feedback in simulations of interacting galaxies. MNRAS, 312:859–879, March 2000.

C. C. Steidel, K. L. Adelberger, A. E. Shapley, M. Pettini, M. Dickinson, and M. Giavalisco. Lyα Imaging of a Proto-Cluster Region at z=3.09. ApJ, 532:170–182, March 2000.

T. Storchi-Bergmann, D. Calzetti, and A. L. Kinney. Ultraviolet to near-infrared spectral distributions of star-forming galaxies: Metallicity and age effects. ApJ, 429:572–581, July 1994.

T. Storchi-Bergmann, R. Nemmen da Silva, M. Eracleous, J. P. Halpern, A. S. Wilson, A. V. Filippenko, M. T. Ruiz, R. C. Smith, and N. M. Nagar. Evolution of the Nuclear Accretion Disk Emission in NGC 1097: Getting Closer to the Black Hole. ApJ, 598: 956–968, Dec 2003.

K. Subramanian and S. A. Cowling. On local conditions for multiple imaging by bounded, smooth gravitational lenses. MNRAS, 219:333–346, March 1986.

A. M. Swinbank, M. L. Balogh, R. G. Bower, G. K. T. Hau, J. R. Allington-Smith, R. C. Nichol, and C. J. Miller. Gemini Multi-Object Spectrograph Integral Field Spectroscopy of a Merging System with Enhanced Balmer Absorption. ApJ, 622:260–266, March 2005a.

A. M. Swinbank, I. Smail, R. G. Bower, C. Borys, S. C. Chapman, A. W. Blain, R. J. Ivison, S. R. Howat, W. C. Keel, and A. J. Bunker. Optical and near-infrared integral field spectroscopy of the SCUBA galaxy N2 850.4. MNRAS, 359:401–407, May 2005b.

A. M. Swinbank, I. Smail, S. C. Chapman, A. W. Blain, R. J. Ivison, and W. C. Keel. The Rest-Frame Optical Spectra of SCUBA Galaxies. ApJ, 617:64–80, Dec 2004.

A. M. Swinbank, J. Smith, R. G. Bower, A. Bunker, I. Smail, R. S. Ellis, G. P. Smith, J.-P. Kneib, M. Sullivan, and J. Allington-Smith. Galaxies under the Cosmic Microscope: A Gemini Multiobject Spectrograph Study of Lensed Disk Galaxy 289 in A2218. ApJ, 598:162–167, Nov 2003.

L. J. Tacconi, R. Genzel, D. Lutz, D. Rigopoulou, A. J. Baker, C. Iserlohe, and M. Tecza. Ultraluminous Infrared Galaxies: QSOs in Formation? ApJ, 580:73–87, Nov 2002.

M. Tecza, A. J. Baker, R. I. Davies, R. Genzel, M. D. Lehnert, F. Eisenhauer, D. Lutz, N. Nesvadba, S. Seitz, L. J. Tacconi, N. A. Thatte, R. Abuter, and R. Bender. SPIFFI Observations of the Starburst SMM J14011+0252:Already Old, Fat, and Rich by z=2.565. ApJ, 605:L109–L112, Apr 2004.

M. Tegmark, M. A. Strauss, M. R. Blanton, K. Abazajian, S. Dodelson, H. Sandvik, X. Wang, D. H. Weinberg, I. Zehavi, N. A. Bahcall, F. Hoyle, D. Schlegel, R. Scoccimarro, M. S. Vogeley, A. Berlind, T. Budavari, A. Connolly, D. J. Eisenstein, D. Finkbeiner, J. A. Frieman, J. E. Gunn, L. Hui, B. Jain, D. Johnston, S. Kent, H. Lin, R. Nakajima, R. C. Nichol, J. P. Ostriker, A. Pope, R. Scranton, U. Seljak, R. K. Sheth, A. Stebbins, A. S. Szalay, I. Szapudi, Y. Xu, J. Annis, J. Brinkmann, S. Burles, F. J. Castander, I. Csabai, J. Loveday, M. Doi, M. Fukugita, B. Gillespie, G. Hennessy, D. W. Hogg, Ž. Ivezić, G. R. Knapp, D. Q. Lamb, B. C. Lee, R. H. Lupton, T. A. McKay, P. Kunszt, J. A. Munn, L. O'Connell, J. Peoples, J. R. Pier, M. Richmond, C. Rockosi, D. P. Schneider, C. Stoughton, D. L. Tucker, D. E. vanden Berk, B. Yanny, and D. G. York. Cosmological parameters from SDSS and WMAP. Phys. Rev. D, 69(10):103501–+, May 2004.

H. I. Teplitz, I. S. McLean, E. E. Becklin, D. F. Figer, A. M. Gilbert, J. R. Graham, J. E. Larkin, N. A. Levenson, and M. K. Wilcox. The Rest-Frame Optical Spectrum of MS 1512-CB58. ApJ, 533:L65–L68, Apr 2000.

Abazajian et al. (The SDSS collaboration). The First Data Release of the Sloan Digital Sky Survey. AJ, 126:2081–2086, Oct 2003.

D. Thompson, S. V. W. Beckwith, R. Fockenbrock, J. Fried, H. Hippelein, J.-S. Huang, B. von Kuhlmann, C. Leinert, K. Meisenheimer, S. Phleps, H.-J. Röser, E. Thommes, and C. Wolf. The Surface Density of Extremely Red Objects. ApJ, 523:100–106, Sept 1999.

J. L. Tonry, B. P. Schmidt, B. Barris, P. Candia, P. Challis, A. Clocchiatti, A. L. Coil, A. V. Filippenko, P. Garnavich, C. Hogan, S. T. Holland, S. Jha, R. P. Kirshner, K. Krisciunas, B. Leibundgut, W. Li, T. Matheson, M. M. Phillips, A. G. Riess, R. Schommer, R. C. Smith, J. Sollerman, J. Spyromilio, C. W. Stubbs, and N. B. Suntzeff. Cosmological Results from High-z Supernovae. ApJ, 594:1–24, Sept 2003.

T. Totani, Y. Yoshii, T. Maihara, F. Iwamuro, and K. Motohara. Near-Infrared Faint Galaxies in the Subaru Deep Field: Comparing the Theory with Observations for Galaxy Counts, Colors, and Size Distributions to K ~ 24.5. ApJ, 559:592–605, Oct 2001.

R. B. Tully and J. R. Fisher. A new method of determining distances to galaxies. A&A, 54:661–673, Feb 1977.

R. B. Tully and M. J. Pierce. Distances to Galaxies from the Correlation between Luminosities and Line Widths. III. Cluster Template and Global Measurement of Ho. ApJ, 533:744–780, Apr 2000.

P. G. van Dokkum, M. Franx, N. M. Förster Schreiber, G. D. Illingworth, E. Daddi, K. K. Knudsen, I. Labbé, A. Moorwood, H. Rix, H. Röttgering, G. Rudnick, I. Trujillo, P. van der Werf, A. van der Wel, L. van Starkenburg, and S. Wuyts. Stellar Populations and Kinematics of Red Galaxies at z> 2: Implications for the Formation of Massive Galaxies. ApJ, 611:703–724, Aug 2004.

R. van Ojik, H. J. A. Roettgering, G. K. Miley, and R. W. Hunstead. The gaseous environments of radio galaxies in the early Universe: kinematics of the Lyman α emission and spatially resolved H I absorption. A&A, 317:358–384, Jan 1997.

A. Vazdekis and N. Arimoto. A Robust Age Indicator for Old Stellar Populations. ApJ, 525:144–152, Nov 1999.

S. Veilleux, D.-C. Kim, and D. B. Sanders. Optical Spectroscopy of the IRAS 1 JY Sample of Ultraluminous Infrared Galaxies. ApJ, 522:113–138, Sept 1999.

S. Veilleux, D.-C. Kim, D. B. Sanders, J. M. Mazzarella, and B. T. Soifer. Optical Spectroscopy of Luminous Infrared Galaxies. II. Analysis of the Nuclear and Long-Slit Data. ApJS, 98:171–+, May 1995.

S. Veilleux and D. E. Osterbrock. Spectral classification of emission-line galaxies. ApJS, 63:295–310, Feb 1987.

M. A. W. Verheijen. The Ursa Major Cluster of Galaxies. V. H I Rotation Curve Shapes and the Tully-Fisher Relations. ApJ, 563:694–715, Dec 2001.

N. P. Vogt, D. A. Forbes, A. C. Phillips, C. Gronwall, S. M. Faber, G. D. Illingworth, and D. C. Koo. Optical Rotation Curves of Distant Field Galaxies: Keck Results at Reshifts to Z approximately 1. ApJ, 465:L15+, July 1996.

N. P. Vogt, A. C. Phillips, Deep Extragalactic Evolutionary Probe (DEEP) Collaboration, European Network on the Formation, and Evolution of Galaxies (TMR) Collaboration. Distant Disk Galaxies: Kinematics and Evolution to Redshift z = 1.3. *American Astronomical Society Meeting*, 200:0–+, May 2002.

N. P. Vogt, A. C. Phillips, S. M. Faber, J. Gallego, C. Gronwall, R. Guzman, G. D. Illingworth, D. C. Koo, and J. D. Lowenthal. Optical Rotation Curves of Distant Field Galaxies: Sub-L Systems. ApJ, 479:L121+, Apr 1997.

T. P. Walker, G. Steigman, H. Kang, D. M. Schramm, and K. A. Olive. Primordial nucleosynthesis redux. ApJ, 376:51–69, July 1991.

W.-H. Wang, L. L. Cowie, and A. J. Barger. An 850 Micron SCUBA Survey of the Hubble Deep Field-North GOODS Region. ApJ, 613:655–671, Oct 2004.

Y. Wang, K. Freese, P. Gondolo, and M. Lewis. Future Type Ia Supernova Data as Tests of Dark Energy from Modified Friedmann Equations. ApJ, 594:25–32, Sept 2003.

M. J. Ward, C. Done, A. C. Fabian, A. F. Tennant, and R. A. Shafer. X-ray observations of IRAS selected Seyfert galaxies and obscuration of the broad-line region. ApJ, 324: 767–775, Jan 1988.

T. M. A. Webb, S. J. Lilly, D. L. Clements, S. Eales, M. Yun, M. Brodwin, L. Dunne, and W. K. Gear. The Canada-UK Deep Submillimeter Survey. VII. Optical and Near-Infrared Identifications for the 14 Hour Field. ApJ, 597:680–698, Nov 2003.

S. D. M. White, C. S. Frenk, and M. Davis. Clustering in a neutrino-dominated universe. ApJ, 274:L1–L5, Nov 1983.

S. D. M. White and M. J. Rees. Core condensation in heavy halos - A two-stage theory for galaxy formation and clustering. MNRAS, 183:341–358, May 1978.

R. J. Wilman, M. J. Jarvis, H. J. A. Röttgering, and L. Binette. HI in the protocluster environment at z 2: absorbing haloes and the Lyα forest. MNRAS, 351:1109–1119, July 2004.

L. Yan, P. J. McCarthy, W. Freudling, H. I. Teplitz, E. M. Malumuth, R. J. Weymann, and M. A. Malkan. The Hα Luminosity Function and Global Star Formation Rate from Redshifts of 1-2. ApJ, 519:L47–L50, July 1999.

L. Yan, P. J. McCarthy, R. J. Weymann, M. A. Malkan, H. I. Teplitz, L. J. Storrie-Lombardi, M. Smith, and A. Dressler. Extremely Red Objects from the Hubble Space Telescope NICMOS Parallel Imaging Survey. AJ, 120:575–582, Aug 2000.

Y. Yang, A. I. Zabludoff, D. Zaritsky, T. R. Lauer, and J. C. Mihos. E+A Galaxies and the Formation of Early-Type Galaxies at z˜0. ApJ, 607:258–273, May 2004.

A. I. Zabludoff, D. Zaritsky, H. Lin, D. Tucker, Y. Hashimoto, S. A. Shectman, A. Oemler, and R. P. Kirshner. The Environment of "E+A" Galaxies. ApJ, 466:104–+, July 1996.

D. Zaritsky, R. C. Kennicutt, and J. P. Huchra. H II regions and the abundance properties of spiral galaxies. ApJ, 420:87–109, Jan 1994.

B. L. Ziegler, A. Böhm, K. J. Fricke, K. Jäger, H. Nicklas, R. Bender, N. Drory, A. Gabasch, R. P. Saglia, S. Seitz, J. Heidt, D. Mehlert, C. Möllenhoff, S. Noll, and E. Sutorius. The Evolution of the Tully-Fisher Relation of Spiral Galaxies. ApJ, 564: L69–L72, Jan 2002.

F. Zwicky. . *Helv. Phys. Acta.*, 6:10, 1933.

F. Zwicky. . *Phys. Rev.*, 51:L290, 1937a.

F. Zwicky. . *Phys. Rev.*, 51:L679, 1937b.